UCLA Structural / Earthquake Engineering Research Laboratory

Experimental Study of Concrete Coupling Beams Subjected to Wind and Seismic Loading Protocols

Final Report

Saman A. Abdullah
John W. Wallace

University of California, Los Angeles
Department of Civil & Environmental Engineering

Kevin Aswegan
Ron Klemencic

Magnusson Klemencic Associates, Inc.

Report to Magnuson Klemencic Associates Foundation
Henry Samueli School of Engineering and Applied Science
University of California, Los Angeles

May 2020

UCLA SEERL
2020/01
May 2020

Experimental Study of Concrete Coupling Beams Subjected to Wind and Seismic Loading Protocols

Final Report

Saman A. Abdullah
John W. Wallace

University of California, Los Angeles
Department of Civil & Environmental Engineering

Kevin Aswegan
Ron Klemencic

Magnusson Klemencic Associates, Inc.

Report to Magnuson Klemencic Associates Foundation
Henry Samueli School of Engineering and Applied Science
University of California, Los Angeles

May 2020

This page intentionally left blank

ABSTRACT

Despite advances in the characterization of wind hazards, wind tunnel testing, and structural analysis techniques, wind design of buildings is still based on prescriptive code provisions and essentially linear elastic response under ASCE 7 strength-level demands. This contrasts with seismic design, where performance-based seismic design (PBSD) of tall buildings has become common in regions impacted by strong shaking. This inconsistency in philosophy between seismic and wind design results in cases where wind loads control the design strength of either the overall lateral system (i.e., base overturning moment), some portion of the lateral system (e.g., upper one-third levels), or some structural elements (e.g., buckling-restrained brace outriggers), resulting in greater demands on energy dissipating ductile elements or actions (fuses) than needed to resist seismic demands. Furthermore, increasing demands on fuses results in greater demands for capacity protected elements (e.g., foundation, diaphragm, columns, joints) and actions (shear, anchorage), which can negate the many of the benefits of PBSD. Therefore, application of performance-based wind design (PBWD) for tall concrete buildings subjected to strong wind events, where modest nonlinearity in coupling beams (and other prescribed components) is allowed, is an attractive option. However, nonlinear wind design presents challenges that are unique to wind demands such as ratcheting effects in the along-wind direction, low cycle fatigue in the crosswind direction, and computational difficulties due to the long duration of windstorms that last for hours as opposed to an earthquake event which are generally less than a couple of minutes.

Although progress has been made on evaluating the reserve/residual seismic capacity of moderately earthquake-damaged concrete buildings in countries that have recently experienced moderate-to-strong earthquakes (i.e., Japan, New Zealand, and Chile), there is currently a lack of

robust guidelines in the US for engineers and building owners to assess post-earthquake reserve capacity and reparability in such cases. This lack of knowledge will become even more critical when evaluating reserve seismic capacity of buildings following an extreme windstorm event that generates limited damage and nonlinearity in the building, as such studies are currently not available.

This study focuses on addressing some of the above issues, with an emphasis on concrete coupling beams in coupled walls systems, which are predominantly used as lateral force-resisting systems for tall buildings constructed in many parts of the world. In particular, the study goals are to: 1) establish experimental evidence that limited nonlinearity in concrete coupling beams subjected to extreme wind events can be permitted and does not result in an unacceptable behavior, 2) provide experimental coupling beam data to help develop modeling parameters for nonlinear dynamic analysis of coupled concrete wall systems, and 3) study the impact of prior limited nonlinear wind demands on the post-windstorm reserve seismic capacity of concrete coupling beams in terms of strength, stiffness, ductility, energy dissipation capacity, and failure mode. To accomplish these objectives, eight 2/3-scale concrete coupling beams (seven reinforced concrete, RC, beams and one, steel-reinforced concrete, SRC, beam) were tested in two phases under quasi-static, cyclic loading protocols simulating extreme windstorm events followed by a standard seismic loading protocol. The test parameters included aspect ratio, presence of floor slab, level of detailing, and variation of wind loading protocol, epoxy injection repair, and type of coupling beam (RC vs. SRC). The wind test results indicated that rotational ductility demands of 1.5 can be achieved with only small residual crack widths (less than 1/16 in.; 1.6 mm) and no concrete spalling, or bar buckling or fracture, indicating that allowing modest inelastic response during extreme wind events is a viable approach. The seismic test results revealed that the prior limited nonlinear wind demands did not produce a noticeable influence on the reserve seismic capacity of the beams, except for the initial residual stiffness and, in some cases, the energy dissipation capacity.

ACKNOWLEDGEMENTS

The work presented in this research report was supported by funding from the Magnusson Klemencic Associates (MKA) Foundation under Grant Number A102. This financial support is gratefully acknowledged. Without the significant in-kind support provided by Webcor Builders Inc in materials and construction and demolition of the test specimens, this project would not have been possible. Their generous support is gratefully acknowledged. We would also like to express our gratitude for donations from Pacific Steel Group (PGS), CalPortland, Herrick Corporation, Structural Technology for materials and fabrication of the test specimens. Without their support, this research could have not been completed. Any opinions, findings, and conclusions or recommendations expressed in this report are those of the authors and do not necessarily reflect the views of the funding agencies.

We are thankful for the assistance given by Dr. Eric Ahlberg, Laboratory Manager and Principal Development Engineer in the Department of Civil and Environmental Engineering at UCLA. His extensive knowledge and expertise were vital in facilitating and conducting the experiments. We would also like to particularly thank Shahab Jaberansari, a master's student at UCLA for his help and contribution during construction and testing of the specimens and processing the experimental data. Our acknowledgments extend to other UCLA PhD students (Amin Safdari, Elham Moore, and Matias Rojas) and undergraduate students (Abhimanyu Singh, Amir Parsa Arefian, Bryan Hong, Lenn Kushigemachi, Jackob Stanley, Joshua Wang, Ada Cheng) for their assistance during fabrication and testing of the specimens. We appreciate Abhimanyu Singh's help in processing the digital image correlation (DIC) data.

TABLE OF CONTENTS

LIST OF FIGURES

LIST OF TABLES

LIST OF NOTATIONS

A_{cw} = area of concrete section of a coupling beam resisting shear

A_s = bar cross-sectional area

A_{sh} = total cross-sectional area of transverse reinforcement, including crossties, within spacing s and perpendicular to dimension b_c

$A_{sh,provided}$ = area of provided transverse reinforcement;

$A_{sh,required}$ = area of transverse reinforcement required by ACI 318-14§18.10.7.4 (d)

A_{vd} = total area of reinforcement in each group of diagonal bars in a diagonally reinforced coupling beam

b_w = beam web width;

d = distance from extreme compression fiber to centroid of tension reinforcement;

d_b = nominal diameter of bar

E_c = Young's modulus of concrete computed in accordance with ACI 363R-10 for high strength concrete ($f'_{c,test}$ > 6,000 psi [41.4 MPa]),

f_c' = specified (design) compressive strength of concrete

$f_{c,7day}$ = measured (tested) compressive strength of concrete at 7-day age

$f'_{c,28day}$ = measured (tested) compressive strength of concrete at 28-day age

$f'_{c,test}$ = measured (tested) compressive strength of concrete at test-day age

ε_{test} = measured (tested) compressive strain of concrete corresponding to $f'_{c,test}$

$f_{st,test}$ = measured (tested) split tensile strength of concrete at test-day age

f_y = specified (design) yield strength of reinforcement

$f_{y,test}$ = measured (tested) yield strength of reinforcement

$f_{y,cert}$ = mill certified yield strength of reinforcement

$f_{u,cert}$ = mill certified tensile strength of reinforcement

$f_{u,test}$ = measured (tested) tensile strength of reinforcement

$f_{rup,test}$ = measured (tested) rupture strength of reinforcement

h = beam total depth;

h_s = slab thickness

I_{eff} = effective moment of inertia

I_g = beam gross-section moment of inertia about centroidal axis, neglecting presence of longitudinal reinforcement and floor slab

l_n = clear span (length) of beam measured from face-to-face of wall

l_n/h = beam aspect ratio

M_n = nominal moment strength determined in accordance with ACI 318-14 for RC beams and AISC 360-10 for SRC beams

M_{pr} = probable moment strength determined in accordance with ACI 318-14 for RC beams and AISC 360-10 for SRC beams

M_p = plastic moment capacity of structural steel section

s = center-to-center horizontal spacing of transverse reinforcement

s/d_b = bar slenderness ratio computed as the ratio of center-to-center horizontal spacing of transverse reinforcement to diameter of smallest longitudinal bar

V = applied lateral load

V_u = design shear demand

$V_{@Mn}$ = shear strength corresponding to nominal moment capacity, M_n

$V_{@Mpr}$ = shear strength corresponding to probable flexural strength, M_{pr}

V_{peak} = peak (maximum) shear strength obtained during seismic testing

$V_{peak,w}$ = peak (maximum) shear strength obtained during wind testing

V_n = design (nominal) shear strength computed from ACI 318-14 Eq. 22.5.5.1 and Eq. 22.5.10.5.3 for beams with conventional reinforcement and standard detailing, from ACI 318-14 Eq. 18.10.7.4 for beams with diagonal reinforcement, and from AISC 360-10 provisions for SRC (concrete encased) beams

V_y = yield strength of beam at first yield

z_x = plastic section modulus about x-axis of the cross-section

α_c = centroid of curvature distribution profile

α = angle between the diagonal bars and the longitudinal axis of beam

Δ_{total} = relative displacement of beam end

Δ_{axial} = beam axial growth of beam

Δ_y = yield displacement

$\delta_{flexure}$ = flexural displacement

δ_{shear} = shear displacement

$\delta_{slip/ext.}$ = displacement due to slip/extension of longitudinal/diagonal reinforcement at beam-wall interface

δ_{slide} = sliding displacement at beam-wall interface

δ_{total} = total deformation

$\varepsilon_{sh,test}$ = measured (tested) reinforcement strain at onset of strain hardening strain

$\varepsilon_{y,test}$ = measured (tested) yield strain of reinforcement

$\varepsilon_{rup,test}$ = measured (tested) strain of reinforcement at $f_{rup,test}$

$\varepsilon_{u,test}$ = measured (tested) strain of reinforcement at $f_{u,test}$

θ_{total} = beam chord rotation

$\theta_{flexure}$ = beam chord rotation due to flexure

θ_{shear} = beam chord rotation due to shear

θ_{slide} = beam chord rotation due to sliding

$\theta_{slip/ext.}$ = beam chord rotation due to bar slip/extension

θ_y = beam chord rotation at first yield

μ = Ductility demand defined as rotation demand, θ, divided by yield rotation, θ_y,

ρ = reinforcement ratio calculated in accordance with ACI 318-14

ϕ = strength reduction factor taken as 0.75 and 0.9 for shear and flexural strengths of RC beams, respectively, in accordance with ACI 318-14 §21.2.1 for RC beams, or as specified by AISC 360-10 for SRC beams

CHAPTER 1. INTRODUCTION

1.1. Background and Motivation

Many regions around the world are experiencing tremendous population growth as a result of the trend of movement of people away from rural or suburban areas to large metropolitan areas. These regions are, in many cases, located along or near the coastlines, including fast-growing cities in the US such as Los Angeles, San Francisco, Seattle, Houston, Miami, and New York City, as well as other regions around the world, e.g., Philippines, Taiwan, and Indonesia. Many of these areas are subject to strong ground shaking, extreme wind storms, or a combination of the two, as shown in **Figure 1-1**. The population concentration along the coastlines has resulted in powerful societal and economic pressures to build taller and taller buildings. Many of the challenges associated with designing and constructing tall buildings in regions of high wind and seismic hazards are compounded by other, sometimes competing, factors. Amongst these is the responsibility to society to provide efficient, affordable, and comfortable housing and work environments, while simultaneously addressing the global issues of sustainability and resiliency (Aswegan et al., 2017). The above challenges are formidable, yet not impossible to address. The solutions will be piecemeal, coming from all corners of the industry and society at large. In response to these challenges, advances have been made such as the development of performance-based seismic design (PBSD) methodology for tall buildings in regions subject to strong ground shaking. Despite significant advancements, such as improvements in the characterization of wind hazards, wind tunnel testing, and structural analysis techniques, wind design of buildings, unlike seismic design, has not fundamentally changed and is still based on prescriptive code provisions and essentially linear elastic response under ASCE 7 strength-level load-combinations. However, two principal factors have recently motivated the structural wind engineering community to initiate an effort to establish an alternative methodology and framework that embraces the concepts of performance-based design, similar to PBSD, to design buildings subjected to extreme wind events. First, the current prescriptive, code-based design philosophy that relies simply on meeting provisions stipulated in building codes and standards does not guarantee meeting the target reliability levels set by society and stakeholders (Ellingwood, 2001; FEMA 2012). Currently, ASCE 7-16 uses component reliability for wind analysis as opposed to system reliability used for seismic analysis– a method that ignores the ability of the structure to reorganize the load path following controlled yielding of a member. The topic of reliability has recently been addressed by the ASCE Prestandard for Performance-Based Wind Design, PBWD, (2019). Second, wind demands may control the design strength of either the overall lateral system, some portion of the lateral system (e.g., upper one-third levels), or some structural elements (e.g., buckling-restrained brace outriggers), resulting in greater demands on energy dissipating ductile elements or actions (fuses) than needed to resist seismic demands. Increasing demands on fuses results in greater demands for capacity protected elements (e.g., foundation, diaphragms, columns, joints) and actions (shear, anchorage), which can negate the many of the benefits of PBSD. In these cases, utilizing code prescriptive wind load provisions may limit the potential benefits of the PBSD, negatively impacting the expected seismic performance of the building and significantly increasing the cost of the structural system, including the foundation. Therefore, a framework for PBWD is needed that establishes appropriate modeling approaches and acceptance criteria. Test data of building components are needed to validate and advance the framework.

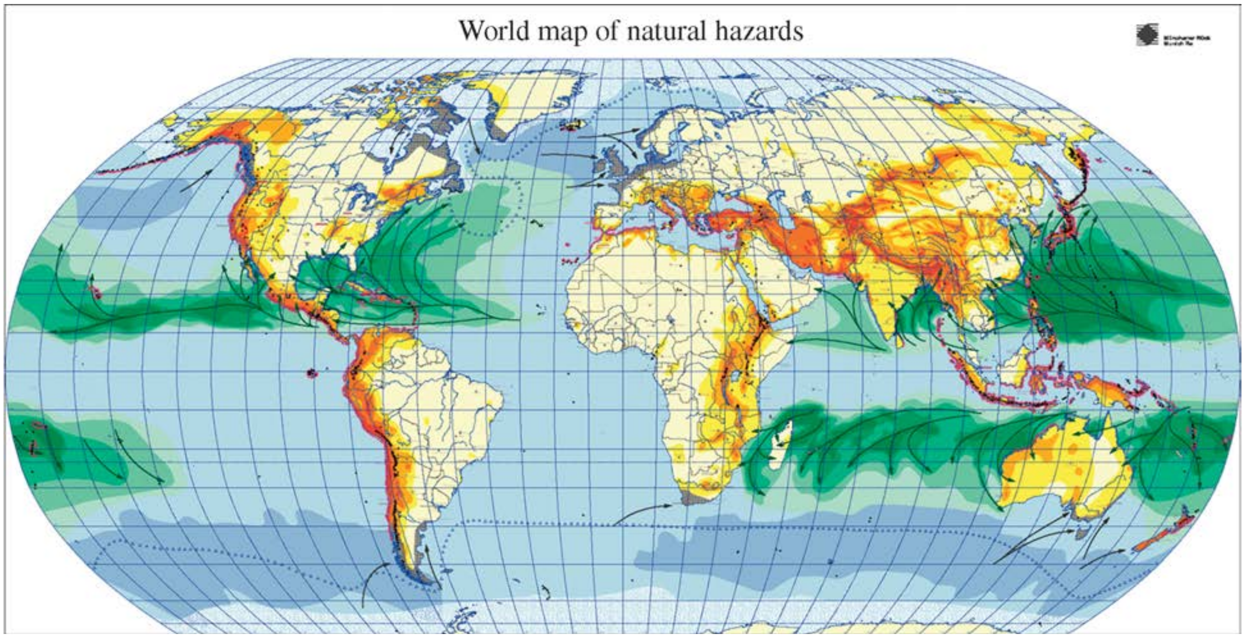

Figure 1-1. World map of natural hazards (Smikle, 2006). Earthquake hazard is shown in yellow–brownish colors, and tropical windstorms hazard is shown in green colors, with the darkest color representing the highest hazard.

Reinforced concrete (RC) core wall systems, with coupling beams to accommodate openings, provide an efficient lateral-force-resisting system to resist seismic and wind demands for mid- and high-rise buildings. This system has been predominantly used for tall buildings constructed on the West Coast of the US, for which PBSD is used when the height of the building exceeds 160 ft (48.8 m) or 240 ft (73.2m) if certain requirements are satisfied. For seismic design, inelastic response of ductile elements, typically coupling beams, outrigger elements, and wall critical regions, has long been permitted by building codes (e.g., ASCE 7; UBC; IBC). Coupling beams act as the primary fuses to limit force demands on capacity protected elements and actions (e.g., foundation flexure and shear, and wall shear) and provide reliable energy dissipation mechanisms. Current seismic design requirements for coupling beams are based on numerous experimental results reported in the literature (e.g., Paulay and Binney, 1974; Tassios et al., 1996; Xiao et al., 1999; Galano and Vignoli, 2000; Kwan and Zhao, 2001; Naish et al., 2013; Motter et al., 2017). Results reported in these studies cannot readily be directly applied when considering nonlinear behavior under wind demands because of issues that are unique to wind demands such as ratcheting effect in the along-wind direction, low cycle fatigue in the crosswind direction, and the difference in expected ductility demands for wind versus seismic demands. An earthquake event lasts for a relatively short time (tens of seconds to a few minutes), whereas a windstorm event could last for hours or more. Thus, the displacement amplitudes and number of cycles used for wind tests should significantly differ from those of seismic tests.

Although progress has been made on evaluating the reserve/residual seismic capacity of moderately earthquake-damaged concrete buildings in countries that have recently experienced moderate-to-strong earthquakes (i.e., Japan, New Zealand, and Chile), there is currently a lack of robust guidelines in the US for engineers and building owners to assess post-earthquake reserve capacity and reparability of moderately damaged buildings. This lack of knowledge will become even more critical when evaluating reserve seismic capacity of buildings following an extreme windstorm event that generates limited damage and nonlinearity in the building, as such studies are currently not available. Given that coupling beams act as primary fuses, enabling engineers to better understand how the nonlinear wind demands impact coupling beam behavior in terms of strength, stiffness, ductility, energy dissipation capacity is vital.

To address these issues, eight 2/3-scale concrete coupling beams (seven RC beams and one SRC beam) were tested in two phases under quasi-static, cyclic loading protocols simulating extreme windstorm events followed by a standard seismic loading protocol. The test parameters included aspect ratio, presence of floor slab, level of detailing, and variation of wind loading protocol, epoxy injection repair, and type of coupling beam (RC vs. SRC).

1.2. History of Wind Engineering of Buildings

Over the past four decades, the definition and requirements of wind loads on buildings have evolved significantly as the science and knowledge of the probability of wind speed occurrence and how buildings respond to wind events have advanced (Mehta, 2010). Prior to 1972, design of structures for wind loading was generally governed by local authorities. In most instances, a simple horizontal (or vertical) pressure distribution was prescribed to be applied to building surfaces generating demands on the primary structural frame, which was then designed to respond elastically for the combined effects of gravity and wind loading. There was little, if any, consideration given to building displacement, story drift, or occupant comfort (Klemencic, 2019). From 1972 to 1988, those minimum requirements were specified in consensus standards for structural loads published by American National Standards Institute (ANSI), with the first standard being ANSI A58.1-1972. ANSI A58.1-1972 provided the first wind loading criteria using wind hazards determined in a probabilistic manner, including basic wind speed contours and tabulated effective velocity pressures for various regions around the US. The basic wind speeds (i.e., 25-year MRI, 50-year MRI, and 100-year MRI) were given as the fastest-mile wind speed referenced at 30 ft (9 m) above ground and in flat, open terrain (Exposure C). In the subsequent version of the standard in 1982, the wind load provisions were refined and extended based on additional data from wind events and wind tunnel tests. Notably, the three wind speed maps for different MRI were replaced with one wind speed map for a 50-year MRI with load and importance factors to approximate wind speeds for other MRIs (i.e., 300-year, 700-year, and 1,700-year MRIs). In 1985, the American Society of Civil Engineers (ASCE) assumed responsibility for publishing the ANSI A58.1 standard, with no revisions to the ANSI A58.1-1982 wind load criteria in the first version of ASCE 7 standard published in 1988. Significant revisions of the wind loading criteria were adopted in ASCE 7-95, where, among other changes, the basic wind speed was changed from the fastest-mile to a 3-second gust. Unlike the prior versions, ASCE 7- 10 published ultimate wind-speed maps for different risk categories directly representing the 300-year, 700-year, and 1,700-year MRIs. This resulted in more accurate ultimate wind speeds for different regions of the US.

Wind tunnel studies were initiated in the early-to-mid-1960s, with the World Trade Center Towers in New York City being the first significant building to consider the results of such studies (Klemencic, 2019). During the 1960s and 1970s, wind tunnel studies were generally limited to "special" or very tall structures. Since then, wind tunnel tests have been used by designers to improve designs through more accurate knowledge of the expected wind loads and how the building responds to those loads (Irwin et al., 2013).

Despite these many improvements in the definition of design wind speeds, and thus wind loading, the ASCE 7 standard and other codes have remained silent on requirements guiding acceptable building movements and occupant comfort criteria because these performance parameters are viewed as serviceability related and not life safety related. As well, lateral system response to extreme wind events has also remained in the essentially linear elastic response domain, which is contrary to seismic design, where extreme loading demands are managed through absorbing the energy imparted by the strong ground shaking in the form of nonlinear response of specially designed structural elements. It is within this context that PBWD has great value.

1.3. Performance-Based Wind Design

Performance-based engineering is a methodology through which a building system is explicitly modeled, analyzed, and evaluated to meet certain performance requirements as specified by owners, end-users, or other stakeholders. As noted earlier, extensive research over the last two decades has resulted in the development of PBSD (SEAOC Vision 2000, 1995; FEMA 273/274, 1997; LATBSDC, 2017; PEER TBI, 2017; CTBUH (Golesorkhi et al., 2017)); however, the same cannot be said for PBWD. The primary factors that have hindered the use of PBWD in the design of wind excited systems are: 1) the general lack of comfort with the idea of a wind excited system experiencing nonlinearity, particularly due to issues relating to ratcheting and P-delta effects in the along-wind direction and low cycle fatigue in the crosswind direction, 2) the computational challenges of modeling the inelastic response of structural systems under dynamic events that can last for several hours (Spence et al., 2016; Aswegan et al., 2017), and 3) the lack of experimental data on the performance of key elements subjected to wind loading protocols.

Prior to 2013, efforts to develop PBWD were mainly concerned with assessing feasibility and developing a conceptual framework (e.g., Ciampoli et al., 2011; Smith and Caracoglia, 2011; Spence and Gioffrè, 2012; Bernardini et al., 2013; Bernardini et al., 2014; Spence and Kareem, 2014; Spence et al., 2015). During the development cycle of ASCE 7-16, ASCE 7 formed an ad hoc PBWD task group from the ASCE 7 Wind Loads Subcommittee membership to assemble the available work and identify research needs for PBWD. Since 2016, the industry has expressed substantial interest in conducting research and developing performance assessment guidelines similar to those used for PBSD. Thus, the subsequent efforts focused on the development of general frameworks that could be used to assess the performance of a wide range of wind excited building systems and the possibility of allowing these systems to experience limited inelasticity under extreme wind events. Spence et al. (2016) proposed a performance-based design framework specifically for multi-story wind excited buildings in order to mitigate structural and non-structural damage and loss. In particular, the post-yield behavior of the structural system is modeled using the theory of dynamic shakedown, thus providing a full portrait of the post-yield behavior without the need for computationally expensive non-linear finite element models. The work by Spence has also shown that the reliability of a structural system can be efficiently determined for wind loading, and that a building properly designed can achieve levels of safety equal to or better than required by ASCE 7 provided that nonlinear demands are limited. Larsen et al. (2016) and Aswegen et al. (2017) have put forward a proposal to extend the performance-based design framework to wind engineering. These efforts, along with knowledge gained from seismic research and PBSD, have collectively culminated in the publication of an ASCE Prestandard for PBWD (2019). The ASCE Prestandard serves as an actionable guide to inform practicing engineers regarding the use PBWD as an alternative for code prescriptive wind design and the definition of wind demand levels, performance objectives, analysis techniques, and acceptance criteria. The Prestandard also includes recommendations for serviceability limits, including occupant comfort and drift limits, and for design and performance of non-structural components and cladding. To ensure that a system reliability consistent with the reliabilities defined in ASCE 7-16 is achieved, the Prestandard includes three alternative analysis and design paths, with the first being simple and more prescriptive and the third being more rigorous and less restrictive: Path 1: a quasi-prescriptive time history method with acceptance criteria, Path 2: a first-order reliability technique similar to FEMA P-695, and Path 3: a system reliability evaluation technique. Regardless of the path taken, a peer-review process, similar to that of PBSD, is required to ensure that the design meets the intent of the code.

1.4. Objectives

Given the needs noted in the preceding sections, the objectives of this study are to:

1. develop quasi-static, cyclic loading protocols that simulate extreme windstorm demands and could be used to statically test building components in a laboratory, similar to tests under standard seismic loading protocols,
2. establish experimental evidence that limited nonlinearity in coupling beams subjected to extreme wind events can be allowed and does not result in an unacceptable behavior,
3. provide experimental concrete coupling beam data to help develop modeling parameters for nonlinear dynamic analysis of coupled concrete wall systems,
4. evaluate the effectiveness of epoxy injection repair of cracks as a performance restoration measure in beams subjected to mild nonlinear wind demands,
5. assess the reserve (residual) seismic capacity (i.e., strength, stiffness, ductility, and energy dissipation capacity) of concrete coupling beams subjected to prior limited non-linear wind demands.

1.5. Report Outline

This report is comprised of eight chapters and eight appendices. Chapter 1 includes an introduction, objectives, and overall organization. Details of the experimental program, including design and fabrication of the test specimens, material properties, test setup, instrumentation, and loading protocols, are described in Chapter 2. Chapter 3 presents the results of the tests under the wind loading protocols followed by the discussion and comparison of the results in Chapter 4. Chapter 5 summarizes the key findings and conclusions of the wind tests and provides recommendations. Chapter 6 presents the results of the tests under the seismic loading protocol followed by the discussion and comparison of the results in Chapter 7. Chapter 8 summarizes the key findings and conclusions of the seismic tests and provides recommendations. Appendices A through G present additional information on the tests specimens and the collected test results.

CHAPTER 2. EXPERIMENTAL PROGRAM

2.1. General

The experimental program consisted of designing, constructing, and testing eight large scale coupling beams, referred to hereafter as CB1 through CB8, in two phases. Phase I included CB1 through CB4, and Phase II included CB5 through CB8. Test beams in Phase I were constructed during Spring 2018 and tested during Summer and Fall 2018. Results from Phase I tests, along with feedback from practicing engineers in the structural and wind engineering community, guided the decisions and design of the beams in Phase II, which were constructed and tested during Spring and Summer 2019, respectively. The following sections describe the experimental program, including design of the test beams, material properties, test setup, instrumentation, loading protocols, and fabrication.

2.2. Design of Test Specimens

2.2.1. Phase I

The test beam prototypes were based on two common tall building configurations for residential and office buildings, where typical wall openings and story heights produce coupling beams with aspect ratios (clear length/depth, l_n/h) of approximately 2.5 and 3.67, respectively. Coupling beams with cross-sectional dimensions (width × depth, $b_w \times h$) of 24 in. × 24 in. (610 mm × 610 mm) and 24 in. × 36 in. (610 mm × 914 mm) are common for residential and office construction, respectively. Due to geometric and strength constraints of the laboratory test setup, the prototype beams were scaled down to 2/3-scale replicas of the prototype beams, resulting in cross-sections ($b_w \times h$) of 16 in.×16 in. (406 mm × 406 mm) and 16 in. × 24 in. (406 mm × 610 mm) for the residential and office beams, respectively. The test beams in this phase were designed with two levels of detailing: three RC beams with conventional (longitudinal) reinforcement and standard (or non-seismic) detailing and one RC beam with diagonal reinforcement and seismic detailing. Detailed information is provided in subsequent sections, as well as **Table 2-1**, and **Figure 2-1** through **Figure 2-4**:

Standard Detailing

Since ASCE 7-16 does not contain explicit provisions for nonlinear behavior under wind demands, buildings in low-seismic hazard areas are not required to be specially detailed for ductility, and thus standard detailing is commonly used (i.e., conformity to ACI 318-14 Chapter 18 is not required). Therefore, three of the test beams, namely CB1, CB2, and CB3, were designed with standard detailing and conventional top and bottom longitudinal reinforcement in accordance with the requirements of ACI 318-14 Chapter 9. CB1, with l_n/h of 2.5, represents a coupling beam for residential construction, whereas CB2 and CB3, with l_n/h of 3.67, represent coupling beams with and without a floor slab, respectively, for office construction. The prototype and test beams were designed with a target shear stress, $V_u/b_w d$, of $5\sqrt{f_c'(psi)}$ [$0.42\sqrt{f_c'(MPa)}$]. This value was judged to be representative of coupling beam shear demands in tall coupled wall buildings based on input from practicing engineers. The longitudinal reinforcement was selected such that the factored nominal moment strength, ϕM_n, is as close to the design moment, $M_u = (V_u \times l_n)/2$, as possible, and that the shear stress corresponding to the probable moment strength, $V_{@Mpr}/b_w d$, is close to, but does not exceed, $7.5\sqrt{f_c'(psi)}$ [$0.625\sqrt{f_c'(MPa)}$]. For these calculations, the impact of the floor slab on M_n and M_{pr} is ignored. Similarly, the transverse reinforcement was selected such that the ratio of design shear strength (ϕV_n) to the design shear demand (V_u) is close to 1.0 (to limit shear overstrength). As such, the test beams were not capacity-designed to prevent shear failure prior to flexural yielding, as is done for beams designed in accordance with ACI 318-14 §18.10.7.

Seismic Detailing

A 2/3-scale beam with l_n/h of 2.5 (CB4, **Figure 2-4**), was designed and tested to assess the wind performance of a diagonally reinforced coupling beam with seismic detailing, to highlight the potential improvements that might result from providing seismic detailing (versus standard detailing), and to evaluate the impact of loading protocols (wind versus seismic) on the performance of coupling beams subjected to the same ductility demands. A 1/2-scale RC coupling beam (CB24F-RC, **Figure 2-5**) tested by Naish et al. (2013) under a standard seismic loading protocol was used as the prototype beam for CB4 and as the baseline beam for comparison of behavior under the wind and seismic loading protocols. CB24F-RC has an l_n/h of 2.4 and is reinforced with two groups of diagonally placed bars and full-cross-section confinement conforming to the seismic detailing requirements of ACI 318-14 §18.10.7.4(d). **Table 2-1** indicates that CB4 and CB24F-RC are similar, with the same configuration and level of confinement, same level of shear strength and shear demand, and only a slight difference in geometry that resulted in a 4% increase in l_n/h ratio and a 13% reduction in the angle between the diagonal bars and the longitudinal axis of the coupling beam (α) for CB4. As shown in **Figure 2-4**, the horizontal reinforcement in the beam (12 No. 3 bars) used to anchor the hoops and crossties are embedded into the walls (end blocks) by 4 in. (100 mm), which is less than the 6 in. (150 mm) development length required by ACI 318-19 §25.4.2.4 [or 10 in. (250 mm) if §25.4.2.3 is applied], to prevent the bars from developing yield strength as required by ACI 318-19 §18.10.7.4(d) or contributing significantly to the beam flexural strength.

An 8 in. (203 mm) thick post-tensioned flat plate slab with No. 4 bars spaced at 12 in. (d_b = 12.7 mm at 305 mm) near the walls is typical of residential buildings with coupled wall systems. For office construction, RC slabs with similar thickness are often used inside a core wall, while a concrete slab on metal deck may be more common outside of a core wall. For this study, an 8 in. (203 mm) thick RC flat plate slab with No. 4 bars spaced at 12 in. (d_b = 12.7 mm at 305 mm) was used for the prototype beams that included a floor slab. Thus, a slab thickness, h_s, of 5-1/3 in. (135 mm) was used for the 2/3-scale specimens with No. 3 bars spaced at 10 in. (d_b = 9.5 mm at 254 mm) for top and bottom reinforcement perpendicular to the beam length and top reinforcement only parallel to the beam length. The effective overhanging flange width, b_{over}, was selected as $8h_s$, in accordance with ACI 318-14 §6.3.2.1. Details of the floor slab for each beam are given in **Table 2-1**. Lastly, the beams were built with heavily reinforced and post-tensioned end blocks to simulate the wall boundary zones in coupled wall systems and to enable anchoring of the test specimens to the lab strong floor and test setup, as will be shown later.

2.2.2. Phase II

As noted previously, the results and conclusions from Phase I tests, along with feedback from practicing engineers in the structural and wind engineering community, were used to guide the design of the test coupling beams in Phase II. As will be discussed later in Chapters 3 and 4, the beams in Phase I performed well under the wind loading protocol used, with only relatively minor cracks and no concrete crushing or bar buckling or fracture; therefore, no enhanced design or detailing (e.g., need for capacity design, improved confinement, and/or adding admixtures to improve bond and control cracking) were investigated in Phase II tests (these options were considered as potential topics for Phase II if the performance of the Phase I beams was unsatisfactory). Instead, three other issues were identified for investigation in Phase II: 1) the impact of various alternative wind loading protocols, 2) the performance of steel reinforced concrete (SRC) coupling beams under wind loading protocols, and 3) the impact of epoxy injection repair on wind performance of coupling beam subjected to prior limited inelastic wind demands.

To address these issues, four additional concrete coupling beams were constructed and tested in Phase II. To address the first item, three RC coupling beams from Phase I were replicated (CB5, CB7, and CB8), where CB5 is identical to CB1 with l_n/h of 2.5, and CB7 and CB8 are identical to CB2 with l_n/h of 3.67, as shown in as **Table 2-1**, **Figure 2-1,** and **Figure 2-2**. Details of the alternative wind loading protocols are given later in this chapter. The second item was addressed by constructing and testing an SRC coupling beam (CB6) with standard detailing and l_n/h of 2.5. Lastly, CB5 was repaired using epoxy injection (hereafter called CB5R) after the wind loading protocol and was retested using the same wind loading protocol. Details of the last two items are presented in the following sections.

SRC Coupling Beam Design

Steel reinforced concrete (SRC) coupling beams are structural steel (commonly wide-flange steel sections) coupling beams encased in concrete with transverse reinforcement and embedded into the boundary zones of coupled structural walls. They are referred to as concrete-encased steel coupling beams or simply composite coupling beams by AISC 360-10 and AISC 341-16 standards. SRC coupling beams are commonly used in seismic applications because they provide an alternative to RC coupling beams with either conventional or diagonal reinforcement. In seismic design, use of properly designed SRC beams typically offers benefits such as reduced section depth, ease of construction (and thus savings) by reducing congestion in the boundary zones of the coupled walls, improved degree of coupling for a given beam depth, and increased ductility (deformation) capacity prior to strength degradation. Since most of these benefits also apply to non-seismic applications, SRC coupling beams are also relevant for regions with modest seismic hazards where design of the lateral force-resisting system is controlled by wind. Therefore, the behavior of non-seismically detailed SRC coupling beams under wind loading protocols was investigated using a 2/3-scale SRC coupling beam, referred to as CB6, with l_n/h of 2.5 (residential construction) and standard detailing was designed and detailed in accordance with the requirements of AISC 360-10 and ACI 318-14 (**Table 2-1**, **Table 2-2**, and **Figure 2-6**). Similar to the other non-seismically detailed coupling beams, CB6 was designed with a target shear stress, $V_u/b_w d$, of $5\sqrt{f_c'(psi)}$ $[0.42\sqrt{f_c'(MPa)}]$. The beam geometries and slab details are selected to be identical to that of CB1, CB4, and CB5. Thus, a W12x40 wide flange section was selected for the embedded section, and transverse reinforcement in the form of U-shaped stirrups with cap crossties was provided, as shown in **Table 2-1** and **Figure 2-6**. As shown in **Figure 2-6**, the corner horizontal reinforcement in the beam (4 No. 3 bars) used to anchor the hoops and crossties are embedded into the walls (end blocks) by 4 in. (100 mm), which is less than the minimum 6 in. (150 mm) development length required by ACI 318-19 §25.4.2.4 [or 10 in. (250 mm) if §25.4.2.3 is applied], to prevent the bars from developing yield strength or contributing significantly to the beam flexural strength.

Since the test setup used for this experimental program was not capable of simulating the steel section embedment region subjected to stress and strain demands representative of actual conditions of an SRC beam in a coupled wall system, i.e., embedding the steel section into a wall subjected to reversed cyclic lateral loading and overturning moment (e.g., Motter et al., 2017), the embedment connection was capacity-designed such that the shear strength associated with the steel section embedment length (computed based on AISC 341-16) was greater than the shear strength of the beam and strength associated with composite flexural strength of the beam (both computed based on AISC 360-10), as shown in **Table 2-2**.

Epoxy Injection Repair

To evaluate the effectiveness of epoxy injection repair, as a performance restoration measure, on the wind performance of coupling beams in general and restoring the effective stiffness in particular, CB5 was repaired using injected epoxy (after the wind loading protocol was completed) and was retested under the same wind loading protocol. The repaired CB5 is hereafter referred to as CB5R. For the repair, residual cracks, which are typically used to assess and classify the severity of damage in reinforced concrete components (i.e., FEMA 306), with widths smaller than 1/80 in. (0.3 mm) were not repaired. Generally, only cracks at the interface of the beam-wall (end blocks) were large enough to be repaired, as shown in **Figure 2-7**. As will be shown later, the residual diagonal (shear) cracks in the web ranged from 4/1000 in. (0.1 mm) to 1/100 in. (0.25 mm) and residual flexural cracks in the hinge region (over a distance of *h* from the beam-wall interface) did not exceed 4/1000 in. (0.1 mm). Although it might be possible to inject smaller cracks using low viscous epoxy (ACI 503.7-07; ACI 224.1R-07), similar to that used for liquid containment structures, the additional cost was not considered practical in this study.

The repair was performed by an experienced local contractor. The properties of the epoxy material used and the application procedure followed are given in **Appendix A**. Testing of CB5R was initiated nine days after testing of CB5 was concluded, with two days for performing the repair and seven days for the epoxy material to set, as was recommended by the repair supplier.

Table 2-1. Test matrix

Beam ID	CB1, CB5	CB2, CB7, CB8	CB3	CB4	CB24F-RC [1]	CB6
Beam detail and geometry						
Type	Residential	Office	Office	Residential		
Size, $b_w \times h \times l_n$ (in.)	16×16×40	16×24×88	16×24×88	16×16×40	12×15×36	16×16×40
Aspect Ratio, l_n/h	2.50	3.67	3.67	2.50	2.40	2.50
Detailing [2]	Standard			Seismic		Standard
Top and bottom reinforcement	4No.6+2No.7	6No.7+4No.8	6No.7+4No.8	-	-	-
ρ_{top} and ρ_{bottom}	0.0138	0.0197	0.0197	-	-	-
Diagonal reinforcement	-	-	-	8No.8/bundle	6No.7/bundle	-
Steel section	-	-	-	-	-	W12x40
Angle of diagonal bars, α (°)	-	-	-	13.59	15.7	-
$\rho_{diag.}$	-	-	-	0.0272	0.0220	-
Transverse reinforcement	No.3@3.33 in.	No.3@4.38 in.	No.3@4.38 in.	No.3@2.33 in.	No.3@3 in.	No.3@7 in.
$(A_{sh,provided}/A_{sh,required})_x$	-	-	-	1.26	1.12	-
$(A_{sh,provided}/A_{sh,required})_y$	-	-	-	1.26	1.16	-
Bar slenderness, s/d_b	4.4	5.0	5.0	-	-	-
Slab detail and geometry						
Shape	T-shaped	L-shaped	No slab	T-shaped	T-shaped	T-shaped
Slab thickness, h_s (in.)	5-1/3	5-1/3	-	5-1/3	4	5-1/3
Overhanging width, b_{over} (in.)	42	42	-	42	36	42
Slab Reinforcement [3]	No.3@10 in.	No.3@10 in.	-	No.3@10 in.	No.3@12 in.	No.3@10 in.
ρ_{slab}	0.00206	0.00206	-	0.00206	0.00229	0.00206
Demands and strengths [4]						
Design f_c'; f_y (psi)	8,000; 60,000				7,000; 60,000	8,000; 50,000
$V_u/\sqrt{f_c'(psi)}b_w d$	5.0	5.0	5.0	5.5	5.5	5.0
$V_n/\sqrt{f_c'(psi)}b_w d$	7.56	7.29	7.29	7.74	7.78	6.72
$\emptyset V_n/\sqrt{f_c'(psi)}b_w d$	5.67	5.47	5.47	5.81	5.84	5.04
$\emptyset V_n/V_u$	1.13	1.09	1.09	1.06	1.06	1.01
$V_{@Mn}/\sqrt{f_c'(psi)}b_w d$ [5]	6.04 (7.21)	5.83 (6.50)	5.83	12.28 (14.54)	10.33 (11.90)	(8.18)
$V_{@Mpr}/\sqrt{f_c'(psi)}b_w d$ [5]	7.30 (8.85)	7.17 (7.95)	7.17	14.47 (17.50)	12.42 (14.55)	9.85

Conversions: 1in. = 24.5 mm; 1psi = 0.0069 MPa; No.3 bar = 10 mm dia. bar; No.6 bar = 19 mm dia. bar; No.7 bar = 22 mm dia. bar; No.8 bar = 25 mm dia. bar.

Footnotes:
[1] Tested by Naish et al. (2013).
[2] Standard detailing = detailing in accordance with ACI 318-19 Chapter 9 for RC beams and ACI 318-19 Chapter 9 and AISC 360-10 for SRC beams, and seismic detailing = detailing in accordance with ACI 318-19 Chapter 18.
[3] Top and bottom layers perpendicular to the beam length and top layer parallel to the beam length.
[4] Determined based on design material strengths
[5] Values in parentheses include the impact of floor slab on moment strength.

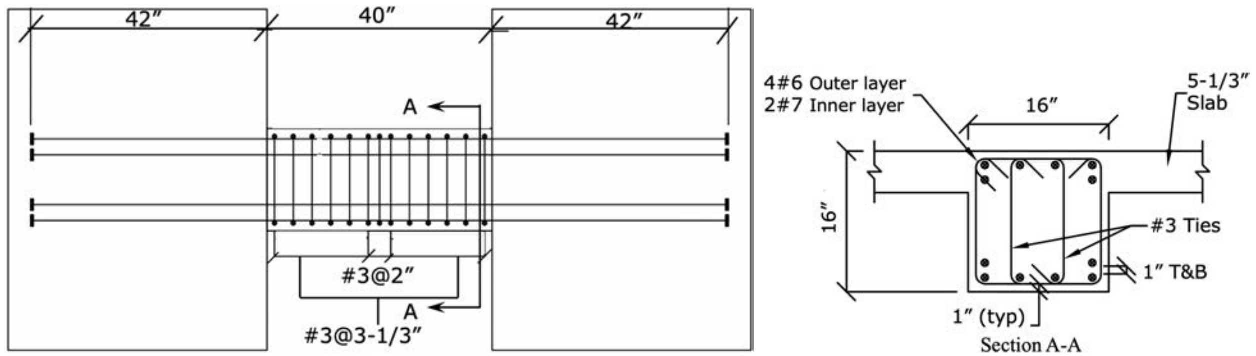

Figure 2-1. Reinforcement layout and geometries of CB1 and CB5. (Note: dimensions are in inches; 1 in.=25.4 mm; reinforcement in slab and end blocks not shown)

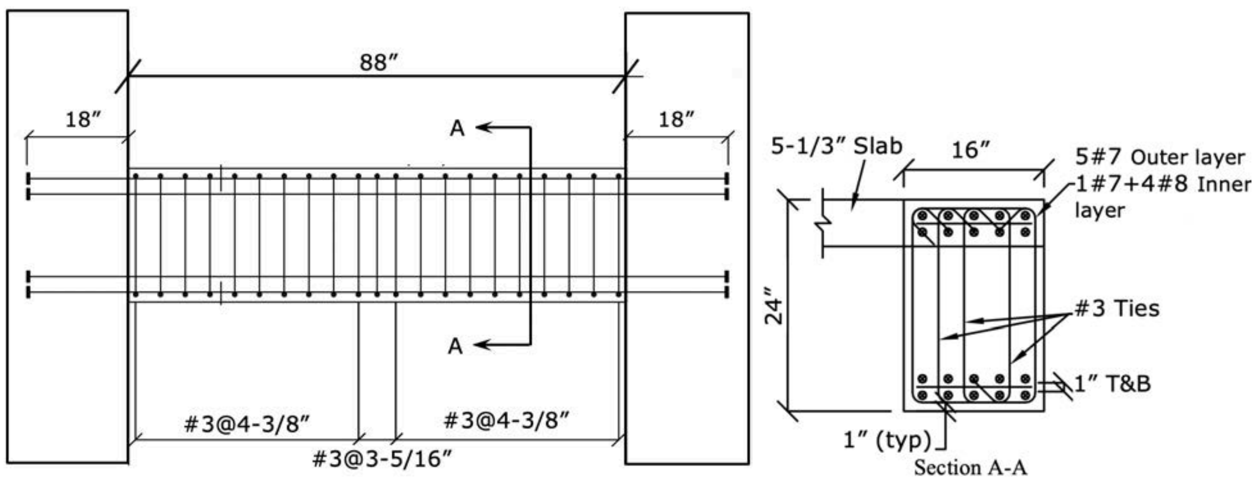

Figure 2-2. Reinforcement layout and geometries of CB2, CB7, and CB8. (Note: dimensions are in inches; 1 in.=25.4 mm; reinforcement in slab and end blocks not shown)

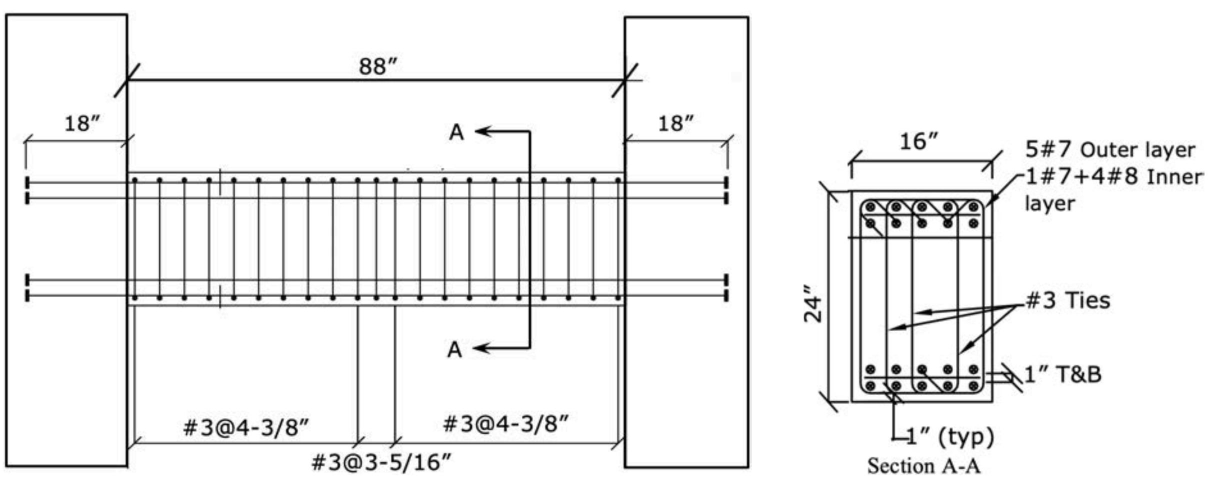

Figure 2-3. Reinforcement layout and geometries of CB3. (Note: dimensions are in inches; 1 in.=25.4 mm; reinforcement in slab and end blocks not shown)

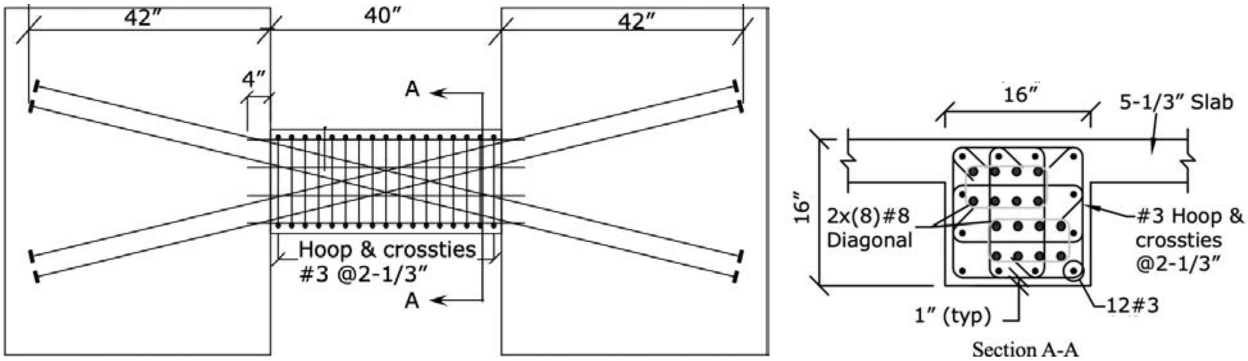

Figure 2-4–Reinforcement layout and geometries of CB4. (Note: dimensions are in inches; 1 in.=25.4 mm; reinforcement in slab and end blocks not shown)

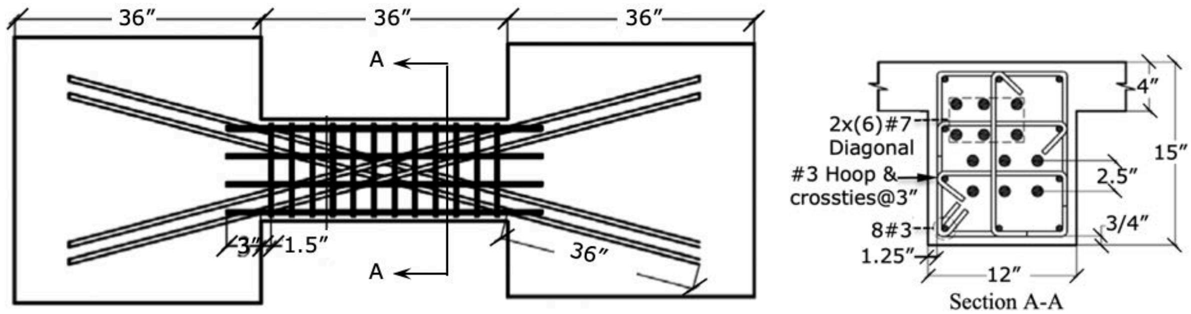

Figure 2-5. Reinforcement layout and geometries of CB24F-RC tested by Naish et al., (2013) [adapted from Naish et al., 2013]. (Note: dimensions are in inches; 1 in.=25.4 mm; reinforcement in slab and end blocks not shown)

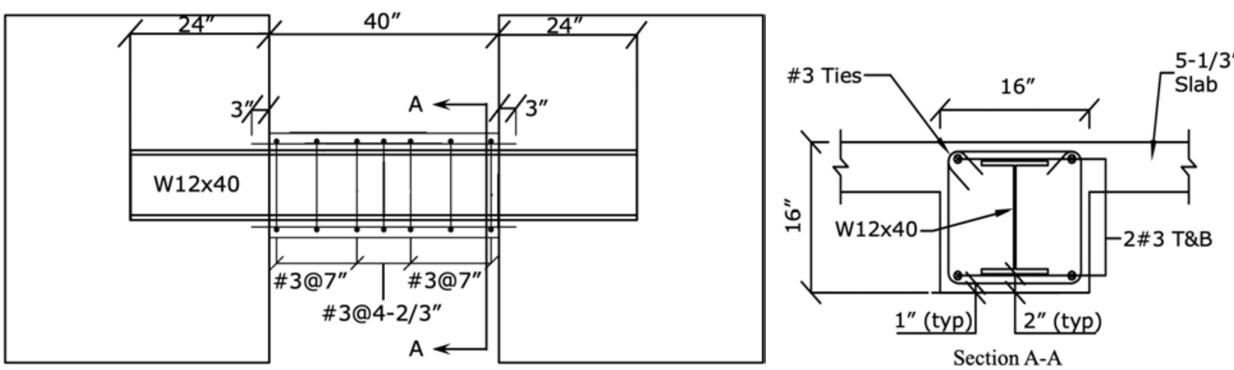

Figure 2-6. Reinforcement layout and geometries of CB6. (Note: dimensions are in inches; 1 in.=25.4 mm; reinforcement in slab and end blocks not shown)

Table 2-2. Calculated strengths of CB6 (the SRC beam)

Variable			Standard	Comment
Calculated Section Moment Strength:	M_y (ft-kips)	267	AISC 360-10 §I3.3.a	Superposition of elastic stresses for composite section (slab included)
	M_p (ft-kips)	238	AISC 360-10 §I3.3.b	Plastic strength of steel section alone obtained from AISC steel Manual
	M_p (ft-kips)	300	AISC 341-16	Plastic strength of steel section and concrete
	M_{pr} (ft-kips)	322	AISC 341-16	Plastic strength of steel section & concrete using expected material properties
Shear Demand at Moment Strength	$V_{n@My}$ (kips)	160	AISC 360-10 §I3.3.a	Superposition of elastic stresses for composite section (slab included)
	$V_{n@My}/\sqrt{f_c'(psi)}b_w d$	8.19		
	$\phi\ V_{n@My}$ (kips)	144		$\phi = 0.9$
	$V_{n@Mp}$ (kips)	143	AISC 360-10 §I3.3.b	Plastic strength of steel section alone
	$V_{n@Mp}/\sqrt{f_c'(psi)}b_w d$	7.27		
	$\phi\ V_{n@Mp}$ (kips)	128		$\phi = 0.9$
	$V_{n@Mp}$ (kips)	181	AISC 341-16	Plastic strength of steel section and concrete
	$V_{n@Mp}/\sqrt{f_c'(psi)}b_w d$	9.22		
	$V_{n@Mpr}$ (kips)	193	AISC 341-16	Plastic strength of steel section & concrete using expected material properties
	$V_{n@Mpr}/\sqrt{f_c'(psi)}b_w d$	9.85		
Section Shear Strength	V_n (kips)	105	AISC 360-10 §I4.1.a	Steel section alone included
	$V_n/\sqrt{f_c'(psi)}b_w d$	5.37		
	$\phi\ V_n$ (kips)	105		$\phi = 1.0$
	V_n (kips)	66	AISC 360-10 §I4.1.b	Concrete & transverse reinforcement included
	$V_n/\sqrt{f_c'(psi)}b_w d$	3.38		
	ϕ	50		$\phi = 0.75$
	V_n (kips)	132	AISC 360-10 §I4.1.c	Steel section & transverse reinforcement included
	$V_n/\sqrt{f_c'(psi)}b_w d$	6.72		
	$\phi\ V_n$ (kips)	99		$\phi = 0.75$
	V_n (kips)	172	AISC 341-16 Eq. H4-2	Steel section, transverse reinforcement, and concrete included based on AISC 341-16
	$V_n/\sqrt{f_c'(psi)}b_w d$	8.75		
	$\phi\ V_n$ (kips)	154		$\phi = 0.9$
Embedment Strength	L_e (in.)	24		Embedment length
	$V_{n,connection}$ (kips)	219	AISC 341-16 Eq. H4-1	Calculated based on AISC 341-10. No provisions available in AISC 360
	$V_{n,connection}/\sqrt{f_c'(psi)}b_w d$	11.19		
	$\phi V_{n,connection}$ (kips)	197		$\phi = 0.9$

Conversions: 1in. = 24.5 mm; 1kips = 4.4485 kN.

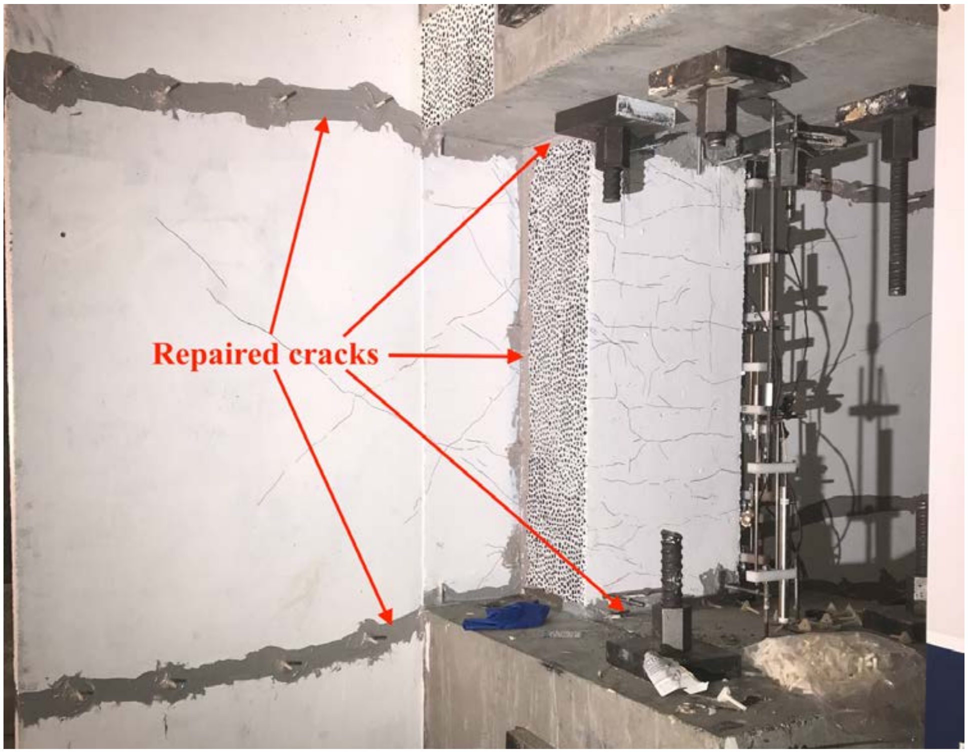

(*a*) East view
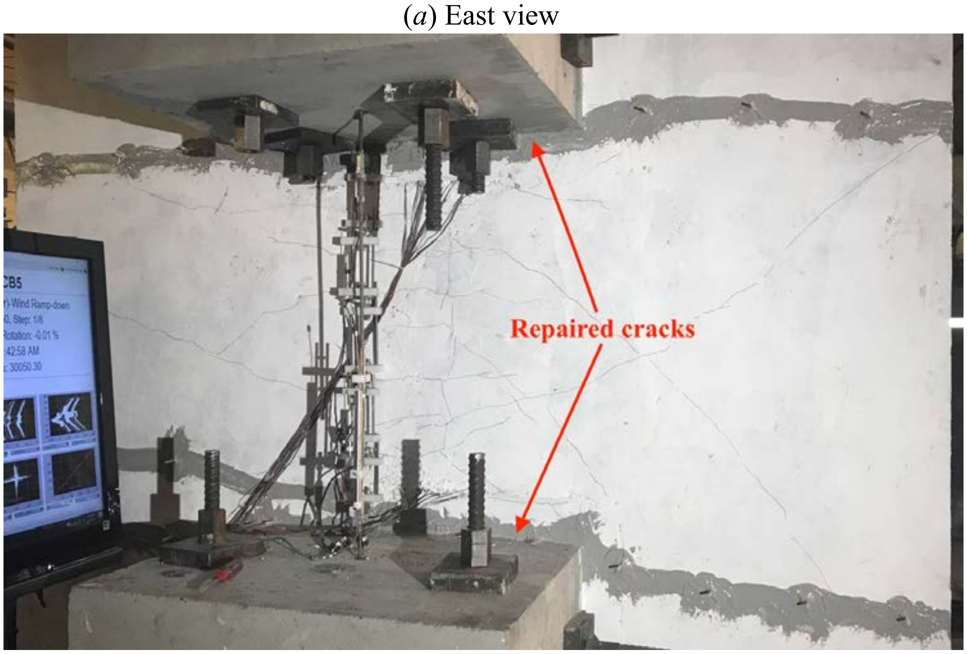

(*b*) West view

Figure 2-7. CB5R beam after repaired is completed.

2.3. Material Properties

2.3.1. Concrete

A design 28-day concrete compressive strength (f_c') of 8,000 psi (55 MPa), a maximum aggregate (crushed Orca rock) size of 1/2 in. (12.7 mm), and a slump of 8 in. (203 mm) were specified for all test specimens. The specimens were constructed in two phases; all specimens in the same phase were cast on the same day using ready-mixed normal weight concrete of the same batch at the UCLA Structural/Earthquake Engineering Research Laboratory. It should be noted that although an f_c' of 8,000 psi (55 MPa) was specified for the design calculations, a lower concrete compressive strength [6,000 psi (41.4 MPa)] was specified for the selected mix design in an effort to limit significant overstrength in the actual (tested) compressive strength. The material proportions of the mix design are provided in **Table 2-3**, and further details of the mix design used is given in **Appendix B**.

Standard 4×8 in. (100×200 mm) cylinders were cast and tested in accordance with ASTM C31/C31M and ASTM C39/C39M specifications, respectively, to evaluate mechanical properties of concrete used for the beams at 7-day, 28-day, and test-day ages (**Table 2-4**). The tests results presented in **Table 2-4** are taken as the average of three or four cylinder tests, consistent with §26.5.3.2 and §26.12.1.1 of ACI 318-14 that require concrete strength tests for acceptance to be the average of at least three 4x8 in. (100x200 mm) cylinders. Compression stress-strain relationships for the test-day age of the cylinders are shown in **Figure 2-8**.

Table 2-3. The proportions of the mix design

Constituent	Quantity, lb/yard^3 (kg/m^3)
Coarse Aggregate[1]	1549 (919)
Fine Aggregate[2]	1495 (860)
Cement Type II/V	563 (334)
Water	300 (178)
Fly Ash	187.2 (111)
WRDA64[3]	29 (17.2)
ADVA[4]	29 (17.2)
Sum	**4094 (2429)**

Note: 1 lb = 4.448 N and 1 yard^3 = 0.76 m^3
[1]Orca rock with ½ in. (12.7 mm) maximum size aggregate
[2]Orca rock washed concrete sand (WCS) with 4% moisture content
[3]Water-reducing admixture ASTM C494
[4]High-range water-reducing admixture

Table 2-4. Tested material properties of concrete

Beam ID	$f_{c,7day}$ (ksi)	$f'_{c,28day}$ (ksi)	Test-Day Age (day)	$f'_{c,test}$ (ksi)	ε_{test} at $f'_{c,test}$	$f_{st,test}$ (ksi)
CB1	5.31	6.90	71	8.14	0.00187	-
CB2			248	9.57	0.00202	-
CB3			187	8.05[(1)]	0.00180	-
CB4			104	8.09	0.00165	-
CB5&CB5R	5.25	7.42	89	8.96	0.00199	0.549
CB6			76	8.25	0.00204	0.606
CB7			55	7.87	0.00190	0.654
CB8			71	8.94	0.00204	0.707
CB24F-RC[(2)]	-	-	-	7.31 (50.4)	-	-

Note: 1 ksi = 6.9 MPa.
[(1)] Some water was added to the mix during pouring without approval of the project engineer.
[(2)] Reported by Naish et al. (2013).

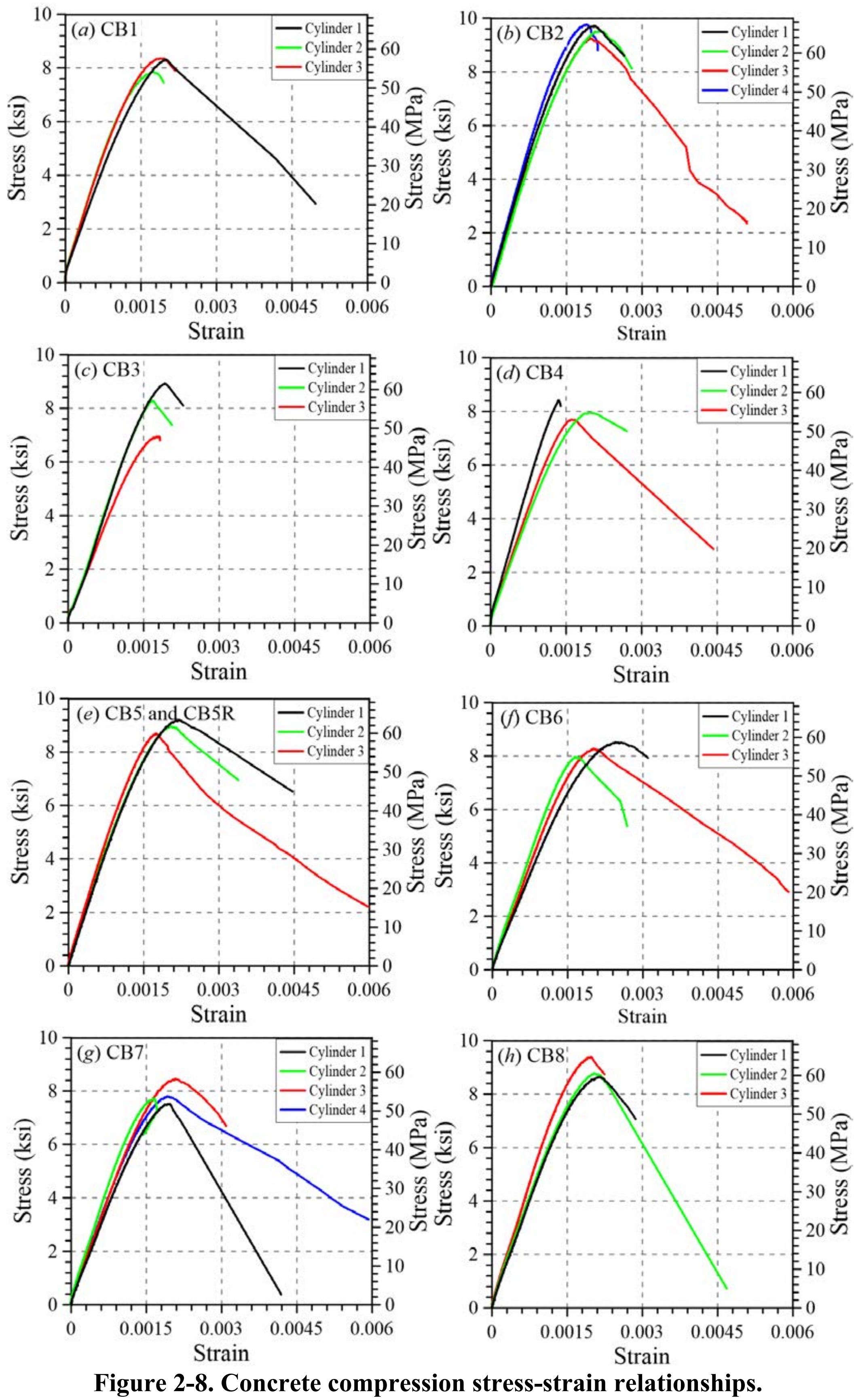

Figure 2-8. Concrete compression stress-strain relationships.

2.3.2. Reinforcement

All the reinforcement bars used to fabricate the test specimens was dual grade ASTM A615/A706 Grade 60 (nominal yield strength of 60 ksi [414 MPa]) deformed bars. All bars of a given size were obtained from the same heat to minimize variations in reinforcement properties between test specimens. The W12x40 steel section used in CB6 was ASTM A992 grade 50 (nominal yield strength of 50 ksi [345 MPa]). The mill certified mechanical properties of the reinforcement bars and steel section are given in **Table 2-5**. Tested mechanical properties of the reinforcement were determined from direct tensile tests performed on three or four representative 24 in. (610 mm) long coupons for each bar size. Cross-sectional dimensions and results of the tensile tests corresponding to yield ($f_{y,test}$, $\varepsilon_{y,test}$), tensile strength ($f_{u,test}$, $\varepsilon_{u,test,}$), and rupture ($f_{rup,test}$, $\varepsilon_{rup,test}$), along with the strain at which strain-hardening initiated ($\varepsilon_{sh,test}$) are given in **Table 2-6**. The yield strength ($f_{y,test}$) was determined from the 0.2% offset method. The stress at which this line crosses the test data is $f_{y,test}$. The corresponding yield strain was calculated as $\varepsilon_{y,test} = f_{y,test}/E_s$, where E_s is the elastic modulus of steel and taken as 29,000 ksi (200,000 MPa) for all bars. Tension stress-strain results of the tested reinforcement bars are shown in **Figure 2-9** and **Figure 2-10**. No test was performed for the W12x40 steel section in CB6; therefore, the mill certified yield and tensile strengths and elongation provided by the supplier (**Appendix C**) are used.

Table 2-5. Mill certified mechanical properties of the reinforcements

Beam ID	Bar No. or steel section	$f_{y,cert}$ (ksi)	$f_{u,cert}$ (ksi)	Elongation(1)
CB1, CB2, CB3, and CB4	No. 3	68.53	105.15	0.140
	No. 6	70.73	96.51	0.160
	No. 7	72.50	102.00	0.170
	No. 8	73.00	102.00	0.120
CB5, CB5R, CB7, and CB8	No. 3	69.94	108.85	0.130
	No. 6	75.00	105.00	0.140
	No. 7	71.34	99.16	0.144
	No. 8	69.00	96.50	0.170
CB6	No. 3	69.94	108.85	0.130
	W12x40	56.00	73.00	0.256

(1) Elongation of an 8"-long gage length.
Note: 1 ksi = 6.9 MPa; 1 in. = 25.4 mm; 1 in^2 = 645.2 mm^2.

Table 2-6. Tested mechanical properties of the reinforcement

Beam ID	Bar No. or steel section	d_b (in.)	A_s (in^2)	$f_{y,test}$ (ksi)	$\varepsilon_{y,test}$	$\varepsilon_{sh,test}$	$f_{u,test}$ (ksi)	$\varepsilon_{u,test}$	$f_{rup,test}$ (ksi)	$\varepsilon_{rup,test}$
CB1, CB2, CB3, and CB4	No. 3	0.375	0.11	66.1	0.00228	0.010	102.0	0.10	89.7	0.132
	No. 6	0.750	0.44	68.6	0.00237	0.010	96.4	0.133	76.0	0.165
	No. 7	0.875	0.60	69.8	0.00240	0.014	98.4	0.152	80.0	0.186
	No. 8	1.000	0.79	68.5	0.00236	0.010	97.0	0.135	79.0	0.165
CB5, CB5R, CB7, and CB8	No. 3	0.375	0.11	65.0	0.00234	0.008	103.0	0.110	89.5	0.130
	No. 6	0.750	0.44	72.3	0.00249	0.012	99.7	0.110	86.7	0.140
	No. 7	0.875	0.60	69.0	0.00234	0.010	98.0	0.149	78.0	0.195
	No. 8	1.000	0.79	69.0	0.00234	0.018	95.0	0.158	77.0	0.199
CB6	No. 3	0.375	0.11	65.0	0.00234	0.008	103.0	0.110	89.5	0.130
	W12x40(1)	-	11.7	56.0	-	-	73.0	-	-	0.256
CB24F-RC(2)	No. 3	0.375	0.11	70.0	-	-	90.0	-	-	-
	No. 7	0.875	0.60	70.0	-	-	90.0	-	-	-

Note: 1 ksi = 6.9 MPa; 1 in. = 25.4 mm; 1 in^2 = 645.2 mm^2.
(1) Reported properties are taken from the mill certificate.
(2) Reported by Naish et al. (2013).

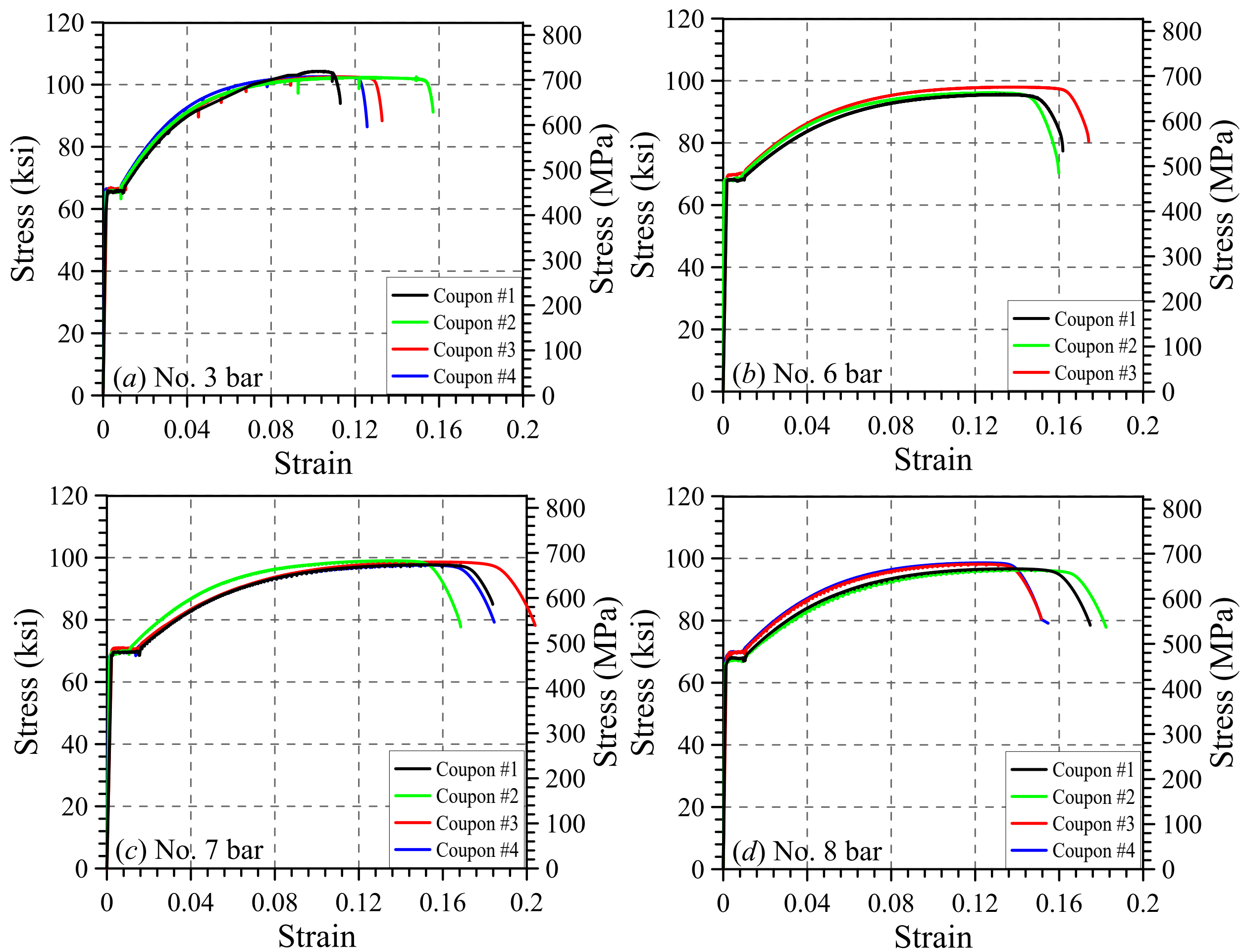

Figure 2-9. Stress-strain relationships for reinforcement bars used for beams in Phase I (CB1 through CB4).

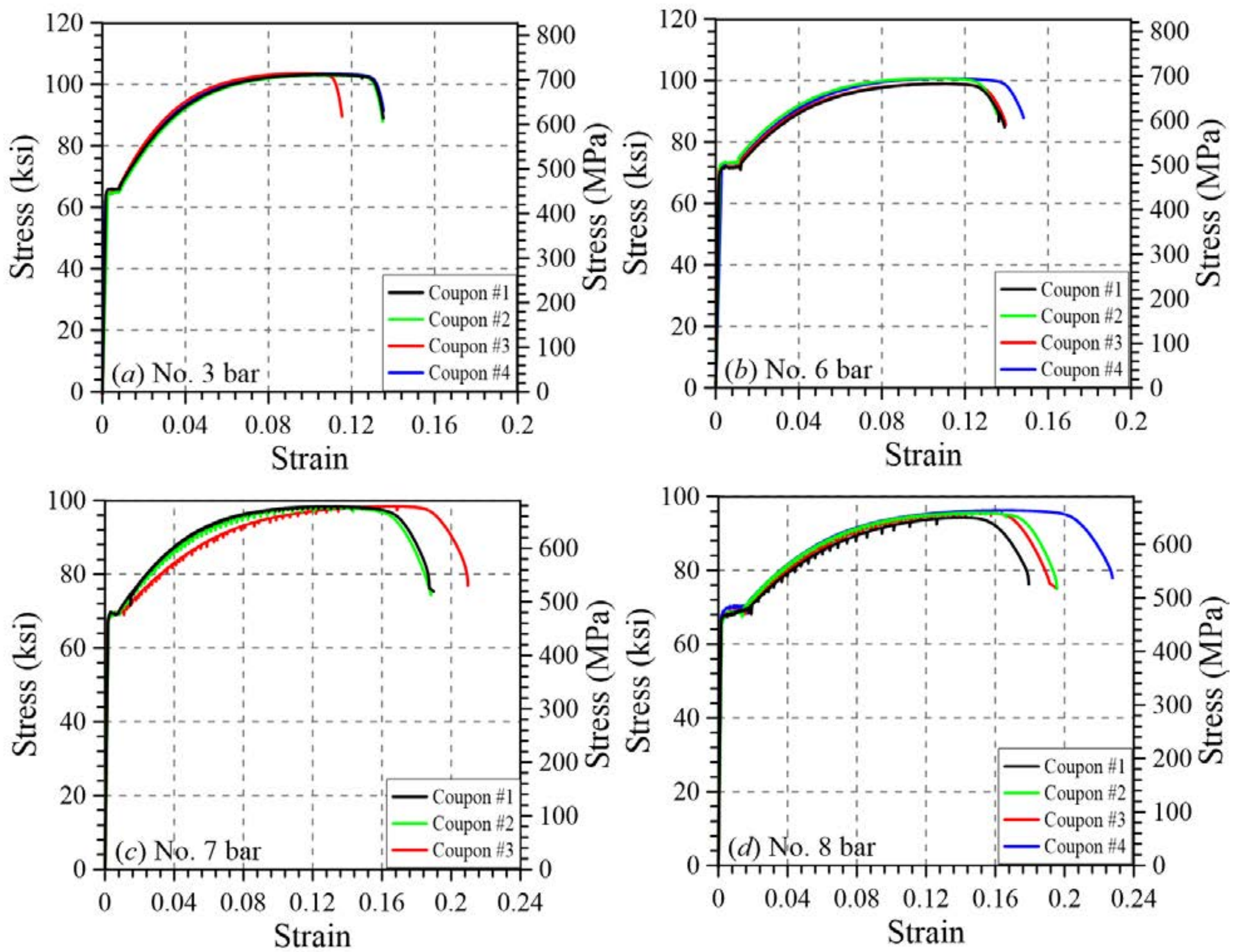

Figure 2-10. Stress-strain relationships for reinforcement used for beams in Phase II (CB5 through CB8).

2.4. Test Setup

The setup shown in **Figure 2-11** through **Figure 2-14** was used to test the coupling beams in a vertical position, where the end blocks were grouted using hydro-stone and post-tensioned to the laboratory strong floor at the bottom and to a structural steel loading beam at the top using 1-1/4 in. (32 mm) diameter high-strength post-tensioning Dywidag bars. A horizontal hydraulic actuator was used to apply the lateral load using the steel loading beam, and the two vertical hydraulic actuators were used to ensure zero rotation of the top block and to achieve zero moment at beam midspan (i.e., a double curvature loading condition). No axial load (or axial restraint) was applied to the beams during testing. To prevent out-of-plane rotation or twisting, the steel loading beam was connected to two out-of-plane actuators, which were attached to steel reaction braced frames (**Figure 2-12** through **Figure 2-14**).

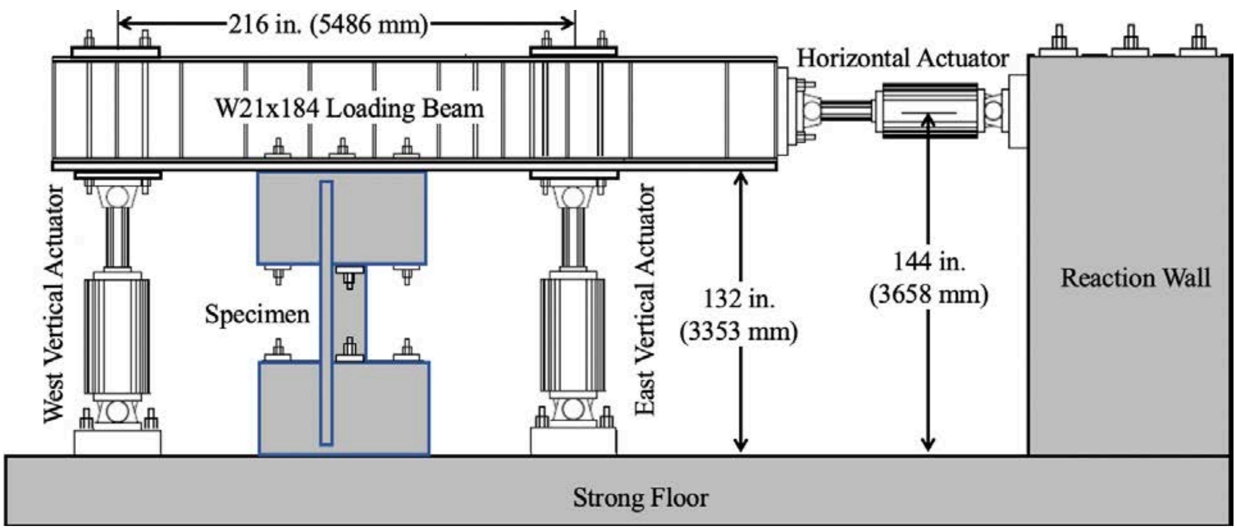

Figure 2-11. Schematic test setup (not drawn to scale).

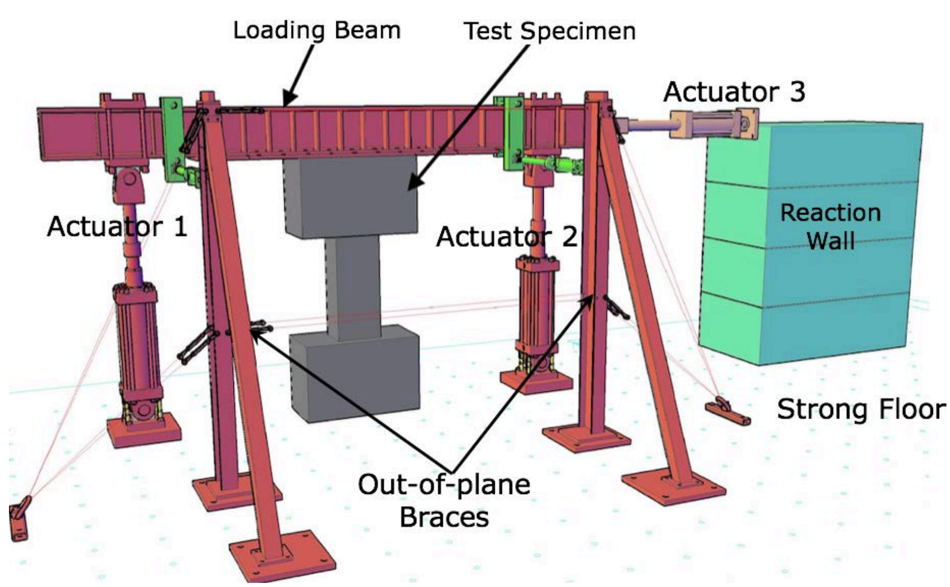

Figure 2-12. Isometric view of the test setup.

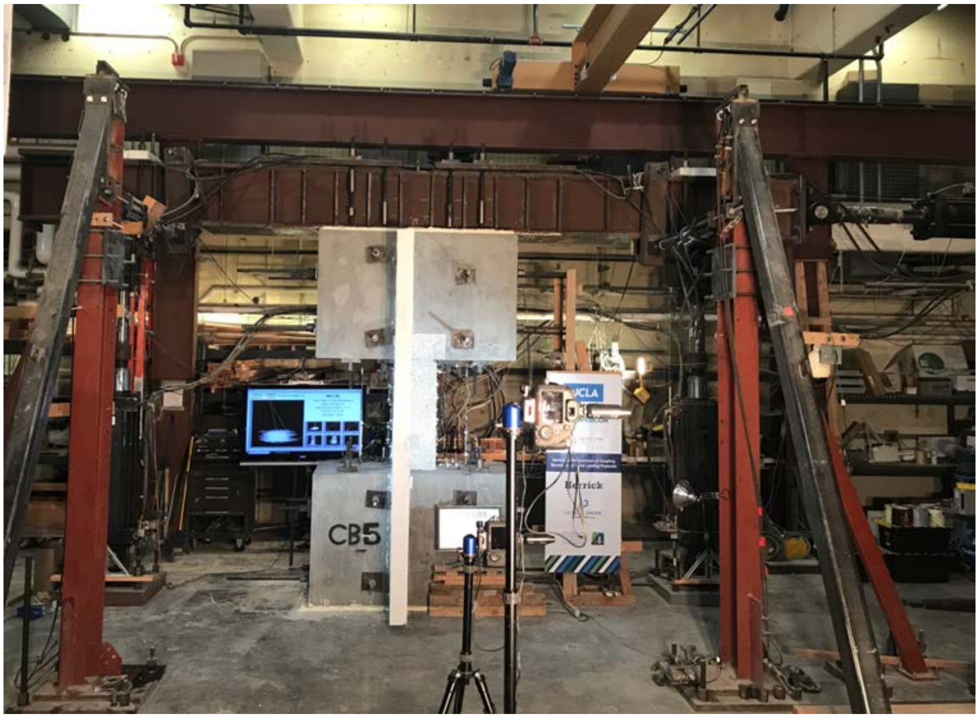

Figure 2-13. Test setup with a 2.5 aspect ratio test beam under testing.

Figure 2-14. Test setup with a 3.67 aspect ratio test beam under testing.

2.5. Instrumentation

Each test specimen was instrumented with approximately 40 linear variable differential transformers (LVDTs) and string potentiometers to measure global displacements and beam local deformations due to flexure, shear, and sliding (**Figure 2-15**) and load cells to measure loads in each of the actuators. Strain gages were installed on longitudinal, diagonal, and transverse reinforcement to measure strains in the reinforcing bars and steel section at about 20 to 28 specific locations (**Figure 2-16** and **Appendix D**). In addition to marking crack propagation and taking digital photographs, crack widths were manually measured at peak and zero rotations of at least one cycle at the beginning and one cycle at the end of each loading stage.

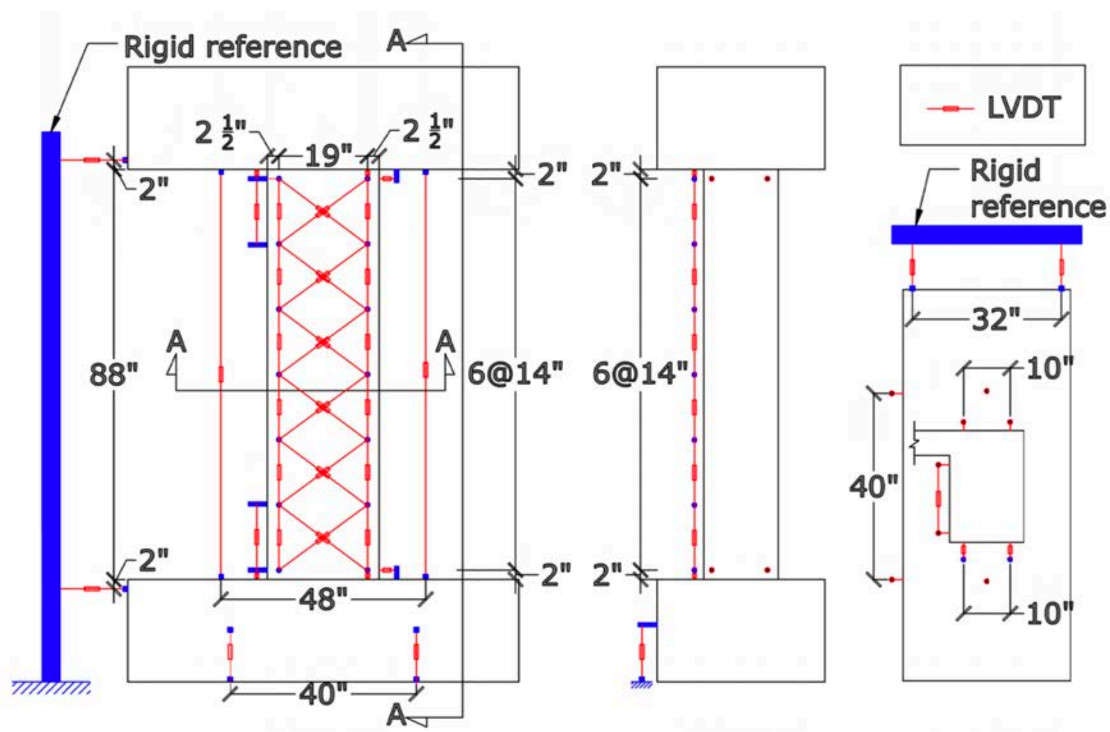

(*a*) North view (*b*) Section A-A (*c*) Section B-B

Figure 2-15. Typical LVDT configuration.

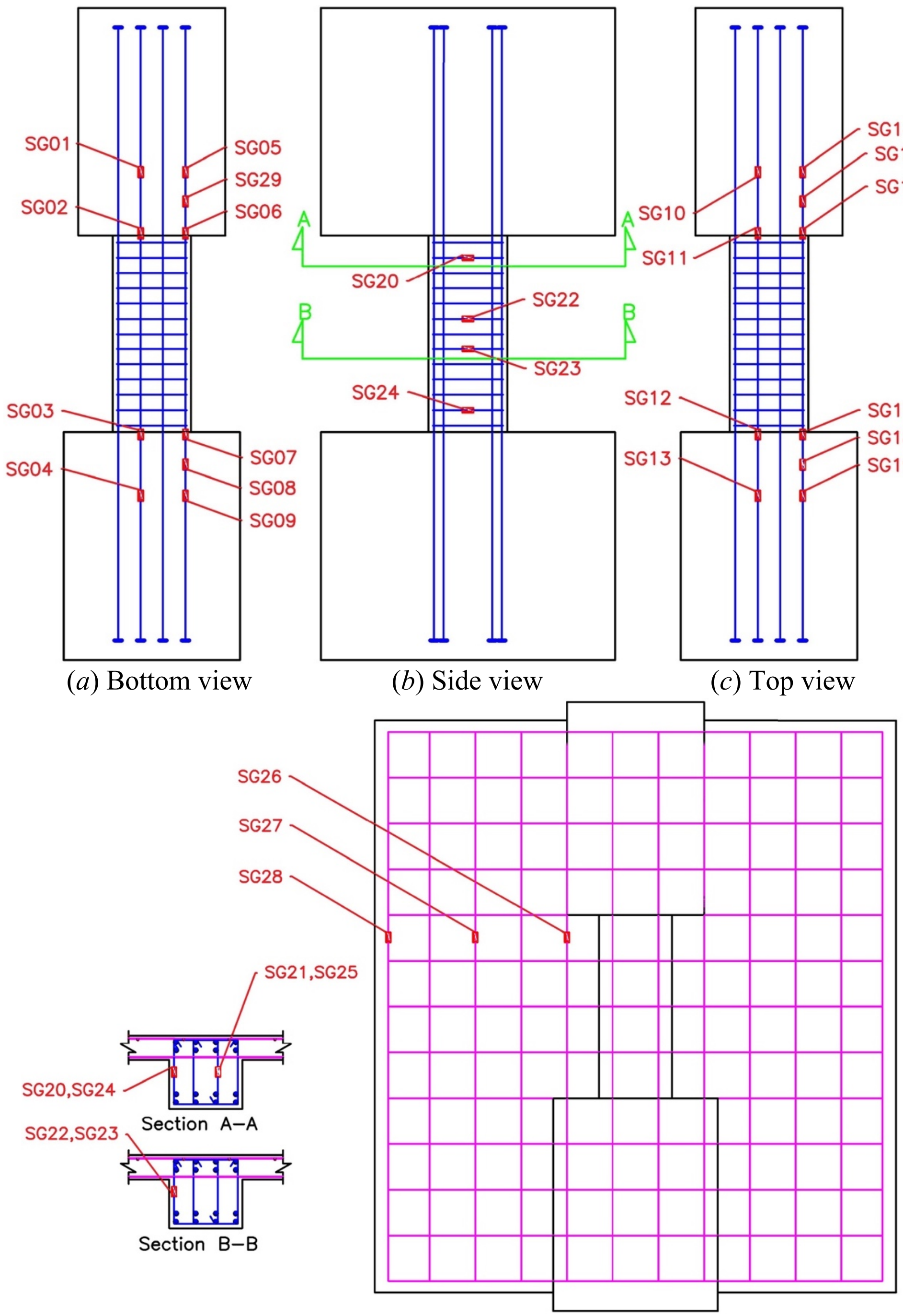

(*a*) Bottom view (*b*) Side view (*c*) Top view

(*d*) Cross-section views (*e*) Top slab view

Figure 2-16. Typical strain gage configuration. (Note: SG = strain gage)

An optical non-contact measurement system, referred to as digital image correlation (DIC), was used to measure surface strains on the south web face of the beams, as shown in **Figure 2-17**. The system utilizes one or two digital single-lens reflex (DSLR) camera and a lightening system. The surface of test specimens was prepared with a light coat of white paint that served as a contrast for a random speckle pattern applied with black paint (**Figure 2-17**). Each black speckle was approximately 5 to 20 pixels in width and height. Approximately 30 high resolution images were taken during each selected cycle. The images were processed by GOM© Correlate software (2018), a digital image correlation and evaluation software for materials research and component testing, to get surface strains and crack pattern and width**.**

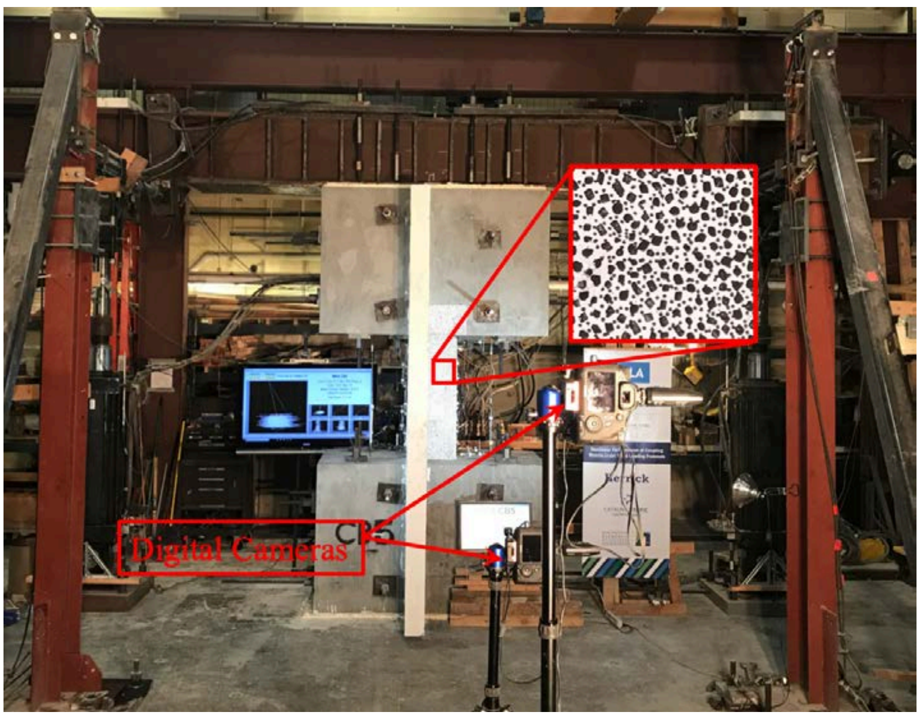

Figure 2-17. Digital image correlation setup.

2.6. Loading Protocols

As noted previously, the test beams were first subjected to a wind loading protocol followed by a standard seismic loading protocol. Different wind loading protocols were used in each phase of the program. This section describes, in detail, how the wind loading protocols were developed, and gives a short description of the seismic loading protocol.

2.6.1. Wind Loading Protocol–Phase I

Unlike seismic loading, standardized quasi-static, cyclic wind loading protocols are not available for testing structural building components; therefore, a wind loading protocol was developed in this study for Phase I tests. The protocol was based on a representative wind hazard curve and results of nonlinear response history analysis of a tall coupled core wall building subjected to loading histories recorded from a wind tunnel test. Developing the wind loading protocol involved specifying the amplitude of the peak loading cycles (i.e., maximum ductility demands) and determining the number and amplitude of the cycles before and after the peak cycles (i.e., ramp-up and ramp-down loading cycles), as follows:

Amplitude of the Peak Loading Cycles

The amplitude of the peak loading cycles was based on the maximum ductility demand expected to be permitted for coupling beams, which was set equal to 1.5. This value was judged to result in a modest amount of material nonlinearity—significantly less than the deformation capacity expected of a coupling beam with seismic or standard detailing (e.g., see ASCE 41-17). The maximum ductility demand was determined by comparing expected demands for a building subjected to a "collapse level" windstorm with a mean recurrence interval (MRI) of approximately 3,000 years to demands from a windstorm with an MRI of 100 years, closer to the MRI for which these coupling beams would be designed if utilizing a performance-based wind design approach. **Figure 2-18** shows a wind hazard curve for a site in Miami, Florida using data provided by Rowan Williams Davies & Irwin Inc., RWDI (personal communication, April 23, 2019). For this site, the wind speeds for the 3,000-year and 100-year MRIs are 181 mph (81.8 m/s) and 134 mph (60 m/s), respectively. Using the relationship that wind demands are approximately proportional to the square of the wind speed (e.g., ASCE 7-16 Equation 26.10-1), the 3,000-year wind demands are approximately 1.82 times the 100-year wind demands (i.e., $V_{@3000MRI}/V_{@100MRI} = [181/134]^2 = 1.82$), ignoring the impact of material nonlinearity due to concrete cracking and the aerodynamic effects of wind. For a typical RC beam, the overstrength ratio due to material overstrength and strain hardening of reinforcement, defined as the ratio of probable (or expected) moment capacity (M_{pr}) to factored nominal moment capacity (ϕM_n), can approximately be taken as 1.30 to 1.35, as can be seen from **Table 2-1**. Using the equal displacement approximation and dividing the collapse-level force amplification of 1.82 by the beam overstrength ratio of 1.3 yields a required beam ductility demand of 1.4, as illustrated in **Figure 2-19**. This indicates that the beam force and displacement demands for the 3,000-year MRI wind are approximately 140% of those corresponding to the beam probable capacity (**Figure 2-19**), which is only slightly smaller than the value of 1.5 set by the authors for the peak ductility demand.

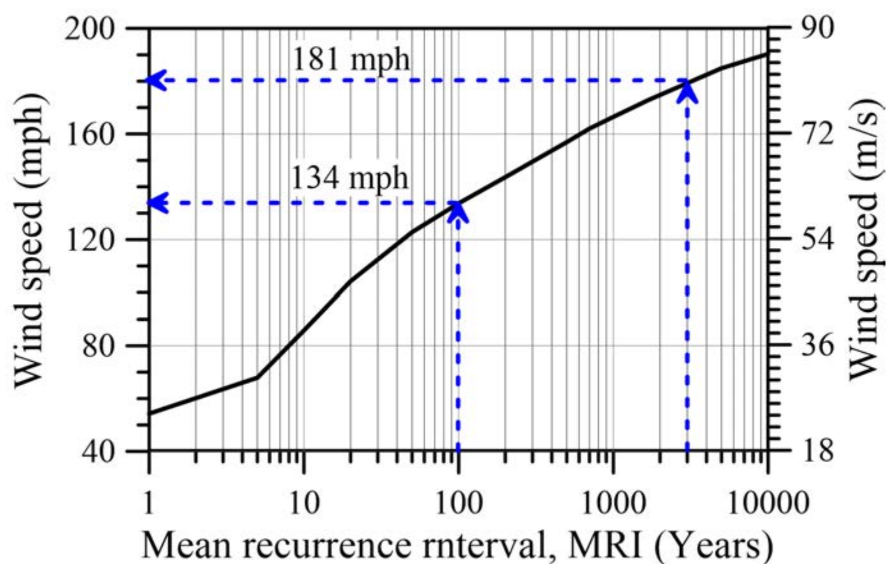

Figure 2-18. A representative wind hazard curve for Miami, Florida created with data from RWDI (Note: wind speeds are 3-s gust, 33 ft (10 m) for open terrain-Exposure C).

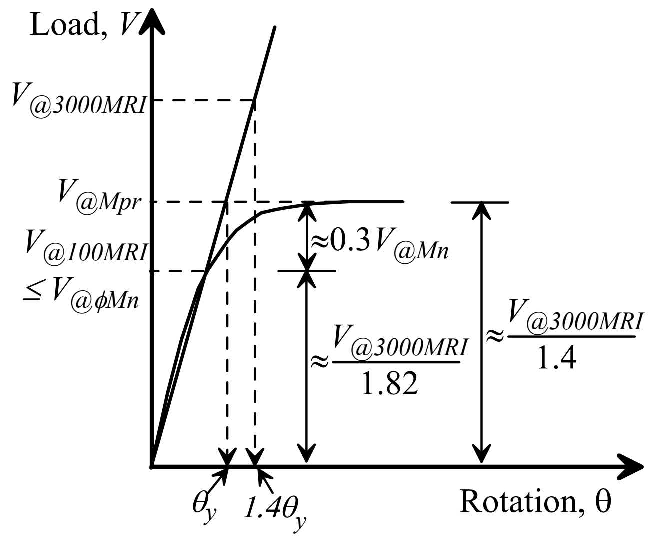

Figure 2-19. Illustration of the expected maximum ductility demand.

Number and Amplitude of Cycles Before and After the Peak Cycles

Results from nonlinear response history analysis of a 58-story building with a coupled core wall lateral force resisting system subjected to loading histories recorded from wind tunnel tests were reviewed. The core wall coupling beam demands at several stories were determined, and then the number of times the demands exceeded several different fractions of the peak demand in the positive and negative directions were counted and averaged (e.g., see **Figure 2-20**). As discussed above, the peak rotation was set equal to 150% of the expected yield rotation (ductility ratio of 1.5), with the demands for all other loading levels set equal to a fraction of the probable strength, set equal to values of 15%, 40%, 75% of M_{pr} and 120% of θ_y for this study. Based on these results, the loading protocol shown in **Figure 2-21** was developed. To simulate the effects of a windstorm approaching and then passing a site (not simulated in the results shown in **Figure 2-20**), the loading protocol ramps up to the peak ductility demand and then symmetrically ramps back down. Since wind loading is force-based in nature, all cycles prior to yield were applied in a force-controlled protocol, whereas cycles beyond yield were applied in a displacement-controlled protocol (**Figure 2-21**). The total number of cycles in the protocol is 2,162. For a building whose fundamental period is about six seconds (roughly a 50-70 story building), this results in a total simulated windstorm duration of slightly more than three and a half hours.

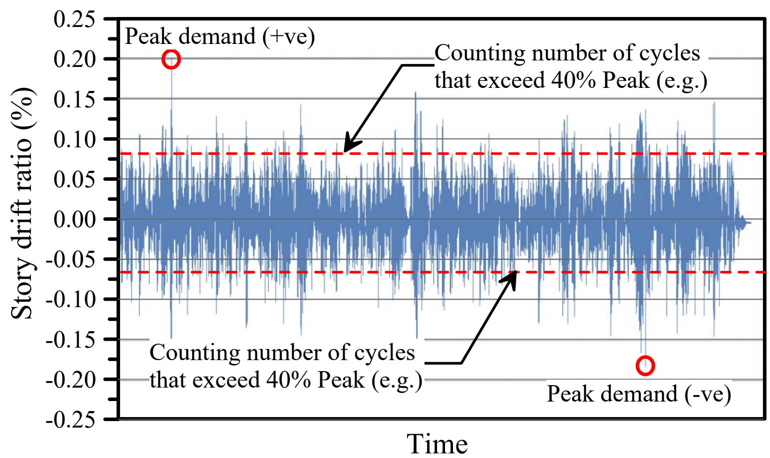

Figure 2-20. Example demand of a core wall subjected to time histories recorded from wind tunnel tests (non-zero mean component of the drift ratio was removed).

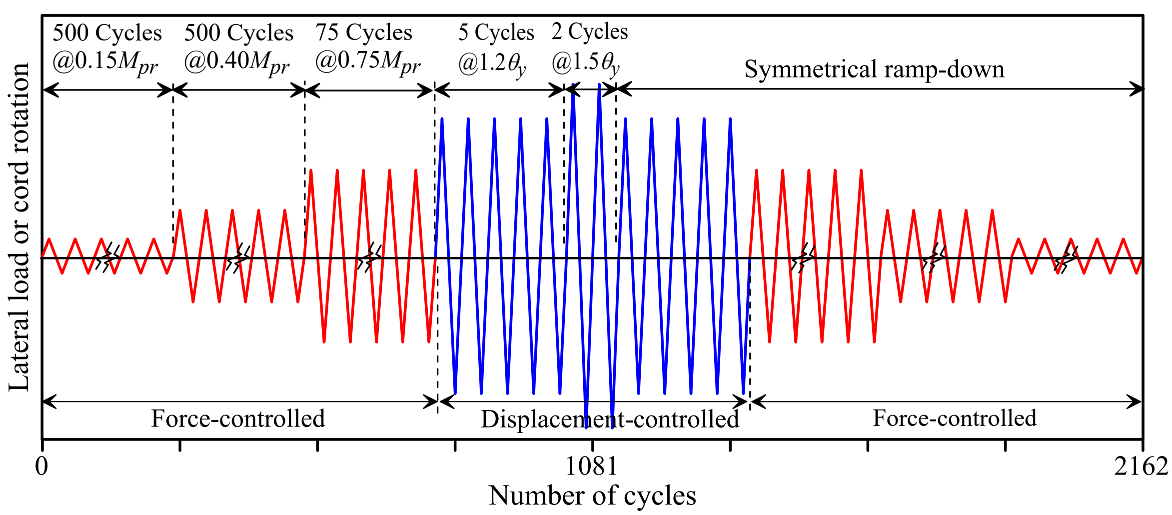

Figure 2-21. Wind loading protocol used to test beams in Phase I.

It is noted that, during a windstorm, tall buildings are subjected to wind loads not only in the direction of wind flow, but also in the crosswind direction. As well, torsional response may occur if the building lacks symmetry (either structurally or architecturally), the surroundings cause asymmetrical wind flow around the building, and/or due to the random fluctuations in the wind pressures. The wind loading protocol shown in **Figure 2-21** is intended to simulate the dynamic response of a tall building in the cross-wind direction, where the direction of sway is perpendicular to the direction of the wind, but the structure responds around a zero-mean reference (i.e., the mean base shear tends to zero over time). This protocol was used to test the coupling beams in Phase I: CB1 through CB4 (

Table 2-7). The impact of variations of this loading protocol was examined in Phase II, as described the section below.

2.6.2. Wind Loading Protocol –Phase II

As noted previously, after the first phase of testing, in recognition of the inherent uncertainty associated with determination of the wind loading protocol, questions were raised by the structural and wind engineering community regarding the effects of variation in the wind loading protocol on the performance of coupling beams. Specifically, committee members involved in the development of the ASCE/SEI Prestandard for Performance-Based Wind Design (2019) requested that Phase II of the experimental program investigate the impact of: 1) increasing the number of inelastic cycles, 2) introducing a non-zero mean component (simulating the ratcheting effect of wind in the along-wind direction), and 3) having more than one ramp-up and ramp-down (i.e., spreading out the yielding cycles). To address each of these concerns individually, the original wind loading protocol used for Phase I testing (**Figure 2-21**) was modified as follows:

Alternative Loading Protocol #1: This protocol is similar to the Phase I wind loading protocol, except that the total number of yielding cycles was increased from 12 to 50 cycles. In recognition of their negligible impact observed during Phase I tests, the total number of the low-amplitude cycles at $0.15M_{pr}$ was reduced from 1,000 to 500 cycles with half applied at the beginning and the other half applied at the end of the loading protocol, as shown in **Figure 2-22** (***a***). This loading protocol consists of a total of 1700 cycles and was used to test CB5, CB5R, and CB6 (

Table 2-7).

Alternative Loading Protocol #2: This protocol is similar to the Phase I wind loading protocol, except that a non-zero mean component was introduced by decreasing the amplitude of the cycles by half in the negative direction of loading, as shown in **Figure 2-22** (***b***). This protocol was intended to simulate the ratcheting effect (the tendency for a building to progressively deform in a particular direction) due to the wind pushing on the building in the along-wind direction (i.e., building oscillating about a non-zero reference point). This protocol consists of a total of 2162 cycles and was used to test CB7 (

Table 2-7).

Alternative Loading Protocol #3: This protocol is also similar to the Phase I wind loading protocol, except that the cycles were divided in half and run back-to-back, introducing a ramp up–

ramp down–ramp up–ramp down effect, as shown in **Figure 2-22** (*c*). This loading protocol consists of a total of 2163 cycles and was used to test CB8 (

Table 2-7).

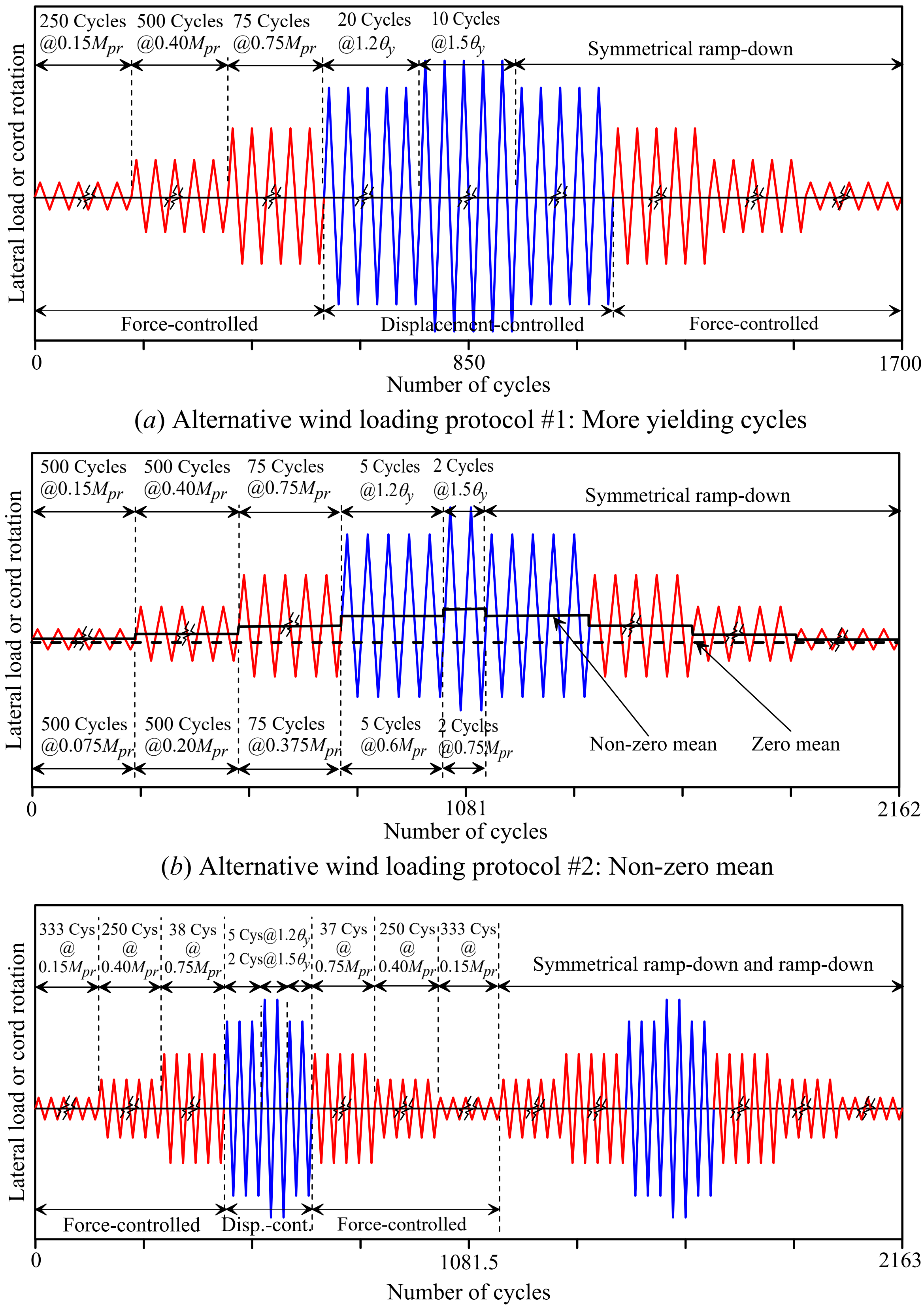

(a) Alternative wind loading protocol #1: More yielding cycles

(b) Alternative wind loading protocol #2: Non-zero mean

(c) Alternative wind loading protocol #3: Two ramp-up and ramp-downs

Figure 2-22. Alternative wind loading protocols used in Phase II.

Table 2-7. Wind loading protocol used to test each specimen

<table>
<tr><th>Testing Phase</th><th>Beam ID</th><th>Loading Protocol Used</th><th>Total Number of Cycles</th><th>Figure Reference</th></tr>
<tr><td rowspan="4">Phase I</td><td>CB1</td><td rowspan="4">Original Protocol</td><td rowspan="4">2162</td><td rowspan="4">Figure 2-21</td></tr>
<tr><td>CB2</td></tr>
<tr><td>CB3</td></tr>
<tr><td>CB4</td></tr>
<tr><td rowspan="5">Phase II</td><td>CB5</td><td rowspan="3">Alternative Protocol #1
(increased number of yielding cycles)</td><td rowspan="3">1700</td><td rowspan="3">Figure 2-22 (a)</td></tr>
<tr><td>CB5R</td></tr>
<tr><td>CB6</td></tr>
<tr><td>CB7</td><td>Alternative Protocol #2–Non-zero mean</td><td>2162</td><td>Figure 2-22 (b)</td></tr>
<tr><td>CB8</td><td>Alternative Protocol #3–two ramp-up and ramp-down excursions</td><td>2163</td><td>Figure 2-22 (c)</td></tr>
</table>

2.6.3. Seismic Loading Protocol

As noted previously, to assess the seismic performance of coupling beam subjected to prior mildly inelastic wind demands, the coupling beams were subjected to a standard, quasi-static, reversed cyclic loading protocol simulating seismic loading (ACI 374.2R-13; Naish et al., 2010), following the wind load testing. The seismic loading protocol initiates at the largest wind displacement demand, e.g., either at 1.5% or 2% chord rotation, (**Figure 2-23**) and was applied under displacement-control. The initial cycles at lower demands were not applied since the beams had already gone under a larger number of pre-yield and post-yield cycles during the wind loading protocols. Three cycles were applied at each displacement level up to 3% rotation, and thereafter two cycles were applied at each displacement level, as shown in **Figure 2-23**.

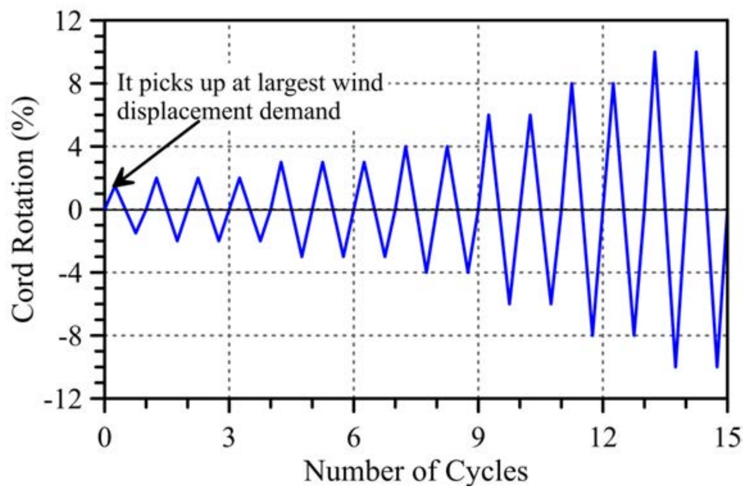

Figure 2-23. Standard seismic loading protocol.

2.7. Fabrication of Test Specimens

The coupling beams were constructed and tested in two phases at the UCLA Structural/Earthquake Engineering Research Laboratory. Phase I included CB1 through CB4 beams, and Phase II included CB5 through CB8 beams (**Figure 2-24**). Test beams in Phase I were constructed during Spring 2018 and tested during Summer and Fall 2018, whereas test beams in Phase II were constructed and tested during Spring and Summer 2019, respectively. Formwork and concrete placement were handled by Webcor Builders, reinforcement was supplied and fabricated by Pacific Steel Group (PGS), concrete was supplied by CalPortland, and epoxy injection repair was supplied and performed by Structural Technology. The formwork was erected in a horizontal position to facilitate construction and concrete placement and to avoid creating construction joints at the beam-block (wall) interfaces (**Figure 2-24**). **Figure 2-25** shows close-up photos of typical reinforcement cages. End blocks and beam reinforcement cages were built separately, and then, after installing strain gages on the reinforcing bars and steel section (see **Appendix D**), they were assembled. PVC pipes were placed in appropriate locations to allow for anchoring the specimens to the test frame and the strong floor and to post-tension the end blocks using 1-1/4 in. (32 mm) diameter high-strength post-tensioning Dywidag bars (**Figure 2-13**, **Figure 2-14**, and **Figure 2-24**).

All specimens in the same phase were cast at the same time, one after another, using ready-mix concrete (**Figure 2-26**). During casting, the freshly placed concrete was consolidated using electric vibrators to release trapped air and excess water and to ensure that the concrete settles firmly in the formwork. The exposed, finished surfaces of the freshly placed concrete were sprayed using a concrete curing and sealing compound to maintain moisture while the concrete gained strength. The formwork was stripped one week after the concrete placement.

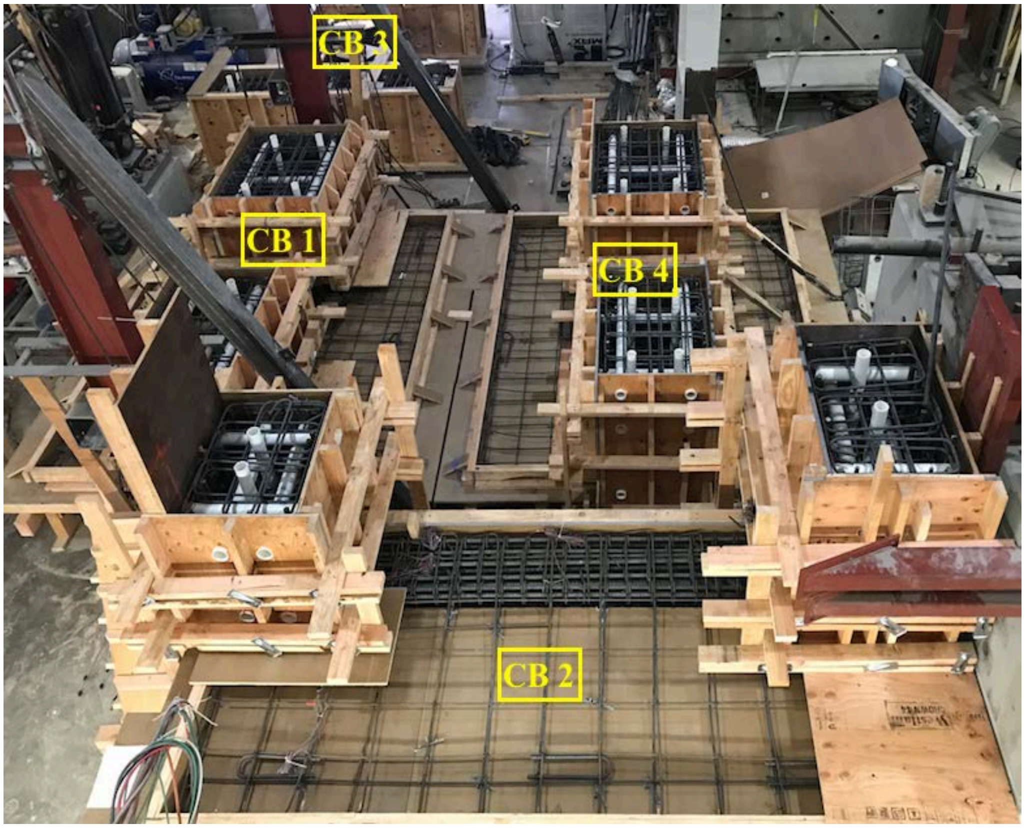

(*a*) Formwork and cages of Phase I beams

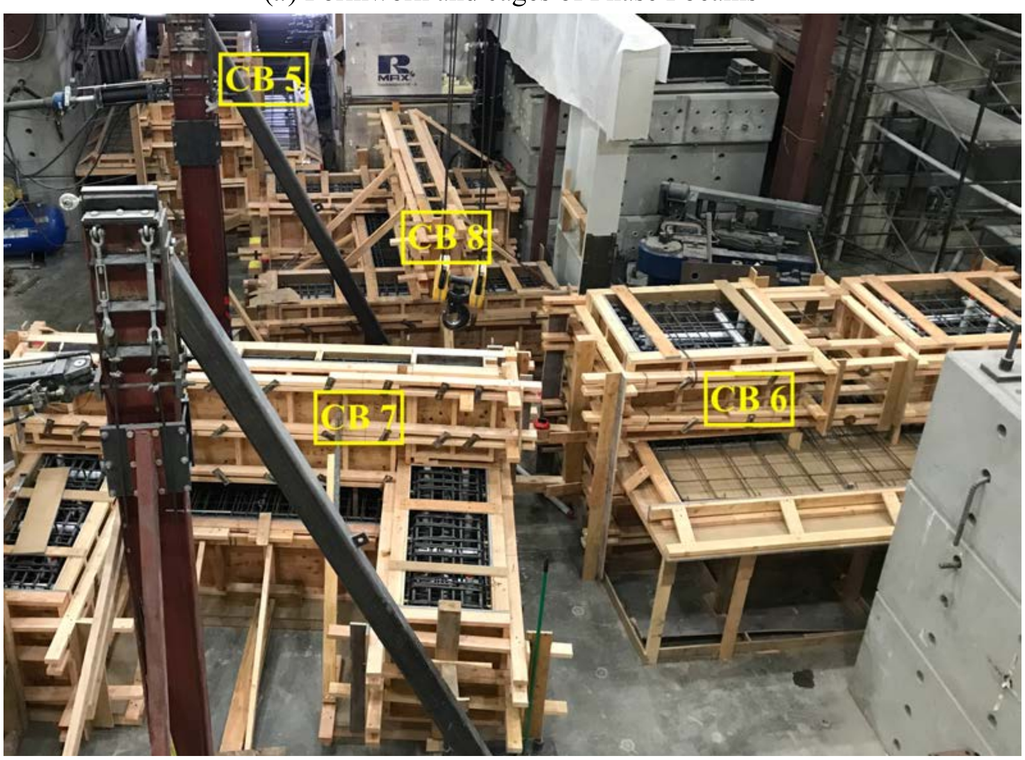

(*b*) Formwork and cages of Phase II beams

Figure 2-24. The test beams under construction

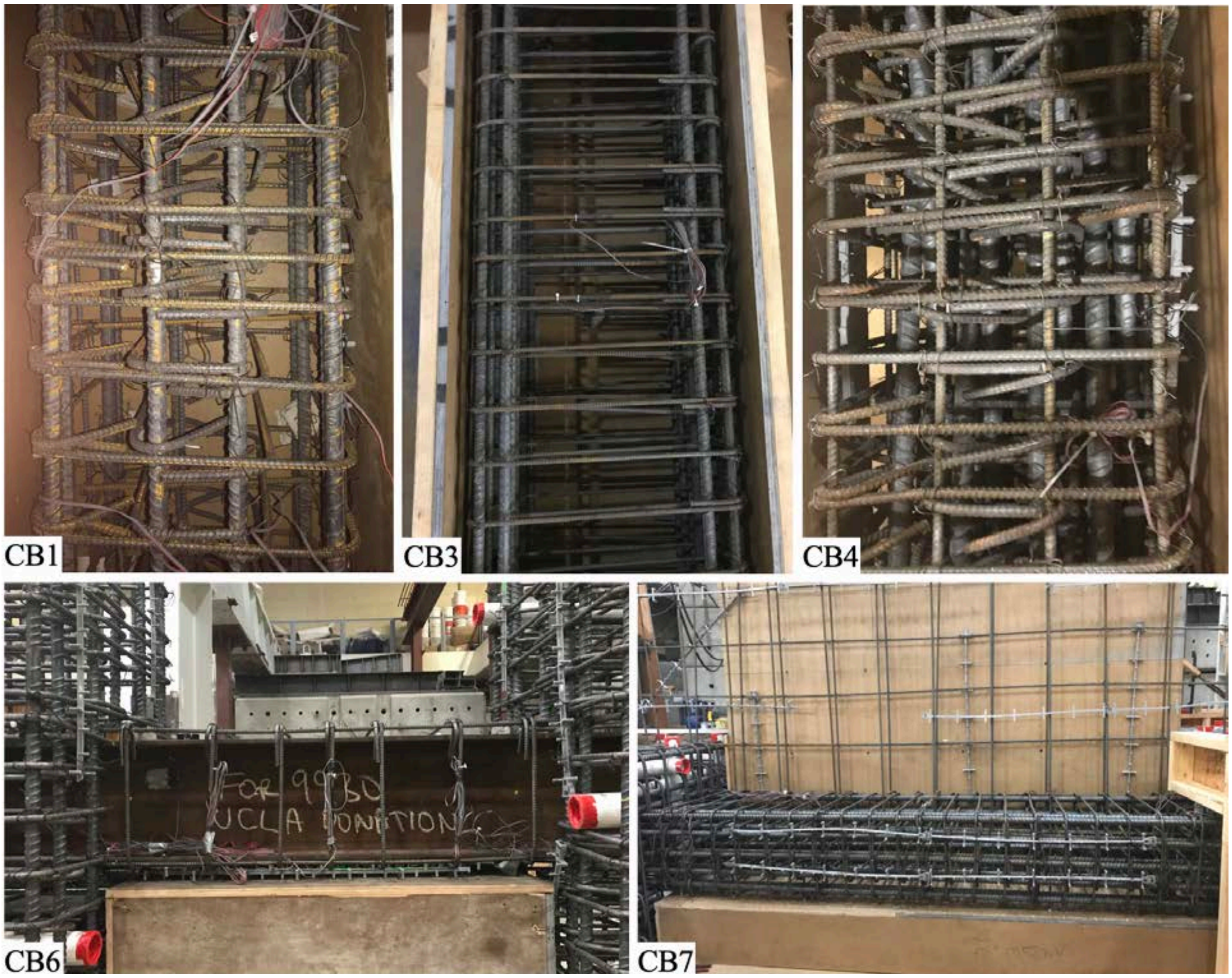

Figure 2-25. Close-up photos of reinforcement cages under construction.

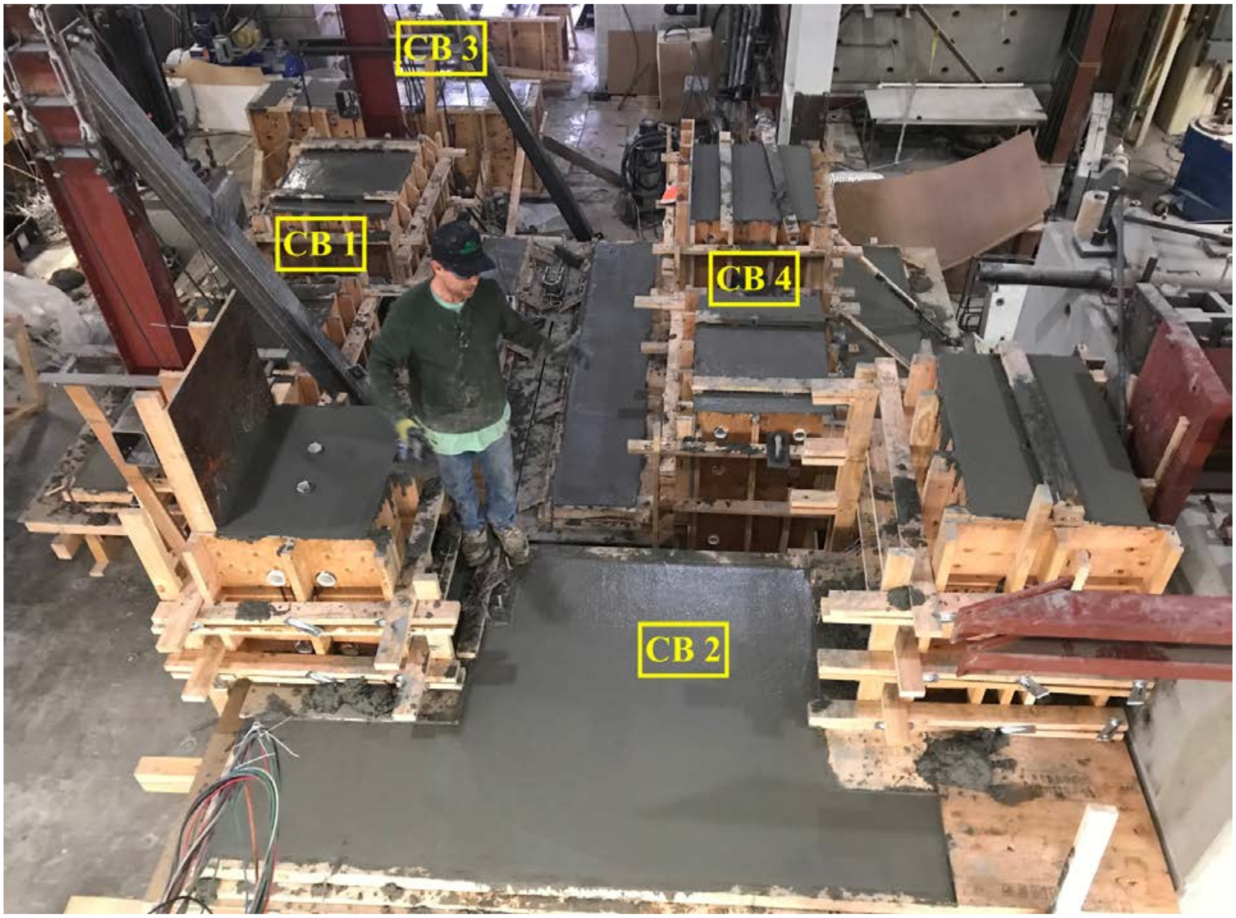

(*b*) Phase I beams.

(*b*) Phase II beams.

Figure 2-26. Concrete casting.

CHAPTER 3. EXPERIMENTAL WIND TEST RESULTS

3.1. General

This chapter presents the experimental results of the wind tests from both phases of the study. The results presented include observed damage and cracking, load-deformation responses, lateral stiffness, axial growth, components of total chord rotation, and energy dissipation capacity.

3.2. Observed Damage and Cracking

All test beams exhibited relatively similar cracking patterns during the wind loading protocols. Visible flexural (slip/extension) cracks first formed at the interfaces between the beams and the end blocks (beam-wall interfaces) during the first cycle at $0.15M_{pr}$ for CB2 through CB4 and CB6 through CB8, and during loading to $0.40M_{pr}$ for CB1 and CB5 (i.e., cracking moment was larger than $0.15M_{pr}$ for CB1). Hairline diagonal tension (shear) cracks were first observed during loading to $0.40M_{pr}$. **Table 3-1** presents width of cracks at the peak of the largest ductility demand and zero rotation at the end of the wind loading protocol (i.e., residual crack widths). Residual cracks are reported because they are better indicators of the required potential repair or restoration technique and cost as opposed to crack widths at peak transient demands. Generally, during the ramp-up cycles of the unrepaired beams, new cracks formed, and existing cracks propagated as the number of cycles increased within each loading stage, whereas during the ramp-down cycles, typically no new cracks formed, and existing crack lengths did not increase. Both flexural and diagonal tension (shear) cracks were primarily concentrated within a distance of h (beam depth) from the beam-wall interface (i.e., plastic hinge region), with the largest crack widths at the beam-wall interfaces (i.e., slip/extension cracks). Since shear strength (V_n) is greater than the strength corresponding to nominal moment capacity ($V_{@Mn}$), but close to the strength corresponding to probable moment capacity ($V_{@Mpr}$), for CB1, CB2, CB3, CB5, CB7 and CB8 (**Table 2-1**), the diagonal tension (shear) cracks were significantly smaller than the flexural cracks (**Table 3-1**), which suggests that the beams longitudinal reinforcement yielded in tension whereas stirrup yielding did not occur or was limited to minor yielding at the peak ductility demand, which was consistent with strain gage readings installed on the reinforcement (**Appendix G**).

Figure 3-1 through **Figure 3-18** show the state of cracking of the beams at the end of the wind loading protocol and reveal that the cracks are relatively minor, and that no significant damage (e.g., concrete crushing, bar buckling, or bar fracture) was observed. The bottom interface of CB4 experienced spalling a thin layer of concrete (≈1/8 to 1/2 in. [3 to 13 mm] thick over a distance of ≈ 2 to 4 in. [51 to 102 mm]) that initiated during the five cycles at ductility demand of 1.2 on the ramp-up and slightly deteriorated during the cycles that followed (**Figure 3-8** (***b***)), whereas the top interface did not experience such spalling and the cracks there were significantly smaller than at the bottom interface (**Figure 3-8** (***c***)). This is because CB4 possessed high flexural capacity, and the top structural steel loading beam, shown in **Figure 2-11**, experienced slight bending (i.e., the top block did not quite maintain zero rotation), which caused the rotation demand to be greater at the bottom end of the beam. The slight rotation of the top block was measured and taken into consideration when calculating the beam stiffness. CB1, which was tested first, did not experience this issue because its lateral strength was only about 60% of that of CB4. For testing CB2, CB3, and CB5 through CB8, which were tested after CB4, the top steel beam was stiffened to address this issue.

For CB5R, the repaired cracks generally remained closed and did not re-form, and new cracks adjacent to epoxied cracks formed during loading to $0.15M_{pr}$ and $0.40M_{pr}$ on the ramp-up. Generally, after loading to $0.40M_{pr}$ on the ramp-up, no new cracks were formed. It was also observed that the shear cracks deteriorated faster than the flexural cracks as the demands increased, partly because the shear cracks were not repaired. The residual shear crack widths of CB5R were larger than those of CB5 (**Table 3-1**).

For CB6, as seen in **Table 3-1**, **Figure 3-13**, and **Figure 3-14**, the flexural and diagonal tension (shear) cracks within distance ***h*** from beam-wall interfaces were significantly smaller than slip/extension cracks at the interfaces both at peak ductility demand and at the end of the wind loading protocol. Furthermore, as the demands increased, the number and width of flexural and diagonal tension (shear) cracks within distance ***h*** from beam-wall interface only slightly increased, whereas width of cracks at the interface increased significantly.

For the beams with floor slabs, which includes all beams except CB3, there were generally two major cracks in the slab wings, propagating from the beam-wall interfaces. At the peak ductility demands, these cracks were slightly larger than cracks at the beam-wall interfaces because the slabs are not post-tensioned and are relatively lightly reinforced compared to the beams. Additionally, the residual widths of the slab cracks were slightly larger than cracks at the beam-wall interfaces due to shear lag effects such that portions of the slab away from the beam web are less stressed when the flange goes in compression, leading to a lesser degree of crack closure.

Table 3-1. Measured crack widths of the test beams

Beam ID	Stage	Flexural cracks: At interfaces (slip/exten. cracks)	Flexural cracks: Within distance ***h*** from interfaces (hinge region)	Diagonal tension (shear) cracks within distance ***h*** from interfaces
CB1	Peak of largest ductility demand	1/16–3/32	1/32–1/16	4/1000–1/100
	Zero rotation at end of wind protocol(1)	1/32–1/16	1/64–1/32	0–4/1000
CB2	Peak of largest ductility demand	1/16–1/8	1/100–1/32	4/1000–1/32
	Zero rotation at end of wind protocol	1/100–1/32	1/100–1/64	0–1/64
CB3	Peak of largest ductility demand	1/64–1/8	1/100–1/32	4/1000–1/32
	Zero rotation at end of wind protocol	1/64–1/32	1/100–1/64	0–1/64
CB4	Peak of largest ductility demand	1/24–1/6(2)	1/64–1/16	4/1000–1/64
	Zero rotation at end of wind protocol	1/32–1/24(2)	4/1000–1/100	0–4/1000
CB5	Peak of largest ductility demand	1/32–1/16	1/100–1/64	1/100–1/50
	Zero rotation at end of wind protocol	1/64–1/32	4/1000	4/1000–1/100
CB5R	Peak of largest ductility demand	1/64–1/16	1/100–1/64	1/100–1/32
	Zero rotation at end of wind protocol	1/64–1/32	6/1000	4/1000–1/50
CB6	Peak of largest ductility demand	1/8–1/4	(0–1/64)	1/100–1/64
	Zero rotation at end of wind protocol	1/16–3/32	0–4/1000	0-4/1000
CB7	Peak of largest ductility demand	1.5/32–2.5/32	1/100–1/16	1/100–1/50
	Zero rotation at end of wind protocol	1/100–1/32	4/1000–1/64	0–4/1000
CB8	Peak of largest ductility demand	2.5/32–3/32	1/100–1.5/32	4/1000–1/32
	Zero rotation at end of wind protocol	1/32–1/16	1/64–1/32	4/1000–1/64
CB24F-RC(3)	Peak of 0.01 rotation	1/10	1/22	hairline
	Peak of 0.03 rotation	1/2	1/8	1/64

(1) Residual cracks at the end of the loading protocol;
(2) A thin layer of concrete spalling (≈1/8 to 1/2 in. [3 to 13 mm] thick over a distance of ≈ 2 to 4 in. [51 to 102 mm]) was observed at the bottom interface;
(3) Reported by Naish et al. (2013).

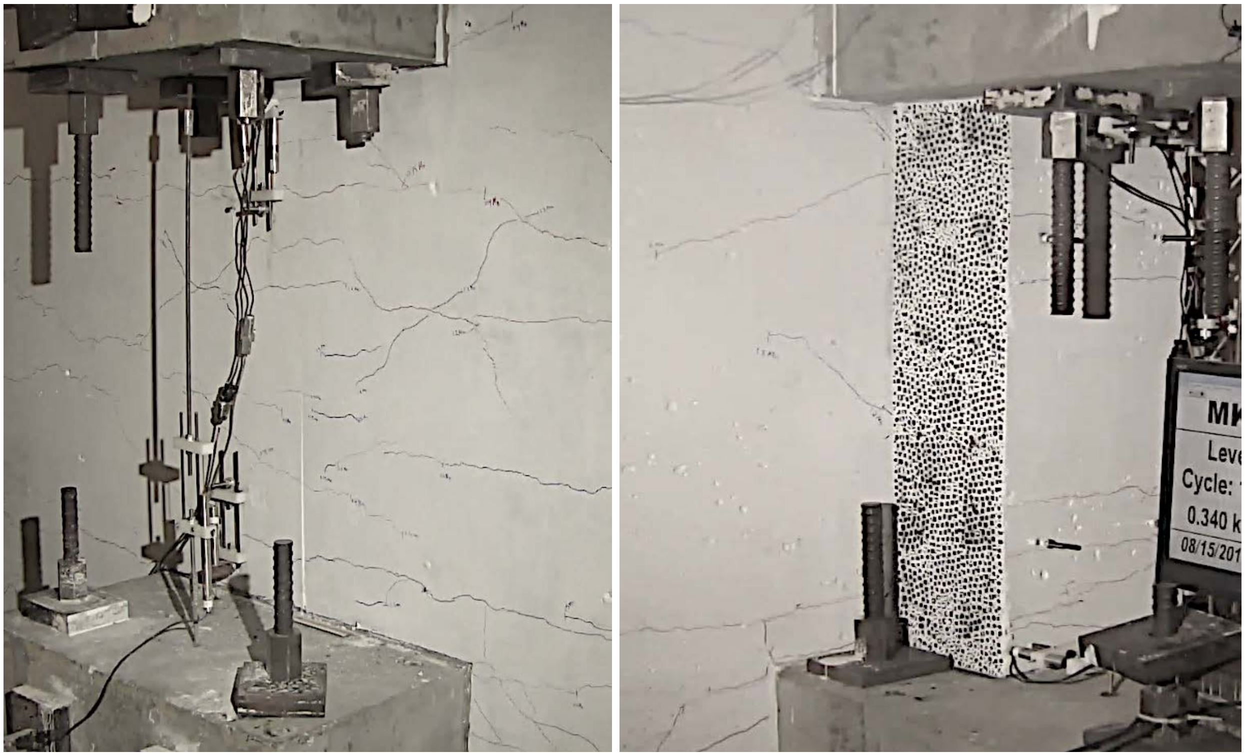

(*a*) West view (*b*) Southeast view

Figure 3-1. Cracking condition of CB1 at the end of the wind loading protocol.

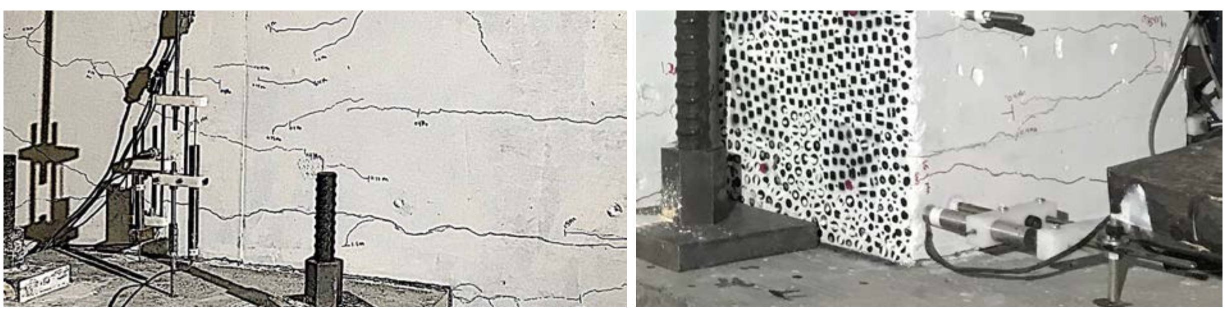

(*a*) Bottom of west view (*b*) Bottom of southeast view

Figure 3-2. Close up cracking conditions of CB1 at the end of the wind loading protocol.

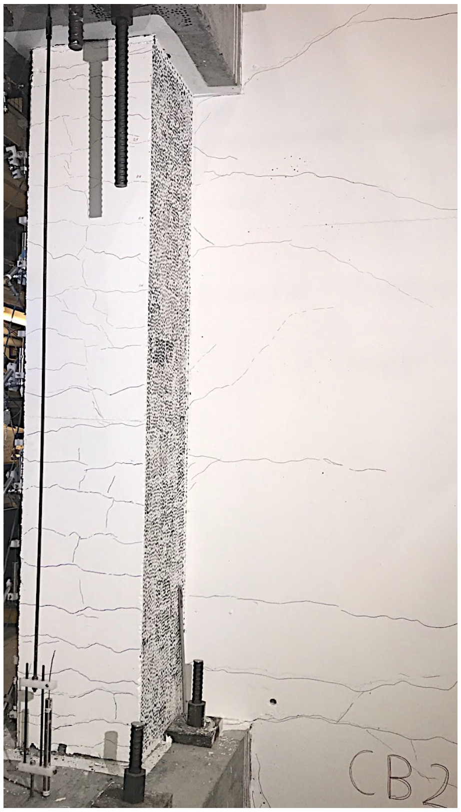

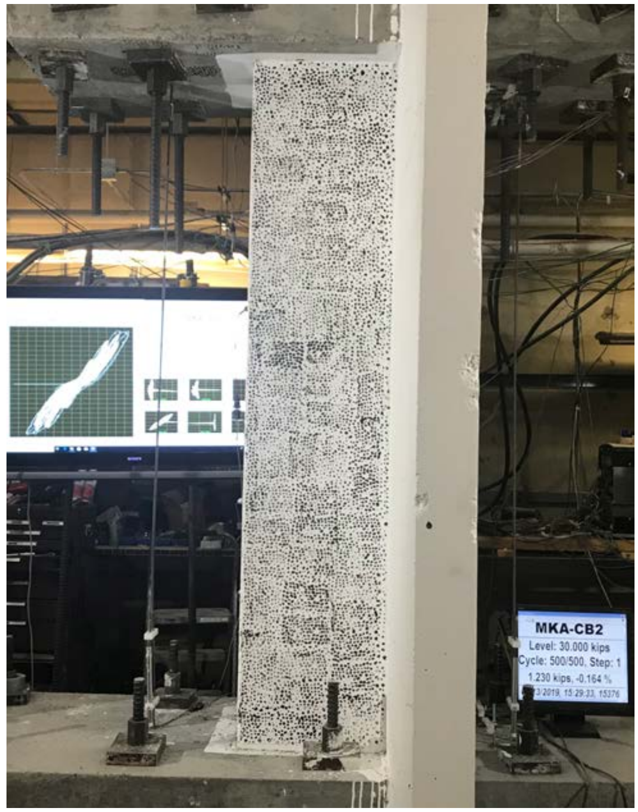

(*a*) West view (*b*) South view

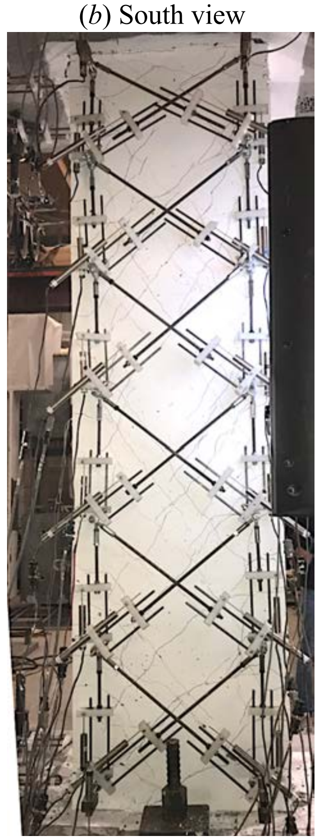

(*c*) East view (*d*) North view

Figure 3-3. Cracking condition of CB2 at the end of the wind loading protocol.

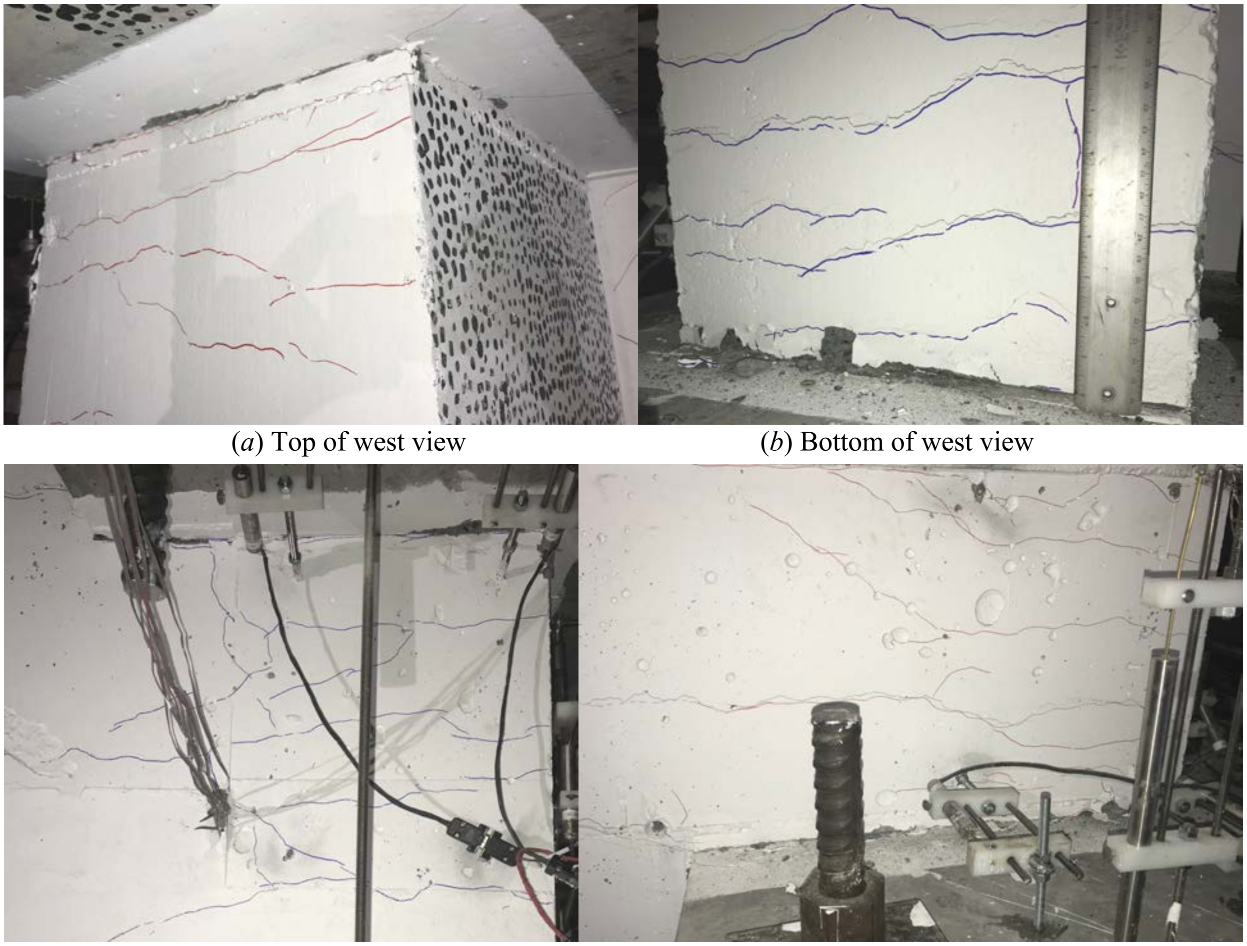

(*a*) Top of west view (*b*) Bottom of west view

(*c*) Top of east view (*d*) Bottom of east view

Figure 3-4. Close-up cracking conditions of CB2 at the end of the wind loading protocol.

(*a*) West view (*b*) South view (*c*) East view (*d*) North view

Figure 3-5. Cracking condition of CB3 at the end of the wind loading protocol.

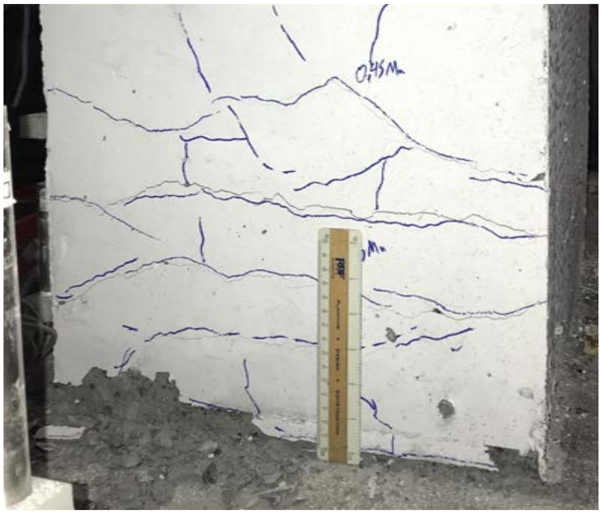

(*a*) Top of west view

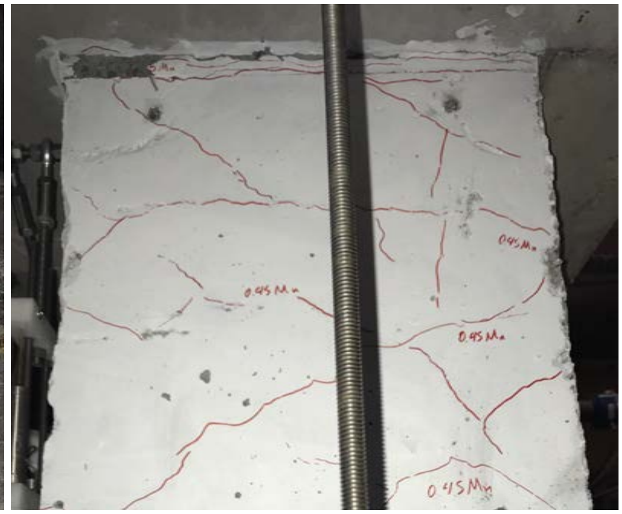

(*b*) Bottom of west view

(*c*) Top of east view

(*d*) Bottom of east view

Figure 3-6. Close-up cracking conditions of CB3 at the end of the wind loading protocol.

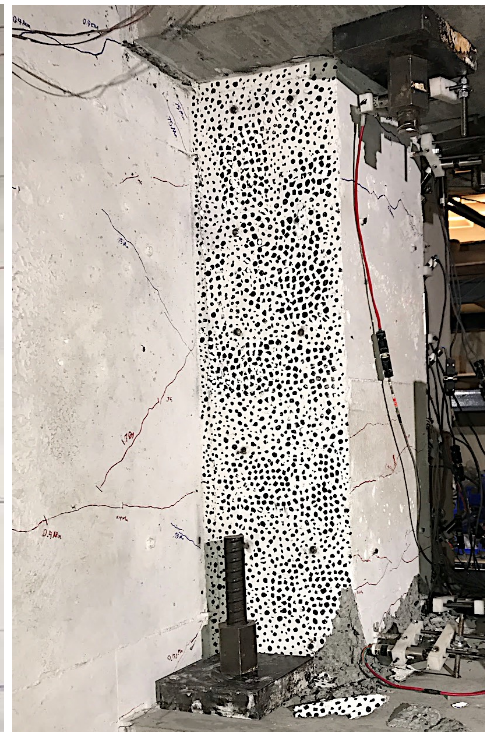

(*a*) West view (*b*) Southeast view

Figure 3-7. Cracking condition of CB4 at the end of the wind loading protocol.

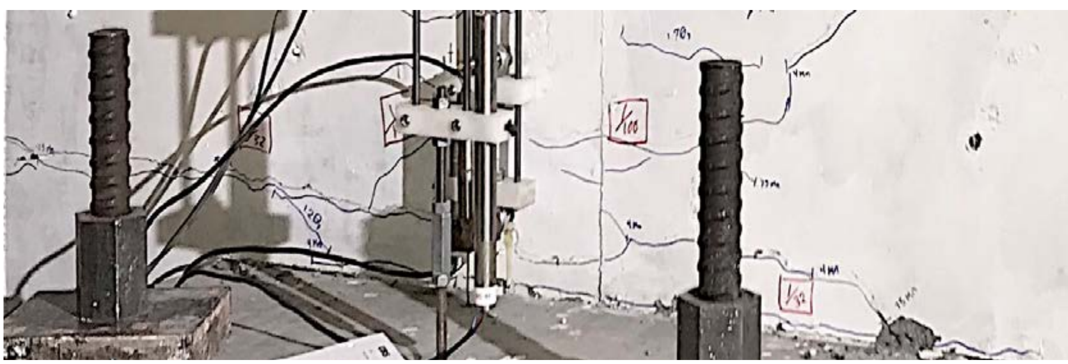

(*a*) Bottom of west view

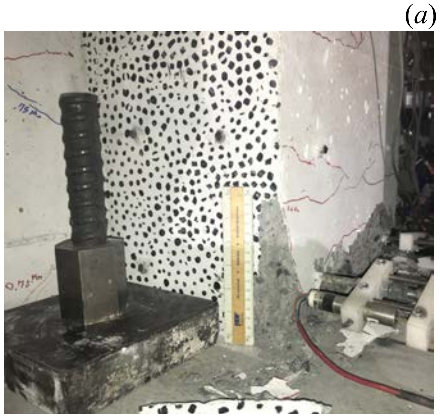

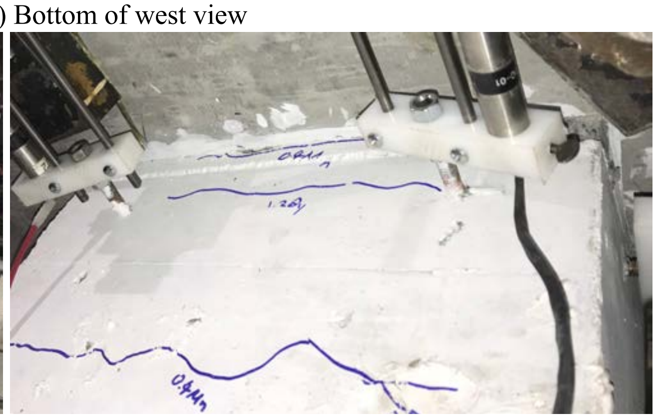

(*b*) Bottom of east view (*c*) Top of east view

Figure 3-8. Close-up cracking conditions of CB4 at the end of the wind loading protocol.

(*a*) South view

(*b*) Southeast view

(*c*) Northeast view

(*d*) West view

Figure 3-9. Cracking condition of CB5 at the end of the wind loading protocol.

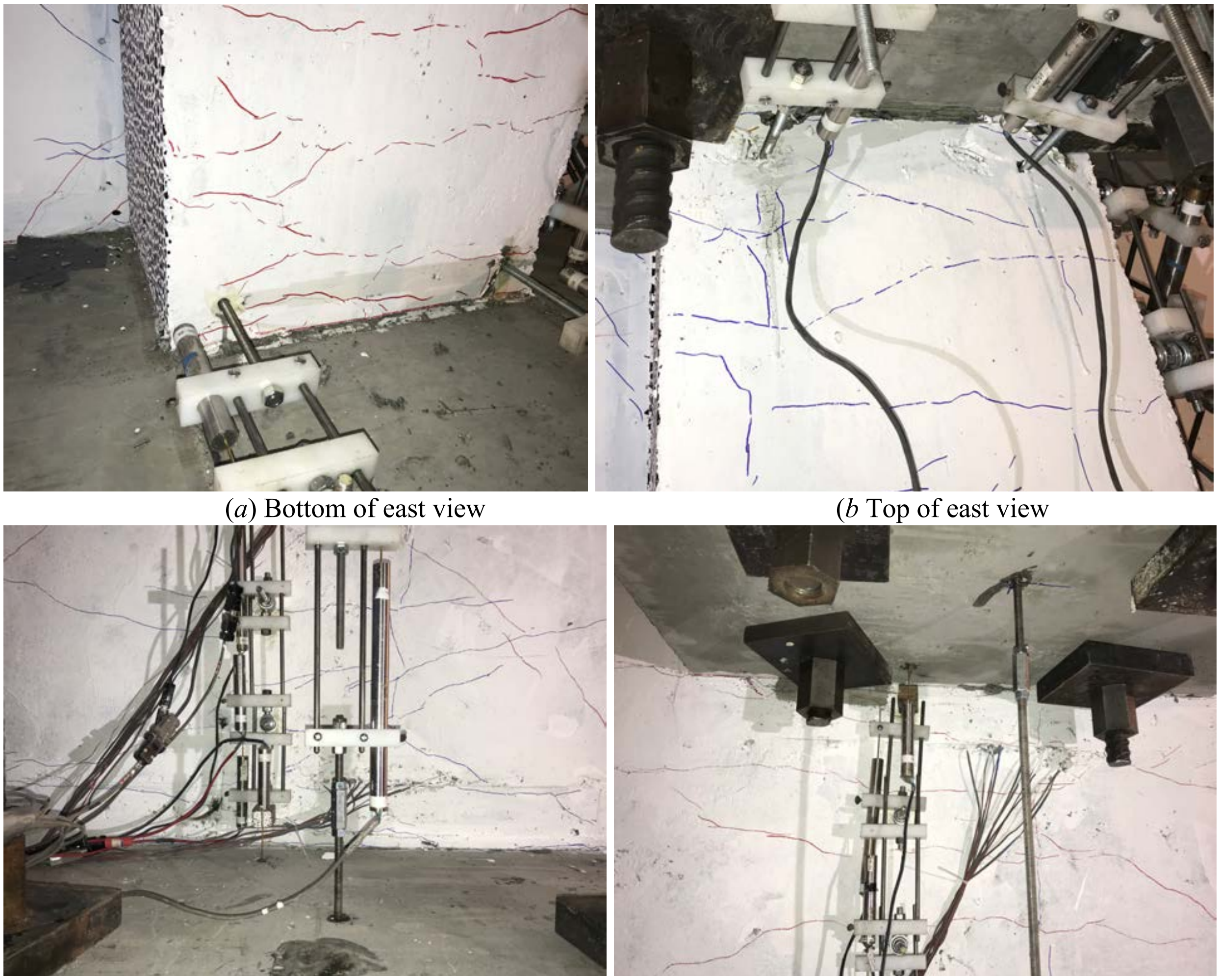

(*a*) Bottom of east view (*b* Top of east view

(*c*) Bottom of west view (*d*) Top of west view

Figure 3-10. Close-up cracking conditions of CB5 at the end of the wind loading protocol.

(*a*) Southeast view (*b*) West view

Figure 3-11. Cracking condition of CB5R at the end of the wind loading protocol.

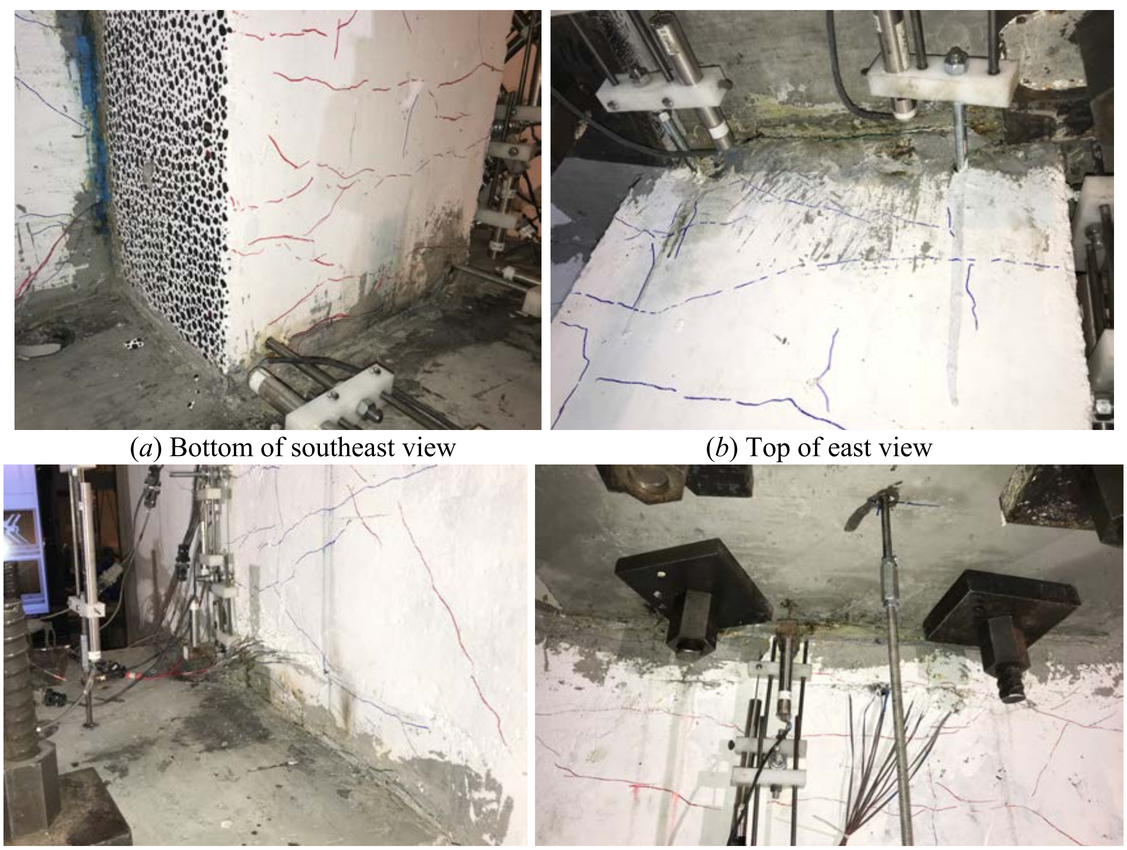

(*a*) Bottom of southeast view (*b*) Top of east view

(*c*) Bottom of west view (*d*) Top of west view

Figure 3-12. Close-up cracking conditions of CB5R at the end of the wind loading protocol.

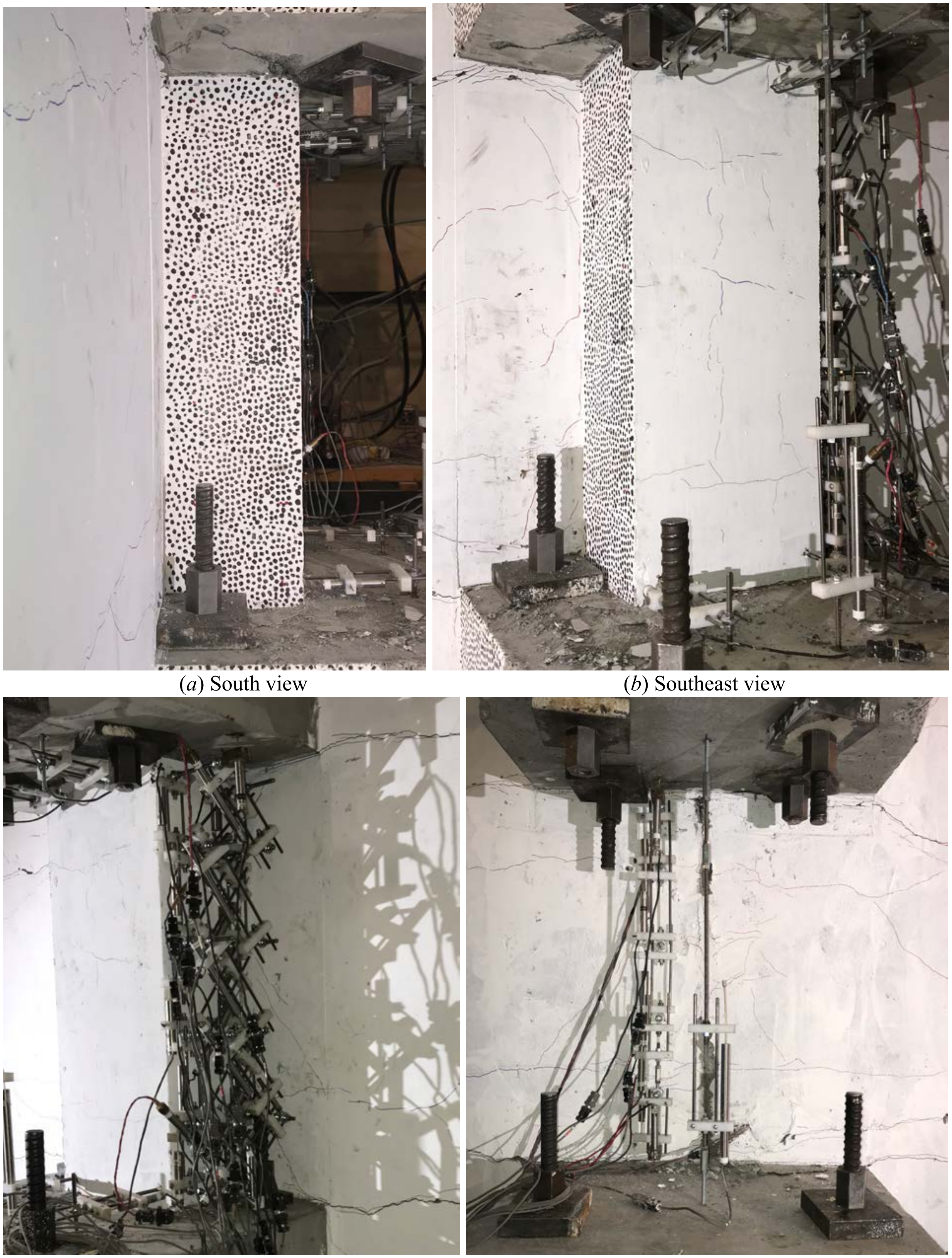

(*a*) South view (*b*) Southeast view

(*c*) Northeast view (*d*) West view

Figure 3-13. Cracking condition of CB6 at the end of the wind loading protocol.

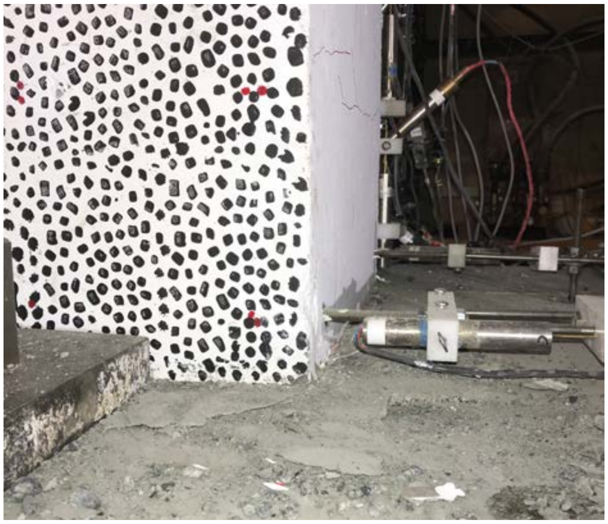

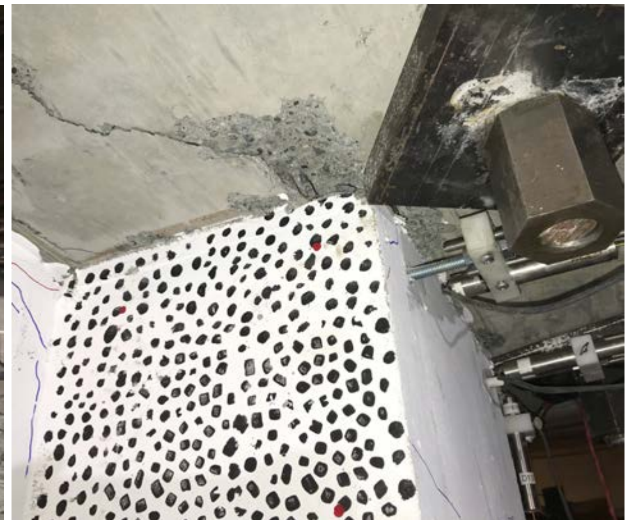

(*a*) Bottom of southeast view (*b*) top of southeast view

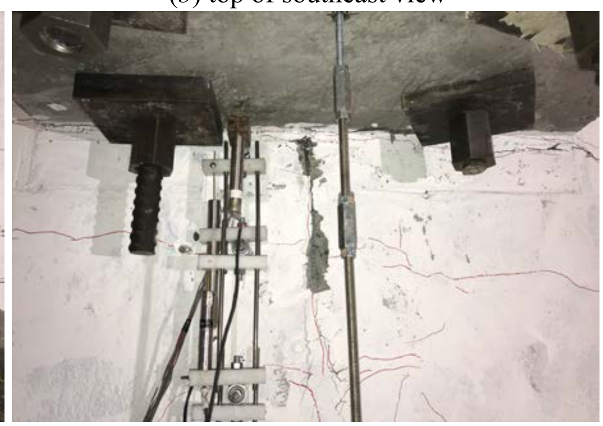

(*c*) Bottom of west view (*d*) Top of west view

Figure 3-14. Close-up cracking conditions of CB6 at the end of the wind loading protocol.

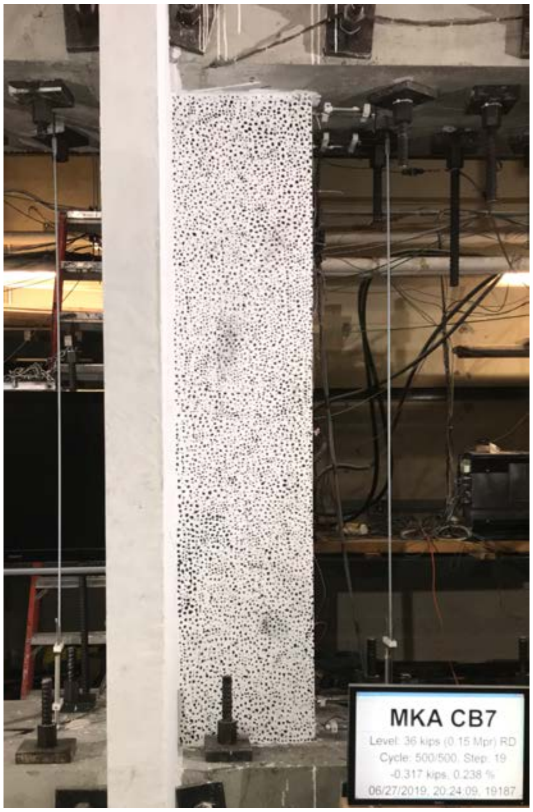

(*a*) South view

(*b*) Southeast view

(*c*) North view

(*d*) West view

Figure 3-15. Cracking condition of CB7 at the end of the wind loading protocol.

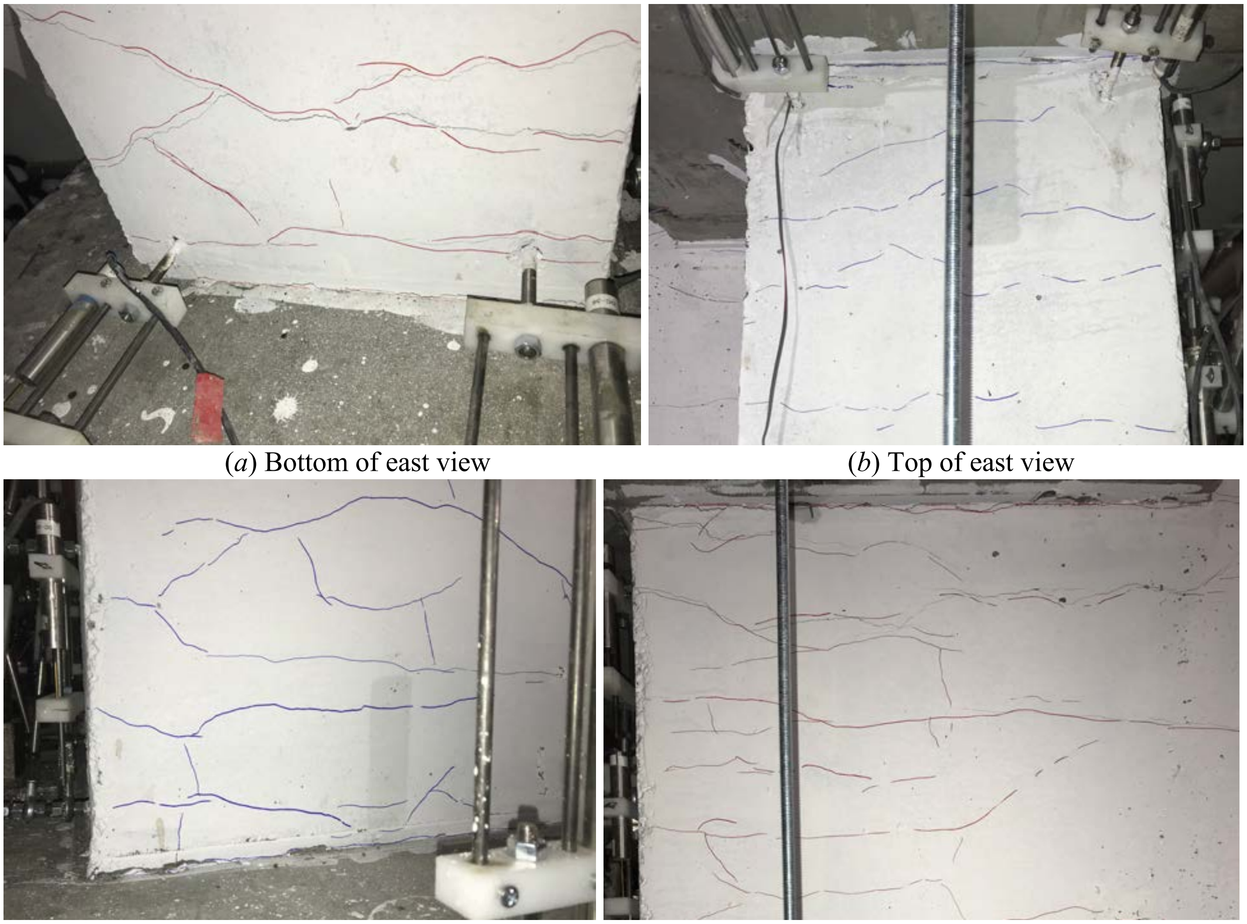

(*a*) Bottom of east view (*b*) Top of east view

(*c*) Bottom of west view (*d*) Top of west view

Figure 3-16. Close-up cracking conditions of CB7 at the end of the wind loading protocol.

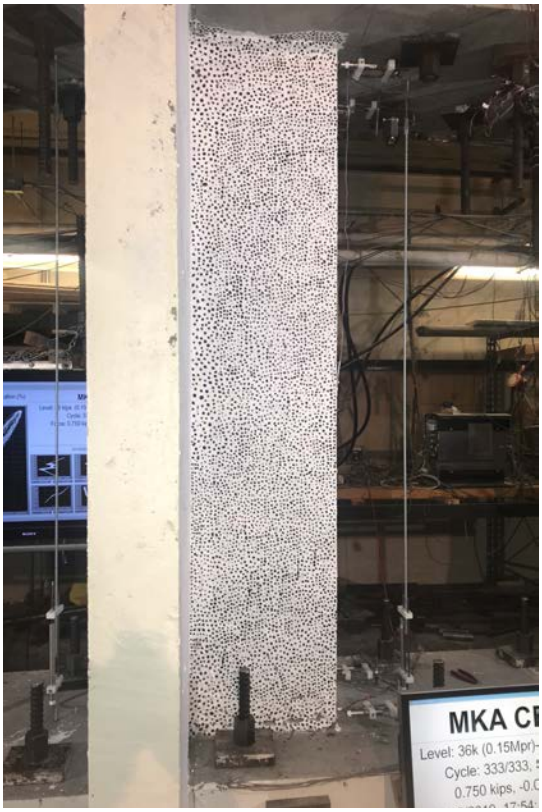

(*a*) South view

(*b*) Southeast view

(*c*) North view

(*d*) West view

Figure 3-17. Cracking condition of CB8 at the end of the wind loading protocol.

(*a*) Bottom of southeast view

(*b*) Top of east view

(*c*) Bottom of west view

(*d*) Top of west view

Figure 3-18. Close-up cracking conditions of CB8 at the end of the wind loading protocol.

3.3. Load-Deformation Responses

Figure 3-19 presents the lateral load versus total chord rotation responses of the beams. Ductility demand (μ) is defined as rotation demand divided by average (of negative and positive loading) yield rotation (θ_y), which is defined as the point at which a straight line from the origin crosses the backbone curve (corresponding to the first cycle at each load/displacement level) at 2/3 of experimental peak lateral strength ($V_{peak,w}$) and a horizontal line at $V_{peak,w}$, as illustrated in **Figure 3-20**. It is noted that $V_{peak,w}$ at these ductility demands does not necessarily represent the ultimate (peak) lateral strength of the beams, but rather a general yield or an average peak lateral strength (e.g., see Naish et al., 2013) since higher lateral strengths than $V_{peak,w}$ would be expected if the beams were pushed to higher ductility demands as a result of strain hardening of reinforcement, as will be shown in Chapter 6. **Figure 3-19** shows that CB2 through CB8 were all pushed to peak ductility demands of approximately 1.5. In case of CB1, the target ductility demands of 1.2 and 1.5 were exceeded due a minor control issue with the horizontal actuator, especially during the first cycle to the target ductility demand of 1.5 in the positive direction of loading, such that peak ductility demands of 2.1 and 1.7 were applied in the positive and negative directions of loading, respectively, as opposed to 1.5. Furthermore, as shown in the loading protocol in **Figure 2-21** and **Figure 2-22** the 75 cycles at $0.75M_{pr}$ on the ramp-down were expected to be essentially elastic cycles (i.e., $\theta_{@0.75Mpr} < \theta_y$); however, since at this stage the beams had softened, and their lateral stiffness had reduced significantly (as will be shown in the next section), those 75 cycles turned out to be inelastic cycles ($\theta_{@0.75Mpr} \geq \theta_y$), except for CB1 where the 75 cycles on the ramp-down were inadvertently applied at the same displacement, rather than the same lateral load, as the 75 cycles on the ramp-up, as seen in **Figure 3-19** (***a***).

Additionally, **Figure 3-19** shows that, unlike CB1, CB5 and CB6, CB2 through CB4, CB7, and CB8 did not quite reach their probable flexural strengths ($V_{@Mpr}$) calculated with consideration of the slab impact (**Table 2-1**). CB1 reached a lateral strength that is 13% higher than $V_{@Mpr}$ in the positive direction of loading (**Figure 3-19** (***a***)) partly due to larger strain hardening of longitudinal reinforcement as a result of pushing the beam to a higher ductility demand in that direction. Nonetheless, the beams would be expected to reach higher lateral strengths, if they were pushed to greater ductility demands than those applied in the tests, as will be discussed in Chapter 6. **Figure 3-19** (***d***) demonstrates that use of ACI 318-19 Equation 18.10.7.4 to calculate nominal shear strength (V_n) of diagonally reinforced coupling beams results in significant underestimation of strength, and that results obtained from sectional analysis of the cross-section provide better estimates of beam strength (i.e., $V_{peak,w} \approx V_{@Mn}$ as given in **Table 2-1**). This is consistent with results reported by Naish et al (2013) for seismically tested diagonally reinforced coupling beams, where the experimentally obtained peak strengths (V_{peak}) ranged from 1.55 to 1.17 times V_n, depending on whether a slab was included and if the slab was post-tensioned. Similarly, **Figure 3-19** (***f***) shows that the requirements of AISC 360-10 §14.1 provide a lower estimate of nominal shear strength of SRC coupling beams. An estimate of shear strength that includes contributions from concrete, steel section, and transverse reinforcement, which is not allowed by AISC 360-10 §14.1, would provide a closer, but still conservative, estimate of shear strength (**Table 2-2**). **Figure 3-19** (***f***) also demonstrates that the probable moment strength calculated as the plastic strength of the steel section with the consideration of presence of concrete ($V_{@Mpr}$) would yield a good estimate of beam flexural strength.

Residual rotations are of interest because they indicate whether or not the building or element returns to its original vertical or horizontal position after the windstorm stops. Residual chord rotations of the beams, which are defined as rotations at which lateral load is zero (**Figure 3-19**), are shown in **Table 3-2**. Residual rotations are the largest and smallest during the second cycle to the peak ductility demand (ranging from 0.001 to 0.005) and the last cycle of the loading protocol (ranging from zero to 0.0028), respectively. Since CB7 was subjected a wind loading protocol with a non-zero mean component, the largest residual rotations were observed for this beam. However, the values presented in **Table 3-2** are considered practically negligible, given that, during extreme wind events, not all coupling beams in a building will be stressed to this level of ductility demand, and thus, the residual drift of the building would be smaller.

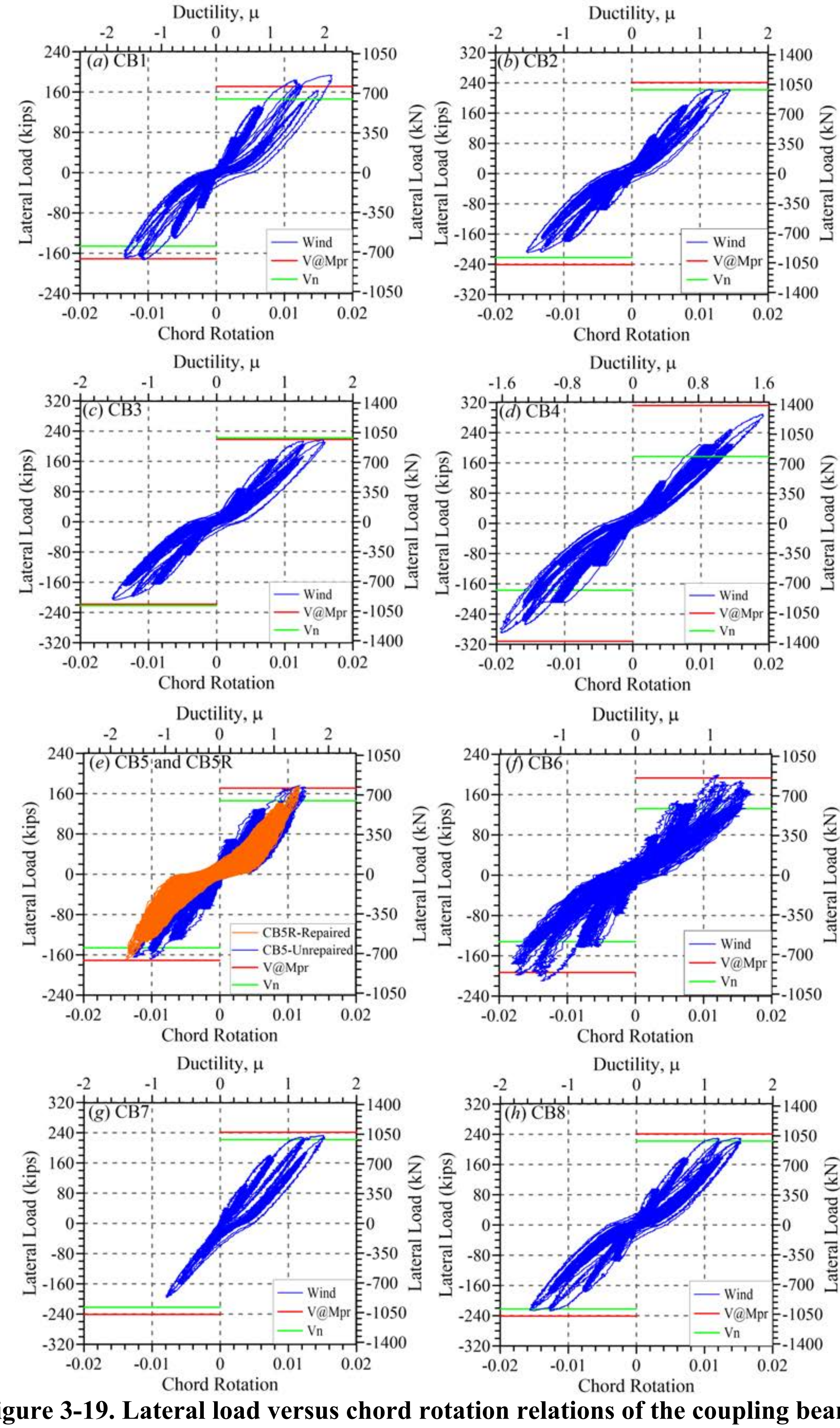

Figure 3-19. Lateral load versus chord rotation relations of the coupling beams.

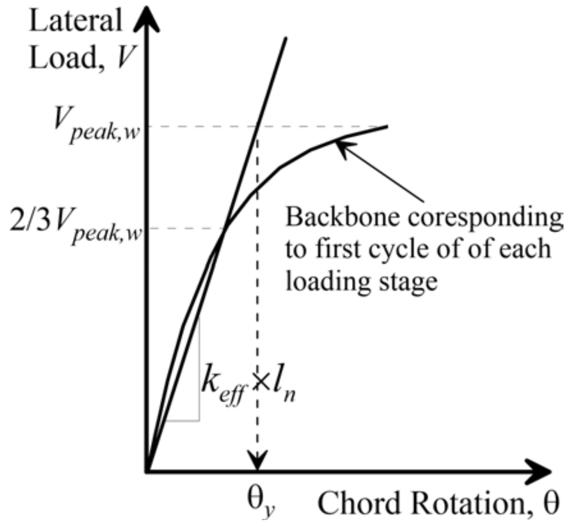

Figure 3-20. Determination of yield rotation and effective flexural stiffness.

Table 3-2. Residual rotations

Beam ID	2nd cycle of peak ductility demand		Last cycle of loading protocol	
	+ve	-ve	+ve	-ve
CB1	0.0035	-0.0025	0.0004	-0.0007
CB2	0.0020	-0.0035	-0.0013	-0.0023
CB3	0.0030	-0.0035	-0.0005	-0.0016
CB4	0.0028	-0.0025	-0.0017	-0.0023
CB5	0.0020	-0.0020	0.0005	-0.0005
CB5R	0.0010	-0.0020	0.0000	0.0010
CB6	0.0040	0.0050	-0.0012	-0.0023
CB7	0.0050	0.0009	0.0028	0.0021
CB8	0.0035(1)	-0.0030(1)	0.0000	-0.0010

(1)Values from second ramp-up and ramp-down

3.4. Lateral Stiffness

The secant stiffness values of the beams (defined as E_cI_s) corresponding to the peak lateral load (and its associated total rotation) of each cycle in the wind loading protocol were computed and normalized by the gross-section stiffness (E_cI_g), using the procedure provided in **Appendix E**. The results are shown in **Figure 3-21**. It should be noted that the chord rotations used in the calculation of stiffness values are total rotations, which include deformation contributions due to flexure (curvature), slip/extension, shear, and sliding. The contributions of each of these sources of chord rotation are discussed later in Section 3.6. **Figure 3-21** demonstrates that secant stiffness values significantly reduce as ductility demands increase to the peak ductility (ramp-up) and then only slightly reduce during the ramp-down cycles. Furthermore, stiffness reduces within each loading stage on the ramp-up (e.g., 500 cycles at $0.40M_{pr}$) as the number of cycles increases, whereas it remains essentially the same during each loading stage on the ramp-down. This is because, as noted previously, during the ramp-up cycles, new cracks developed and existing cracks propagated further as the number of cycles increased within each loading stage, whereas typically no new cracks were observed on the ramp-down. The low stiffness values during the 500 cycles at $0.15M_{pr}$ on the ramp-down were not because the beams became softer during that stage, but rather due to pinching of the hysteretic loops at such small lateral loads (i.e., the beams have not begun to pick up some load as cracks have not closed). Additionally, there is a significant dispersion in the stiffness values at $0.15M_{pr}$ on the ramp-up because the lateral displacements at this stage were fairly small (ranging from 0.03 to 0.10 in.) as a few to no cracks were visually observed and were significantly impacted by measurement noise (wire potentiometers). The stiffness values of CB7 for the negative direction of loading at $0.075M_{pr}$ are not included (**Figure 3-21** (**g**)), because the readings indicated significant variation (were noisy).

Figure 3-22, **Figure 3-23**, and **Table 3-3** present the E_cI_s/E_cI_g averaged for each loading stage (negative and positive, except CB7), which indicate that the beams with l_n/h of 3.67 have overall larger stiffness values (modifiers) than the beams with l_n/h of 2.5, which is consistent with stiffness data of coupling beams tested under seismic loading protocols, as discussed in the next paragraph. **Figure 3-22** also shows that stiffness values of CB4 become modestly larger than those of CB1, CB5 and CB6, starting at loading to $0.75M_{pr}$ on the ramp-up. This is because studies of coupling beams subjected to seismic loading protocols have demonstrated that coupling beams with diagonal reinforcement have moderately larger effective stiffness values than beams with conventional (longitudinal) reinforcement or steel sections, as discussed in the next paragraph. The stiffness values of CB2 are slightly larger than those CB3 during the early load cycles on the ramp-up, suggesting that the L-shaped floor slab of CB2 resulted in a slight increase in the initial stiffness. Stiffness values of CB7 and CB8 are somewhat different than those of CB2 and CB3, due to the variation in the loading protocol used for CB7 and CB8, which, along with the impact of epoxy repair on stiffness, will be discussed in Chapter 4.

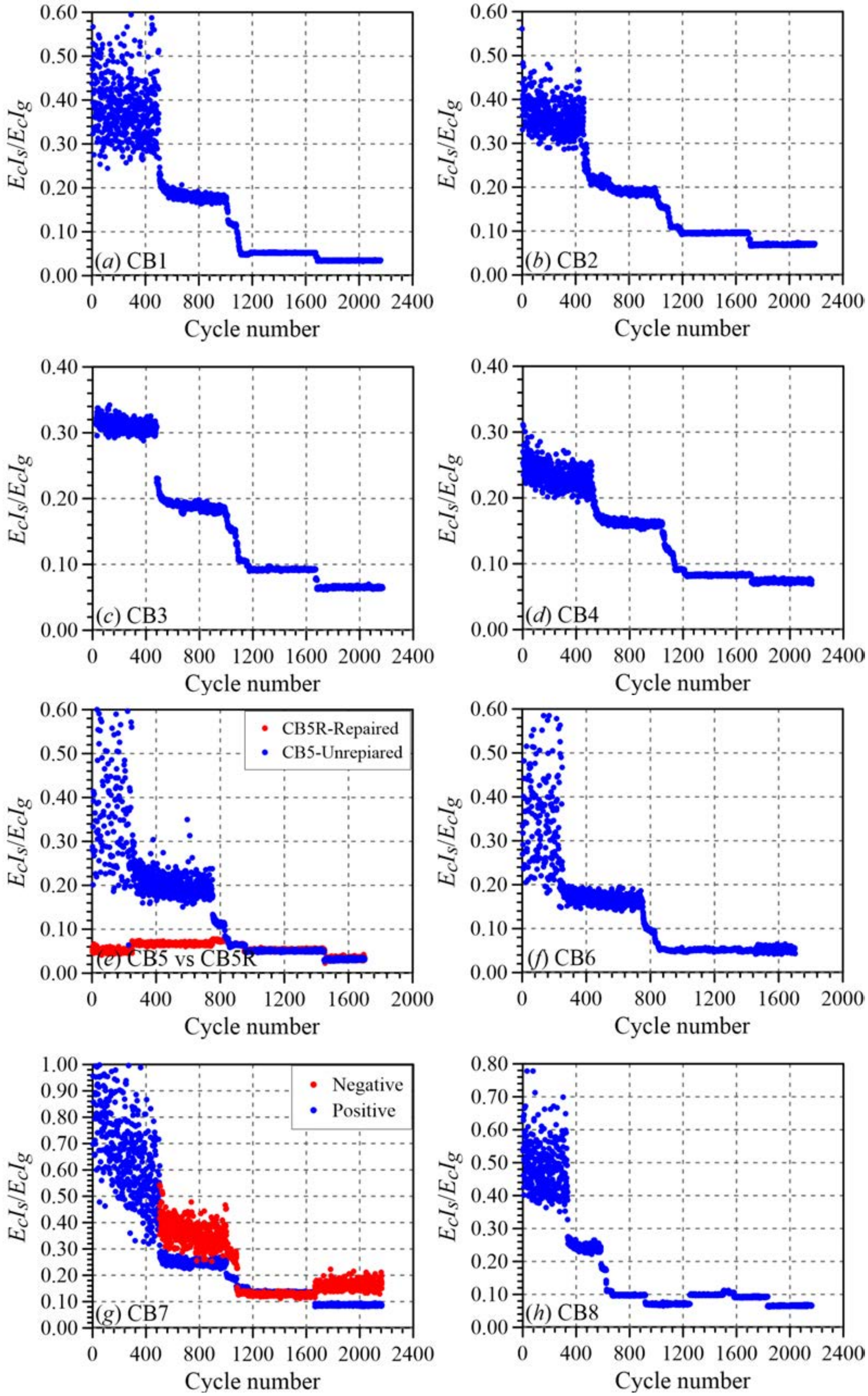

Figure 3-21. Variation of average (of positive and negative loading, except CB7) secant stiffness (E_cI_s) normalized by gross-section stiffness (E_cI_g).

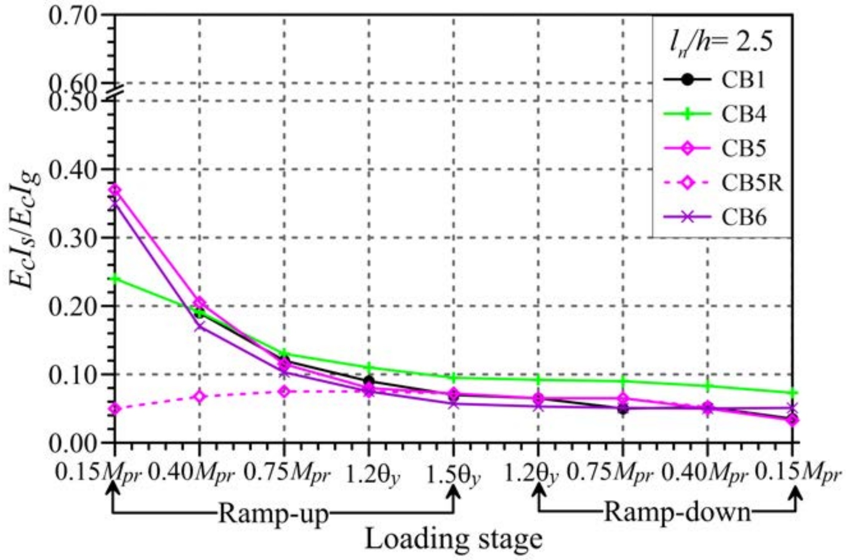

(*a*) Beams with aspect ratio, l_n/h, = 2.5

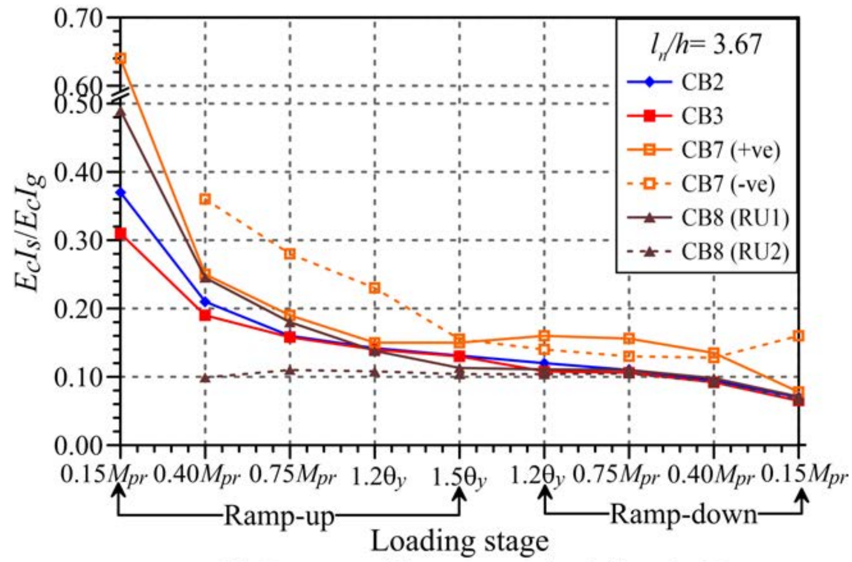

(*b*) Beams with aspect ratio, l_n/h, = 3.67

Figure 3-22. Normalized secant stiffness (E_cI_s/E_cI_g) for each loading stage.

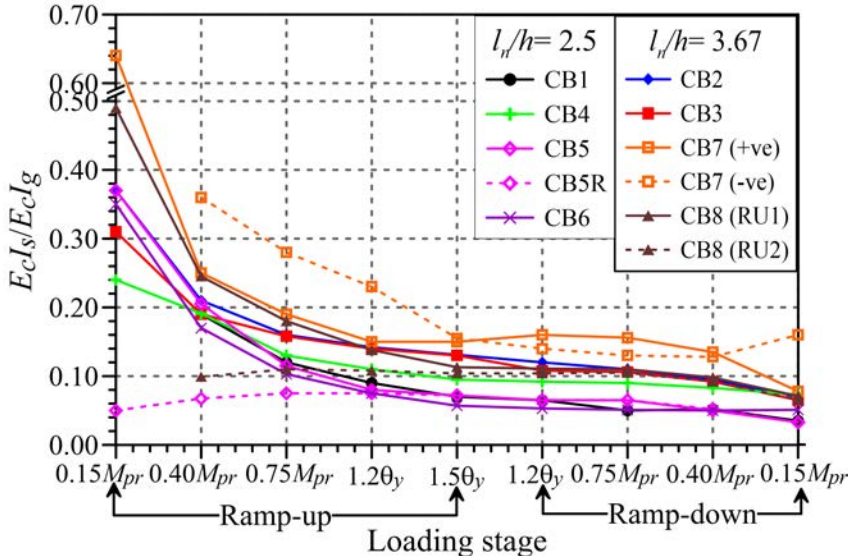

Figure 3-23. Comparison of normalized secant stiffness values (E_cI_s/E_cI_g) of the beams.

Table 3-3. Normalized averaged secant stiffness (E_cI_s/E_cI_g) for each loading stage.

Beam ID	Loading Stage								
	Ramp-up					Ramp-down			
	$0.15M_{pr}$	$0.40M_{pr}$	$0.75M_{pr}$	$1.2\ \theta_y$	$1.5\ \theta_y$	$1.2\ \theta_y$	$0.75M_{pr}$	$0.40M_{pr}$	$0.15M_{pr}$
CB1	0.38	0.190	0.120	0.090	0.070	0.065	0.050[1]	0.052	0.035
CB2	0.370	0.210	0.160	0.1420	0.131	0.120	0.110	0.095	0.070
CB3	0.310	0.190	0.155	0.140	0.130	0.108	0.106	0.092	0.065
CB4	0.240	0.191	0.130	0.110	0.095	0.092	0.090	0.083	0.073
CB5	0.370	0.205	0.115	0.080	0.072	0.065	0.065	0.050	0.033
CB5R	0.050	0.068	0.075	0.075	0.072	0.065	0.065	0.052	0.033
CB6	0.350	0.170	0.103	0.075	0.057	0.053	0.051	0.050	0.051
CB7 (+ve)	0.640	0.250	0.190	0.150	0.150	0.160	0.156	0.135	0.078
CB7 (-ve)[2]	Noise	0.360	0.280	0.230	0.155	0.14	0.130	0.128	0.160
CB8 (RU1)[3]	0.490	0.245	0.180	0.138	0.113	0.111	0.110	0.098	0.071
CB8 (RU1)[3]	-	0.099	0.110	0.108	0.104	0.104	0.105	0.092	0.066

[1]The amplitude of the cycles at this stage correspond to the displacement reached during cycles at $0.75M_{pr}$ on the ramp-up.
[2]RU1 = first ramp-up and RU2 = second ramp-up (Figure 2-22(***c***))
[3]Values are for the negative direction of loading, where the amplitude of cycles are half of the values shown in this table (**Figure 2-22**(***b***))

Furthermore, the effective stiffness values (E_cI_{eff}) of the beams were calculated using the total chord rotation based on the approach shown in **Figure 3-20** and normalized by E_cI_g, as shown in **Table 3-4**. The results are compared with effective stiffness data of seismically tested coupling beams (diagonally and conventionally reinforced) collected by Tauberg et al. (2019) and the flexural effective stiffness relationship given by LATBSDC (2017) and TBI (2017) for performance-based seismic design ($E_cI_{eff}/E_cI_g = 0.07\ l_n/h \leq 0.30$) in **Figure 3-24**. This figure indicates that, similar to secant stiffness, effective stiffness is significantly impacted by l_n/h, and that the beams tested in this study have slightly larger effective stiffness values than the mean trends of the seismically tested coupling beams. This is likely due to two factors. First, except for a few tests, the test beams in the seismically tested dataset do not include floor slabs. Research (e.g., Naish et al., 2013) has shown that floor slabs are expected to modestly increase lateral strength of coupling beams due to greater strain hardening of reinforcement when the flange is in compression and due to yielding of slab reinforcement when the flange is in tension, which results in larger effective stiffness, as will be discussed in Chapter 4. Second, the effective stiffness of the beams in the dataset is computed using data from reported load-deformations plots and assuming perfect double curvature test setups (i.e., the top block maintains zero rotation); however, slight rotation of the end blocks may occur, particularly the top block (observed in this study; see **Appendix E**), which does not impact force-deformation response but does impact lateral stiffness. It is noted that the relationship given by LATBSDC (2017) and TBI (2017) is for full-scale coupling beams with an estimate of the impact of adjacent floor slabs (out-of-plane stiffness and axial restraint) and walls (axial restraint) on coupling beam effective stiffness. Beams tested at reduced scales could have smaller stiffness values than full scale beams if the longitudinal or diagonal bars are not scaled down using the same scale factor used for the geometry of the beam (i.e., larger bars sizes are used) because the deformation contributed by bar slip/extension increases, and, as a result, stiffness reduces (Naish et al., 2013). Adjusting for the impact of reduced scale and slab axial restraint might bring the experimental effective stiffness values of the beams tested in this study close to the values given by LATBSDC (2017) and TBI (2017). Other factors affecting the variation of the effective stiffness of the beams (e.g., type of wind loading protocol and epoxy repair) are discussed in Chapter 6.

Table 3-4. Normalized effective stiffness (E_cI_{eff}/E_cI_g) of the beams

Beam ID	l_n/h	E_cI_{eff}/E_cI_g
CB1	2.5	0.137
CB2	3.67	0.175
CB3	3.67	0.170
CB4	2.50	0.144
CB5	2.50	0.135
CB5R	2.50	0.077
CB6	2.50	0.140
CB7 (+ve)	3.67	0.210
CB7 (-ve)	3.67	0.155
CB8 (RU1)[(1)]	3.67	0.185
CB8 (RU2)[(1)]	3.67	0.185

[(1)]RU1 = first ramp-up and RU2 = second ramp-up (**Figure 2-22(*c*)**)

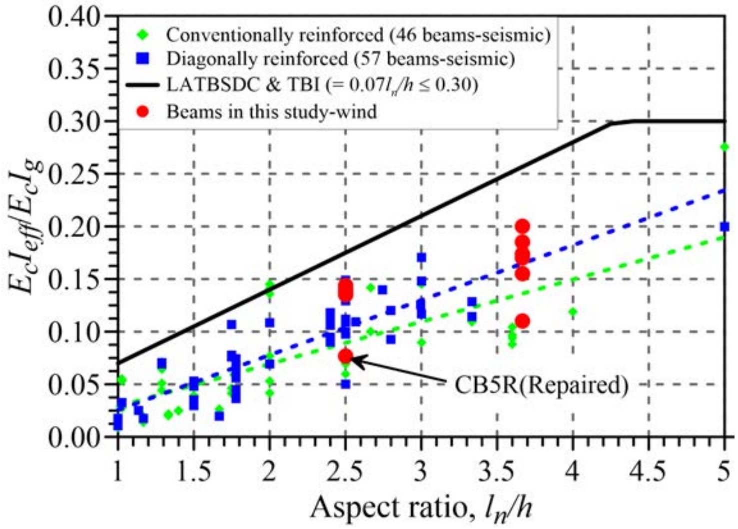

Figure 3-24. Normalized effective stiffness (E_cI_{eff}/E_cI_g) as a function of aspect ratio (l_n/h).

3.5. Axial Growth

As noted previously, no axial load or restraint was applied to the beams during testing. Axial load or restraint has been observed to impact axial growth, crack widths, stiffness, strength, and deformation capacity of coupling beams tested under seismic loading protocols (e.g., Naish et al., 2013; Motter et al., 2017; Poudel et al., 2018). **Figure 3-25** presents axial growth of the beams versus chord rotation and indicates that the accumulated axial growth of the beams at the end of the test is small, ranging from 0.10% to 0.22% of the beam clear length (l_n) for RC coupling beams (CB1 through CB5, CB7, and CB8) and 0.57% for the SRC beam (CB6). **Figure 3-25** also reveals that all the axial growth takes place during the ramp-up cycles, with almost no axial growth during the ramp-down cycles, which is another indication that during the ramp-down cycles, no (or few) new cracks formed, and the width of the existing cracks remained mostly the same. Furthermore, axial growth of CB4 is somewhat smaller than that of CB1 (**Figure 3-25** (***a***)), which could partly be because of the relatively small crack widths at the top interface of CB4 as a result of flexibility of the structural steel loading beam, as was highlighted previously, such that axial growth at the top plastic hinge region of CB4 was smaller than that at the bottom plastic hinge region. Additionally, **Figure 3-25** (***e***) demonstrates that after repair, CB5R experienced additional axial growth. This is because the major residual cracks were filled in with epoxy material – locking in the axial growth – such that under retest, new cracks formed adjacent to epoxied cracks during the ramp-up loading cycles, leading to additional axial growth. The post-repair axial elongation is about 1/3 of the pre-repair elongation because, as noted previously, only the slip/extension cracks at the interfaces were repaired (thus slip/extension residual crack widths were locked in) and growth associated with other flexural cracks in the plastic hinge regions were not repaired and could close and open during the retest.

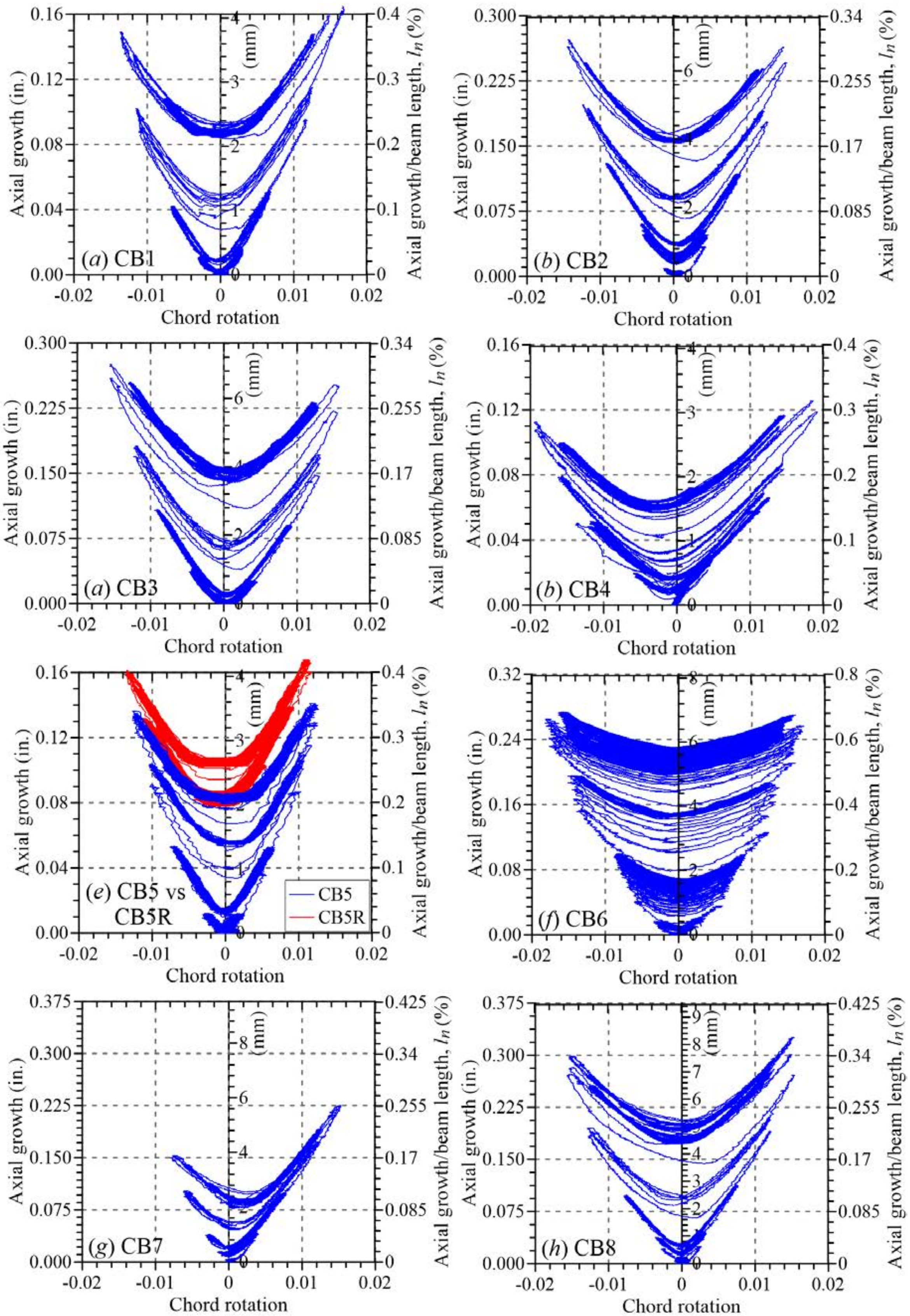

Figure 3-25. Axial growth versus chord rotation of the beams.

3.6. Deformation Components

Figure 3-26 provides information on the contribution of flexure (curvature), shear distortion, slip/extension from walls (end blocks), and sliding at the beam-wall interfaces to total chord rotation measured using LVDTs as discussed in **Appendix F**. Flexure and shear deformations were determined using LVDTs attached to the coupling beams (vertical and X-shaped configurations), whereas the slip/extension deformations were determined from LVDTs spanning across the beam-wall interfaces, and the sliding displacements were determined from LVDTs installed at the beam-wall interfaces measuring the displacement of the beam ends relative to the walls in the direction of loading. Contribution of each deformation component to the total chord rotation during each load/displacement level was determined as shown in **Figure 3-27**, except for loading at $0.15M_{pr}$ during ramp-up at, because these deformations were too small and impacted by sensor noise. It is noted that the summation of the rotations contributed by these local deformation components do not necessarily add to 100% of the total rotation measured globally (**Figure 3-27**) because measurements of these local deformations are affected by the noise in the sensors, minor flexibility or slippage in the LVDT mounting accessories, and assumptions used to calculate shear deformations (e.g., Massone and Wallace, 2004).

Figure 3-27 shows that for CB1 and CB5, conventionally reinforced coupling beams with l_n/h of 2.5, the rotation contributed by bar slip/extension into the wall accounts for roughly 40 to 70% of the total rotation, whereas for CB2, CB3, CB7, and CB8, conventionally reinforced coupling beams with l_n/h of 3.67, the rotations contributed by bar slip/extension to the total rotation account for 30 to 40% of the total rotation. For CB6, the SRC beam, the vast majority of the rotation is a result of slip/extension cracks at the beam-wall interfaces (i.e., 60 to 80% of the total rotation), and that rotations contributed by other sources are relatively small, especially after yielding. This is because the flexural and diagonal tension (shear) cracks within distance ***h*** from beam-wall interfaces were significantly smaller than slip/extension cracks at the interfaces, as seen in **Table 3-1**, **Figure 3-13**, and **Figure 3-14**. Except for CB4 (diagonally reinforced beam) and CB6 (SRC beam), the rotation contributed by shear distortion increases as the number of cycles increase during the loading protocol. In case of CB5R, the contribution of shear deformation to total rotation increased compared with CB5 because, as noted previously, the shear cracks were not repaired and thus deteriorated faster than the flexural cracks as the demands increased. A slight increase in flexural deformations and a decrease in slip/extension deformations were also observed for CB5R compared with CB5.

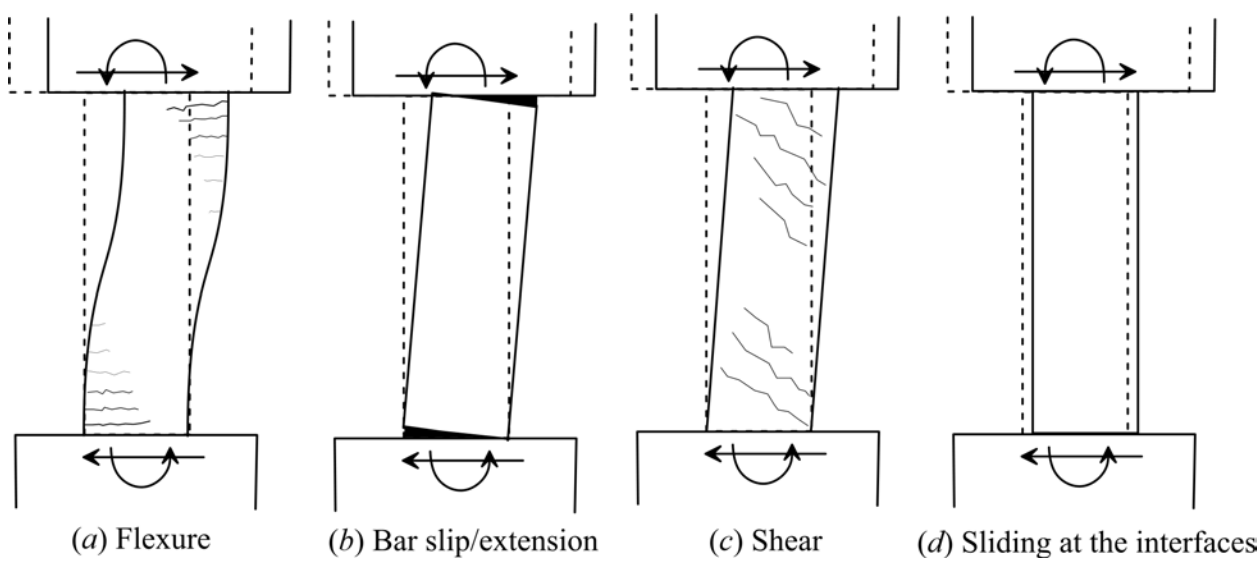

Figure 3-26. Various sources of deformation in coupling beams.

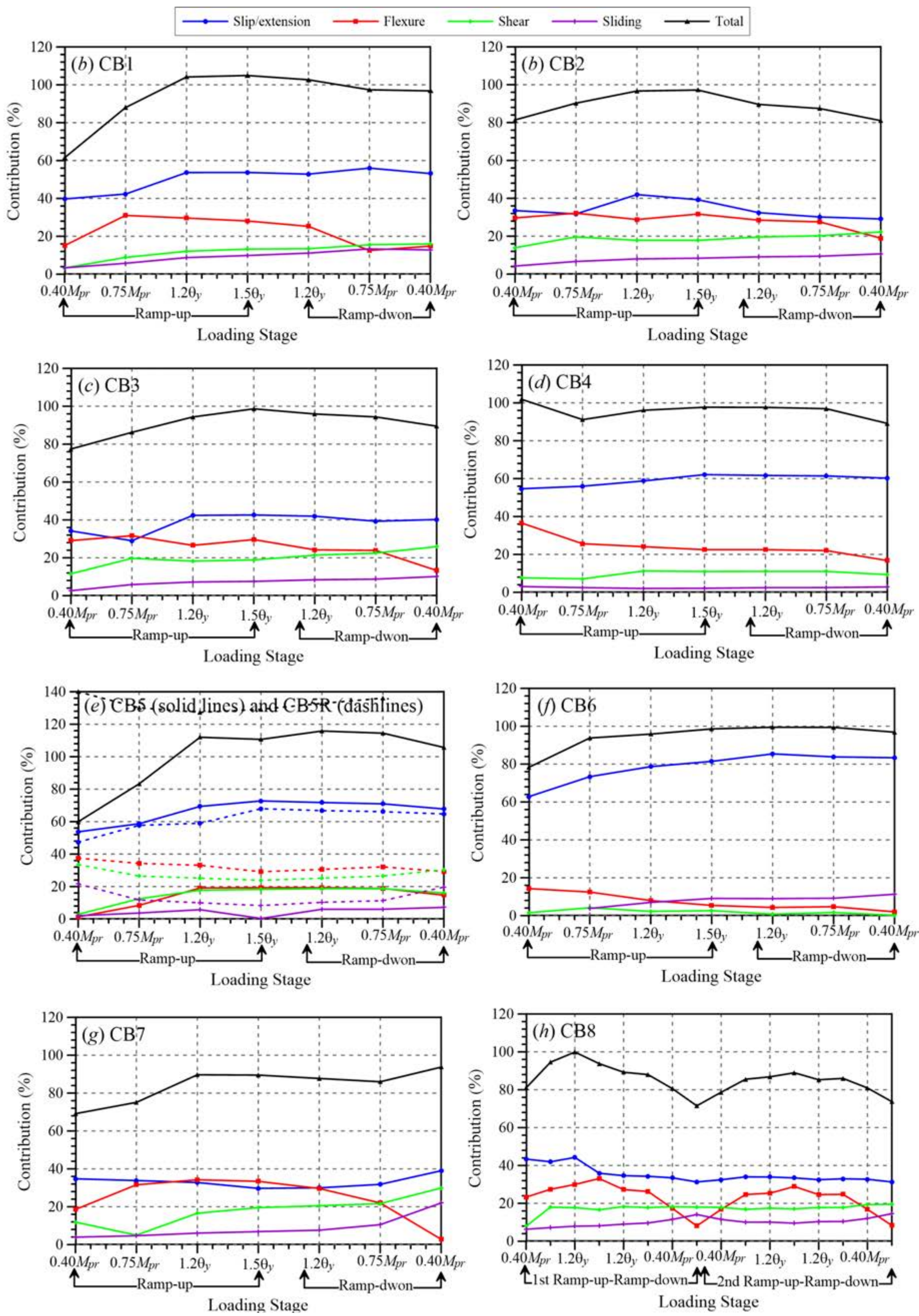

Figure 3-27. Contributions of various deformation components to total rotation.

3.7. Energy Dissipation Capacity

The energy dissipated was calculated as the area enclosed by the hysteretic loop during each loading cycle. **Figure 3-28** shows the dissipated energy during each cycle for the wind loading protocol, whereas **Figure 3-29** shows the accumulative energy dissipated during a test. **Figure 3-28** shows that the energy dissipated spikes during the first cycle of each loading stage of the ramp-up loading because, during those cycles, new cracks formed and existing cracks propagated further leading to a fatter loop for the first cycle at a given load/displacement demand than subsequent cycles at the same load/displacement demand. **Figure 3-28** and **Figure 3-29** show that energy is primarily dissipated during the cycles where yielding of reinforcement occurred (i.e., the ramp-up cycles at $0.75M_{pr}$ through ramp-down cycles at 0.40 M_{pr}).

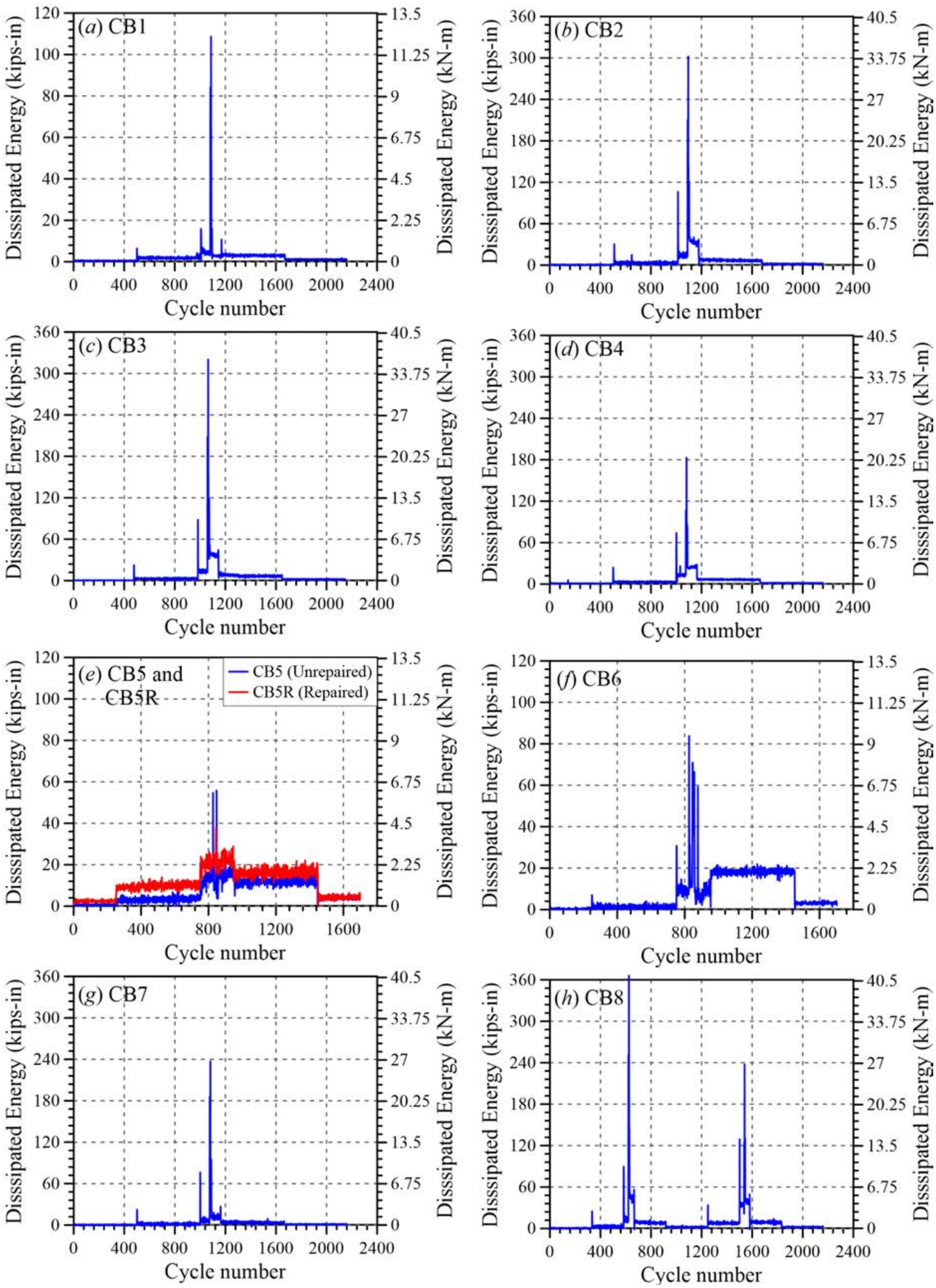

Figure 3-28. Energy dissipated per cycle.

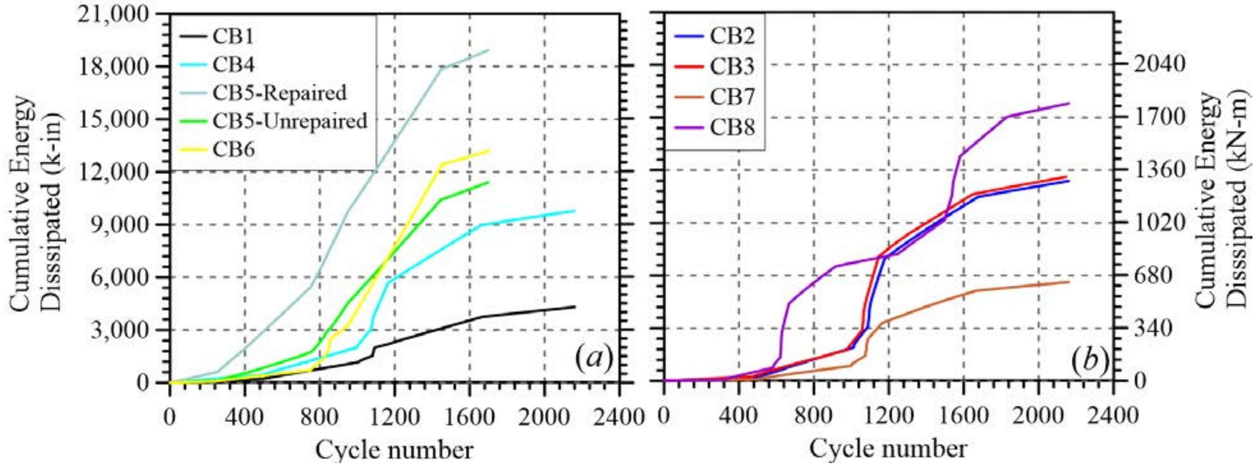

Figure 3-29. Accumulative energy dissipated: (*a*) beams with l_n/h = 2.5; (*b*) beams with l_n/h = 3.67.

3.8. Digital Image Correlation (DIC) Results

As noted previously, in addition to the contact measurement system (i.e., LVDTs, Wire potentiometers, load cells, and strain gages) and manual measurements, an optical, non-contact measurement system, referred to as digital image correlation (DIC), was used to measure surface strains and crack widths to display crack patterns on the south web face of the beams. Typical results for CB1 are presented in this section, whereas the results for all the test beams are presented in **Appendix H**.

Figure 3-30 shows surface strains and crack widths and pattern (mostly diagonal shear cracks) for CB1 during the second cycle at peak rotational ductility demand of about 1.9 (i.e., at chord rotation of 1.5%) in both directions of loading, whereas **Figure 3-31** shows the crack widths history of the cracks shown in **Figure 3-30**. **Figure 3-30** shows that CB1 developed seven to eight major diagonal cracks over the clear length of the beam. The results also show that the manually measured crack widths (**Table 3-1**) are relatively close to those measured using the DIC system, recognizing the inaccuracies involved in both measurement approaches (e.g., human error for the manual measurements; the focus and resolution of the camera, exposure of light to the surface of the beam, and detail of the random speckle pattern for the DIC measurements). **Figure 3-31** reveals that at zero rotation demand during the second cycle at peak ductility demand (unloading from the peak ductility demand to zero rotation) the majority of the cracks either close or reduce width significantly.

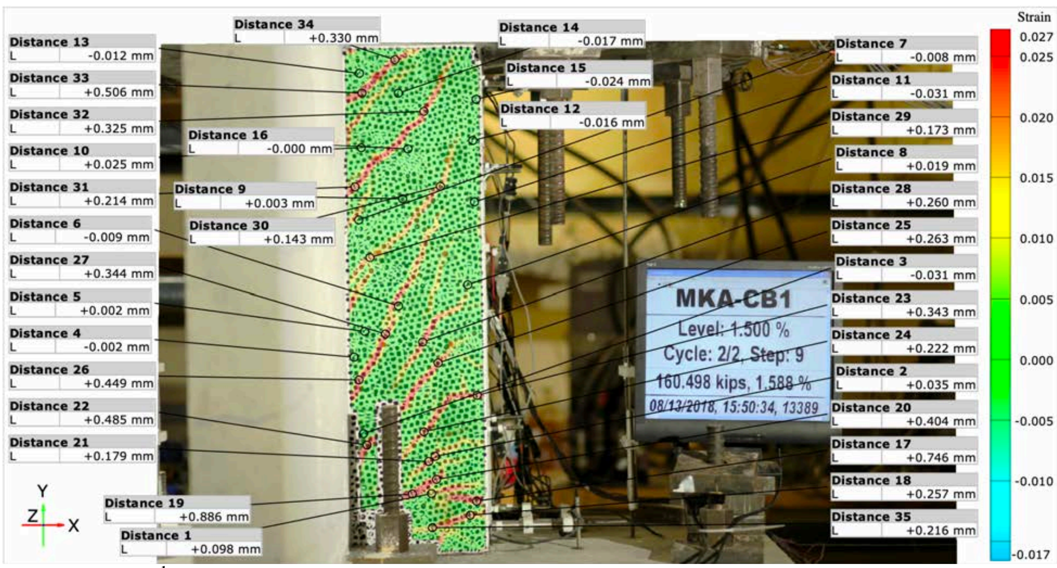

(*a*) 2nd cycle at peak ductility demand of about 1.9 in the positive direction

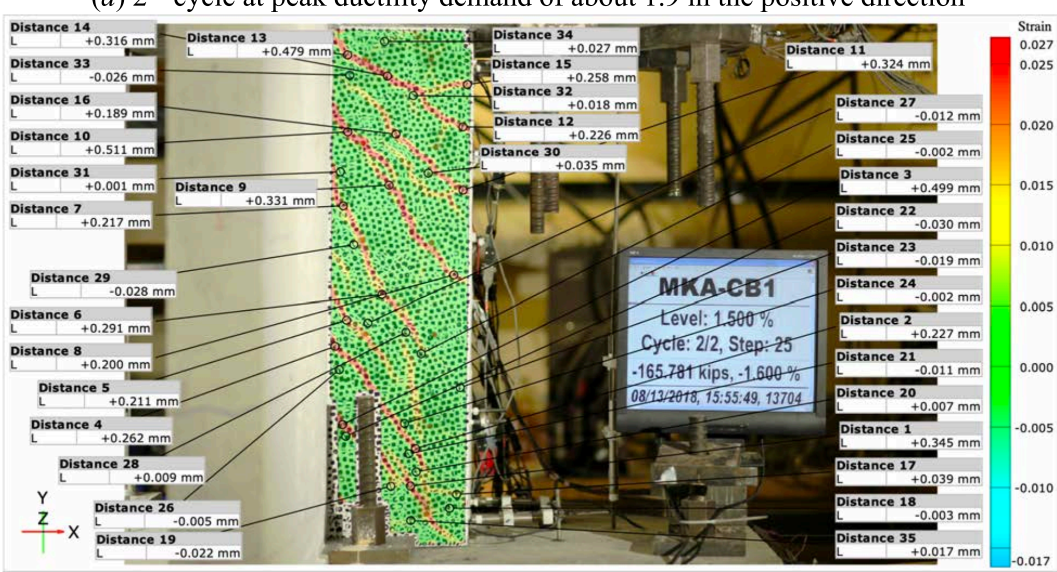

(*b*) 2nd cycle at peak ductility demand of about 1.9 in the negative direction

Figure 3-30. Crack pattern and widths obtained from DIC for CB1. (Note: 1 mm = 0.0394 in.)

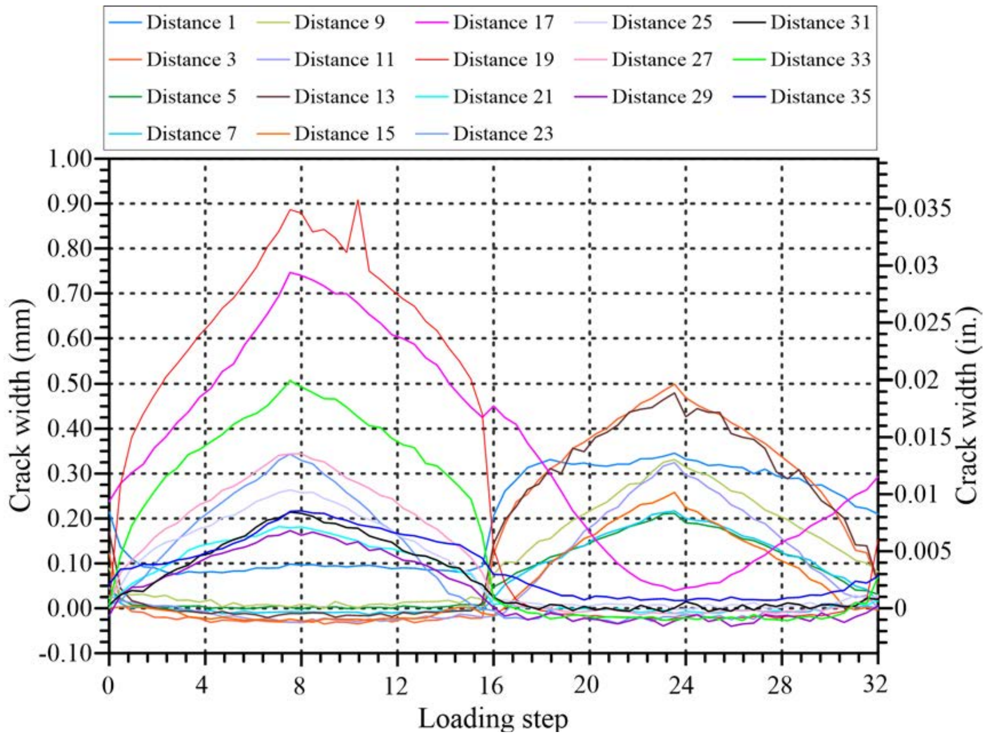

Figure 3-31. Crack width history during 2nd cycle at ductility demand of about 1.9 for CB1 (Note: the labels in the legend refer to the locations identified in Figure 3-30).

Figure 3-30 shows the surface strains and crack pattern and widths obtained from the DIC system for CB1 at zero rotation at end of wind loading protocol. This figure demonstrates that the residual diagonal shear cracks either closed or were very minor, similar to manual measurement results reported in **Table 3-1**.

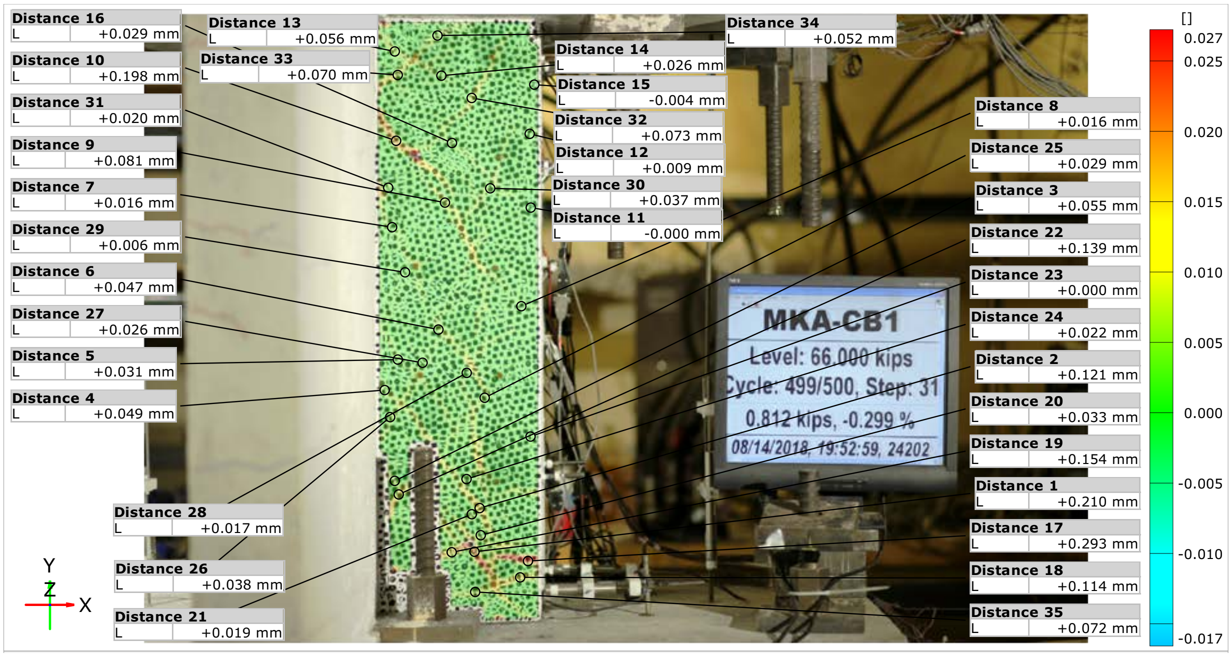

Figure 3-32. Crack pattern and widths obtained from DIC for CB1 at zero rotation at end of wind loading protocol. (Note: 1 mm = 0.0394 in.)

CHAPTER 4. DISCUSSION OF WIND TEST RESULTS

4.1. General

This chapter provides a discussion of the wind test results presented in the preceding chapter, including the impacts on observed behavior of concrete cracking, epoxy repair, reinforcement detailing, beam aspect ratio, presence of a floor slab, loading protocol, and reinforcement type (RC vs SRC).

4.2. Cracking and Damage Classification

The level of damage observed in the coupling beams, as was shown in **Table 3-1** and **Figure 3-1** through **Figure 3-18**, is considered minor for beams subjected to ductility demands representative of those from a windstorm with an MRI of 1,700-year or 3,000-year, depending on the risk category (ASCE Prestandard for PBWD, 2019). Experience suggests that such events would be expected to significantly damage non-structural components, such as cladding, which are typically designed to only remain attached during such events (ASCE Prestandard for PBWD, 2019).

The FEMA 306 document provides guidance on classifying the severity of damage to RC components subjected to earthquake demands, including walls, coupling beams, and piers, along with the necessary restoration measures for each damage level. For each component of the structural system, damage is classified based on the predominant behavior (or failure mode, i.e., shear-, flexure-, or sliding-controlled behavior); the damage classification guidelines and the restoration measures of FEMA 306 are summarized in **Table 4-1**. It is noted that the crack width limits given in **Table 4-1** as criteria for distinguishing the damage severity levels are maximum residual crack widths, rather than crack width at peak transient demands. Based on the maximum residual crack widths reported in **Table 3-1**, as well as the damage information reported in section **3.2**, the damage level of the beams tested in this study can be classified as “insignificant” using the FEMA 306 criteria given in **Table 4-1**, and that repair is not necessary to restore the structural characteristics of the beams; however, cosmetic repairs (e.g., painting cracks) to improve the visual appearance of the beams could be considered.

It is noteworthy that in real buildings, coupling beams have some degree of axial restraint imposed by the coupled wall piers and the floor slab, which could result in residual crack widths smaller than those reported in **Table 3-1** (Naish et al., 2013; Motter et al., 2017; Poudel et al., 2018; Marder et al., 2018).

Table 4-1. Classification of damage severity in RC coupling beam (FEMA 306, 1998)

Severity Level	Qualitative Description of Damage	Criteria[1]	Performance Restoration Measures
Insignificant	Damage does not significantly affect structural properties in spite of a minor loss of stiffness.	• No crack widths exceed 3/16 in., and • No shear cracks exceed 1/8 in., and • No significant spalling or vertical cracking	Repairs may be necessary for restoration of nonstructural characteristics. That is, restoration measures are cosmetic unless the performance objective requires strict limits on nonstructural component damage in future events.
Slight	Damage has a small effect on structural properties. Relatively minor structural restoration measures are required.	Not used for coupling beams	Not used for coupling beams
Moderate	Damage has an intermediate effect on structural properties. Typical appearance: Similar to insignificant damage except wider cracks, possible spalling, and typically more extensive cracking.	• Shear crack widths do not exceed 1/8 in., and • Flexural crack widths do not exceed 1/4 in., and • Shear cracks exceed 1/16 in., or limited spalling (or incipient spalling as identified by sounding) occurs at web or toe regions, and • No buckled or fractured reinforcement, and • No significant residual displacement.	The scope of restoration measures depends on the component type and behavior mode. Measures may be relatively major in some cases, such as removing and patching spalled and loose concrete, and injecting cracks.
Heavy	Damage has a major effect on structural properties.	Shear crack widths may exceed 1/8 in., but do not exceed 3/8 in. Higher width cracking is concentrated at one or more cracks.	The scope of restoration measures is generally extensive. Replacement or enhancement is required for full restoration of seismic performance. For partial restoration of performance, inject cracks.
Extreme	Damage has reduced structural performance to unreliable levels.	Reinforcement has fractured. *Typical indications:* Wide shear cracking typically concentrated in a single crack.	The scope of restoration measures generally requires replacement or enhancement of components.

[1]Crack widths are maximum residual crack widths

4.3. Impact of Epoxy Repair

Notwithstanding the minor damage observed, the impact of epoxy injecting cracks on restoring the structural characteristics of the beams, especially stiffness, was investigated for CB5. After testing of CB5 (unrepaired) was concluded, the beam was repaired by injecting cracks with epoxy (CB5R), as discussed in section **2.2.2**, and then the beam was retested using the same wind loading protocol (**Figure 2-22** (***a***)). The repaired cracks generally did not re-form, which is an indication that the repair was effective, and new cracks formed in the vicinity of the repaired cracks, which led the beam to experience additional axial growth (**Figure 3-25** (***e***)). The residual widths of the new cracks were comparable to those of the repaired cracks (**Table 3-1**).

Results reported in **Figure 3-23** (***e***) and **Table 3-3** show that the repair restored the initial secant stiffness values to about 150% (0.05 versus 0.033) and 115% (0.075 versus 0.065) of the values for loading at $0.15M_{pr}$ to $0.75M_{pr}$, respectively, when comparing the ramp-down stiffness values of CB5 with the ramp-up stiffness values of CB5R at the same demand.. The load-deformation responses of CB5R and CB5 during the 75 cycles at $0.75M_{pr}$ are compared in **Figure 4-1**. This loading level was selected because the slope of the cycles roughly represents the initial effective stiffness (secant to yield) of the beams. Comparing the response of the ramp-up (RU) cycles of CB5R with the response of the ramp-down (RD) cycles of CB5, **Figure 4-1** (***a***) shows that the repair resulted in moderate and slight restoration of stiffness in the positive and negative directions of loading, respectively, with an average improvement of about 15% (**Table 3-3**). **Figure 4-1** (***b***) compares the responses of CB5R and CB5 during the 75 cycles of ramp-up loading, which indicates that the repaired initial stiffness is significantly smaller than the unrepaired initial stiffness, i.e., the repaired stiffness is on average about 65% of the unrepaired stiffness at this loading stage (**Table 3-3**).

Prior research (e.g., Marder 2018) has shown that, at the same ductility demand, repaired beams could attain strength higher than unrepaired strengths when the repaired beam is retested after a time period in the order of at least few months due the strain ageing phenomena of the steel bars containing inadequate contents of certain alloying metals such as Titanium or Vanadium, especially low strength bars (Loporcaro, 2017; Momtahan et al., 2008; Van Rooyen, 1986; Pussegoda, 1978; Rashid, 1976). However, this was not an issue in this study because grade 60 bars, which were used in this study, are not susceptible to strain aging (Zhao and Ghannoum, 2016). As well, the reinforcing bars in CB5 had low residual strains prior to repair (i.e., low axial growth), and CB5R was tested nine days after testing of CB5 was concluded, not enough time to allow for rebar strain aging to occur.

In summary, the epoxy injection repair did not result in an appreciable restoration of the structural characteristics of the beam, especially the stiffness. Therefore, given the cost and building function disruption associated with the repair, the authors believe that repairing cracks observed in the tested beams is not warranted.

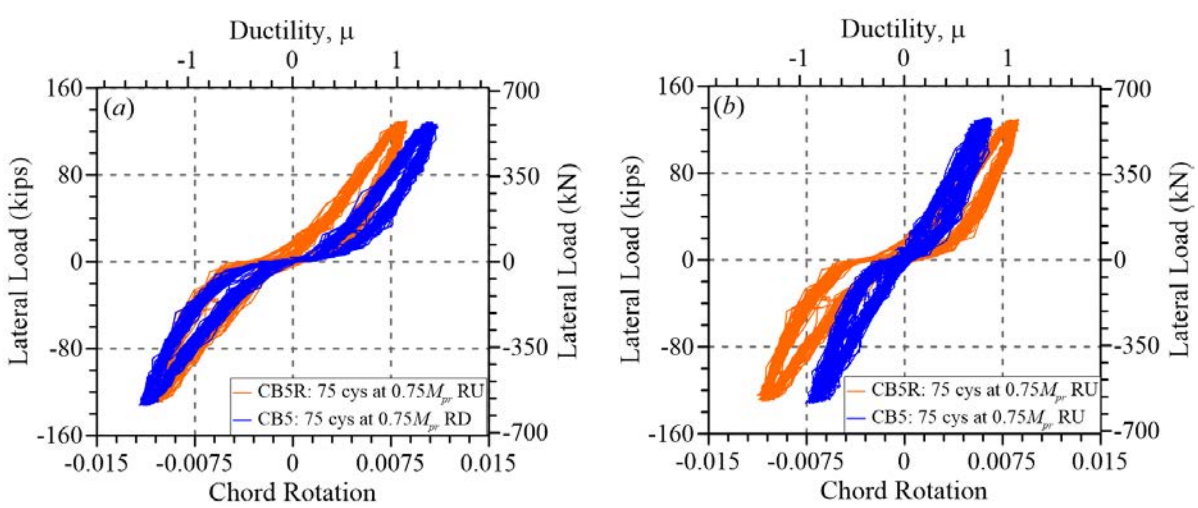

(*a*) Repaired RU vs. unrepaired RD (*b*) Repaired RU vs. unrepaired RU

Figure 4-1. Load deformation responses of CB5 and CB5R during 75 cycles of loading at 0.75M_{pr}. (Note: RU = ramp-up, and RD = ramp-down)

4.4. Impact of Detailing

Two beams with aspect ratio of 2.5 were tested to evaluate the influence of reinforcement detailing. CB1 had standard detailing and conventional (longitudinal) reinforcement, whereas CB4 had seismic detailing and diagonal reinforcement. In addition to an increase in shear strength, an increase in transverse reinforcement provides confinement to the concrete core and lateral restraint to longitudinal/diagonal bars to restrain bucking. However, since no significant damage, such as concrete spalling or crushing or bar buckling, was observed, the increased level of detailing did not play a noticeable role in the performance of the beams (i.e., confinement activates when significant compression strains (>0.002) or compressive stresses (>0.85f_c') are reached), and the performance of the two beams was essentially the same. Therefore, based on these tests, enhancing detailing or employing capacity-design principles to prevent shear failure prior to flexural yielding are not warranted to ensure adequate performance of coupling beams during extreme wind events.

4.5. Impact of Aspect Ratio (l_n/h)

Two beams with standard detailing and floor slabs were tested to assess the influence of l_n/h. CB1 had an l_n/h of 2.5 and T-shaped floor slab, whereas CB2 had an l_n/h of 3.67 and L-shaped floor slab. For the ductility demands applied, l_n/h did not have a noticeable influence on the degree of concrete cracking, force-deformation response, axial growth, and residual deformation of the two beams. The only noticeable difference was that CB2 had larger secant and effective stiffness values than CB1; however, it is well-established in the literature (e.g., Paulay and Preiestley, 1992) that the stiffness of coupling beams is significantly impacted by l_n/h (**Figure 3-24**).

4.6. Impact of Floor Slab

Two beams with l_n/h of 3.67 were tested to assess the impact of RC floor slab. CB2 included an L-shaped floor slab, whereas CB3 did not have a floor slab. The results indicate that the presence of the floor slab did not produce a significant influence on the behavior of CB2 compared to CB3, and that concrete cracking, axial growth, energy dissipation, and strength of the two beams were comparable. A slightly larger initial stiffness was observed for CB2 compared with CB3 (see **Figure 4-2**, **Table 3-3**, and **Figure 3-22**). As will be discussed in Chapter 6, at higher ductility demands than applied during the wind tests, slabs are expected to modestly increase lateral strength of coupling beams due to greater level of strain hardening of reinforcement when flange is in compression and due to yielding of slab reinforcement when flange is in tension. Naish et al. (2013) also observed a slight increase in stiffness due to presence of RC slab in coupling beams with T-shaped floor slab and diagonal reinforcement.

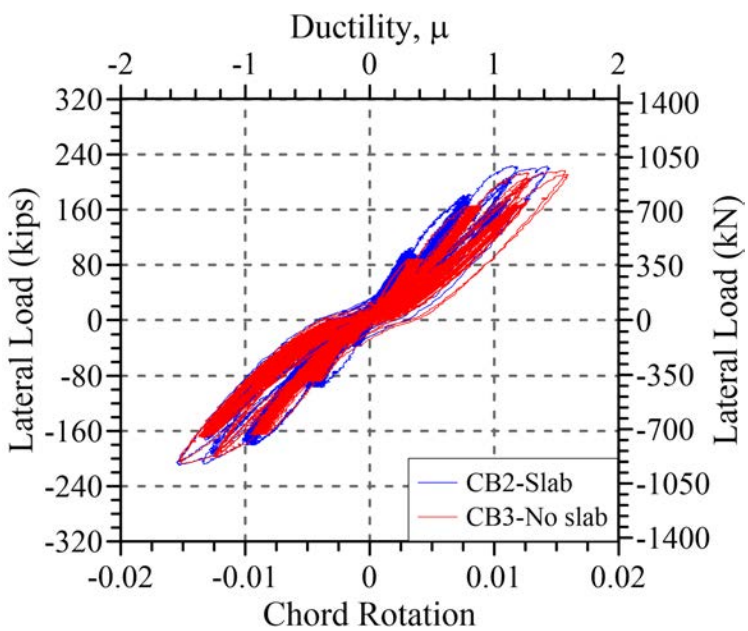

Figure 4-2. Comparison of load-deformation response of CB2 and CB3.

4.7. Impact of Loading Protocol

4.7.1. Seismic Versus Wind Loading Protocol

Results from two essentially identical coupling beams with seismic detailing and diagonal reinforcement are compared to assess the influence of loading protocol. CB4 was tested under the wind loading protocol shown in **Figure 2-21** (2162 cycles and a maximum ductility demand of ~1.5), whereas CB24F-RC was tested by Naish et al. (2013) under a standard seismic loading protocol (which included 24 cycles up to a ductility demand of ~1.6). The lateral load (V) normalized by $V_{@Mpr}$ versus chord rotation responses of the two beams are compared in **Figure 4-3**, which shows that the responses of the two beams are very similar, except that CB4 has slightly smaller initial stiffness and more pinching of hysteretic loops, especially in the positive loading direction, as a result of cyclic softening due to the large number of cycles applied during the wind loading protocol. **Figure 4-4** (***a***) and (***b***) show the damage state of CB4 at the end of the wind loading protocol and CB24F-RC at rotation demand of 0.02, respectively, and reveal that neither beam sustained any significant damage at this stage. As shown in **Table 3-1**, Naish et al. (2013) only reports crack widths for CB24F-RC at peak rotations of 0.01 and 0.03. Performing linear interpolation between crack widths at 0.01 and 0.03 rotations to approximate crack widths at 0.019 rotation for CB24F-RC results in flexural and diagonal crack widths within a distance h from the beam-wall interface that are comparable to those of CB4. Crack widths at the beam-wall interface are slightly larger for CB24F-RC relative to CB4, possibly due to the smaller scale used.

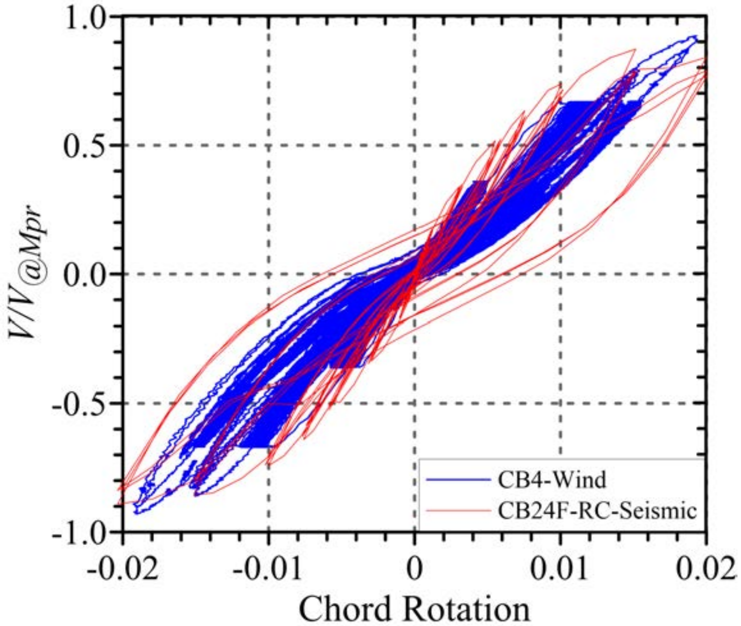

Figure 4-3. Comparison of lateral load-chord rotation responses of CB4 and CB24F-RC.

(*a*) CB4 (End of wind loading) (*b*) CB24F-RC (0.02 rotation)

Figure 4-4. Cracking condition of CB4 and CB24F-RC.

4.7.2. Alternative Wind Loading Protocols

In recognition of the uncertainty associated with the wind loading protocol, a principal objective of the Phase II tests was to investigate the influence of varying the wind loading protocol, which included loading protocols with increased number of the mildly inelastic cycles (i.e., cycles at $1.2\theta_y$ and $1.5\theta_y$), a non-zero mean component (to simulate ratcheting effect), and two ramp-up-ramp-down events.

Increased Number of Inelastic Cycles: performance of CB1 tested under a wind loading protocol with 12 intended inelastic cycles (**Figure 2-21**) was compared with that of CB5 tested under a wind loading protocol with 50 intended inelastic cycles, i.e., mildly inelastic cycles were increased by a factor of about four (**Figure 2-22** (***a***)). The results indicate that the increased number of inelastic cycles did not produce a noticeable influence on the behavior of CB5 compared to CB1, and that concrete cracking, axial growth, stiffness, and strength of the two beams were practically the same (**Table 3-1**, **Figure 3-1**, **Figure 3-2**, **Figure 3-9**, **Figure 3-10**, and **Figure 4-5**). The energy dissipated by CB5 was significantly larger than that dissipated CB1 (**Figure 3-29**) because CB5 was subjected to a larger number of inelastic cycles. As well, in the case of CB1, the 75 cycles at $0.75M_{pr}$ on the ramp-down were inadvertently applied at the same displacement, rather than the same lateral load, as the 75 cycles on the ramp-up, which led to smaller hysteretic loops and thus reduced energy dissipation capacity.

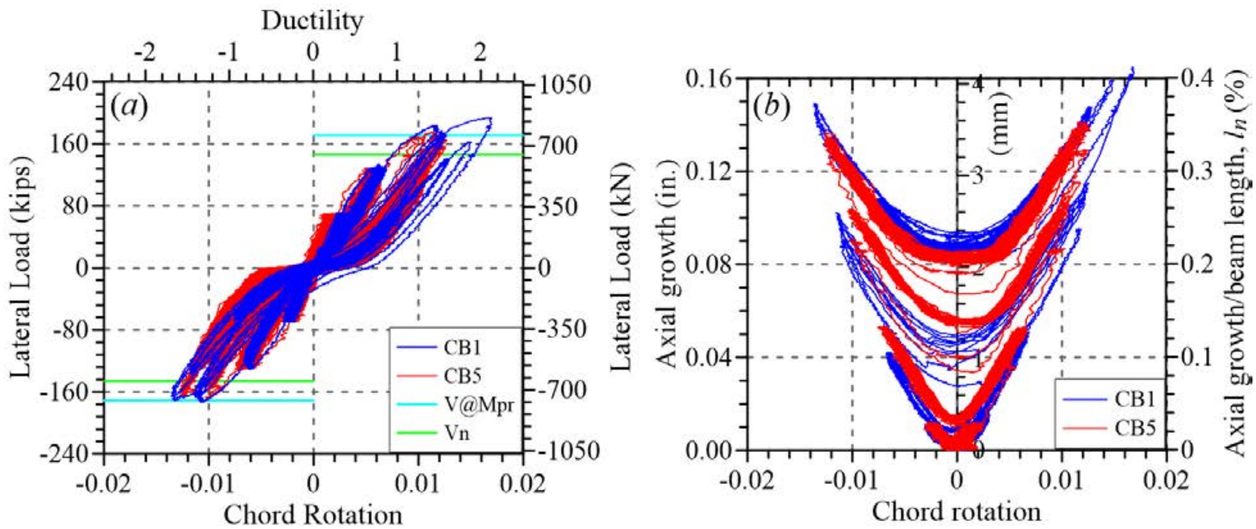

Figure 4-5. Comparison of CB1 vs CB5: (*a*) load-deformation response; (*b*) axial growth.

Non-zero Mean Component: The performance of CB7 tested under the wind loading protocol shown in **Figure 2-22** (***b***) (non-zero mean component) was compared with that of CB2 tested under the wind loading protocol shown in **Figure 2-21** (zero mean component). The results reported in **Table 3-1**, **Figure 3-3**, **Figure 3-4**, **Figure 3-15**, **Figure 3-16**, and **Figure 4-6** reveal that introducing a non-zero mean component to the wind loading protocol, in fact, led to better performance in terms of concrete cracking, axial growth, and stiffness. Since CB7 did not sustain the same extent of concrete cracking in the negative direction of loading as it did in the positive direction, it had larger secant and effective stiffness values than CB2 (**Figure 4-6** (***a***)). **Figure 4-6** (***b***) shows that CB7 had significantly less axial growth than CB2 (i.e., almost half of that experienced by CB2), which is also an indication of the lesser extent of concrete cracking and smaller residual crack widths sustained by CB7. As far as energy dissipation capacity is concerned, CB7 dissipated significantly less energy than CB2 because the cycles did not fully reverse to the same loading/displacement demands in both directions of loading (**Figure 4-6** (***a***)), and thus less concrete cracking and reinforcement yielding (sources of energy dissipation) in the negative direction of loading and overall smaller hysteretic loops than those of CB2. Additionally, use of the non-zero mean component wind loading protocol, as expected, resulted in larger residual rotations in CB7 than those of CB2 (**Table 3-2**), which are still significantly smaller than values allowed by PBSD guidelines, e.g., LATBSDC (2017) and PEER TBI (2017).

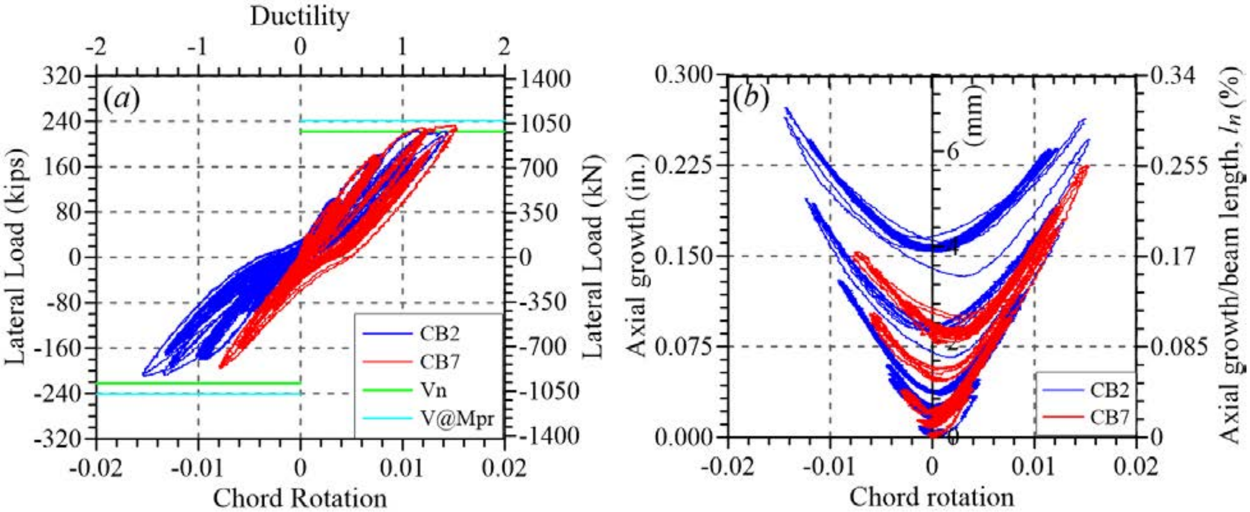

Figure 4-6. Comparison of CB2 vs CB7: (*a*) load-deformation response; (*b*) axial growth.

Two Ramp-up-Ramp-down Events: The performance of CB8 tested under the wind loading protocol shown in **Figure 2-22** (***c***) (two ramp-up and ramp-downs) is compared with CB2 tested under the wind loading protocol shown in **Figure 2-21** (one ramp-up and ramp-down). **Figure 4-7** (***a***) shows that the lateral load-deformation response of the two beams is similar. The results also demonstrate that the wind loading protocol with two ramp-up-ramp-down events used for CB8 was slightly more demanding than that used for CB2 with respect to crack widths (**Table 3-1**) and axial growth (**Figure 4-7(*b*)**). CB8 had slightly larger stiffness values on the first ramp-up than CB2 (**Table 3-3** and **Figure 3-23**) owing to the smaller number of cycles used on the first ramp-up of CB8 than the ramp-up of CB2 and thus less cyclic softening for CB8. Moreover, as shown in **Figure 3-29**, CB8 possessed greater energy dissipation capacity (i.e., ~35% increase) because this beam was pushed to yield earlier in the loading protocol (i.e., pushed to yield after 621 cycles) than CB2 (pushed to yield after 1075 cycles) and thus more cycles beyond yield were applied to CB8 relative to CB2.

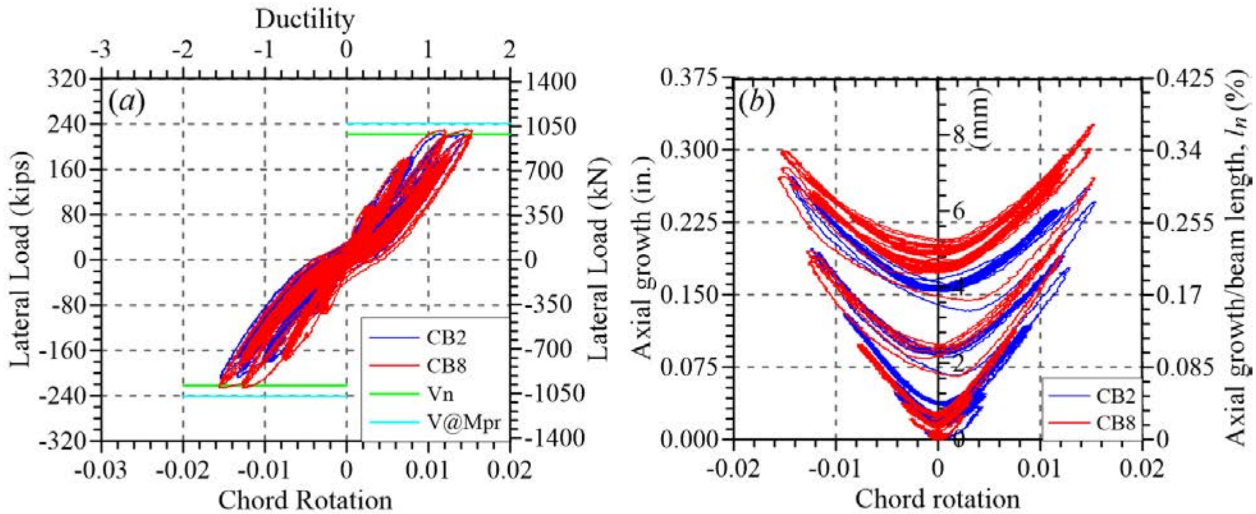

Figure 4-7. Comparison of CB2 and CB8: (*a*) load-deformation response; (*b*) axial growth.

4.8. Comparison of Steel Reinforced and Reinforced Concrete Beams

Two beams with l_n/h of 2.5, standard detailing, and floor slabs were tested to assess the influence of employing a structural steel section reinforced concrete coupling beam (SRC, CB6) versus a conventionally reinforced concrete coupling beam (RC, CB5) tested under the same wind loading protocol (**Figure 2-22** (***a***)). **Figure 4-8** (***a***) shows that the lateral load-deformation responses of the two beams are very similar. Unlike CB5, where, in addition to major cracks at the beam-wall interface, other sizable flexural and diagonal shear cracks opened in the plastic hinge regions, CB6 developed one major crack at each beam-wall interface that was roughly three times wider than that of CB5 (**Table 3-1**), and relatively small cracks elsewhere. The larger interface cracks resulted in CB6 sustaining a residual axial growth that was roughly three times larger than that of CB5 (**Figure 4-8**). In case of CB6, the axial growth occurred gradually as the number of cycles increased, whereas for CB5 all the axial growth takes place during the ramp-up cycles, particularly at the transition between the loading stages, with almost no axial growth during the ramp-down cycles. **Table 3-3** and **Figure 3-29** show that the two beams have similar secant stiffness values and energy dissipation capacity, respectively.

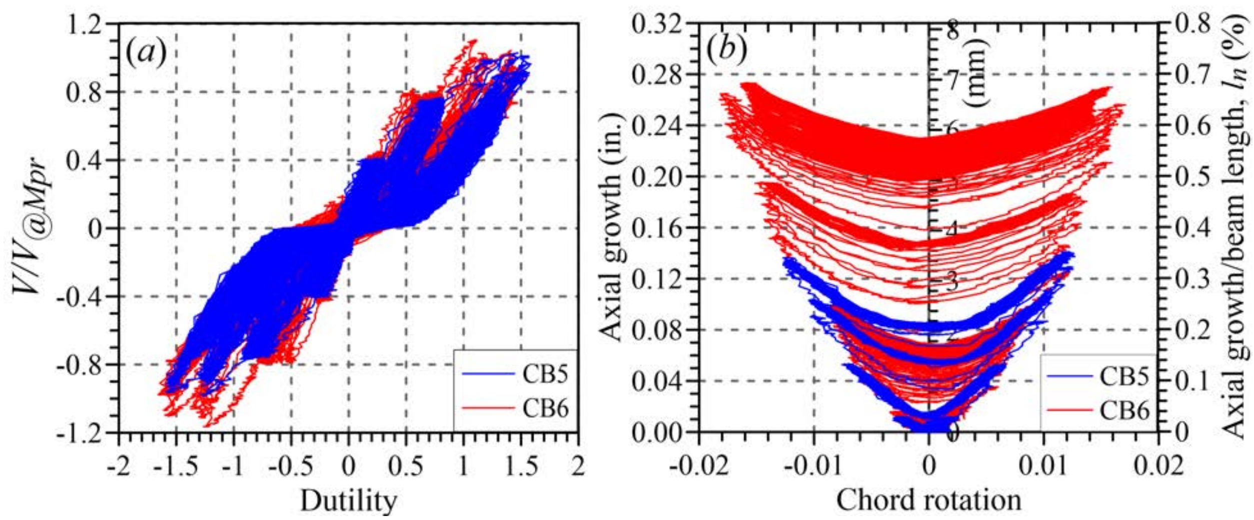

Figure 4-8. Comparison of CB5 and CB6: (*a*) load-deformation response; (*b*) axial growth.

CHAPTER 5. CONCLUSIONS AND RECOMMENDATIONS FROM WIND TESTS

The first part of this study presents results of a two-phase experimental program of concrete coupling beams, in which eight beams were constructed and tested under simulated quasi-static, cyclic wind loading protocols. The test beams included six RC coupling beams with standard detailing and conventional reinforcement, one RC coupling beam with seismic detailing and diagonal reinforcement, and one SRC coupling beam with standard detailing and capacity-designed embedment. Four of the beams had an aspect ratio (l_n/h) of 2.5, representing coupling beams in residential buildings, while the other four beams had an l_n/h of 3.67, representing coupling beams in office buildings, including one beam without a floor slab. One of the beams, with conventional reinforcement and l_n/h of 2.5, was epoxy-repaired after the wind loading protocol was applied and was retested using the same wind loading protocol to evaluate the impact of epoxy injection repair on restoring the wind performance of the beam. Since standardized quasi-static, cyclic wind loading protocols are not known to be available for testing structural building components, a wind loading protocol, intended to simulate coupling beam demands under hurricane or other extreme wind events, was developed for Phase I tests, which consisted of a large number of elastic load cycles (2150 cycles) and a dozen mildly inelastic displacement cycles with target peak ductility demand of 1.5. In recognition of the inherent uncertainty related to the prediction of wind loading histories, variations in the wind loading protocol were considered in Phase II tests. The variations included: 1) increasing the number of mildly inelastic cycles, 2) introducing a non-zero mean component (simulating the ratcheting effect of wind in the along-wind direction), and 3) having more than one ramp-up and ramp-down (i.e., spreading out the yielding cycles). Based on the experimental findings, the following conclusions and recommendations with regards to behavior of concrete coupling beams tested under the described wind loading protocols can be drawn:

1. All of the coupling beams performed well, with no crushing or spalling of concrete, or buckling or fracture of reinforcing bars or of the structural steel section. The residual crack widths at the end of the wind tests were the largest at the beam-wall interfaces and typically ranged from 1/100 in. (0.25 mm) to 1/16 in. (1.6 mm) for the RC beams and from 1/16 in (1.6 mm) to 3/32 in. (2.36 mm) for the SRC beam. Smaller crack widths were measured in the beam web (diagonal tension cracks), with residual widths ranging from zero to 1/64 in. (0.40 mm) for the RC beams and from zero to 4/1000 in (0.10 mm) for the SRC beam.
2. The level of structural damage and concrete cracking observed in the coupling beams is considered minor for beams subjected to ductility demands representative of those from a windstorm with an MRI of 1,700-year or 3,000-year, depending on the risk category (ASCE Prestandard for PBWD, 2019). Experience indicates that such events would be expected to significantly damage the non-structural components such as cladding, which are typically designed to only remain attached during such events (ASCE Prestandard for PBWD, 2019). Additionally, based on the observed residual crack widths, the damage level of the beams is classified as "insignificant" using the FEMA 306 criteria, and that repair is not necessary to restore the structural characteristics of the beams; however, cosmetic repairs (e.g., painting cracks) to improve the visual appearance of the beams could be considered. It is noteworthy that in real buildings, coupling beams have some degree of axial restraint imposed by the adjacent walls and floor slabs, which could result in reduced residual crack widths.
3. Beams with seismic and standard detailing performed similarly. Since no significant damage (e.g., concrete crushing, or bar buckling) was observed, the increased level of detailing did not

play a noticeable role in beam performance. Therefore, enhancing detailing or employing capacity-design principles for efficiently designed beams (i.e., $\phi M_n \approx M_u$; $\phi V_n \approx V_u$) to prevent shear failure prior to flexural yielding are not recommended to ensure adequate performance for extreme wind events.

4. The presence of the floor slabs did not significantly impact concrete cracking, axial growth, energy dissipation, or strength; however, a slightly larger initial stiffness was observed for CB2 with an L-shaped floor slab compared with CB2 with no slab. It is noted that, at higher ductility demands than applied during the wind tests, slabs are expected to modestly increase lateral strength of coupling beams due to greater level of strain hardening of reinforcement when flange is in compression and due to yielding of slab reinforcement when flange is in tension.
5. The impact of aspect ratio (l_n/h) was also not apparent on the overall behavior of the beams, except that, as expected, the beams with larger l_n/h possessed larger stiffness values (i.e., E_cI_s/E_cI_g and E_cI_{eff}/E_cI_g), which is consistent with stiffness data of beams tested under seismic loading protocols.
6. The loading protocol (wind versus seismic) did have a significant impact on concrete cracking and strength of the tested coupling beams. For roughly the same ductility demand, slightly less initial stiffness and more hysteretic pinching were observed for CB4 tested under the wind loading protocol, relative to CB24F-RC tested under a seismic loading protocol.
7. The effective stiffness values (E_cI_{eff}) of the beams normalized by the gross-section stiffness (E_cI_g) ranged from 0.14 to 0.21, depending on the aspect ratio and the type of wind loading protocol used. These values were found to be comparable to values obtained from a dataset of coupling beams tested under seismic loading protocols. These values are also comparable to values given in performance-based seismic design guidelines, e.g., LATBSDC (2017) and TBI

(2017), if adjusted for the impact of axial restraint provided by the adjacent floor slab and walls.

8. Except for CB1, CB5 and CB6, the beams did not quite reach their probable flexural strengths calculated under the ductility demands applied but are expected to reach higher lateral strengths if pushed to larger ductility demands, due to additional strain hardening of longitudinal or diagonal reinforcement. The results also demonstrated that ACI 318-19 Equation 18.10.7.4 significantly underestimates nominal shear strength (V_n) of diagonally reinforced coupling beams, and that results obtained from sectional analysis of the cross-section provide better estimates of beam strength. Similarly, the requirements of AISC 360-10 §14.1 provide a low estimate of V_n of SRC coupling beams. An approach that includes contributions of the concrete, steel section, and transverse reinforcement, which is not allowed by AISC 360-10 §14.1, would provide a closer, yet still conservative, estimate of shear strength.
9. Residual rotations, defined as rotations at which lateral load is zero, were the largest during the second cycle to the peak ductility demand (ranging from 0.001 to 0.005) and smallest at the end of the loading protocol (ranging from zero to 0.0028), with larger values being observed for CB7 subjected to the wind loading protocol with a non-zero mean component. Nonetheless, the residual rotations observed are considered practically negligible, given that, during extreme wind events, not all coupling beams in a building will be stressed to this level of ductility demand, and, thus, the residual drift of the building would be smaller.
10. For CB5R, the epoxy-repaired cracks generally did not re-form, which is an indication that the repair was effective in preventing the cracks from re-opening, and new cracks formed in the vicinity of the repaired cracks, leading to additional axial growth. However, the epoxy injection repair did not result in an appreciable restoration of the structural characteristics of the beam,

especially stiffness (~15% restoration of effective stiffness). Therefore, given the cost and building function disruption associated with the repair, the authors believe that repairing cracks observed in the tests is not warranted.

11. Increasing the number of inelastic cycles by a factor of about four in the wind loading protocol did not produce a significant influence on the behavior of CB5 compared to CB1, and that the concrete cracking, axial growth, stiffness, and strength of the two beams were nearly the same. CB5 dissipated more energy because its wind loading protocol contained a larger number of inelastic cycles.
12. Introducing a non-zero mean component to the wind loading protocol resulted in better performance in terms of concrete cracking, axial growth, and stiffness. Since CB7 did not sustain the same extent of cracking in the negative direction of loading as it did in the positive direction, it had larger secant and effective stiffness values than CB2. CB7 dissipated significantly less energy than CB2 because cycles applied to CB7 did not fully reverse to the same amplitude in both directions of loading, resulting in less cracking and yielding and smaller hysteretic loops.
13. The results also demonstrated that the wind loading protocol with two ramp-up-ramp-downs used for CB8 was slightly more demanding than that used for CB2 with respect to crack widths and axial growth. Moreover, CB8 possessed greater energy dissipation capacity (i.e., ~35% increase) because this beam was pushed to yield earlier in the loading protocol (i.e., pushed to yield after 621 cycles) than CB2 (pushed to yield after 1075 cycles) and thus more cycles beyond yield were applied in case of CB8 than CB2.
14. The results demonstrated that allowing limited nonlinearity with a maximum ductility demand of 1.5 in coupling beams provides a reliable mechanism to dissipate energy through concrete

cracking and reinforcement yielding, without compromising the strength and stability of the beam.

CHAPTER 6. EXPERIMENTAL SEISMIC TESTS RESULTS

6.1. General

After testing of the coupling beams under the wind loading protocols was concluded, the beams were subsequently subjected to a standard seismic loading protocol to assess the influence of the prior nonlinear wind demands on the overall seismic performance and reserve capacity of the coupling beams. The seismic loading protocol, as shown in **Figure 2-23**, picked up at either 1.5% or 2% chord rotation, depending on the peak rotation demand applied during the wind loading protocol. The initial smaller amplitude cycles were not applied since the beams had already been subjected to a large number of pre-yield and post-yield cycles during the wind loading protocols. This chapter presents the experimental results collected during the seismic tests, including observations on the extent of concrete cracking and progression of damage, information on lateral load-deformation responses, values of lateral stiffness, degree of axial growth, amount of energy dissipated, and deformation components contributing to total chord rotation.

6.2. Cracking and Damage Progression

6.2.1. Summary

The coupling beams sustained different damage progression and failure modes depending on the type of the coupling beam (i.e., RC versus SRC beams and conventionally- versus diagonally-reinforced beams). In general, concrete cracking and damage primarily concentrated within a distance of h (beam depth) from the beam-wall interfaces (i.e., within the plastic hinge regions), with the largest cracks being developed at the beam-wall interfaces (i.e., slip/extension cracks). The conventionally reinforced coupling beams (i.e., CB1, CB2, CB3, CB5, CB7, and CB8), regardless of their aspect ratios, experienced similar cracking, damage, and failure mode, which included first yielding of longitudinal reinforcement and then deterioration of shear cracks that led to an eventual shear failure in the plastic hinge regions at 4 or 6% rotation. The diagonally reinforced coupling beam (CB4) experienced significant lateral strength loss beyond 10% rotation due to concrete crushing and fracture of diagonal bars. The SRC coupling beam (CB6) did not experience significant lateral strength loss even after reaching 12% rotation demand, at which large cracks [~1.5 in. (38 mm) wide at peak demands] had opened at the beam-wall interfaces; however, no fracture or significant buckling of flanges of the steel section were observed, and, thus, the test was concluded after applying two cycles at 12% rotation. Typical damage of the overhanging floor slabs included one or two major cracks at or near each beam-wall interface that extending out to the edge of the slab, and smaller cracks over the rest of the span. These major cracks generally had larger residual widths than cracks at the beam-wall interface possibly due to shear lag effects (resulting in partial closure of the cracks when flange was in compression) and because the slabs were lightly reinforced (along the beam length) compared to the beams themselves.

Table 6-1 presents the measured widths of slip/extension, flexural, and diagonal tension (shear) cracks of the beams during each chord rotation level at both peak rotation (i.e., transient crack widths) and zero rotation (i.e., residual crack widths). Residual cracks are reported because they are better indicators to relate post-earthquake observed damage to the required potential repair or restoration technique and cost as opposed to transient crack widths at peak demands (e.g., FEMA 306). Additionally, the residual crack widths and observed damage patterns are useful to develop fragility curves and damage indices for structural components. The following subsections present quantitative and qualitative descriptions and comparisons of the cracking and damage progression of the beams during the seismic tests. In addition to the beams tested in this study, cracking and damage information of CB24F-RC beam tested by Naish et al. (2013) and an SRC coupling beam (denoted as SRC1) tested by Motter et al. (2017) are included for comparative purposes. As noted previously in **Table 2-1 Figure 2-4**, and **Figure 2-5**, CB24F-RC is essentially identical to CB4. SRC1 is similar to CB6 as both beams have adequate embedment length of the steel sections (capacity-designed connection), i.e., the connection strength is designed to exceed the demands at the connection associated with the shear and flexural strengths of the beam. More details of SRC1 can be found in Motter et al. (2017).

6.2.2. CB1 and CB5

CB1 and CB5 were identical RC coupling beams with conventional reinforcement, standard detailing, and l_n/h of 2.5 but were subjected to different wind loading protocols (

Table 2-7) prior to the seismic loading protocol. CB1 was tested under the loading protocol shown in **Figure 2-21**, whereas CB5 was tested twice under the loading protocol shown in **Figure 2-22** (***a***), once unrepaired and then after epoxy repaired. Thus, CB5 was subjected to significantly more inelastic cycles than CB1. **Figure 6-1** and **Figure 6-2** show the damage states of CB1 and CB5, respectively, at various chord rotation demands during the seismic loading protocol. These figures, along with **Table 6-1**, show that the two beams generally had similar cracking characteristics up to 4% rotation, with the shear cracks for CB5 being moderately larger than those of CB1, likely due to the increased number of inelastic cycles applied to CB5 during the wind testing. Since the shear strength associated with the development of probable moment strength ($V_{@Mpr}/b_w d$ = $8.85\sqrt{f_c'(psi)}$ [$0.74\sqrt{f_c'(MPa)}$]) was larger than the shear strength ($V_n/b_w d$ = $7.56\sqrt{f_c'(psi)}$ [$0.63\sqrt{f_c'(MPa)}$]), damage appeared to concentrate along diagonal (shear) cracks as the rotation demands gradually increased. During the first cycle to 6% rotation in the negative direction of loading, concrete in the web of CB1 crushed (**Figure 6-1** (***d***)), and, as a result, strength dropped by 9% from the peak strength. During the second cycle, significant web concrete crushing and spalling occurred in the plastic hinge regions, which led to significant lateral strength loss (~50% lateral strength loss). In the case of CB5, diagonal (shear) cracks became very large and the concrete cover in the web started to bulge out during the first cycle at 4% rotation. During the second cycle, concrete in the web crushed and spalled (**Figure 6-2** (***c***)), and, as a result, lateral strength dropped by 25% and 33% in the positive and negative directions of loading, respectively. In the first cycle to 6% rotation (**Figure 6-2** (***d***)), the beam failed in shear, and, as a result, lateral strength dropped by 22% and 30% in the positive and negative directions of loading, respectively. For both beams, opened hooks on crossties were observed at 8% rotation (**Figure 6-1** (***e***) and **Figure 6-2** (***e***)); however, no buckling or fracture of beam longitudinal bars was observed. The failure mode of both beams was flexure-shear (i.e., yielding in flexure prior to failure in shear). CB5 failed earlier than CB1, likely because CB5 was subjected to a wind loading protocol that included four times as many inelastic cycles than that used for CB1. The epoxy repair of CB5 after being subjected to the first wind loading protocol did not seem to improve the seismic performance of the beam since new cracks, with the same characteristics as the pre-repaired cracks, had formed in the vicinity of the repaired cracks early during the second round of the wind loading protocol. Once lateral strength loss initiated, the two beams experienced gradual strength degradation; lateral strength reduced by about 40% to 50% from peak strength at 8% rotation for both beams and by about 75% at 12% rotation for CB5 and at 9% rotation for CB1 (CB1 was only pushed up to 9% rotation).

Table 6-1–Measured crack widths of the beams during seismic testing (in inches)

Beam ID	Crack location & type[(1)]	2% Rotation		3% Rotation		4% Rotation		6% Rotation	
		Peak disp.	Zero disp.	Peak disp.	Zero disp.	Peak disp.	Zero disp.	Peak disp.	Zero disp.
CB1	L1	3/32-1/8	1.5/32	1/8	1/16	3/16-1/6	1.5/32	-	-
	L2	1/64-1/24	1/64-1/32	1/64-1/32	1/64	1/32-3/32	1/64-1/32	-	-
	L3	1/64-1/16	1/100-1/64	1/32-3/64	1/64-1/32	1/32-1/8[(2)]	1/32-1/16[(2)]	-	-
CB2	L1	1/8	3/32	1/8-3/8	1/8-3/16	1/4-3/8	3/16-1/4	-	-
	L2	1/32-3/32	1/32	1/16-1/4	1/16-1/8	1/16-1/4	3/32-3/16	-	-
	L3	1/32-1/16	1/32-1/16	1/8-3/16	3/32-1/8	1/8-1[(2)]	spalling[(2)]	-	-
CB3	L1	3/32-1/8	1/32-1/16	3/16	1/16	-	-		
	L2	1/32-1/16	1/64-1/32	1/16-3/32	1/16	-	-		
	L3	1/32-1/16	1/64-1/32	1/16-3/32	1/16-3/32	-[(2)]	-[(2)]		
CB4	L1	1/32-1/8	1/32-1/16	3/16-1/8	1/16-3/32	1/8-1/4	3/32-1/8	1/4	1/8-3/16
	L2	1/64-1/16	1/100-1/64	1/64-1/16	1/32-1/16	3/32-1/8	1/16	1/8	3/32
	L3	1/100-1/64	4/1000	1/64-1/32	1/100-1/64	1/32-1/16	1/64-1/32	1/32-3/32	1/32-1/16
CB5	L1	3/32	1.5/32	1/8-5/32	1/16	3/16-1/4	1/16	-	-
	L2	1/64-1/32	1/100-1/64	1/64-3/64	1/64-1/32	1/32-3/32	1/32-3/64	-	-
	L3	1/64-1/16	1/100-1/32	1/32-1/16	1/64-3/64	1/16-1/4[(2)]	1/32-3/32[(2)]	-	-
CB6	L1	3/16-5/16	3/16	1/32-1/2	1/4-3/8	3/8-11/16	3/8-9/16	5/8-1	5/8-14/16
	L2	0-1/64	0-1/100	0-1/32	0-1/64	0-1/32	0-1/64	0-1/16	0-1/32
	L3	1/100-1/64	4/1000	1/64	1/100	1/64	1/100	1/32-3/64	1/64
CB7	L1	3/32-1/8	1/16	3/16	1/8-3/16	-	-	-	-
	L2	1/100-1/16	1/250-1/32	1/64-1/8	1/100-3/32	-	-	-	-
	L3	1/100-1/16	1/250-1/32	1/32-1/16	1/100-1/16[(2)]	-	-	-	-
CB8	L1	3/32-1/8	1/16	3/16	1/16-1/8	3/16	-	-	-
	L2	1/100-1/16	1/100-1/32	1/32-3/32	1/64-1/16	3/32-1/8	-	-	-
	L3	1/100-1/16	1/100-1/32	1/32-3/32	1/64-1/16[(2)]	1/64-3/16[(2)]	-	-	-
CB24 F-RC[(3)]	L1	3/10	-	1/2	-	-	-	1/2	-
	L2	1/12	-	1/8	-	-	-	3/8	-
	L3	1/100	-	1/64	-	-	-	1/16	-
SRC1[(4)]	L1	1/2	-	5/16-3/8	3/16	3/8-1.25	5/16-1.0	1.0-2.0	1.0-2.0

Note: All measurements are in inches. [1 in. = 25.4 mm]

(1) L1 = cracks at the interfaces of beam and end blocks (slip/extension cracks), L2 = flexural cracks within distance ***h*** from interfaces, and L3 = Diagonal tension (shear) cracks within distance ***h*** from interfaces;

(2) Concrete in the web crushed during the second cycle

(3) Reported by Naish et al. (2013).

(4) Reported by Motter et al. (2017).

(*a*) 2% (*b*) 3% (*c*) 4%

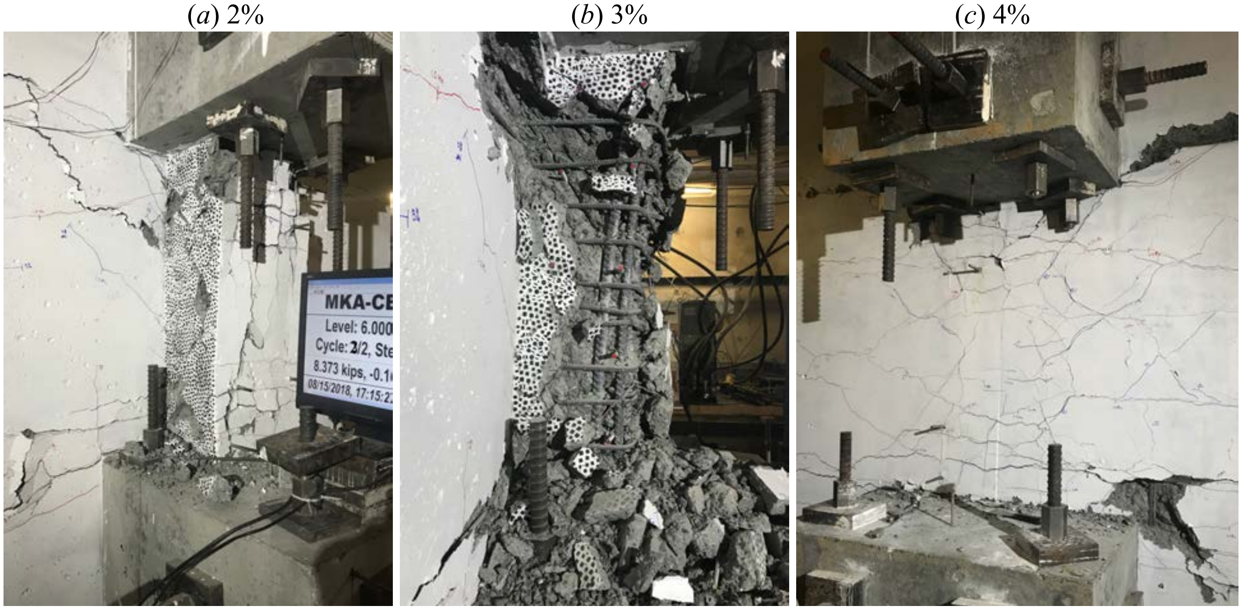

(*d*) 6% (*e*) 8%–southeast view (*f*) 8%–West view

Figure 6-1. Cracking and damage condition of CB1 at various rotation demands during the seismic loading protocol.

(*a*) 2% (*b*) 3% (*c*) 4%

(*d*) 6% (*e*) 8%–East view (*f*) 8%–West view

Figure 6-2. Cracking and damage condition of CB5 at various rotation demands during the seismic loading protocol.

6.2.3. CB2, CB3, CB7, and CB8

CB2, CB7, and CB8 were identical RC coupling beams with conventional reinforcement, standard detailing, and l_n/h of 3.67 but were subjected to different wind loading protocols (

Table 2-7) prior to the seismic loading protocol. CB3 was also identical to the aforementioned beams, except that CB3 had no floor slab. The damage states of the beams at various chord rotation demands are shown in **Figure 6-3** through **Figure 6-6**. These figures, along with **Table 6-1**, indicate that the four beams generally had similar cracking and damage characteristics during the seismic loading protocol and had the same failure mode at significant strength loss. Since the shear demand associated with the development of probable moment strength ($V_{@Mpr}/b_w d$ = $7.97\sqrt{f_c'(psi)}$ [$0.66\sqrt{f_c'(MPa)}$] for CB2, CB7, and CB8, and = $7.17\sqrt{f_c'(psi)}$ [$0.60\sqrt{f_c'(MPa)}$] for CB3) was equal to, or slightly greater than, the shear strength ($V_n/b_w d$ = $7.29\sqrt{f_c'(psi)}$ [$0.61\sqrt{f_c'(MPa)}$]), damage appeared to concentrate along diagonal (shear) cracks as the rotation demands gradually increased. At 4% rotation, lateral strength loss initiated during the first cycle for CB7 and during the second cycle for the other beams as a result of web crushing and sliding along a plane in the bottom plastic hinge region, as shown in **Figure 6-7.** Once lateral strength degradation initiated, the damage concentrated in the bottom plastic hinge region, as shown in **Figure 6-3** through **Figure 6-6**. During the first cycle to 6% rotation, significant concrete crushing and spalling occurred in the web, which led to significant lateral strength degradation, i.e., a drop of 40% to 70% from peak strength. For all beams, opened hooks on crossties were observed at 6% rotation; however, no buckling or fracture of beam longitudinal bars was observed, except the slab bars closest to the beam centerline fractured during loading to 6% rotation. At rotation demand of 9%, the residual strength of the beams ranged from 15% to 25% of the peak lateral strength. The failure mode of all beams was flexure-shear (i.e., yielding in flexure first and then failing in shear).

(*a*) 2% (*b*) 3% (*c*) 4%

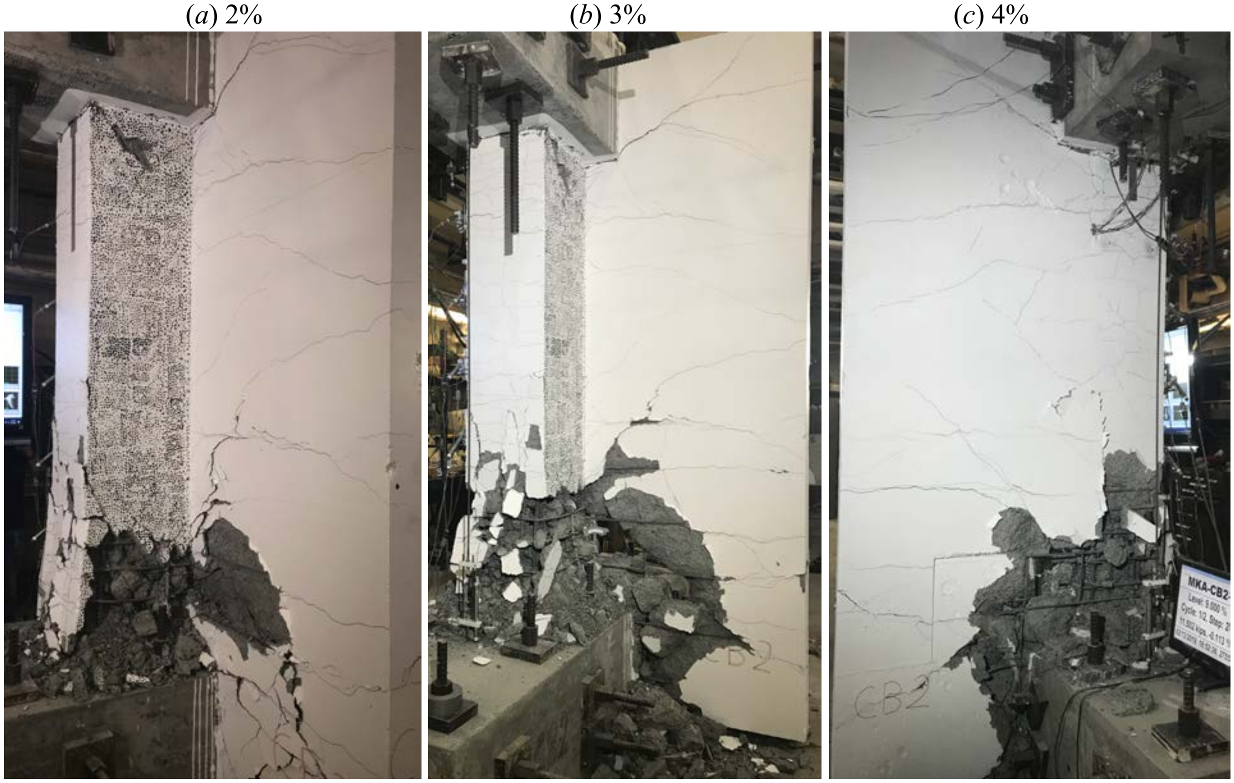

(*d*) 6% (*e*) 9% –Southwest view (*f*) 9%–Southeast view

Figure 6-3. Cracking and damage condition of CB2 at various rotation demands during the seismic loading protocol.

(*a*) 2% (*b*) 3% (*c*) 4% (*d*) 6%

Figure 6-4. Cracking and damage condition of CB3 at various rotation demands during the seismic loading protocol.

(*a*) 2% (*b*) 3% (*c*) 4%

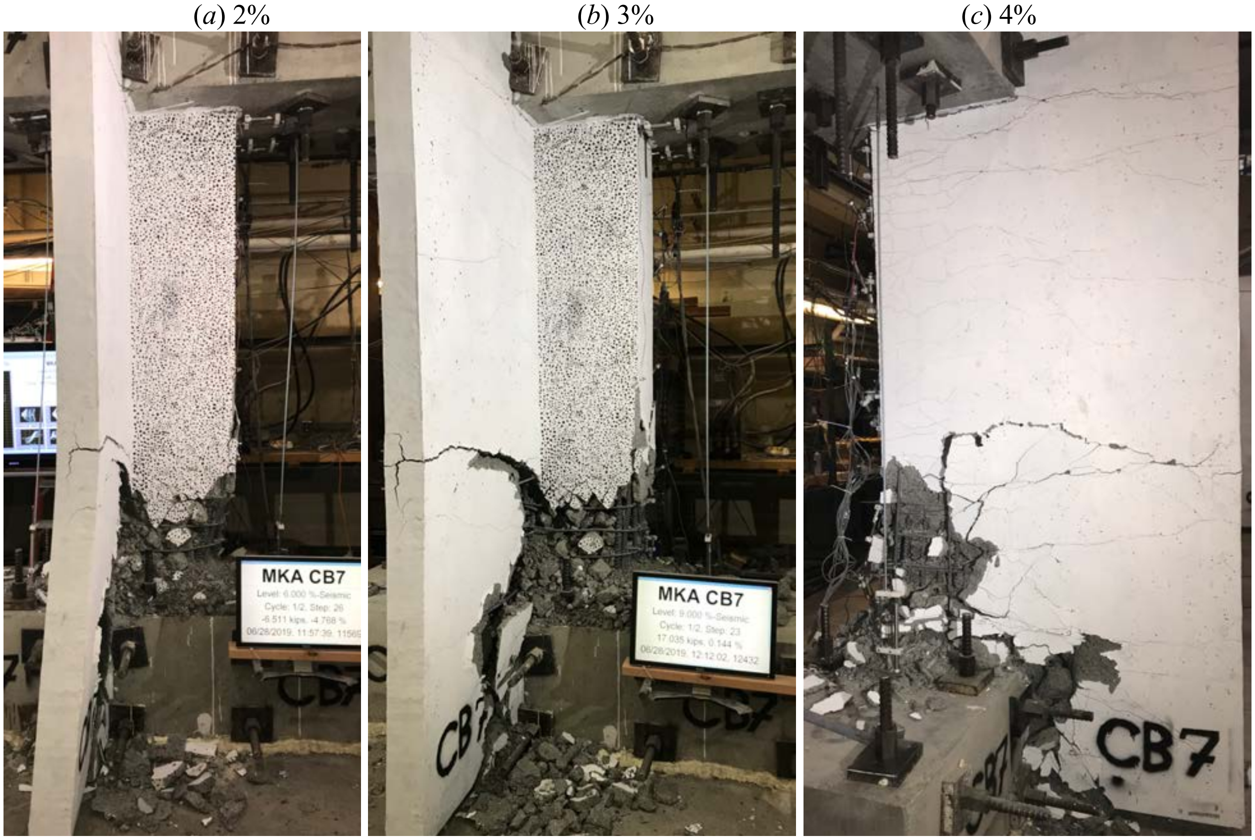

(*d*) 6% (*e*) 9%–Southeast view (*f*) 9%–Southwest view

Figure 6-5. Cracking and damage condition of CB7 at various rotation demands during the seismic loading protocol.

(*a*) 2% (*b*) 3% (*c*) 4%

(*d*) 6% (*e*) 9%–Northeast view (*f*) 9%–West view

Figure 6-6. Cracking and damage condition of CB8 at various rotation demands during the seismic loading protocol.

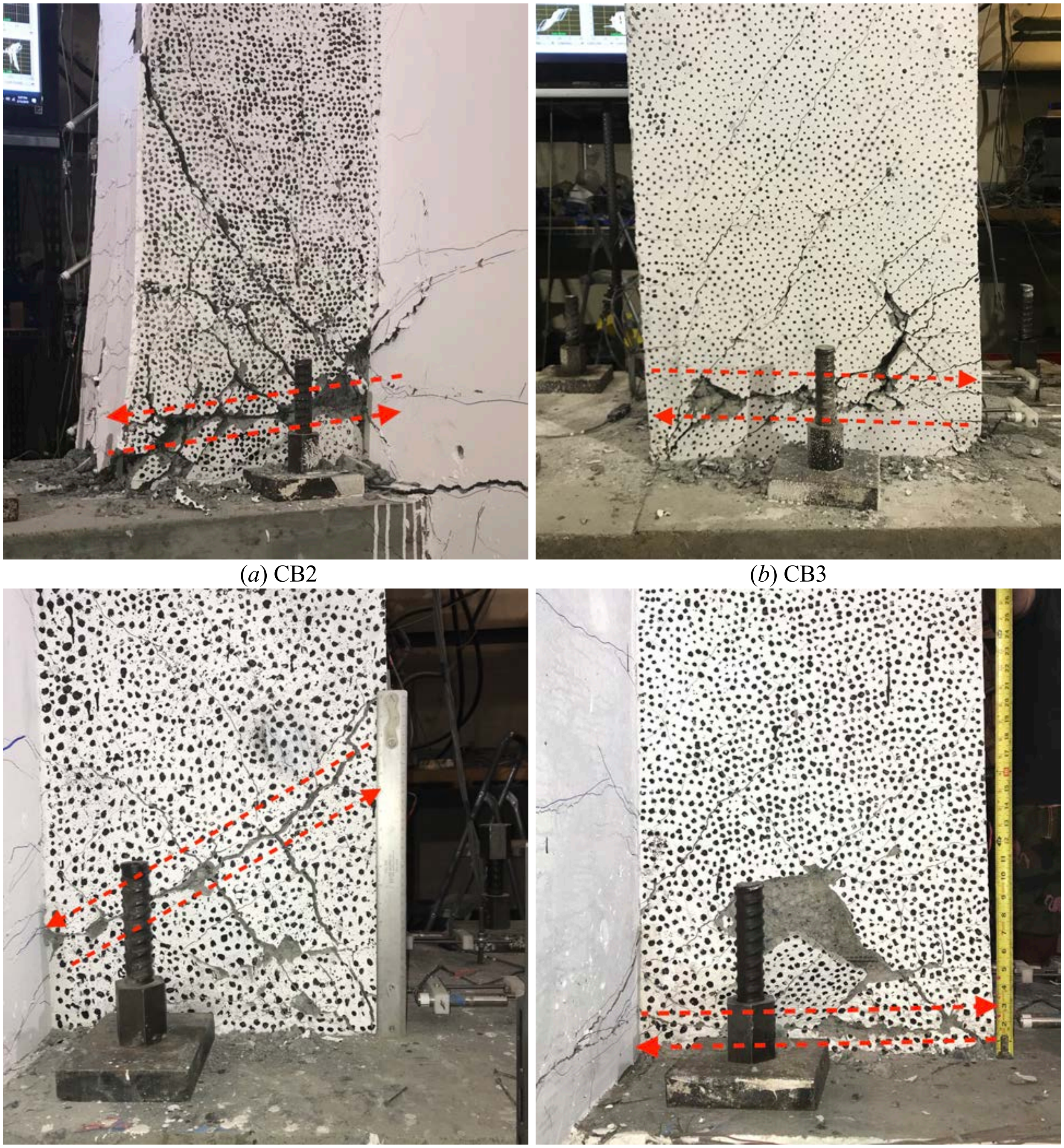

(*a*) CB2 (*b*) CB3 (*c*) CB7 (*d*) CB8

Figure 6-7. Close-up pictures of the bottom hinge region showing a sliding plane at 4% rotation.

6.2.4. CB4

CB4 was an RC coupling beam with diagonal reinforcement, seismic detailing, and l_n/h of 2.5, and was subjected to the wind loading protocol shown in **Figure 2-21** prior to seismic testing. **Figure 6-8** and **Table 6-1** show the damage states and crack widths of CB4 at various chord rotation demands, respectively. Overall, the slip/extension cracks at the interfaces were the largest, whereas diagonal shear cracks were the smallest. During loading to 3% rotation, small, thin pieces of concrete (not as thick as the concrete cover) spalled at the interfaces on the side of the web (**Figure 6-8** (***b***)), and in the subsequent cycles at 4% rotation, concrete cover spalled over a distance of about 8 in. (200 mm) in both plastic hinge regions at the extreme fiber of the web (**Figure 6-8** (***c***)). Concrete in the plastic hinge regions deteriorated gradually as the rotation demands increased to 8%, with no significant lateral strength degradation. During the first cycle to 10% rotation, buckling of diagonal bars were observed, which resulted in about a 10% lateral strength loss. During the second cycle, two diagonal bars fractured while loading in the positive direction. During the two cycles to 12% rotation, multiple other diagonal bars fractured, and hooks on crossties in the plastic hinge regions opened up (**Figure 6-8** (***i***)). As a result, the lateral strength dropped significantly at 12% rotation due to concrete crushing and diagonal bar buckling and fracture. **Figure 6-8** (***g***) through (***i***) show the state of the beam at the end of testing.

Fracture of skin reinforcement [i.e., No. 3 (d_b= 10 mm) horizontal cage bars along the longitudinal axis of the beam], which were embedded 4 in. (100 mm) into the walls (end blocks) as shown in **Figure 2-4**, was observed during loading to 8% rotation. Although the strength contribution of the skin/horizontal cage reinforcement is ignored according to ACI 318-14 §18.10.7.4 (because the embedment is limited to less than the bar development length), the observed fractures suggest that this reinforcement contributed to the lateral strength of the beam. For No. 3 (d_b= 10 mm) bars, a development length of 7.5 in. (190 mm) is required in accordance with ACI 318-14 §25.4.2.4, which is almost twice the length provided [i.e., 4 in. (100 mm)], and yet the reinforcement yielded and fractured. It is noted that these bars were embedded in heavily reinforced, post-tensioned end blocks that, unlike boundary elements of coupled walls in a real building, did not experience cracking and tensile strains at locations where these bars were embedded.

For comparative purposes, cracking and damage information of CB24F-RC tested by Naish et al. (2013) are presented herein. As noted previously in **Table 2-1** and **Figure 2-4**, CB24F-RC is essentially identical to CB4. Comparing **Figure 6-8** with **Figure 6-9**, along with crack widths reported in **Table 6-1**, reveal that the cracking and damage of CB24F-RC is practically the same as that of CB4, and that the prior nonlinear wind demands did not significantly affect the cracking and damage of CB4.

(*a*) 2% (*b*) 3% (*c*) 4%

(*d*) 6% (*e*) 8% (*f*) 10%

(*g*) 12% –East south view (*h*) 12% – West view (*i*) 12% –Close-up of hinge region

Figure 6-8. Cracking and damage condition of CB4 at various rotation demands during the seismic loading protocol.

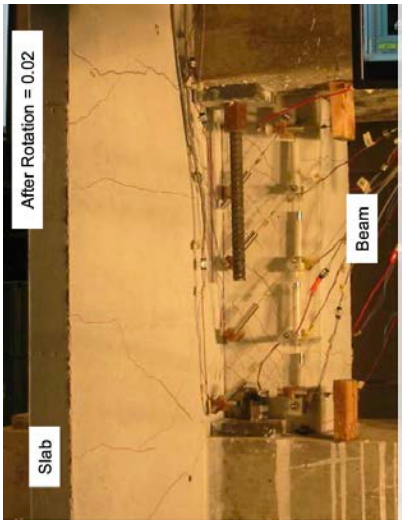

(*a*) 2%

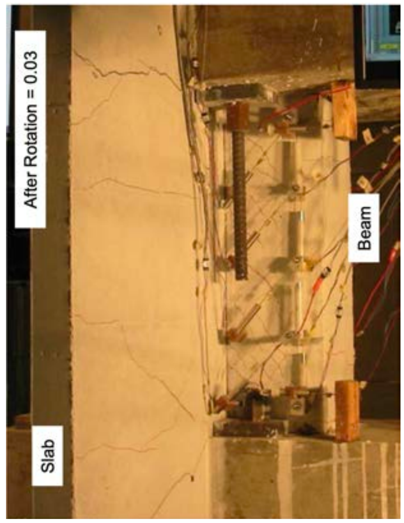

(*b*) 3%

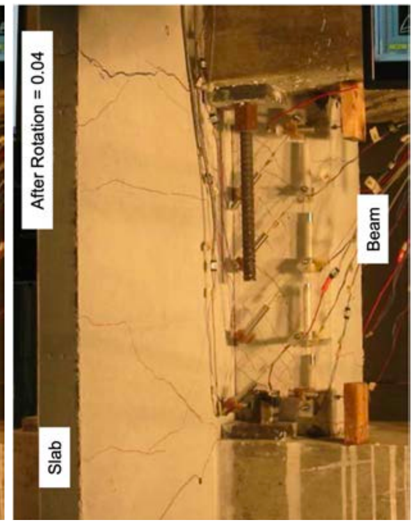

(*c*) 4%

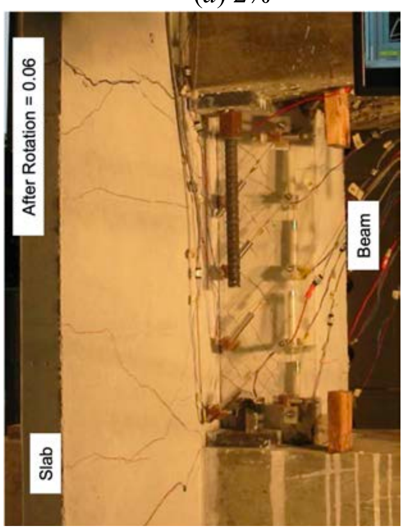

(*d*) 6%

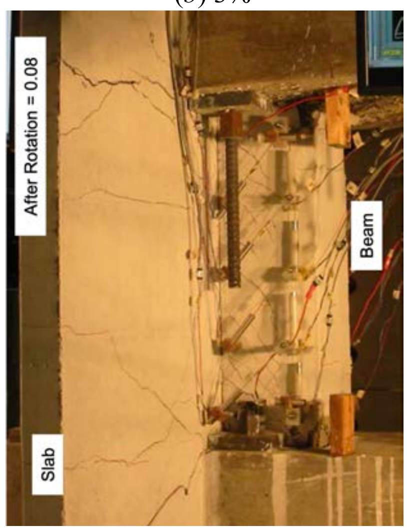

(*e*) 8%

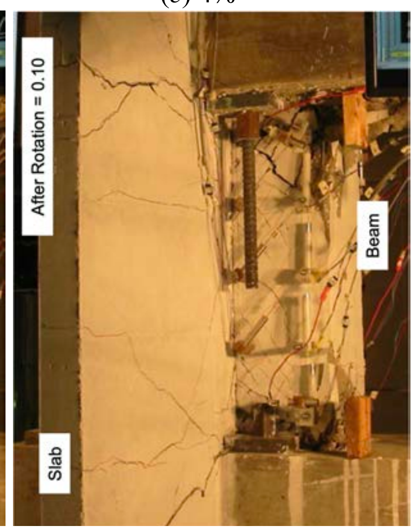

(*f*) 10%

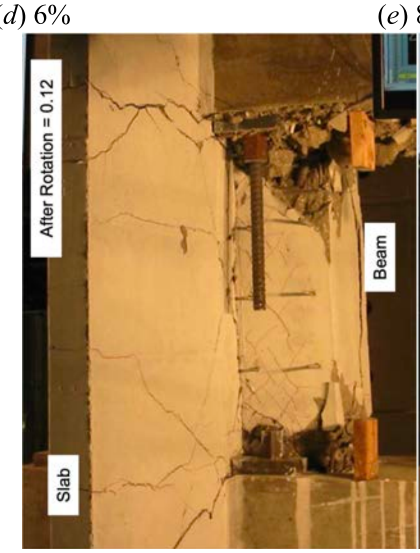

(*g*) 12%

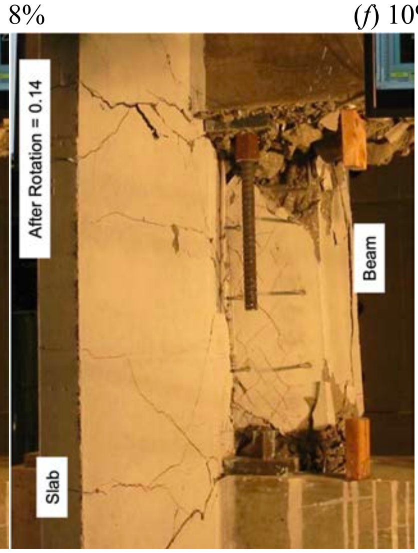

(*h*) 14%

Figure 6-9. Cracking and damage condition of CB24F-RC tested by Naish et al. (2013) at various rotation demands.

6.2.5. CB6

CB6 was an SRC coupling beam with standard detailing (conforming to AISC 360-10 and ACI 318-19 Chapter 9), capacity-designed embedment, and l_n/h of 2.5. The beam was subjected to the wind loading protocol shown in **Figure 2-22** (***a***) prior to seismic testing. **Figure 6-10**, **Figure 6-11**, and **Table 6-1** show the damage states and crack widths of CB6 at various chord rotation demands, respectively, and demonstrate that the damage concentrated primarily at the beam-wall interfaces as only hairline or minor cracks (flexure and shear) were observed elsewhere within the beam span. As the rotation demands gradually increased to 6%, the interface cracks, which extended across the entire slab width, became significantly wider, but minimal spalling occurred, which was limited to the walls rather than the beam itself, as seen in **Figure 6-10** and **Figure 6-11**. After completing two cycles at 6% rotation, significant gapping [approaching 1 in. (25 mm)] at the beam-wall interfaces was evident; however, there was no significant spalling or damage in the embedment regions or the beam itself (**Figure 6-10** (***d***); **Figure 6-11**). As the rotation demand increased, the gap at the beam-wall interface significantly increased such that the steel section could be seen. During the first cycle at 12% rotation, the residual interface gaps were about 1.2 in (30 mm) wide, and two slab bars, spanning along the beam length and closest to the beam centerline, fractured after the concrete cover spalled over the entire beam length (**Figure 6-10** (***i***)). Although, at 12% rotation, the lateral strength had only reduced by 8% and 18% in the positive and negative directions of loading, respectively, and damage was still limited to the interface cracks (**Figure 6-11** (***c***)), and the test was concluded. At 12% rotation, the lateral strength of the beam roughly equaled to the plastic strength of steel section alone [i.e., $V = 2(M_p = f_{y,test}\, z_x)/l_n$) and strength and cyclic degradation occurring beyond 12% rotation was not deemed important, given that rotation demands on coupling beams during MCE level shaking do not typically exceed 6%

rotation. It is noted that CB6, unlike the RC beams, did not form plastic hinges over a distance of roughly *h* from the beam-wall interfaces. Instead, almost all the nonlinearity was localized at the beam-wall interfaces through one large slip/extension crack. Further, similar to CB4, the No. 3 cage/skin reinforcement along the longitudinal axis of the beam fractured at 8% rotation, even though they were embedded only 4 in. (100 mm) into the walls (end blocks) as shown in **Figure 2-6**. See section **6.2.4** for further discussion related to this topic.

For the purpose of comparison, cracking and damage information of an SRC coupling beam (denoted as SRC1) reported by Motter et al. (2017) are presented. SRC1 is similar to CB6 as both beams have adequate embedment length of the steel sections, i.e., the connection strength is designed to exceed the connection demands associated with developing the shear and flexural strengths of the beam (**Table 2-1**). **Table 6-1** and **Figure 6-12** indicate that the observed crack widths and damage of CB6 are similar to that of SRC1 reported by Motter et al. (2017), except that the interface cracks of SRC1 were significantly larger because the steel section of SRC1 was embedded in a wall boundary element that was subjected to reversed cyclic lateral loading and overturning moment, as opposed to a post-tensioned block in case of CB6. In general, the prior nonlinear wind demands did not significantly impact the degree of cracking and observed damage of CB6.

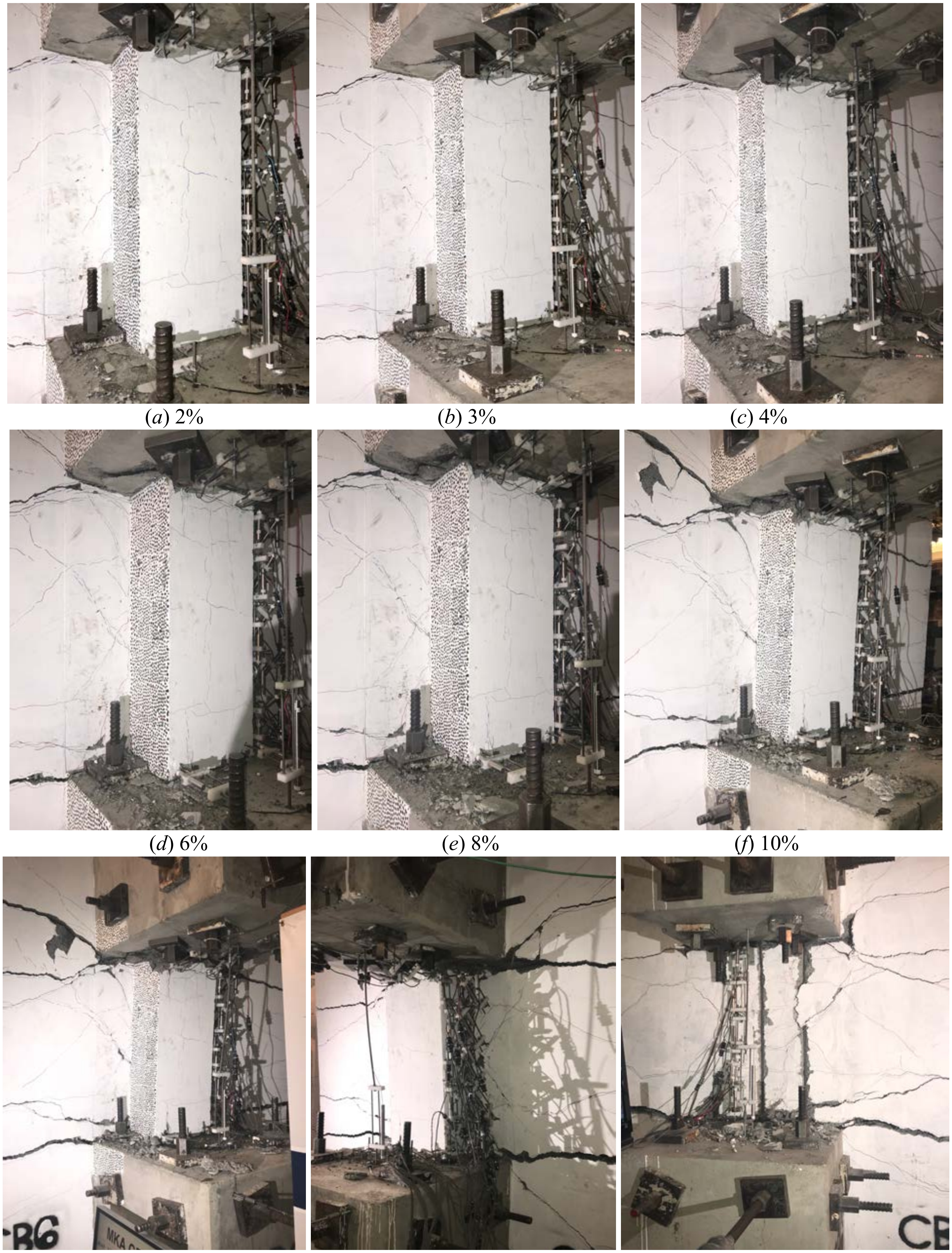

(*a*) 2% (*b*) 3% (*c*) 4%

(*d*) 6% (*e*) 8% (*f*) 10%

(*g*) 12% –East south view (*h*) 12% –East north view (*i*) 12% –West view

Figure 6-10. Cracking and damage condition of CB6 at various rotation demands.

(*a*) After applying 6% rotation demand

(*b*) After applying 8% rotation demand

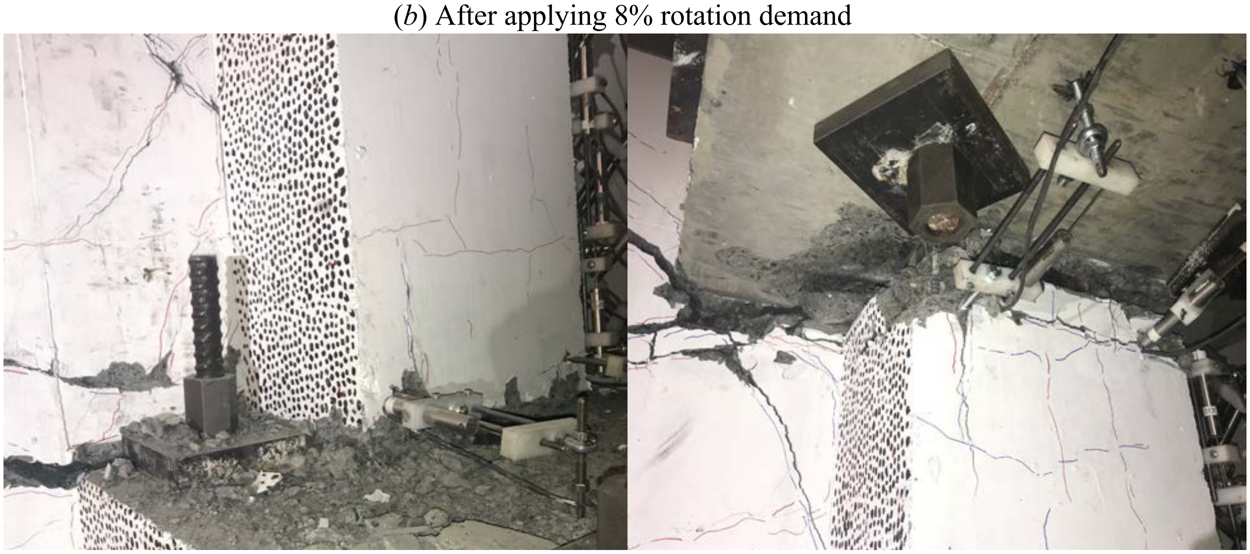

(*c*) After applying 12% rotation demand

Figure 6-11. Close-up pictures of damage condition at the beam-wall interfaces of CB4.

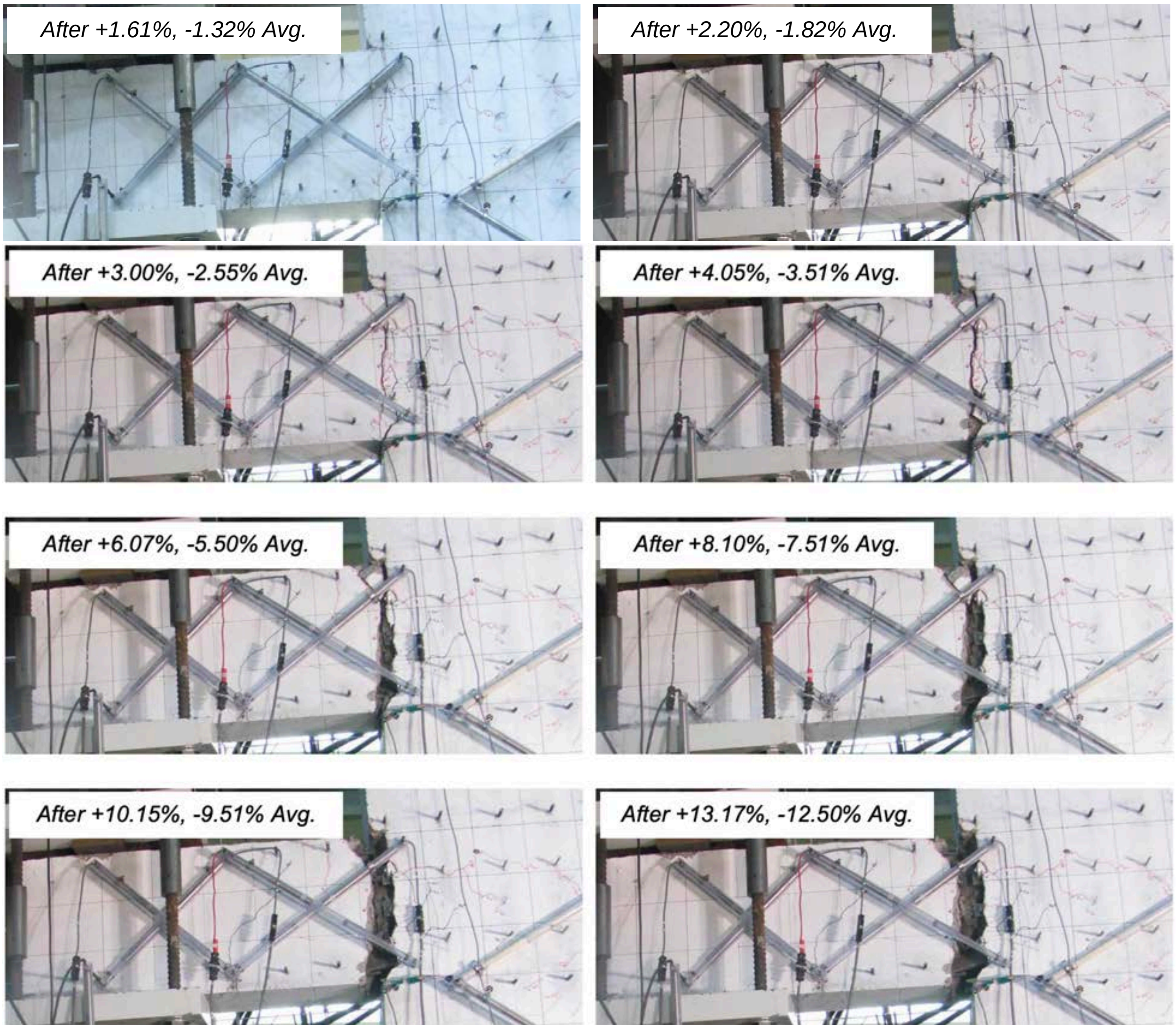

Figure 6-12. Cracking and damage condition of SRC1 tested by Motter et al. (2017) at various rotation demands.

6.3. Load-Deformation Response

Load-deformation response (or hysteretic behavior) is one of the primary means used to evaluate the seismic performance of a lateral force-resisting element. Favorable load-deformation responses are characterized by predictable strength and stiffness values with large ductility and minimal hysteretic pinching. Favorable behavior also is characterized by minimal cyclic and strength degradation, noting that strength degradation refers to a reduction in strength due to an increase in imposed displacement demands, whereas cyclic degradation refers to a reduction in strength (due to a reduction in stiffness) between subsequent cycles at roughly equal imposed displacement demands.

Figure 6-13 presents the load-rotation responses of the test beams during the seismic loading protocol, whereas **Figure 6-14** presents the load-rotation responses of the test beams during both the seismic and wind loading protocols. Comparing **Figure 6-13** with **Figure 6-14** shows that, as a result of the prior wind loading protocols, the initial stiffness of the beams was significantly reduced, as will be discussed in a subsequent section. Two strength-based limit states are indicated on **Figure 6-13** and **Figure 6-14**: one for nominal shear strength (V_n) and the other for shear strength associated with the development of probable moment strength ($V_{@Mpr}$), as reported in **Table 2-1**. The results presented in **Figure 6-13** demonstrate that the maximum strength obtained during the seismic loading protocol (V_{peak}) reached or exceeded the calculated $V_{@Mpr}$, which was higher than V_n for all beams, except CB3, where V_n was roughly equal to $V_{@Mpr}$. The results presented in **Figure 6-14** indicate that the V_{peak} attained during the seismic loading protocol was higher than that attained during the wind load protocol ($V_{peak,w}$), except for CB6 (SRC beam), where no additional strength gain was observed (**Figure 6-14** (***f***)). This is because, at the higher ductility demands applied during the seismic loading protocol, additional strain hardening of reinforcement occurred for the RC coupling beams. It is noted that additional, but minor, strength gain might be expected if the conventionally reinforced coupling beams were pure flexure-controlled as opposed to flexure-shear-controlled due to additional strain hardening of longitudinal reinforcement prior to strength deterioration due to shear cracking. **Figure 6-13** (***d***) demonstrates that use of ACI 318-19 Equation 18.10.7.4 to calculate nominal shear strength (V_n) of diagonally reinforced coupling beams results in significant underestimation of beam strength, and that performing sectional analysis of the cross-section provides better estimates of beam strength (i.e., $V_{peak} \approx V_{@Mpr}$). This is because ACI 318-19 Equation 18.10.7.4 is based on the strength provided by the diagonal reinforcement only, i.e., the strength is not influenced by the slab or the slab reinforcement or by the horizontal No. 3 cage/skin bars (which despite being embedded only 4 in. (100 mm) into the walls, contributed to the lateral strength as previously noted). This is consistent with results reported by Naish et al (2013), where the experimentally obtained strengths (V_{peak}) ranged from 1.55 to 1.17 times V_n from ACI 318-19 Equation 18.10.7.4, depending on whether the beam tested included a PT slab, a RC slab, or no slab. Similarly, **Figure 6-13** (***f***) shows that the requirements of AISC 360-10 §14.1 provide a low estimate of nominal shear strength of SRC coupling beams. An estimate of shear strength as the sum of contributions from concrete, steel section, and transverse reinforcement, which is not allowed by AISC 360-10 §14.1, would provide a better, but still conservative, estimate of shear strength. Results presented in **Figure 6-13** (***f***) demonstrate that the probable moment strength calculated as the plastic strength of the steel section with the consideration of presence of concrete ($V_{@Mpr}$) would yield a good estimate of beam flexural strength.

Prior research (e.g., Marder, 2018) has shown that flexure-controlled beams subjected to prior nonlinear seismic demands (smaller than deformation capacity corresponding to initiation of lateral strength loss) could attain additional strength when the beam is retested after a time period on the order of at least few months as a result of strain ageing of the steel bars, if the bars include insufficient amounts of specific alloying metals such as Titanium or Vanadium, which tends to be the case for some low strength bars (e.g., Grade 300 MPa) (Loporcaro, 2017; Momtahan et al., 2008; Van Rooyen, 1986; Pussegoda, 1978; Rashid, 1976). However, the beams tested herein did not experience rebar strain ageing because the time between the conclusion of the wind test and the start of the seismic test of each beam did not exceed two days (not sufficient time to allow for rebar strain aging to occur). Therefore, strength gain due to strain ageing of reinforcement should be considered when evaluating strength of coupling beams (and other components) that have experienced nonlinear demands in the past, given that the evaluation is performed at least a few months after the nonlinear demands occurred. It is also noted that strain ageing (Loporcaro, 2016) is mostly an issue for lower grade (e.g., Grade 300 MPa) bars, and would not be expected to significantly impact results of these test specimens, which utilized Grade 60 (414 MPa) rebar (Zhao and Ghannoum, 2016).

Unlike the diagonally reinforced and SRC beams (i.e., CB4 and CB6), the conventionally reinforced beams displayed significant hysteretic pinching throughout the loading protocol and lateral strength loss beyond 4% rotation. The residual strengths of the conventionally reinforced beams was roughly 25% of the peak strength at 8% to 9% rotation demand for with l_n/h of 2.5 (i.e., CB1 and CB5) and ranged from 15% to 25% of the peak strength at 6% rotation demand for beams with l_n/h of 3.67 (i.e., CB2, CB3, CB7, and CB8). CB4 had a relatively stable behavior up to 10% rotation demand, beyond which the beam experienced significant strength degradation as a result of concrete crushing and buckling and fracture of diagonal bars. Although the test of CB4 was stopped at 12% rotation due to a limitation associated with the test setup, the residual strength at 12% rotation was about 20% of the peak strength. CB6 displayed a hysteretic response characterized by large ductility with minimal strength degradation and cyclic degradation throughout the loading history. Although the lateral strength had only dropped by 8% and 18% from the peak strength in the positive and negative directions of loading at 12% rotation, respectively, the test was concluded because the lateral strength of the beam was close to the plastic strength of steel section alone [i.e., $V_{@Mp} = 2(f_{y,test}\, z_x)/l_n$ = 143 kips (635 kN)], and the strength degradation and cyclic degradation that might occur at rotations exceeding 12% were not considered important, given that the rotation demands on coupling beams during MCE level shaking do not typically exceed 6%.

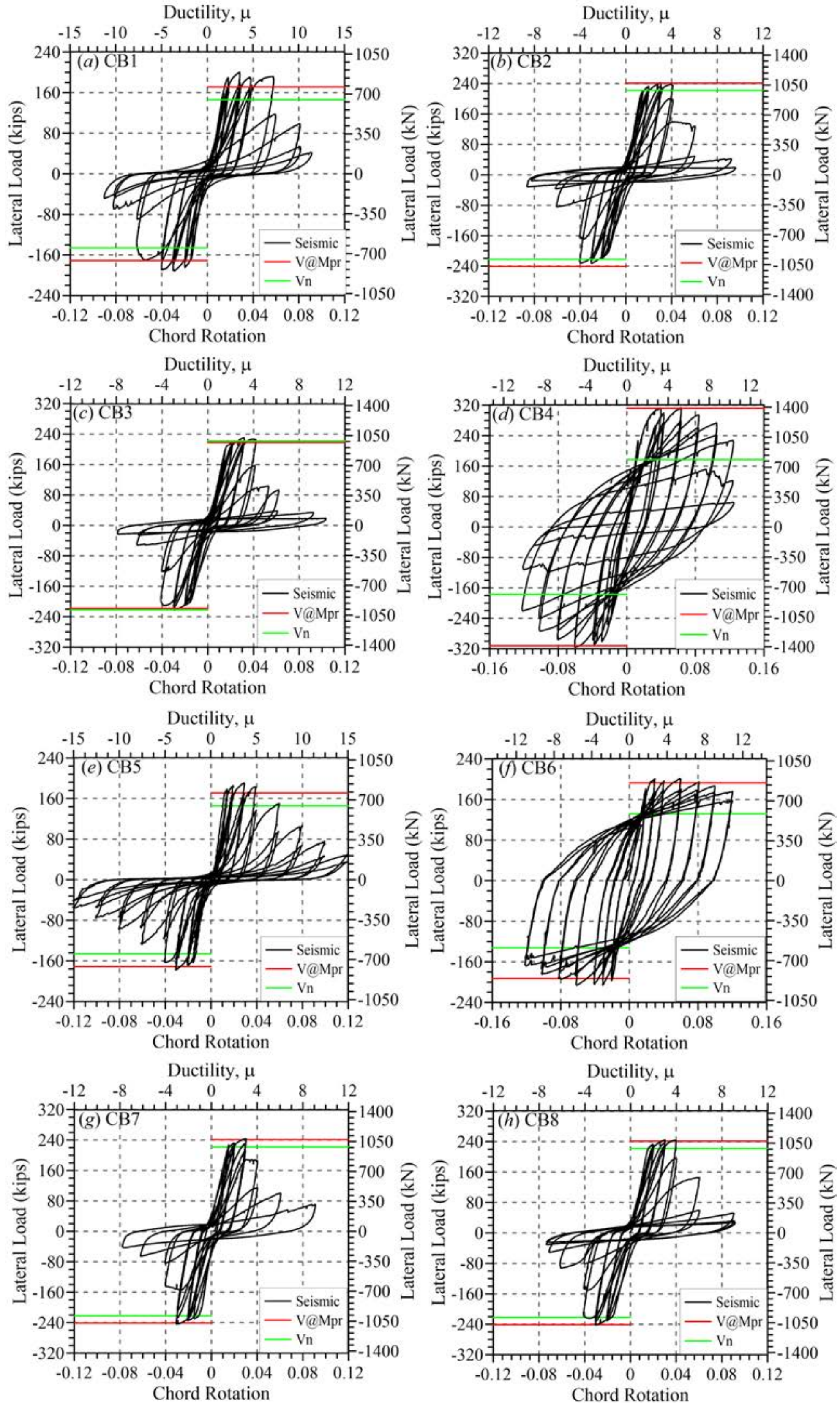

Figure 6-13. Load-chord rotation responses for the seismic loading protocol.

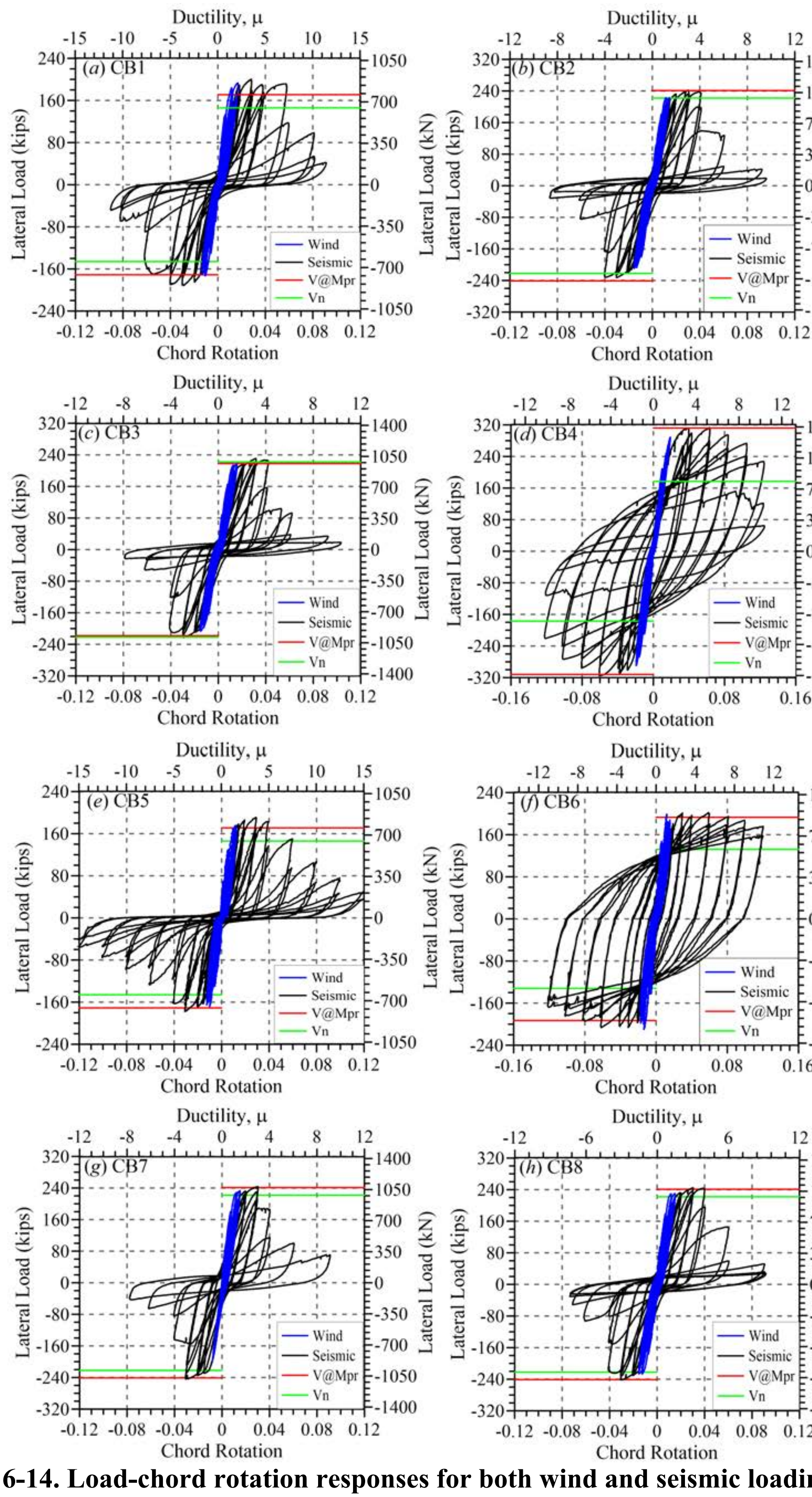

Figure 6-14. Load-chord rotation responses for both wind and seismic loading protocols.

6.4. Lateral Stiffness

6.4.1. Secant Stiffness

The secant stiffness values of the beams (defined as E_cI_s) corresponding to the peak lateral load and total rotation for each cycle during the seismic loading protocol were computed and normalized by the gross-section stiffness (E_cI_g), as shown in **Figure 6-15**. Total chord rotations include deformation contributions associated with flexure (curvature), slip/extension, shear, and sliding. The contributions of each of these sources to total chord rotation are discussed later in section **6.6**. **Figure 6-15** demonstrates that secant stiffness values significantly reduce as rotation demands increase, and that the beams with l_n/h of 3.67 have overall larger secant stiffness values than beams with l_n/h of 2.5 prior to initiation of lateral strength loss (up to ~4% rotation demand); this trend is well established in the literature for coupling beams tested under seismic loading protocols. CB7 possesses slightly larger secant stiffness values than the other companion beams with l_n/h of 3.67 prior to reaching 4% rotation due to the fact that CB7 had less cracking and yielding in the negative direction of loading during the wind loading protocol because of the non-zero mean component. Additionally, CB5 also had slightly larger stiffness values than its companion beam, CB1, which could be ascribed to the fact that CB1 was, as noted previously, unintentionally pushed to higher peak ductility demands than CB5 during the wind loading protocol (**Figure 3-19** (***a***)). CB4 (diagonally reinforced and seismically detailed beam) and CB6 (SRC beam) have stiffness values that are practically the same as those of CB1 (conventionally reinforced and non-seismically detailed beams).

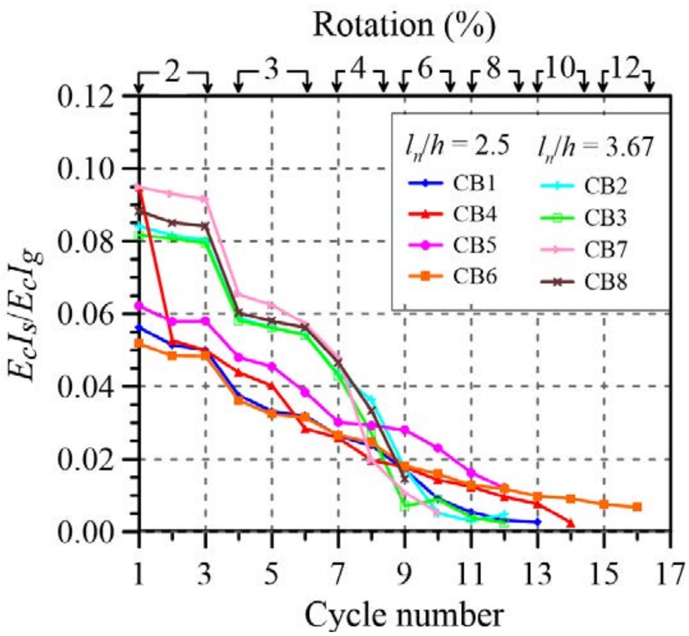

Figure 6-15. Averaged secant stiffness values for each loading stage.

6.4.2. Residual Effective Stiffness

The post-wind (residual) effective stiffness values [$(E_cI_{eff})_{residual}$] of the beams (i.e., initial effective stiffness values obtained from the seismic load-deformation response) were calculated using the total chord rotation and normalized by the gross section stiffness (E_cI_g). The $(E_cI_{eff})_{residual}$ values are compared with the initial effective stiffness values obtained from the wind load-deformation response [$(E_cI_{eff})_{initial}$] in **Table 6-2**. The $(E_cI_{eff})_{initial}$ values are the same values presented in **Section 3.4**; the subscript "initial" is used here to distinguish them from the post-wind (residual) values [$(E_cI_{eff})_{residual}$]. The values in **Table 6-2** demonstrate that the effective stiffness of the beams was significantly reduced as a result of the prior wind loading protocol, with the reduction ranging from 10% to 63% depending on the maximum prior ductility demand applied. CB7 possesses larger $(E_cI_{eff})_{initial}$ values than the other beams with l_n/h of 3.67 because this beam, as noted previously, was not pushed to yield in the negative direction of loading during the wind loading protocol, resulting in less cracking and yielding and thus higher stiffness.

Figure 6-16 compares the $(E_cI_{eff})_{residual}/E_cI_g$ results with the initial effective stiffness data of diagonally and conventionally reinforced coupling beams tested under only seismic loading protocols and the flexural effective stiffness relationship given by LATBSDC (2017) and TBI (2017) for performance-based seismic design ($E_cI_{eff}/E_cI_g = 0.07\ l_n/h \leq 0.30$). **Figure 6-16** indicates that, similar to secant stiffness, effective stiffness is significantly impacted by l_n/h, and that the $(E_cI_{eff})_{residual}$ values of the beams pushed to yield in both directions of loading are smaller than the mean trends of the seismically tested coupling beams as a result of the prior cracking and yielding experienced during the wind loading protocols. This offset could have been larger because, except for few tests, the beams in the datasets did not include floor slabs, and the effective stiffness values were computed assuming perfect double curvature setups (i.e., the top block maintains zero rotation), refer to section **3.4** for further discussion on this topic. As was noted in section **3.4**, the relationship given by LATBSDC (2017) and TBI (2017) produces higher effective stiffness values because this relationship is for full-scale coupling beams with an estimate of the impact of adjacent floor slabs (out-of-plane stiffness and axial restraint) and walls (axial restraint) on coupling beam effective stiffness.

Table 6-2. Effective stiffness values of the beams during the seismic loading protocol.

Beam ID	l_n/h	Max. Prior Ductility Demand	$(E_cI_{eff})_{residual}/E_cI_g$	$(E_cI_{eff})_{residual}/(E_cI_{eff})_{initial}$
CB1	2.5	2.1	0.065	0.47
CB2	3.67	1.5	0.110	0.63
CB3	3.67	1.6	0.105	0.62
CB4	2.5	1.6	0.090	0.63
CB5	2.5	1.6	0.066	0.49
CB6	2.5	1.55	0.052	0.37
CB7 (+ve)	3.67	1.5	0.156	0.78
CB7 (-ve)	3.67	0.75	0.140	0.90
CB8	3.67	1.55	0.105	0.57

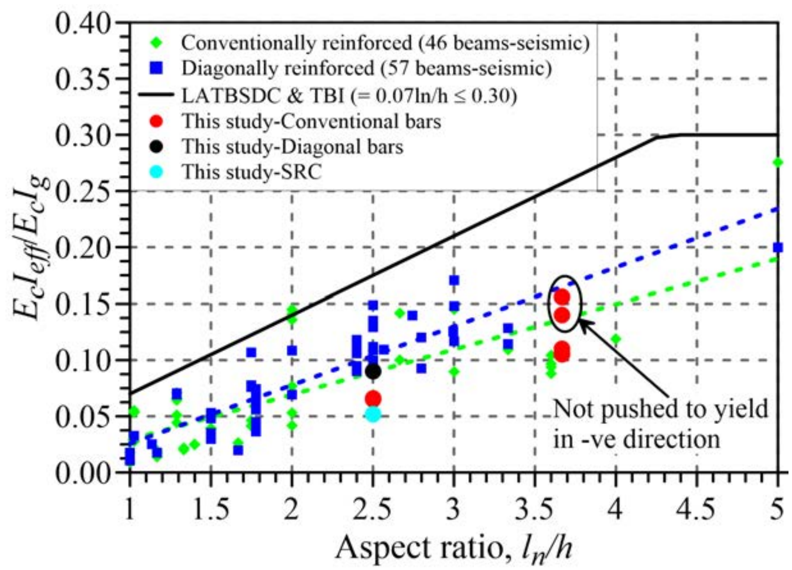

Figure 6-16. Normalized effective stiffness (E_cI_{eff}/E_cI_g) as a function of aspect ratio (l_n/h).

6.5. Axial Growth

As noted previously, no axial load or restraint was applied to the beams during testing. Axial load or restraint has been observed to impact axial growth, as well as crack widths, stiffness, strength, and deformation capacity, of coupling beams tested under seismic loading protocols (e.g., Naish et al., 2013; Motter et al., 2017; Poudel et al., 2018). **Figure 6-17** presents axial growth of the beams versus chord rotation and indicates that the RC coupling beams had similar accumulated axial growths up to 4% rotation (before lateral strength loss initiated), which ranges from 0.75% to 1.00% of the beam clear length (l_n). CB4 had an accumulated axial growth of about $0.03l_n$ at 12% rotation (**Figure 6-17** (***d***)), at which the beam experienced significant strength loss. CB6 (SRC beam) experienced axial growths greater than those of the RC beams for the same rotation demands; CB6 grew by about $0.016l_n$ [0.64 in (16 mm)] and $0.07l_n$ [2.8 in. (71 mm)] at rotation demands of 4% and 12%, respectively, as shown in **Figure 6-17** (***f***). This indicates that the interface slip/extension cracks were about 1.4 in. (35 mm) wide at 12% rotation, as the other cracks along the beam span were very small (**Table 6-1**). The significant outward ratcheting of the steel section observed during testing of CB6 may not appear problematic because in actual buildings axial restraining due to the adjacent coupled walls and floor slab exists, which can limit the axial growth of the beam and the gap opening at the beam-wall interfaces (Motter et al., 2017). However, this restraint might also lead to earlier concrete spalling and flange buckling during the seismic loading protocol.

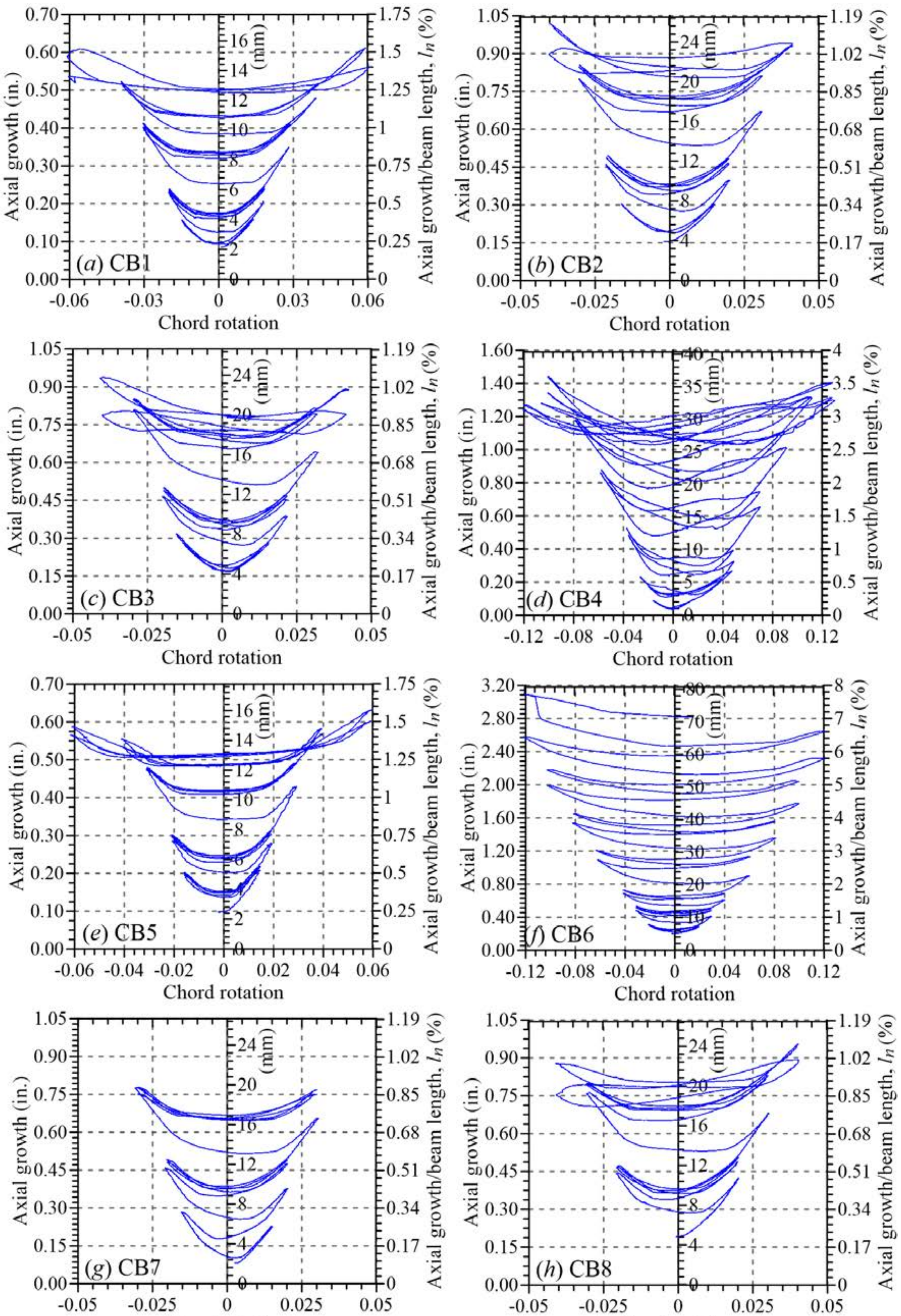

Figure 6-17. Axial growth of the beams during the seismic loading protocol.

6.6. Deformation Components

This section presents the contribution of various sources of deformation to the total chord rotation, which consist of deformations due to flexure (curvature), shear distortion, slip/extension from walls (end blocks), and sliding at the beam-wall interfaces, as was shown in **Figure 3-26**. Contribution of each deformation component to the total chord rotation at each level of rotation demand is shown in **Figure 6-18**. Details of how each of these quantities was determined are given in **Appendix F**. It can be noted from **Figure 6-18** that the summation of the rotations contributed by these local deformation components does not precisely add up to 100% of the total rotation measured globally, values range from 90% to 120%, because the measurements of these local deformations are affected by noise in the sensors, minor deformation or slippage in the LVDT mounting accessories, and assumptions used to calculate shear deformations (e.g., Massone and Wallace, 2004). Results plotted in **Figure 6-18** also show that, for all the conventionally reinforced coupling beams, deformations from bar slip/extension, flexure, and shear contributed significantly to the total rotations (ranging from 20% to 50%), with deformations contributed by bar slip/extension being the largest in most cases. It also was observed that rotations contributed by shear distortion increased as the number of cycles increased during the loading protocol. This is because, as the demands increased, diagonal shear crack widths increased more than flexural crack widths, which led the conventionally reinforced coupling beams to eventually fail in shear after flexural yielding. For CB4, the majority of the chord rotation was contributed by bar slip/extension (ranging from 45% to 68%), whereas the contributions due to flexure and shear are roughly of the same magnitude (ranging from 10% to 30%), especially beyond 3% rotation demand. In the case of CB6, the vast majority of the rotation was contributed by slip/extension cracks at the beam-wall interfaces (~ 80% to 90%), whereas contributions due to other sources were relatively small. This is because CB6, unlike the RC beams, did not form plastic hinges over a distance of roughly *h* from the beam-wall interfaces, and that the flexural and shear cracks within distance *h* from beam-wall interfaces were significantly smaller than the slip/extension cracks (**Table 6-1**). Thus, all the nonlinearity was localized at the beam-wall interfaces, as was seen in **Figure 6-10** and **Figure 6-11**.

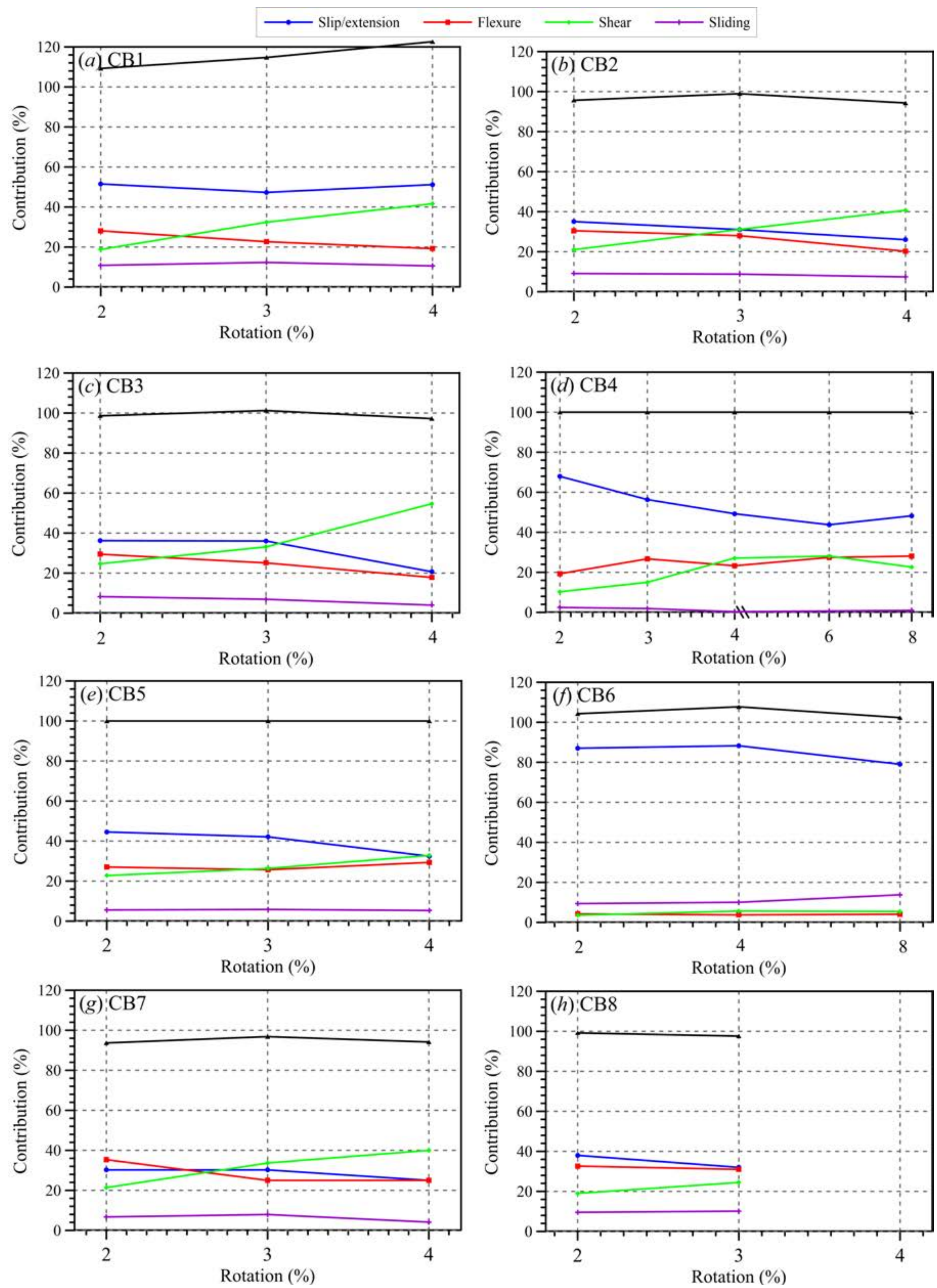

Figure 6-18. Contributions of various deformation components to total rotation. (Note: deformation contributed by bar slip/extension for CB4 and CB5 were back calculated as globally measured total rotation minus rotation contributed by flexure, shear, and sliding

6.7. Energy Dissipation Capacity

The energy dissipated during each loading cycle, calculated as the area enclosed by the hysteretic loop, is shown **Figure 6-19**, while the accumulative energy dissipated during the test is shown **Figure 6-20**. Results presented in **Figure 6-19** demonstrate that all the RC coupling beams experienced cyclic degradation, referring to a reduction in strength (due to a reduction in stiffness) between repeated loading cycles at the same imposed rotation demand, which led to significant pinching of the hysteretic loops and thus reduced energy dissipation capacity, especially for the conventionally reinforced coupling beams. To the contrary, the SRC beam (CB6) did not experience noticeable cyclic degradation and pinching of the hysteretic loops, i.e., almost the same amount of energy was dissipated during the repeated cycles at the same imposed rotation demand. **Figure 6-20** (***a***) indicates that CB1 dissipated more energy than CB5. This is likely because CB5 softened as a result of being subjected the wind loading protocol twice (initially, and then repaired). **Figure 6-20** (***a***) also shows that the diagonally reinforced coupling beam (CB4) had greater energy dissipation capacity and less pinching of the hysteretic loops than the conventionally reinforced coupling beams (CB1 and CB5), which is consistent with results reported in the literature (e.g., Naish et al., 2013). Results presented in **Figure 6-20** (***b***) show that all the beams with conventional reinforcement and l_n/h of 3.67 have the same energy dissipation characteristics, indicating that the type of wind loading protocol used prior to the seismic testing did not have a noticeable influence on the seismic energy dissipation capacity of the beams.

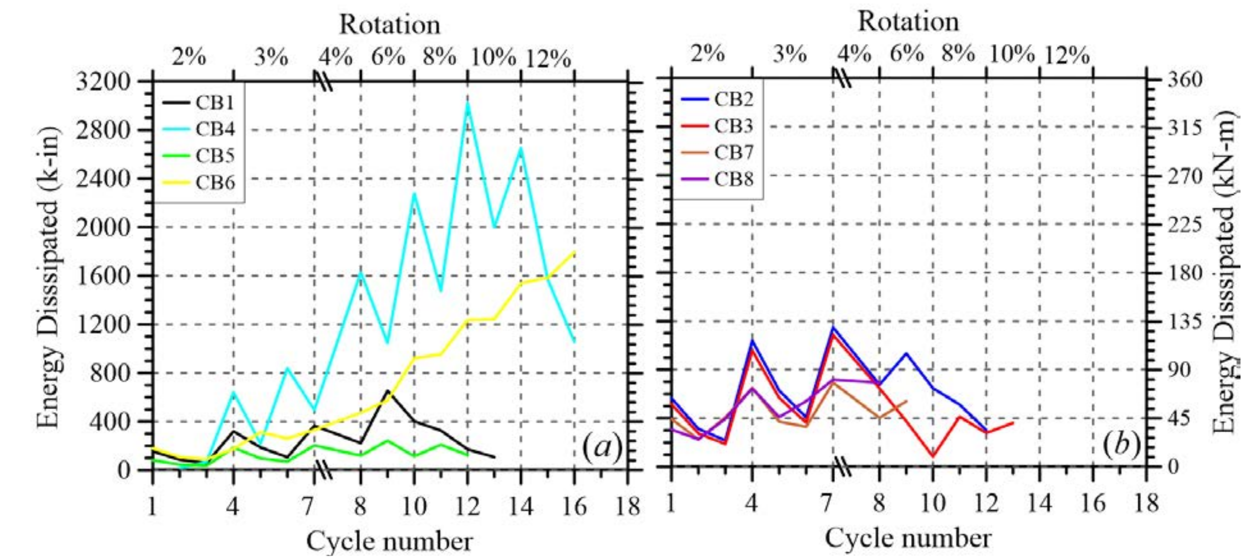

Figure 6-19. Energy dissipated during each cycle of the seismic loading protocol: (*a*) beams with l_n/h =2.5; (*b*) beams with l_n/h =3.67.

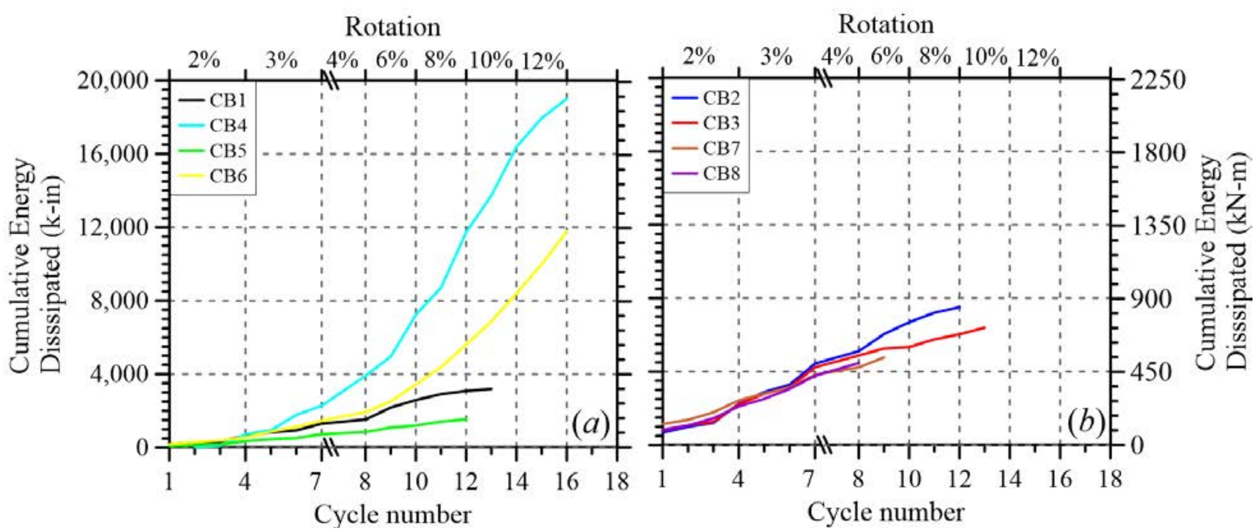

Figure 6-20. Accumulative energy dissipation during the seismic loading protocol: (*a*) beams with l_n/h = 2.5; (*b*) beams with l_n/h = 3.67.

CHAPTER 7. DISCUSSION OF SEISMIC TESTS RESULTS

7.1. General

A discussion of the experimental seismic test results described in the preceding chapter is presented. First, the influence of various design parameters such as aspect ratio, presence of floor slab, variation of wind loading protocol, and type of coupling beam, on the seismic performance of the beams are presented. Then the influence of prior limited nonlinear demands of the wind loading protocols on the residual seismic capacity (capacity to resist future earthquake events) of the beams is evaluated by comparing the performance of the beams with that of similar beams reported in the literature and tested under only seismic loading protocols. The reported results help address the issue of how nonlinear wind demands impact the subsequent seismic behavior of coupling beams in terms of strength, stiffness, ductility, energy dissipation capacity, and failure mode.

7.2. Impact of Aspect Ratio *(l_n/h)*

Five beams with conventional reinforcement, standard detailing, and floor slabs were tested. CB1 and CB5 had an l_n/h of 2.5 and T-shaped floor slab, whereas CB2, CB7, and CB8 had an l_n/h of 3.67 and L-shaped floor slab. Load-deformation responses of CB1 and CB2 are shown in **Figure 7-1**. Generally, the variation of l_n/h did not produce a significant impact on cracking and damage, load-deformation response, axial growth, and energy dissipation capacity. The beams with greater aspect ratio, however, did possess larger secant and effective stiffness values than beams with smaller aspect ratios. As noted previously, this trend, of higher stiffness with increasing aspect ratio, is well established in the literature (e.g., Paulay and Preiestley, 1992) (**Figure 6-15** and **Figure 6-16**).

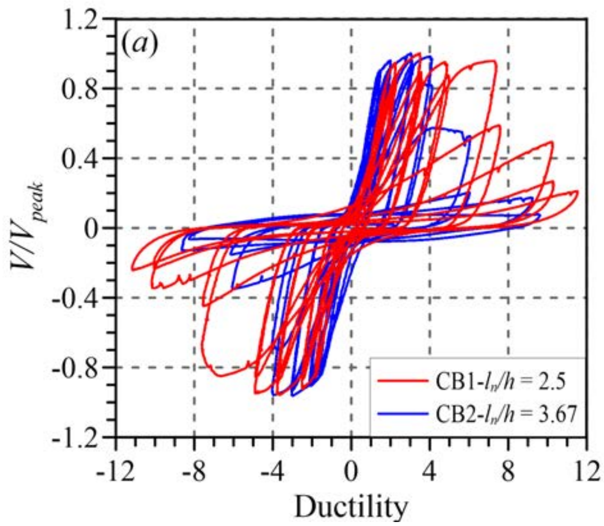

Figure 7-1. Comparison of load-deformation response of CB1 and CB2.

7.3. Impact of Floor Slab

Two beams with l_n/h of 3.67 were tested to assess the influence of the presence of a RC floor slab on the seismic performance of the beams. CB2 included an L-shaped floor slab, whereas CB3 did not have a floor slab. Slabs are expected to modestly increase lateral strength (and thus lateral stiffness) of coupling beams (Naish et al., 2013) due to greater strain hardening of reinforcement when the flange is in compression and due to yielding of slab reinforcement when the flange is in tension. This strength increase in flexure-controlled beams can be accounted for by considering the increase in nominal moment strength due to the presence of the slab, i.e., slab concrete in compression at the beam-wall interface at one end and slab reinforcement in tension at the beam-wall interface at the other end. Comparing the load-deformation response of CB2 versus CB3 in **Figure 7-2** (***a***) and their effective stiffness values in **Table 6-2** reveal that the presence of the floor slab in CB2 increased strength and effective stiffness by about 5%, noting that a larger increase in strength and stiffness could be expected if CB2 had a T-shaped slab as opposed to an L-shaped slab. It also is noted that the effect of the floor slab on the initial stiffness values was more noticeable during the wind loading protocol (**Figure 4-2**). Considering the floor slab of CB2 in moment strength calculations results in an increase of approximately 11% in the nominal moment capacity (**Figure 7-2** (***b***)), which is twice the value observed in the test results of **Figure 7-2** (***a***). This is likely because CB2 and CB3 were flexure-shear controlled beams (as opposed to pure flexure-controlled beams) and thus did not experience significant strain hardening prior to strength degradation. The results also indicate that the presence of the floor slab did not impact cracking and damage, axial growth, energy dissipation capacity, ultimate rotation capacity, and failure mode.

Floor slabs in a real structural system, particularly when post-tensioned, are expected to increase the coupling beam flexural strength and stiffness as a result of restraining axial growth of the beam. However, comparing the axial growths of CB2 and CB3 in **Figure 6-17** indicates that the presence of RC slab did not result in a significant difference between the two beams. This is because the slab was not post-tensioned and axial restraint was not simulated in the tests; therefore, axial growth of the beams was not restrained. Results reported by Naish et al. (2013) demonstrated that diagonally reinforced coupling beams with T-shaped slabs post-tensioned with 150 psi (1.0 MPa) prestress grew 30-40% less than coupling beams with RC slabs, and that beams with and without RC slabs sustained the same level of axial growth. Therefore, it is recommended that the presence of floor slabs, especially when post-tensioned, and axial restraint due to both floor slabs and adjacent walls (although not easy to quantify), be considered when evaluating flexural strength and stiffness of beams.

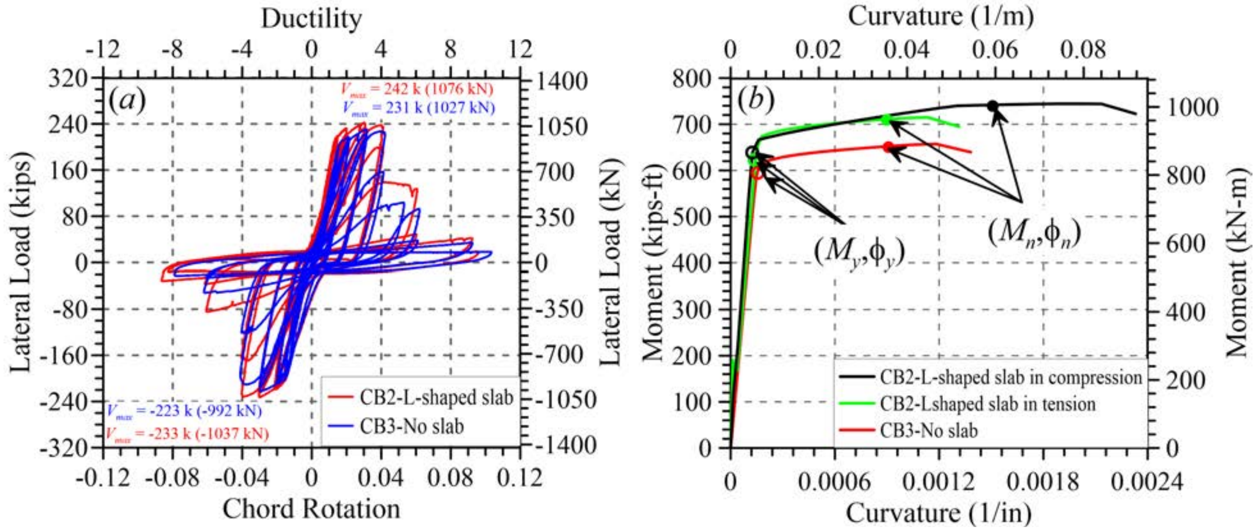

Figure 7-2. Comparison of CB2 and CB3: (*a*) Load-deformation response, (*b*) Moment-curvature response.

7.4. Impact of Variation of Wind Loading Protocol

This section highlights the effect of variation in the wind loading protocols applied to the beams prior to the seismic loading protocol on the overall seismic performance of the beams. As was noted in section **2.6.2**, three variations of the wind loading protocol used in Phase I were considered in Phase II: 1) increasing the number of mildly inelastic cycles, 2) introducing a non-zero mean component (simulating the ratcheting effect of wind in the along-wind direction), and 3) having more than one ramp-up and ramp-down (i.e., spreading out the yielding cycles):

Increased Number of Mildly Inelastic Cycles (Performance of CB1 Versus CB5): CB1 and CB5 were identical RC coupling beams with conventional reinforcement, standard detailing, and l_n/h of 2.5, but were subjected to different wind loading protocols (see

Table 2-7) prior to the seismic loading protocol. CB1 was tested under the wind loading protocol shown in **Figure 2-21**, whereas CB5 was tested twice under the wind loading protocol shown in

Figure 2-22 (***a***), once unrepaired and then epoxy repaired. Thus, CB5 was subjected to considerably more inelastic cycles and demands (eight times more inelastic cycles) than CB1 prior to the seismic loading protocol. **Figure 6-1**, **Figure 6-2**, and **Table 6-1** show the damage states and cracking of the two beams at various chord rotation demands during the seismic loading protocol and indicate that the two beams generally had similar cracking characteristics, with the exception of shear cracks for CB5 being moderately larger than those of CB1 likely due to the increased number of inelastic cycles applied to CB5 during the wind testing phase. Results presented in **Figure 7-3** enable a comparison of the load-deformation responses and axial growths of the beams. Although both beams had the same failure mode, which was flexure-shear (i.e., yielding in flexure prior to failure in shear), lateral strength degradation initiated at 4% rotation for CB5 and at 6% for CB1, as shown in **Figure 7-3** (***a***). This is likely due to the damage concentration along diagonal shear cracks and cyclic softening as a result of the significant increase in number of cycles applied to CB5 during the wind testing phase. This cyclic softening of CB5 also resulted in less energy dissipation capacity and lateral strength (especially in the negative direction) than CB1 (**Figure 6-20** (***a***)). Once lateral strength loss initiated, the two beams experienced gradual strength degradation; lateral strength reduced by about 40% to 50% from the peak strength at 8% rotation for both beams and by about 75% at 12% rotation for CB5 and at 9% rotation for CB1. The epoxy repair of CB5 after applying the first round of the wind loading protocol did not seem to help with the seismic performance of the beam since new cracks, with the same characteristics as the pre-repaired cracks, had formed in the vicinity of the repaired cracks early in the wind loading protocol during retesting.

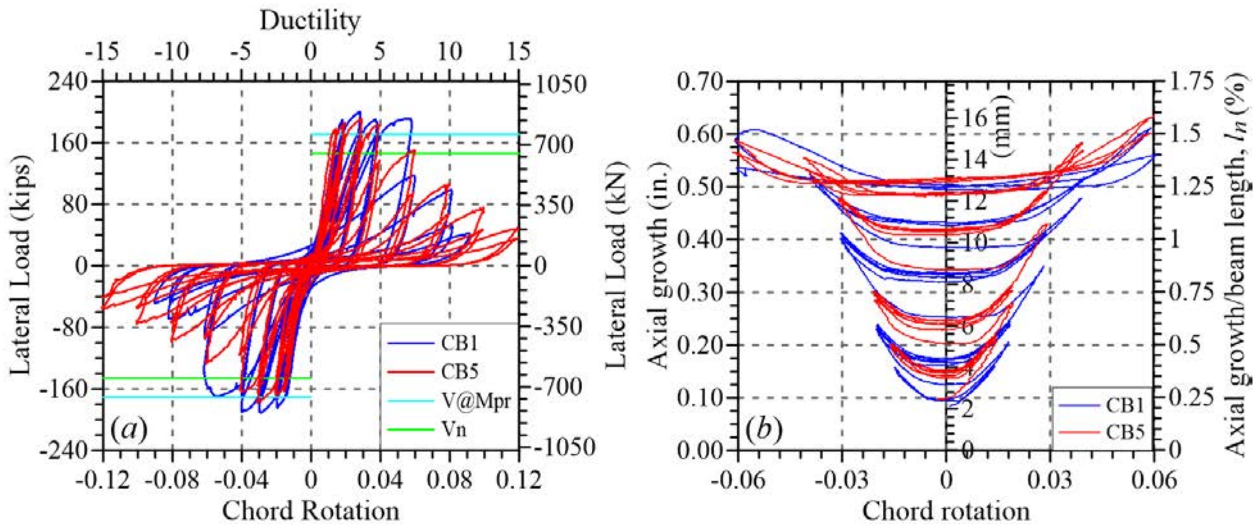

Figure 7-3. Comparison of CB1 versus CB5: (*a*) Load-deformation response, (*b*) Axial growth.

Non-Zero Mean Component and Two Ramp-up and Ramp-Down Events (Performance of CB2 Versus CB7 and CB8): CB2, CB7, and CB8 were identical RC coupling beams with conventional reinforcement, standard detailing, and l_n/h of 3.67, but were subjected to different wind loading protocols prior to the seismic loading protocol, as shown in

Table 2-7. CB2 was tested under the original wind loading protocol from Phase I, whereas CB7 and CB8 were tested under the wind loading protocols with a non-zero mean component and two ramp-up and ramp-down events, respectively. The damage states and cracking of the beams at various chord rotation demands are shown in **Figure 6-3** through **Figure 6-6** and **Table 6-1**, and indicate that the beams generally had similar cracking and damage characteristics during seismic loading protocol, as well as the same eventual failure mode (i.e., yielding in flexure prior to failure in shear). Results presented in **Figure 7-4** enable a comparison of the load-deformation responses and axial growths of the beams. **Figure 7-4** (***a***) indicates that CB7 had slightly larger initial stiffness, especially in the negative direction, than the other two beams because CB7 sustained less cracking in the negative direction of loading during the wind loading protocol. At 4% rotation, lateral strength loss initiated during the first cycle for CB7 and during the second cycle for CB2 and CB8. It is not clear why CB7 failed earlier than the other two beams despite the fact that CB7 sustained less damage and yielding during the wind loading protocol. Furthermore, the beams had similar cyclic degradation and pinching of the hysteretic loops and thus the same energy dissipation capacity (**Figure 6-20 (*b*)**).

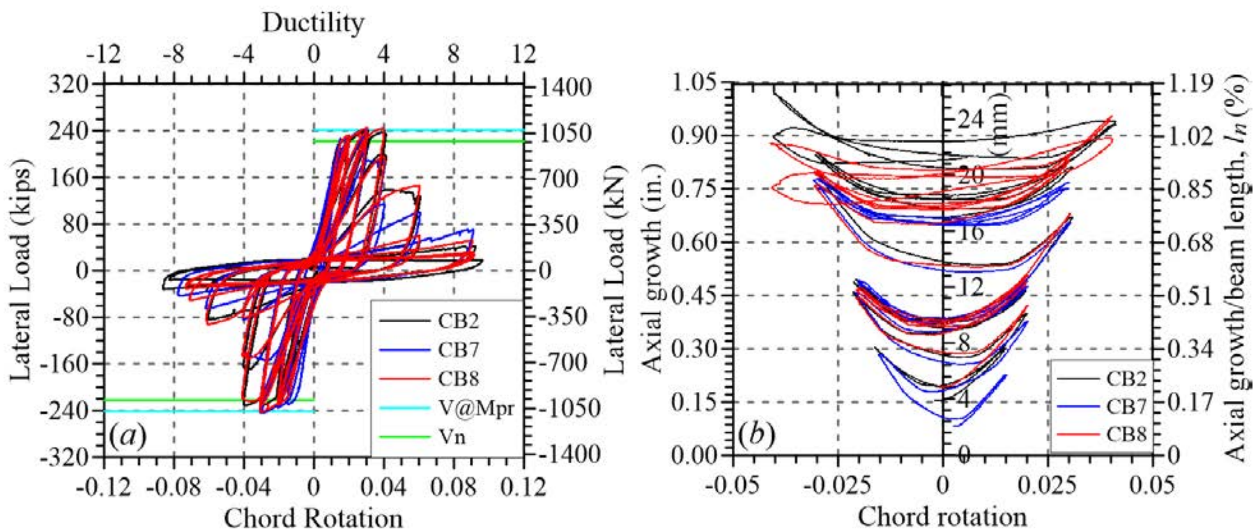

Figure 7-4. Comparison of CB7 and CB8 versus CB2: (*a*) Load-deformation response, (*b*) Axial growth.

7.5. Type of Coupling Beam

This section includes a discussion of the influence of employing different reinforcement options such as use longitudinal (conventional) reinforcement, diagonal reinforcement, or structural steel section on seismic performance of coupling beams. The discussion presented is based on assessing and comparing the performance of four coupling beams with l_n/h of 2.5 and T-shaped floor slabs.

Beams with Conventional versus Diagonal Reinforcement: CB1 was a conventionally reinforced coupling beam with standard detailing, whereas CB4 was a diagonally reinforced coupling beam with seismic detailing. Both beams were subjected to the same wind loading protocol prior to the seismic testing. The results presented in **Figure 7-5** enable a comparison of the load-deformation responses of CB1 and CB4, and demonstrate that, unlike CB4, CB1 experienced considerable hysteretic pinching, an indication of poor energy dissipation capacity. Additionally, CB4 displayed a much higher ductility capacity, reaching chord rotations exceeding 8% prior to significant strength degradation, whereas CB1 initiated lateral strength loss during the first cycle to 6% rotation. However, for cases where low-to-moderate shear stresses (i.e., $<5\sqrt{f_c'(psi)}$ $[0.42\sqrt{f_c'(MPa)}]$) and low rotation demands (< 4.0%) are expected, coupling beams with conventional reinforcement could provide an economically attractive alternative because they are much easier to construct than beams with diagonal reinforcement.

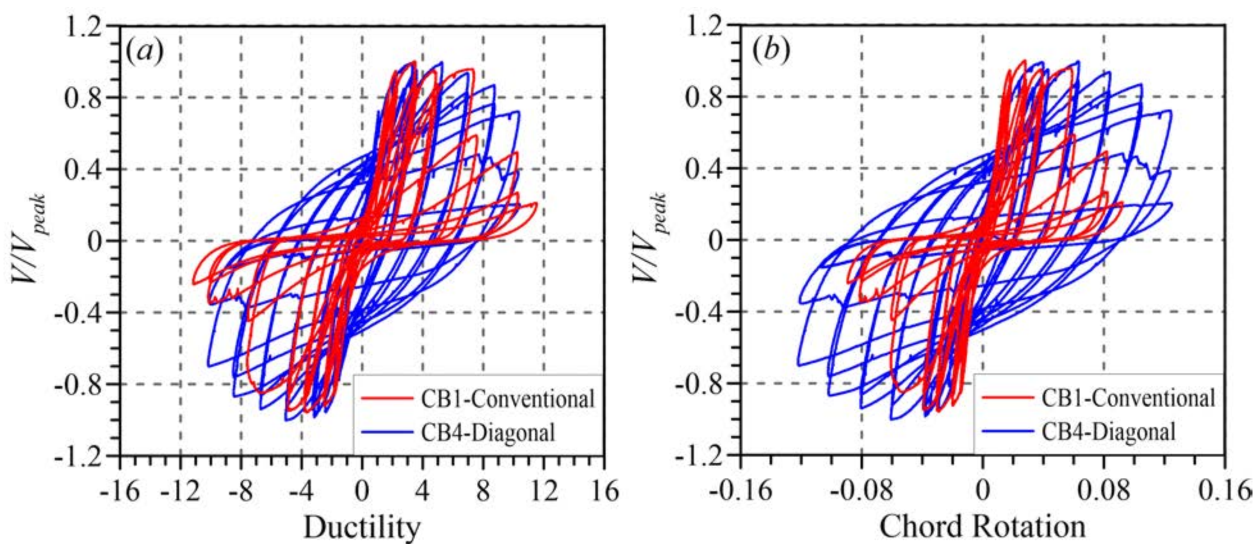

Figure 7-5. Comparison of load-deformation responses of CB1 and CB4.

Beams with Conventional Reinforcement versus SRC Beams: CB5 was a conventionally reinforced coupling beam with standard detailing and no capacity design, whereas CB6 was an SRC coupling beam with standard detailing and capacity-designed embedment. Both beams were subjected to the same wind loading protocol prior to seismic testing, except that CB5 was tested twice under the wind loading protocol, once unrepaired and then epoxy repaired. As was noted in **Figure 6-10**, CB6, unlike CB5, formed major slip/extension cracks at the beam-wall interfaces with only minor cracks elsewhere along the beam span, and thus, did not form plastic hinges over a distance of roughly *h* from the beam-wall interfaces. Instead, all the damage and nonlinearity were localized at a single crack at the beam-wall interfaces. Results presented in **Figure 7-6** enable a comparison of the load-deformation responses of the two beams and indicate that the overall performance of CB6 is far better than CB5, noting that CB5 displayed significant hysteretic pinching throughout the loading protocol and lateral strength degradation beyond 4% rotation. Limited strength and cyclic degradation occurred beyond 10% rotation for CB6; however, given that rotation demands on coupling beams during MCE level shaking are not expected to exceed 6% rotation, this finding is deemed insignificant. Although properly designed and detailed SRC beams can offer a superior performance when compared with beams with conventional reinforcement, their use can result in higher construction costs.

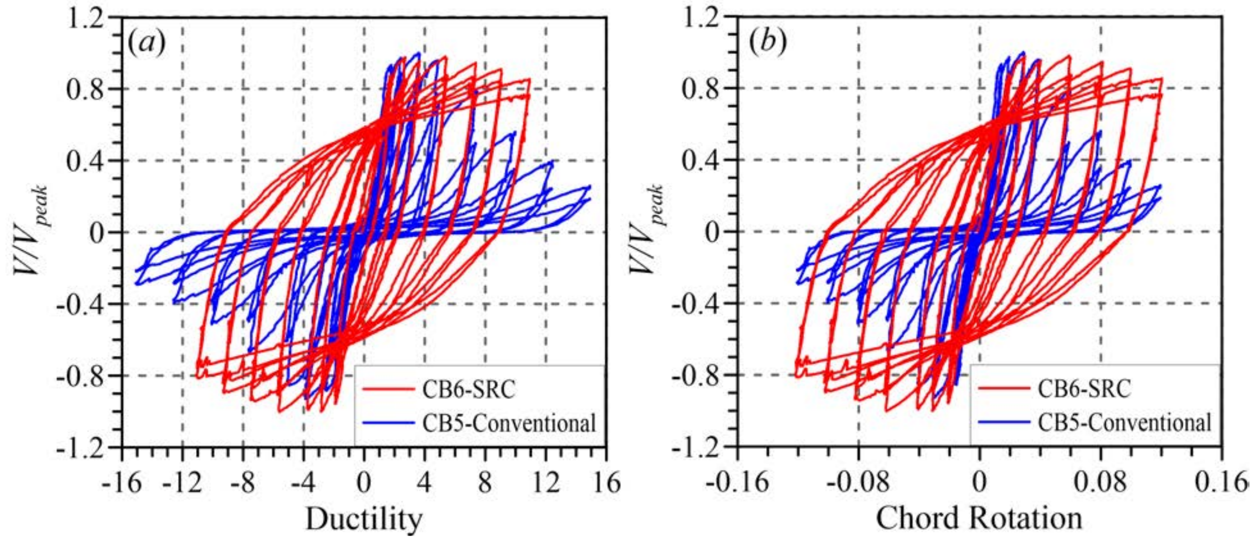

Figure 7-6. Comparison of load-deformation responses of CB6 and CB5.

Beams with Diagonal Reinforcement versus SRC Beams: Seismic performance of CB4, a diagonally reinforced beam with seismic detailing, and CB6, a SRC beam with standard detailing and capacity-designed embedment, are compared. As noted previously, CB6, unlike CB4, did not form plastic hinges over a distance of roughly *h* from the beam-wall interfaces and that all the damage and nonlinearity was localized at a single crack at the beam-wall interfaces. Results presented in **Figure 7-7** enable a comparison of the load-deformation responses of the two beams and demonstrate that beam performance was similarly very good, except that slightly more pinching was observed for CB4. CB6 was pushed to 12% rotation with no significant strength degradation or cyclic degradation observed, whereas for CB4, noticeable hysteretic pinching and significant strength degradation were observed beyond 10% rotation. Strength and cyclic degradation beyond about 6% rotation is not deemed important because demands on coupling beams during MCE level shaking do not typically exceed this level. Given that the performance of SRC coupling beams (with standard detailing and proper embedment length) meets or exceeds that of diagonally reinforced and seismically detailed RC coupling beams, the cost savings associated with employing SRC coupling beams versus diagonally reinforced RC beams might be an attractive option.

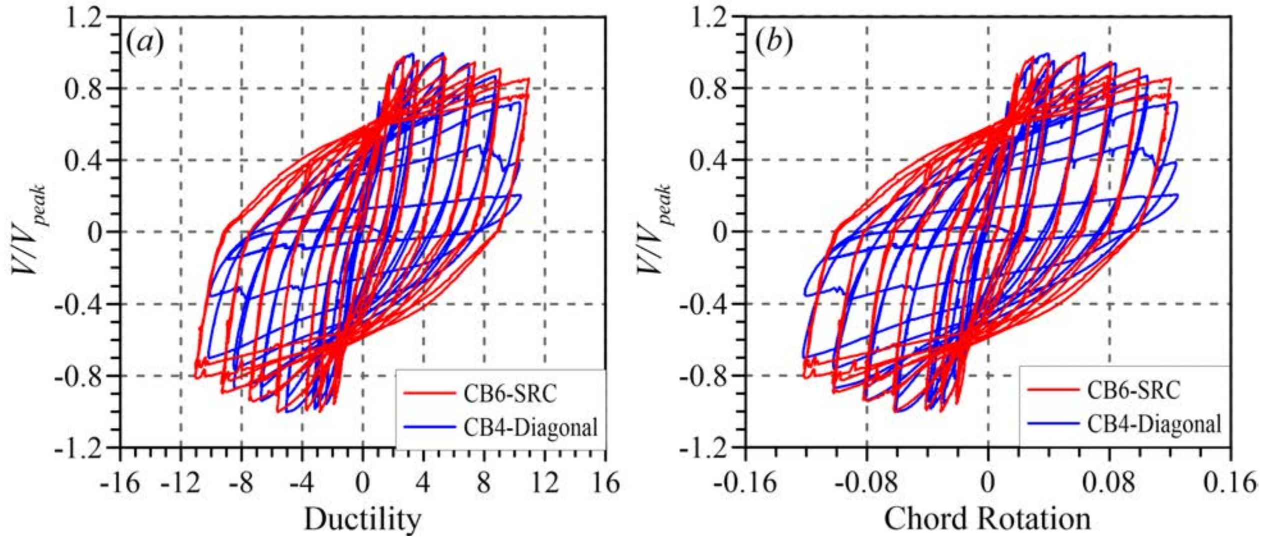

Figure 7-7. Comparison of load-deformation responses of CB6 and CB4.

7.6. Residual Seismic Capacity

Given that one of the objectives of this study was to improve the state of knowledge on residual seismic capacity and repairability of mildly cracked and damaged concrete coupling beams, comparing the performance of the coupling beams tested in this study to that of other similar beams testing under only seismic loading protocols is of interest. This comparison highlights what aspects of the beam behavior are impacted by the prior nonlinear wind demands. For this purpose, the performance of CB3 (with conventional reinforcement and standard detailing), CB4 (with diagonal reinforcement and seismic detailing), and CB6 (SRC) are assessed against four essentially similar beams found in the literature. The selected beams represent the significant design variables used in the program (i.e., conventional, diagonal, and SRC beams, and beams with different l_n/h).

Conventionally Reinforced Beams: The seismic performance of CB3, a conventionally reinforced beam with standard detailing, l_n/h of 3.67, and no floor slab, is compared with performance of two relatively similar beam tests, denoted as HB4-10L-T65 and HB3-10L-T50, reported by Xiao et al. (1999). CB3 was subjected to the wind loading protocol shown in **Figure 2-21** prior to the seismic loading protocol, whereas HB4-10L-T65 and HB3-10L-T50 were tested under only a seismic loading protocol that included one cycle at each load level before yield (about seven cycles) and three cycles at each displacement demand after yield (about 12 to 13 cycles). The details of the three beams are compared in **Table 7-1**. The aspect ratio of CB3 falls in between the aspect ratios of HB4-10L-T65 and HB3-10L-T50 but is closer to that of HB4-10L-T65. The main difference between the beams is that HB4-10L-T65 and HB3-10L-T50 were capacity-designed such that their $V_n/V_{@Mpr}$ ratios are significantly larger than 1.0, which is not the case for CB3, as shown in **Table 7-1**.

Figure 7-8 and **Figure 7-9** provide a comparison of the load-deformation responses and final damage states of the beams, respectively. Results presented in **Figure 7-8** demonstrate that the beams have similar strain hardening behavior, deformations capacity, and lateral strength degradation, but different initial stiffness and hysteretic pinching. As expected, the initial stiffness of CB3 is significantly smaller than those of HB4-10L-T65 and HB3-10L-T50 as a result of the prior nonlinear wind demands. Furthermore, **Figure 7-8** shows that CB3 experienced overall increased pinching of the hysteretic loops and thus had lower energy dissipation capacity compared to HB4-10L-T65 and HB3-10L-T50. The slightly increased pinching of CB3 could be ascribed to the higher shear demand (i.e., $V_n/V_{@Mpr} \approx 1.0$) and the cyclic softening caused by the prior nonlinear wind demands. All three beams had the same failure mode, which is yielding in flexure and eventually failing in shear in the plastic hinge regions, as shown in **Figure 7-9**.

Table 7-1. Comparison of CB3 with HB4-10L-T65 and HB3-10L-T50

Beam ID	CB3	HB4-10L-T65 [(1)]	HB3-10L-T65 [(1)]
Scale	2/3	~ 1/2-2/3	
Size, $b_w \times h \times l_n$ (in.)	16×24×88	8×16×64	8×16×48
Aspect Ratio, l_n/h	3.67	4.0	3.0
Slab	No slab	No slab	
Tested f_c'; f_y (psi)	8,050; 69,000	10,100; 68,000	
Top and bottom reinforcement	6 No.7 + 4 No.8	5 No.6	
ρ_{top} and ρ_{bottom}	0.0197	0.0205	
Transverse reinforcement	4 legs No.3@4.38 in.	2 legs No.3@2.56 in.	2 legs No.3@2 in.
$\rho_{transverse}$	0.0079	0.0108	0.0138
Bar slenderness, s/d_b	5.0	3.4	2.67
Capacity designed?	No	Yes	
$V_n/\sqrt{f_c'(psi)}b_w d$	7.29	8.47	10.28
$V_{@Mpr}/\sqrt{f_c'(psi)}b_w d$	7.17	5.88	7.84
$V_n/V_{@Mpr}$	1.02	1.44	1.31

[(1)] Tested by Xiao et al. (1999).
Conversions: 1in. = 24.5 mm; 1psi = 0.0069 MPa; No.3 bar = 10 mm dia. bar; No.6 bar = 19 mm dia. bar; No.7 bar = 22 mm dia. bar; No.8 bar = 25 mm dia. bar.

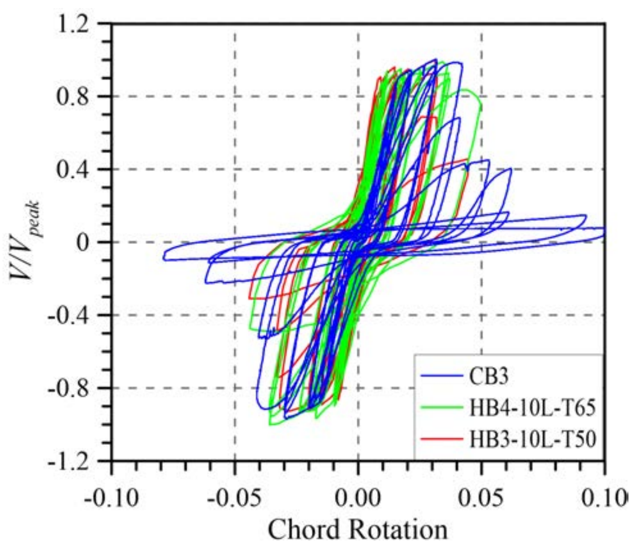

Figure 7-8. Comparison of load-deformation responses CB3 versus HB4-10L-T65 and HB3-10L-T50 tested by Xiao et al. (1999).

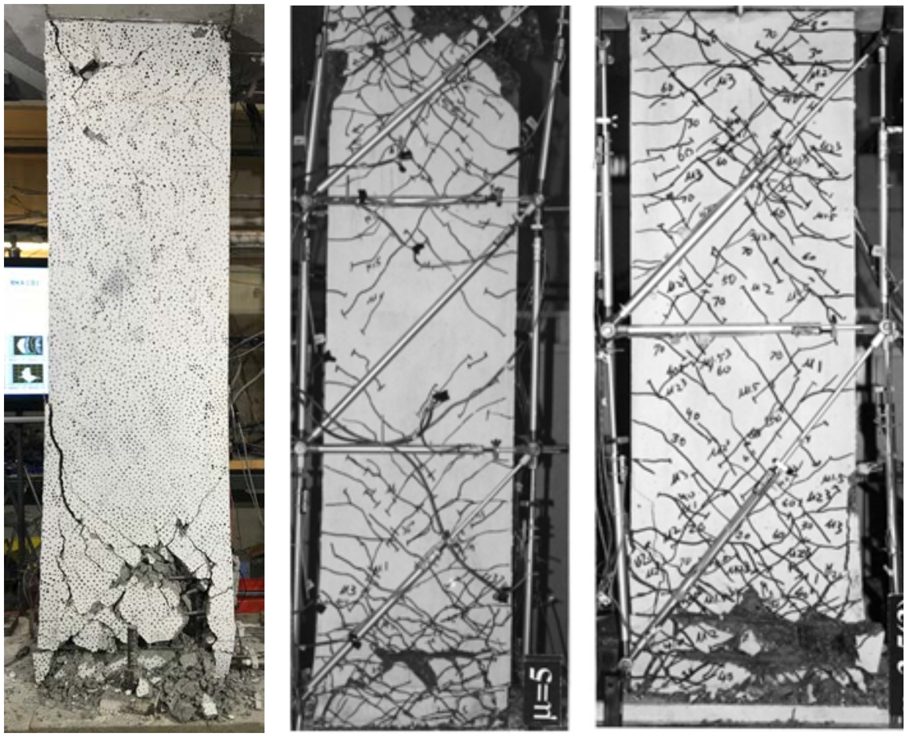

(*a*) (*b*) (*c*)

Figure 7-9. Damage state at lateral strength loss (≈4% rotation): (*a*) CB3; (*b*) HB4-10L-T65 tested by Xiao et al. (1999); and (*c*) HB3-10L-T50 tested by Xiao et al. (1999)

Diagonally Reinforced Beams: Results from two essentially identical coupling beams with seismic detailing and diagonal reinforcement are compared to assess the impact of prior nonlinear wind demands on reserve seismic capacity. CB4 was subjected to the wind loading protocol shown in **Figure 2-21** prior to testing under the standard seismic loading protocol, whereas CB24F-RC was tested by Naish et al. (2013) under only a standard seismic loading protocol. The details of the two beams are given in **Figure 2-4**, **Figure 2-5**, and **Table 2-1**. The lateral load-deformation responses and axial growths of the two beams are compared in **Figure 7-10**. This figure shows that their responses in terms of strength, energy dissipation capacity, deformation capacity, and axial growth, were very similar, and that CB4 had slightly less initial stiffness than CB24F-RC as a result of the prior nonlinear wind demands. **Table 6-1**, **Figure 6-8**, and **Figure 6-9** demonstrate that the cracking, damage progression, and failure modes (characterized by concrete crushing and diagonal reinforcement buckling and fracture) of the two beams were also very similar, except that slip/extension cracks of CB24F-RC were slightly larger than those of CB4. The larger slip/extension cracks of CB24F-RC could be attributed to the fact that CB24F-RC was a half-scale beam with No. 7 (d_b = 22 mm) diagonal bars and CB4 was a 2/3-scale beam with No. 8 (d_b = 25 mm) diagonal bars (i.e., scale ratio of CB4 to CB24F-RC = 1.33 and bar size ratio = 1.14), resulting in more deformation being contributed by bar slip/extension due to larger bar sizes in case of CB24F-RC.

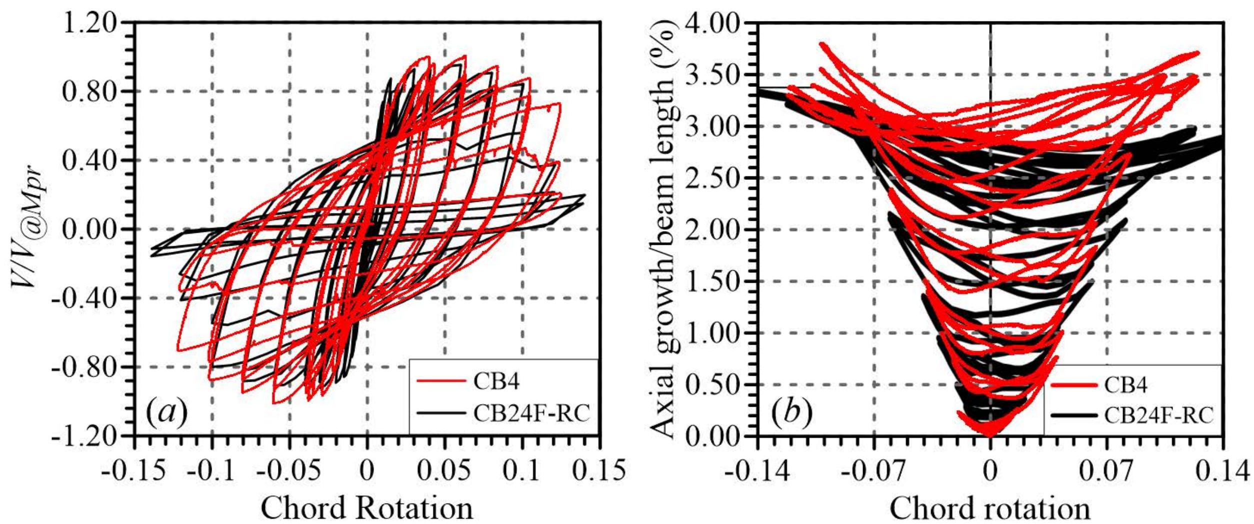

Figure 7-10. Comparison of CB4 versus CB24F-RC tested Naish et al. (2013): (*a*) Load-deformation response, (*b*) Axial growth.

SRC Beams: To assess the impact of prior nonlinear wind demands on reserve seismic capacity of SRC coupling beams, the seismic performance of CB6 with l_n/h of 2.5 and T-shaped floor slab was compared to that of SRC1 with l_n/h of 3.3 and no floor slab (Motter et al., 2017). CB6 was similar to SRC1 in that both beams had adequate embedment length of the steel section such that the connection strength exceeds the demands on the connection when the shear and flexural strengths of the beam develop (i.e., capacity-designed connection). CB6 was subjected to the wind loading protocol shown in **Figure 2-22** (***a***) prior to seismic testing, whereas SRC1was only tested under a seismic loading protocol. Results presented in **Figure 7-11** enable a comparison of the load-deformation responses of the two beams, and show that the responses of the two beams in terms of deformation capacity, cyclic degradation, and energy dissipation capacity, are very similar. The results presented in **Figure 7-11** also indicate that CB6 possesses slightly less initial stiffness than SRC1 as a result of the prior nonlinear wind demands. This difference in stiffness could have been larger if SRC1 had a floor slab and was embedded in post-tensioned blocks simulating the wall boundary elements, slimier to CB6. **Table 6-1** and **Figure 6-12** show that the observed cracking and damage of CB6 is similar to that reported for SRC1, except that the interface cracks of SRC1 were significantly larger (**Figure 7-12**; **Table 6-1**) because the steel section of SRC1 was embedded in a wall boundary element that was subjected to reversed cyclic lateral loading and overturning moment, as opposed to a post-tensioned block, as was the case for CB6.

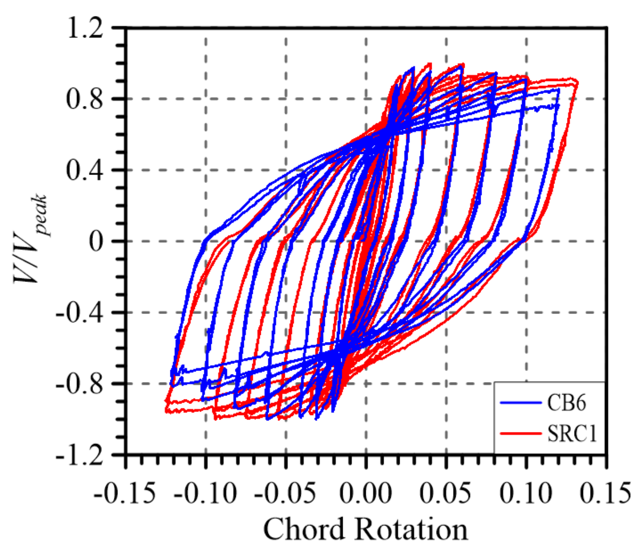

Figure 7-11. Load-chord rotation relation for CB6 versus SRC1 (Motter et al., 2017).

(*a*) CB6 (*b*) SRC1

Figure 7-12. Damage state at end of test (≈12% rotation) for CB6 and SRC1 (Motter et al., 2016).

The results presented in the preceding subsections indicate that the most significant influence of the prior nonlinear wind demands on the residual seismic capacity of beams was a reduction in the initial stiffness, with minor reduction in energy dissipation capacity observed only for the conventionally reinforced beams. This finding is in agreement with results reported for residual seismic capacity of other mildly earthquake-damaged components such as frame beams and walls (e.g., Marder, 2018; Maeda et al., 2017). To enable proper evaluation of residual seismic capacity of coupling beams for future earthquake events, quantification of an effective stiffness reduction factor that could be used for analysis to assess the impact of stiffness reduction is of significant interest. Prior research (e.g., FEMA 306; De Ludovico et la., 2013; Maeda et al., 2017; Marder, 2018) have shown that residual stiffness of earthquake-damaged concrete components (walls, beams, and columns) can be assessed based on the maximum ductility demand previously experienced. **Figure 7-13** presents the $(E_cI_{eff})_{residual}$ normalized by $(E_cI_{eff})_{initial}$ of the beams tested in this study against maximum ductility demand (μ) the beams experienced during the wind loading protocols, where the $(E_cI_{eff})_{residual}$ and $(E_cI_{eff})_{initial}$ values are as defined in **Section 6.4.2**. This figure also presents data from two datasets of ductile RC beams and columns: 1) a dataset of shake table tests on columns was compiled by Marder (2018) from Laplace et al. (1999), Hachem et al. (2003), Arias Acosta (2011), and Schoettler et al. (2013), and 2) data from tests on beams conducted by Marder (2018). The specimens in the datasets were all subjected to earthquake-type loading protocols followed by at least one subsequent loading during which the residual stiffness values were measured. Both the initial and residual effective stiffness values reported by Marder (2018) are defined as secant stiffness to 80% of the maximum base moment (i.e., secant stiffness to yield), which is slightly different from the approach used in this study, which is secant stiffness to 2/3 of the average peak strength; however, since the results are normalized, this difference in defining the effective stiffness should have minimal impact on the comparisons. Based on the results of the beam and column datasets, Marder (2018) recommended a conservative expression for assessing residual effective stiffness as a function of ductility demand, as shown in **Figure 7-13**. Further, Di Ludovico et al. (2013) used regression analysis on data from standard cyclic tests of reinforced concrete columns to derive a stiffness reduction factor for column plastic hinges as a function of the prior displacement ductility demands (**Figure 7-13**). **Figure 7-14** illustrates that the ratio of residual secant stiffness at a given ductility demand (prior to lateral strength loss) to the initial effective stiffness can be estimated as the inverse of the ductility demand. The expressions for residual effective stiffness from Marder (2018) and Di Ludovico et al. (2013), along with the inverse of ductility, are plotted against the experimental data in **Figure 7-13**. It is evident that the expression proposed by Di Ludovico et al. (2013) and $1/\mu$ are almost exactly the same and tend to overestimate residual effective stiffness of the beams tested in this study likely due to the cyclic softening caused by the large number of cycles applied after the peak ductility demands during the wind loading protocols. The expression proposed by Marder (2018) provides a conservative estimate at low ductility demands, i.e., residual effective stiffness is 50% of the initial effective stiffness when maximum ductility demand is between 1 and 2, which might represent the range of demands expected for beams designed using PBWD. Therefore, a refined, and yet conservative, expression is proposed herein to estimate the ratio of residual-to-initial effective stiffness as a fraction of the maximum ductility demand, μ, as given by **Equation 7.1**:

$$\frac{(E_c I_{eff})_{residual}}{(E_c I_{eff})_{initial}} = \begin{Bmatrix} 1\ for\ \mu \leq 0.5 \\ \frac{1}{\mu + 0.5}\ for\ \mu > 0.5 \end{Bmatrix} \tag{7.1}$$

Equation 7.1 is also plotted in **Figure 7-13**, which demonstrates that the proposed expression provides a lower-bound estimate of residual effective stiffness for RC beams subjected to prior nonlinear wind demands. Further research is needed to validate and refine this expression for SRC beams, which appear to experience larger reduction in effective stiffness.

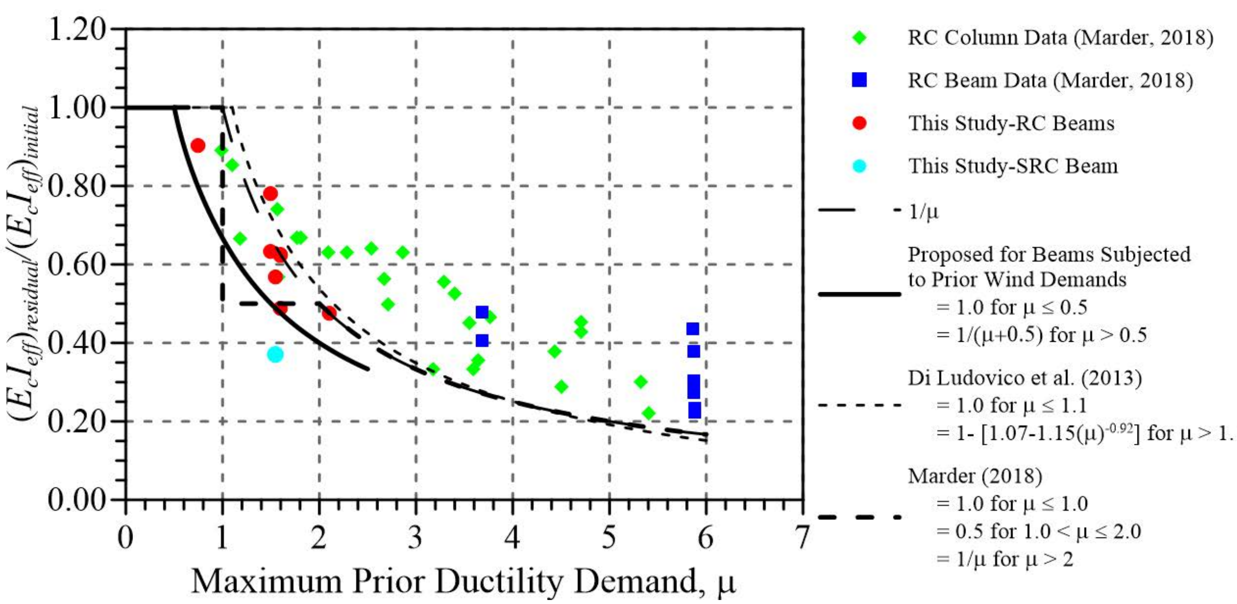

Figure 7-13. Comparison of proposed expression and other available expressions (Di Ludovico et al., 2013; Marder, 2018) for normalized residual stiffness, $(E_cI_{eff})_{residual}/(E_cI_{eff})_{initial}$, versus experimental data.

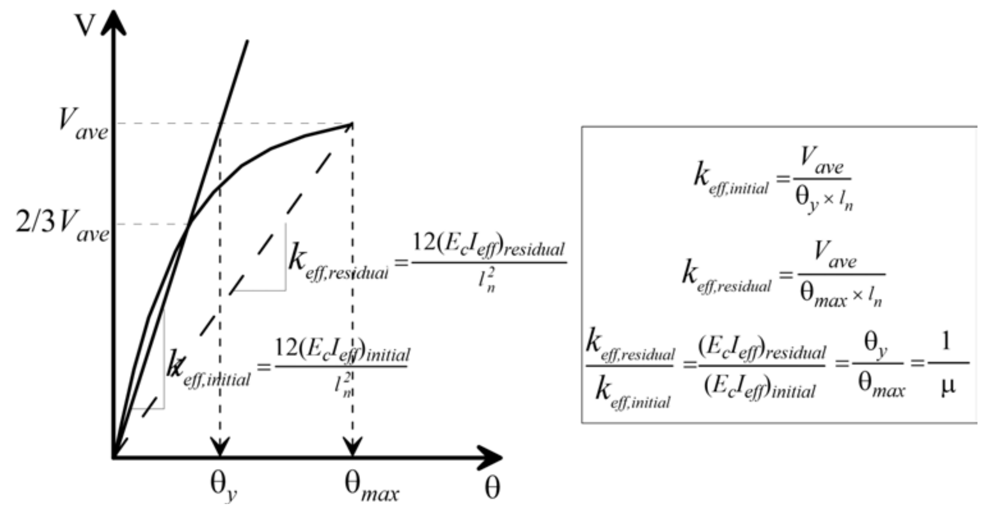

Figure 7-14. Relationship between stiffness degradation and ductility demand.

CHAPTER 8. CONCLUSIONS AND RECOMMENDATIONS FROM SEISMIC TESTS

After testing of the coupling beams under the wind loading protocols was concluded, the beams were subsequently subjected to a standard seismic loading protocol to assess the impact of the prior nonlinear wind demands on the overall seismic performance and reserve capacity of the coupling beams. The seismic loading protocol picked up at either at 1.5% or 2% chord rotation, depending on the peak rotation demand applied during the wind loading protocol. The initial smaller cycles were not applied since the beams had already been subjected to a large number of pre-yield and mildly-yield cycles during the wind loading protocols. It is noted that the time between the conclusion of the wind test and the start of the seismic test did not exceed two days for each beam. Therefore, the reinforcement did not have sufficient time to experience strain ageing. As well, strain ageing should not be important given that Grade 60 (414 MPa) reinforcement was used in this test program. Based on the experimental findings of the seismic tests, the following conclusions and recommendations with regards to the reserve (residual) seismic capacity of concrete coupling beams subjected to prior mild nonlinear wind demands can be drawn:

1. The beams sustained different damage progression and failure modes depending on the type of the coupling beam (i.e., RC versus SRC beams, or conventionally- versus diagonally-reinforced beams). In general, cracking and damage primarily concentrated within a distance of h (beam depth) from the beam-wall interfaces (i.e., plastic hinge regions), with the largest cracks being developed at the beam-wall interfaces (i.e., slip/extension cracks) for the RC coupling beams. The SRC beam (CB6) did not form plastic hinges over a distance of roughly h from the beam-wall interfaces. Instead, a vast majority of the damage and nonlinearity was

localized at a single crack at each beam-wall interface, and only hairline or minor cracks were observed elsewhere along the beam span.

2. The conventionally reinforced coupling beams, regardless of their aspect ratios, experienced similar cracking, damage, and failure mode, which included first yielding of longitudinal reinforcement and then concentration of damage along diagonal (shear) cracks that led to an eventual shear failure in the plastic hinge regions at 4 or 6% rotation. The diagonally reinforced coupling beam (CB4) experienced significant lateral strength loss beyond 10% rotation due to concrete crushing and buckling and fracture of diagonal bars. The SRC coupling beam (CB6) did not experience significant lateral strength loss even after reaching 12% rotation demand, at which large gaps [~1.5 in. (38 mm) wide at peak demands] had opened at the beam-wall interfaces, and no fracture or significant flange buckling of the steel section was observed.
3. Generally, aspect ratio (l_n/h) did not have a significant influence on cracking and damage, load-deformation response, axial growth, energy dissipation capacity, and failure mode of the conventionally reinforced coupling beams. The beams with greater aspect ratios, however, possessed larger secant and effective stiffness values relative to the gross section stiffness than beams with smaller aspect ratios, which is consistent with stiffness data of beams tested under only seismic loading protocols.
4. The presence of L-shaped RC floor slabs in conventional beams was observed to increase strength and effective stiffness by about 5%, noting that a larger increase in strength and stiffness could be expected in case of a T-shaped beam. This increase in strength and stiffness can be accounted for by considering the presence of the slab in moment strength calculations, i.e., slab concrete in compression at the beam-wall interface at one end and slab reinforcement in tension at the beam-wall interface at the other end. The results also indicated that the

presence of the floor slab did not influence cracking and damage, axial growth, energy dissipation capacity, ultimate rotation capacity, and failure mode.

5. Comparing the performance of a conventionally reinforced coupling beam (CB1), with a diagonally reinforced coupling beam (CB4) demonstrated that the conventional beam experienced considerable hysteretic pinching, an indication of substantially less energy dissipation capacity. Additionally, the diagonal beam displayed a much higher deformation capacity, reaching chord rotations exceeding 8% prior to significant strength degradation, whereas the conventional beam initiated lateral strength loss during the first cycle to 6% rotation. However, for cases where low-to-moderate shear stresses (i.e., $<5\sqrt{f_c'(psi)}$ $[0.42\sqrt{f_c'(MPa)}]$) and low rotation demands (< 4.0%) are expected, coupling beams with conventional reinforcement could provide an economically attractive alternative.
6. The overall performance of CB6 (SRC beam) was far better than CB5 (conventional beam), noting that CB5 displayed significant hysteretic pinching throughout the loading protocol and lateral strength degradation beyond 4% rotation. Limited strength degradation and cyclic degradation of CB6 occurred beyond 10% rotation, which is deemed insignificant, given that rotation demands on coupling beams during MCE level shaking do not typically exceed 6% rotation. Although SRC beams with proper design and detailing of the embedment connection can offer a superior performance when compared with conventional beams, their use can result in higher construction costs.
7. Comparing the performance of CB4, a diagonally reinforced beam with seismic detailing, and CB6, an SRC beam with standard detailing and capacity-designed embedment connection, revealed that both beams performed very well, and that their overall performance was comparable, except that a slightly more pinching was observed for CB4. CB6 was pushed to

12% rotation and yet no significant strength degradation or cyclic degradation was observed, whereas CB4 displayed noticeable hysteretic pinching and significant strength degradation beyond 10% rotation. Given that the performance of SRC coupling beams (with standard detailing and capacity-designed embedment length) meets or exceeds that of diagonally reinforced and seismically detailed RC coupling beams, the cost savings associated with employing SRC coupling beams versus diagonally reinforced RC beams might be an attractive option.

8. The variations in the wind loading protocols did not impact on the reserve seismic capacity of the beams, except for the case where the wind loading protocol was applied more than once, as was the case for CB5. In this case, the wind loading protocol was found to reduce the deformation and energy dissipation capacities.
9. The wind loading protocols did not impact the strength, axial growth, energy dissipation capacity (cyclic degradation), deformation capacity, and failure mode of the beams tested in this study when compared to similar test beams reported in the literature and tested under only seismic loading protocols. The most significant influence of the prior nonlinear wind demands on the residual seismic capacity of beams was a reduction in the initial stiffness observed for all beams (ranging from 10% to 63% depending on the maximum prior ductility demand applied) and a minor reduction in energy dissipation capacity observed only for the conventional coupling beams. These findings are in agreement with results reported for residual seismic capacity of other earthquake-damaged concrete components such as frame beams and walls.
10. The residual effective stiffness can be estimated as the initial effective stiffness of undamaged coupling beams reduced by a stiffness reduction factor given by **Equation 7.1**, which results

in reduction factors ranging from 1.0 to 0.4 for maximum ductility demands of 0.75 to 2.0, respectively.

REFERENCES

ACI Committee 318, 2014, "Building Code Requirements for Structural Concrete (ACI 318-14) and Commentary," American Concrete Institute, Farmington Hills, MI, 519 pp.

ACI Committee 363, 2010, "Report on High Strength Concrete (ACI 363R-10)," American Concrete Institute, Farmington Hills, MI, 75 pp.

ACI Committee 374, 2013, "Guide for Testing Reinforced Concrete Structural Elements under Slowly Applied Simulated Seismic Loads," American Concrete Institute, Farmington Hills, MI, 22 pp.

ACI Committee 224, 2007, "Causes, Evaluation, and Repair of Cracks in Concrete Structures (ACI 224.1R-07)," American Concrete Institute, Farmington Hill, MI, 22 pp.

ACI Committee 503, 2007, "Specification for Crack Repair by Epoxy Injection (ACI 503.7-07)," American Concrete Institute, Farmington Hill, MI, 7 pp.

ANSI/AISC 360, 2010, "Specification for Structural Steel Buildings," American Institute of Steel Construction. Chicago, IL.

ANSI/AISC 341, 2016, "Seismic Provisions for Structural Steel Buildings," American Institute of Steel Construction, Chicago, IL.

ANSI A58-1, 1972, "Building Code Requirements for Minimum Design Loads in Buildings and Other Structures," American National Standard Institute, NY.

Arias Acosta, J., 2011, "Seismic performance of circular and interlocking spirals R/C bridge columns under bi-directional shake table loading," PhD Dissertation, University of Nevada, Reno.

ASCE/SEI Standards, 2016, "Minimum Design Loads for Buildings and Other Structures (ASCE/SEI 7-16)," American Society for Civil Engineers, Reston, VA, 690 pp.

ASCE/SEI Standards, 2017, “Seismic Evaluation and Retrofit of Existing Buildings (ASCE/SEI 41-17),” American Society of Civil Engineers, Reston, VA, 576 pp.

ASCE/SEI Prestandard, 2019, “Prestandard for Performance-Based Wind Design,” American Society of Civil Engineers, Reston, VA, 113 pp.

ASTM Standards, 2019, “Standard Practice for Making and Curing Concrete Test Specimens in the Field (ASTM C31/C31M),” ASTM International, West Conshohocken, PA.

ASTM Standards, 2018, “Standard Test Method for Compressive Strength of Cylindrical Concrete Specimens (ASTM C39/C39M),” ASTM International, West Conshohocken, PA.

Aswegan, K., R. Larsen, R. Klemencic, J. Hooper, and J. Hasselbauer, 2017, “Performance-based wind and seismic engineering: Benefits of considering multiple hazards” In *Proceedings of 2017 ASCE/SEI Structures Congress,* April 6–8, Denver, Colorado.

Bernardini, E., Spence, S. M. J., Kwon, D.-K., and Kareem, A., 2015, “Performance-based design of high-rise buildings for occupant comfort.” Journal of Structural Engineering, 141, 04014244.

Bernardini, E., Spence, S. M. J., and Kareem, A., 2013, “A probabilistic approach for the full response estimation of tall buildings with 3D modes using the HFFB.” Structural Safety, Vol. 44, pp. 91–101.

Ciampoli, M., Petrini, F., and Augusti, G., 2011, “Performance-Based Wind Engineering: Towards a general procedure.” Structural Safety, Vol. 33, No. 6, pp. 367–378.

Di Ludovico, M., Polese, M., d’Aragona, M.G., Prota, A., and Manfredi, G., 2013, “A proposal for plastic hinges modification factors for damaged RC columns,” Engineering Structures, Vol. 51, pp. 99-112.

Ellingwood, B. R., 2001, "Acceptable risk bases for design of structures," Progress in Structural Engineering and Materials, Vol. 3, No. 2, pp. 170–179.

FEMA, 2012, "Seismic performance assessment of buildings, Volume 1 – Methodology, FEMA P-58-1," Prepared by the Applied Technology Council for the Federal Emergency Management Agency, Washington, DC.

FEMA 273, 1997, Guidelines to the Seismic Rehabilitation of Existing Buildings, Federal Emergency Management Agency, Washington, D.C.

FEMA 306, 1998, "Evaluation of earthquake damaged concrete and masonry wall buildings," Federal Emergency Management Agency, Washington, DC.

Galano, L., and Vignoli, A., 2000, "Seismic behavior of short coupling beams with different reinforcement layouts," *ACI Structural Journal*, Vol. 97, No. 6, pp. 876–885.

GOM, 2018, "GOM Correlate Software," Available at https://www.gom.com

Golesorkhi, R., Joseph, L., Klemencic, R., Shook, D. and Viise, J., 2017, "Performance-Based Seismic Design for Tall Buildings: An output of the CTBUH Performance-Based Seismic Design Working Group," Council on Tall Buildings and Urban Habitat, Chicago, IL.

IBC, 2018, "International Building Code (IBC 2018)," International Code Council, Falls Church, VA.

Hachem, M. M., Moehle, J. P., and Mahin, S. A., 2003, "Performance of circular reinforced concrete bridge columns under bidirectional earthquake loading," Pacific Earthquake Engineering Research Center, University of California, Berkeley.

Irwin, P., Denoon, R., and Scott, D. (2013, "Wind Tunnel Testing of High-Rise Buildings: An output of the CTBUH Wind Engineering Working Group," Council on Tall Buildings and Urban Habitat, Chicago, IL.

Klemencic, R., 2019, “Performance-based wind design: the path forward,” Proceedings of 2019 LATBSDC Conference, May 3, Los Angeles, CA.

Kwan, A. K. H., and Zhao, Z. Z., 2001, “Testing of coupling beams with equal end rotations maintained and local joint deformation allowed,” *Structures and Buildings*, Vol. 152, No. 1, pp. 67–78.

Laplace, P. N., Sanders, D., Saiidi, M. S., and Douglas, B., 1999, “Shake table testing of flexure dominated reinforced concrete bridge columns,” Center for Earthquake Engineering Research, University of Nevada, Reno.

Larsen, R., Klemencic, R., Hooper, J., and Aswegan, K., 2016, “Engineering Objectives for Performance-Based Wind Design,” Proceedings of ASCE Structures Congress, Feb. 14-17, Phoenix, AZ

LATBSDC, 2017, “An Alternative Procedure for Seismic Analysis and Design of Tall Buildings Located in the Los Angeles Region,” Los Angeles Tall Buildings Structural Design Council, Los Angeles, CA.

Loporcaro, G., 2017, “A least invasive method to estimate the residual strain capacity of steel reinforcement in earthquake-damaged buildings,” PhD dissertation, University of Canterbury.

Maeda, M., Koike, T., Hosoya, N., Suzuki, Y., Tsurugai, K., and Nimura, A., 2017, “Damage and residual seismic performance evaluation of reinforced concreate shear walls,” Proceedings of 16th World Conference on Earthquake (16WCEE 2017), January 9-13, Santiago Chile.

Mehta, K. C., 2010, “Wind Load History: ANSI A58.1-1972 to ASCE 7-05,” Proceedings of Structures Congress, May 12-15, Orlando, Fl.

Marder, J. K., 2018, "Post-Earthquake Residual Capacity of Reinforced Concrete Plastic Hinges" PhD Dissertation, The University of Auckland.

Motter, C. J., Fields, D. C., Hooper, J. D., Klemencic, R., and Wallace, J. W., 2016, "Steel reinforced concrete coupling beams. Part II: Modeling." *Journal of Structural Engineering*, Vol. 143, No. 3, 04016191.

Naish, D., Fry, A., Klemencic, R., and Wallace, J., 2013, "Reinforced concrete coupling beams. Part I: Testing." ACI Structural Journal, Vol. 110, No. 6, pp. 1057–1066.

Paulay, T., and Binney, J. R., 1974, "Diagonally reinforced coupling beams of shear walls," *American Concrete Institute*, SP-42, pp. 579–598.

Poudel, A., Lequesne, R., and Lepage, A., 2018, "Diagonally Reinforced Concrete Coupling Beams: Effects of Axial Restraint," *SL Report 18-3*, University of Kansas, Lawrence, KS.

Rashid, M.S., 1976, "Strain Aging Kintetics of Vanadium or Titanium Strengthened High-Strength Low-Alloy Steels" Metallurgical Transactions A, Vol. 7A, pp. 497-503.

Rowan Williams Davies & Irwin Inc. (RWDI), 2019, "Raw wind speed data from historical and simulated hurricanes for Miami, Florida," Personal communication (April 23, 2019).

Schoettler, M., Restrepo, J., Guerrini, G., Duck, D., and Carrea, F., 2015, "A full-scale, single-column bridge bent tested by shake-table excitation," Pacific Earthquake Engineering Research Center University of California, Berkeley.

Smith, M. A., and Caracoglia, L. (2011). "A Monte Carlo based method for the dynamic "fragility analysis" of tall buildings under turbulent wind loading." Engineering Structures, Vol. 33, pp. 410–420.

Smolka, A., 2006, "Natural disasters and the challenge of extreme events: risk management from an insurance perspective," Royal Society, Vol. 364, No. 1845, pp. 2147–2165.

Spence, S. M. J., Bernardini, E., and Kareem, A., 2015, “A first step towards a general methodology for the performance-based design of wind-excited structures.” Proceedings of the Structures Congress, pp. 1482–1493.

Spence, S. M. J., and Kareem, A., 2014, “Performance-based design and optimization of uncertain wind-excited dynamic building systems.” Engineering Structures, Vol. 78, pp. 133– 144.

Spence, S.M.J., Chuang, W.C., Tabbuso, P., Bernardini, E., Kareem, A., Palizzolo, L., and Pirrotta, A., 2016, “Performance-based engineering of wind excited structures: a general methodology.” Proceedings of ASCE Structures Congress, Feb. 14-17, Phoenix, AZ.

Tassios, T. P., Moretti, M., and Bezas, A., 1996, “On the coupling behavior and ductility of reinforced concrete coupling beams of shear walls,” *ACI Structural Journal*, Vol. 93, No. 6, pp. 711–720.

Tauberg, N. A., Kolozvari, K., and Wallace, J. W., 2019, “Ductile Reinforced Concrete Coupled Walls: P695 Study,” *Report SEERL 2019*, University of California, Los Angeles, CA.

TBI, 2017, “Guidelines for Performance-Based Seismic Design of Tall Buildings,” Tall Building Initiative, Pacific Earthquake Engineering Research Center, Berkeley, CA.

UBC, 1997, “Uniform Building Code (UBC-97),” International Council of Building Code Officials, Whittier, CA.

Van Rooyen, G.T., 1986, “The embrittlement of hardened, tempered low-alloy steel by strain aging,” Journal of the South African Institute of Minining Metallurgy, Vol. 86, No. 2., pp. 67-72

Xiao, Y., Esmaeily-Ghasemabadi, A., and Wu, H., 1999, “High-strength concrete beams subjected to cyclic shear,” *ACI Structural Journal*, Vol. 96, No. 3, pp. 392–399.

Zhao, S.D., and Ghannoum, W.M., 2016, “Setting bar-bending requirements for high-strength steel bars,” Report to Charles Pankow Foundation, University of Taxes at San Antonio, TX.

APPENDEX A–Properties of the Epoxy Material and the Application Procedure

Strengthening Solutions

Tstrata 330

Low Viscosity, High Strength Epoxy

structuraltechnologies.com
+1-410-859-6539

Physical Properties:

Tensile Strength (ASTM D638):	7,200 psi (49.6 MPa)	**Bond Strength (ASTM C882):**	Hardened to Hardened
Tensile Modulus (ASTM D638):	280,000 psi (1,930 MPa)	2 days dry	2,150 psi
Elongation at Break (ASTM D638):	2.2%	14 days moist	2,550 psi
Compressive Strength (ASTM D695)	11,100 psi (76.5 MPa)	14 days dry	2,825 psi
Compressive Modulus (ASTM D695)	265,000 psi (1,827 MPa)	**Viscosity (ASTM D2196)**	300 – 450 cps
Density Mixed Product:	9.06 lbs/gal (1.08 kg/L)	**Percent Solids (ASTM D1259):**	100%
Pot Life:	25 minutes	**VOC Content (ASTM D2369)**	0% VOC

DESCRIPTION:
Tstrata 330 is a two-part, low viscosity 100% solids, high strength epoxy for crack repair. Tstrata 330 is moisture insensitive and has a convenient 2A to 1B mix ratio. Tstrata 330 is an environmentally friendly product with high modulus. It is the perfect solution for general bonding applications and for injecting cracks in concrete and a variety of other substrates

PRODUCT USES:
Tstrata 330 is a multi-use epoxy for: injection of cracks in concrete, gravity feed of horizontal cracks, vertical anchor bolt grouting, and as a binder for sand filled horizontal repairs.

Meets ASTM C881- Type I and IV, Grade 1, Class B and C

ADVANTAGES:
- Deep Penetration
- High strength bond to concrete
- Moisture insensitive
- Virtually no odor

APPROXIMATE POT LIFE:
25 minutes @ 72°F (22°C)

APPLICATION INFORMATION

SURFACE PREPARATION:
The surface must be structurally sound, dry, clean and free of grease, oil, curing compounds, soil, dust and other contaminants. Substrates should be dry and exhibit an open pore structure. Surface laitance must be removed. Concrete surfaces must be roughened and made absorptive, preferably by mechanical means, and then thoroughly cleaned of all dust and debris. Route cracks and blow dust/debris from them with oil-free compressed air. Following surface preparation, the strength of the surface can be tested if quantitative results are required by project specifications.

APPLICATION:
Tstrata 330 can be applied to Concrete, Composites, Wood or Metal. It can bond anchors, dowels and pins.

BASIC APPLICATION EQUIPMENT:
Processes for application of Tstrata 330 will require mixing drill and mixing paddle or pressure injection equipment capable of precisely metered resin delivery.

MIXING:
Pre-mix Part A and Part B separately for approximately 1 minute each. Blend Part A and Part B with a mechanical mixer for 3 minutes until uniformly blended using a low-speed drill and a Jiffy mixing paddle. Combine Part A and Part B in a 2 to 1 ratio by volume.

To make Tstrata 330 mortar, gradually add clean, dry, 20/40 mesh silica sand to previously mixed epoxy and mix thoroughly for an additional 3 minutes. The mix ratio of aggregate to mixed epoxy is approximately 3 to 1 by volume but can be modified depending on the desired consistency of the mortar. The sides and bottom of the container should be scraped at least once during mixing. Avoid entrapping air during mixing. Follow ICRI Guidelines for mortar mixing.

PRESSURE INJECTING OF CRACKS:

Vertical cracks: Attach injection ports and seal the face of the crack with V-Wrap PF or Tstrata GEL. Allow the sealing gel to sufficiently harden before injecting, to prevent blowouts. Pump Tstrata 330 into the crack via the injection ports, using two-component pressure injection equipment. Start at the bottom of the crack and work upwards from port to port. Cap off ports as you proceed up the crack to ensure that the epoxy is kept contained within the crack. DO NOT INJECT IF WATER IS LEAKING FROM THE CRACK.

Horizontal cracks: Open cracks by mechanical means and ensure that the prepared crack is free of all debris and standing water. If pressure injecting, instructions are the

structural TECHNOLOGIES

structuraltechnologies.com

+1-410-859-6539

same as for vertical cracks. If gravity feeding, pump Tstrata 330 until cracks are completely filled. If working on an elevated slab, ensure the bottom of the slab is sealed prior to injecting or gravity feeding the crack, to ensure epoxy does not leak through.

ANCHORING BOLTS, DOWELS, & PINS:
Tstrata 330 can be used neat or as a mortar to grout vertically-aligned anchors (into a horizontal substrate). The anchor hole should be free of all debris before grouting. The hole sides should be scored to facilitate bond. The optimum hole size is 1/16" (1.6 mm) annular space (1/8" (3.2 mm) larger diameter than anchor diameter). Depth of embedment is typically 10 to 15 times anchor diameter.

PATCHING AND REPAIRS:
Apply Tstrata 330 neat as a primer coat to the prepared concrete surface. Mix the Tstrata 330 into an epoxy mortar and apply to the area by trowel or spatula in lifts of 1" to 1-1/2" (25 to 38 mm) before the neat primer coat becomes tack free. Allow each lift to reach initial set before applying subsequent lifts.

COVERAGE:
One-gallon Tstrata 300 is 231 cubic inches. Pressure injection coverage will vary with concrete conditions.

CLEAN UP:
Use methyl ethyl ketone or acetone for clean-up. Clean tools and application equipment immediately. Observe fire and health precautions when using solvents. Dispose of in accordance with local regulations. Clean spills or drips with the same solvents while still wet.

OBSERVE WORKING TIME LIMITATIONS:
Mix no more material than can be applied within the working time. Ambient temperatures should be between 50°F and 90°F (10°C and 32°C). Material temperatures should be at least 50°F (10°C) and rising. Working time and cure time will decrease as the temperature increases and will increase as the temperature decreases.

PACKAGING:

	Volume	Weight	Package
Part A	2.0 gal	19 lbs	1 gal can
Part B	1.0 gal	8.5 lbs	1 gal can

SHELF LIFE:
Stored at 70°F (21°C): 24 months (Parts A and B)

STORAGE:
Store in a cool, dry area (40°F and 90°F [4°C to 32°C]) away from direct sunlight, flame or other hazards.

HANDLING:
Approved personal protection equipment should be worn at all times. Particles mask is recommended when handling airborne particles. Wear chemical resistant clothing /gloves/goggles. Ventilate area. In absence of adequate ventilation, use properly fitted NIOSH respirator. Product Safety Data Sheets (SDS) are available and should be consulted and on hand whenever handling these products.

These products are for professional and industrial use only and are to be installed by trained and qualified applicators. Trained applicators must follow installation instructions.

SAFETY:
WARNING: Vapor may be harmful. Contains epoxy adhesive and curing agent. May cause skin sensitivity, burns or other allergic responses. Keep away from heat, sparks or open flame. In enclosed areas or where ventilation is poor use an approved air mask and utilize adequate safety precautions to prevent fire or explosion. In case of skin contact, wash with soap and water. For eyes, flush immediately (seconds count) with water for 15 minutes and CALL A PHYSICIAN. If swallowed, CALL A PHYSICIAN IMMEDIATELY.

LIMITATIONS:
Do not thin Tstrata 330.Tstrata 330 will discolor upon prolonged exposure to ultraviolet light and high-intensity artificial lighting. Tstrata 330 is not to be used as a finished/aesthetic coating. Do not use Tstrata 330 for horizontally-aligned anchors (into a vertical substrate). Do not use Tstrata 330 for overhead anchoring

STRUCTURAL TECHNOLOGIES, LLC warrants its products to be free from manufacturing defects and to meet STRUCTURAL TECHNOLOGIES' current published properties when applied in accordance with STRUCTURAL TECHNOLOGIES' directions and tested in accordance with ASTM and STRUCTURAL TECHNOLOGIES Standards. User determines suitability of product for use and assumes all risks. Buyer's sole remedy shall be limited to the purchase price or replacement of product and excludes labor or the cost of labor. Any claim for breach of this warranty must be brought within one year of the date of purchase.

No other warranties expressed or implied including any warranty of merchantability or fitness for a particular purpose shall apply. STRUCTURAL TECHNOLOGIES shall not be liable for any consequential or special damages of any kind, resulting from any claim or breach of warranty, breach of contract, negligence or any legal theory. STRUCTURAL TECHNOLOGIES assumes no liability for use of this product in a manner to infringe on another's patent.

APPENDEX B–Concrete Mix Design

CATALINA PACIFIC
A CALPORTLAND Company

STATEMENT OF MIX DESIGN

PROJECT	COP: 95783 UCLA 420 WESTWOOD PLAZA LOS ANGELES, CA	04/21/19
CONTRACTOR	CUST: 1001315 WEBCOR BUILDERS 1751 HARBOR BAY PKWY., STE 200 ALAMEDA, CA 94502	
MIX: O40D2S8	6000 psi @ 28 Days. 1/2" Gravel Pump/Place Mix. 8 ± 1 Inches Slump.	
GRADATIONS	with EAGLEROCK , Port McNeill, B.C. (**Orca**) Aggregates.	

Aggregates	2"	1 1/2"	1"	3/4"	1/2"	3/8"	#4	#8	#16	#30	#50	#100	#200
W.C. SAND						100	99	81	66	49	25	6	2
1/2" AGGR				100	91	68	14	4	0	0	0	0	0
COMBINED	100	100	100	100	96	84	57	43	33	25	13	3	1

Materials	BATCH WEIGHTS 1 CU YD @ SSD		SPECIFIC GRAVITY			ABSOLUTE VOLUME	
CEMENT - TYPE II/V	563 lbs	7.98 equiv.	3.15	X	62.4	2.86	
FLY ASH	187 lbs		2.35	X	62.4	1.28	
W.C. Sand	1495 lbs	50.0 %	2.78	X	62.4	8.62	
1/2" G	1549 lbs	50.0 %	2.88	X	62.4	8.62	
WATER (MAXIMUM)	300.0 lbs	36.0 gals	1	X	62.4	4.81	
WRDA 64	29.00 ozs						Dosage Range: 2.0 - 5.0 ozs/cwt
ADVA	29.00 ozs						Dosage Range: 2.0 - 10.0 ozs/cwt
3.0% ENTRAPPED AIR			3.00%	X	27	0.81	
TOTALS	4094 lbs					27.00	

METHOD: 2016 California Building Code (CBC) ACI 301-16,

WATER/CEMENT RATIO: 4.5 gals/sack (0.40)

STRENGTH RESULTS: 5880 psi @ 7 Days, 8180 psi @ 28 Days with Laboratory Prepared Cylinders.

REMARKS:

LICENSED PROFESSIONAL ENGINEER
DANIEL RAY SUSDORF
C 88335
EXP. 03/31/20
CIVIL
STATE OF CALIFORNIA

Wendi Williams
Laboratory Support Administrator

NOTE: This mix should be approved by the project's structural engineer or architect. Mix designed for CalPortland only. No substitution or alterations may be made. Approval of this mix design carries the inclusion of CalPortland on the distribution list for all concrete Test results.

2025 E. Financial Way • Glendora, CA 91741   Telephone: (626) 852-6200 • Fax: (626) 963-2341

www.calportland.com   **EXPECT MORE... WE DELIVER!**

CATALINA PACIFIC
A CALPORTLAND Company

TRIAL BATCH RESULTS

Mix Design: O40D2S87

Proportioning: CBC

Water/Cementitious Ratio: 0.40

Ingredients	Cu Yd Weights	Specific Gravities	Absolute Volume (Cu Ft)
Cement Type II/V	563 lbs	3.15	2.86
Fly Ash	187 lbs	2.35	1.28
Water (Design)	300 lbs	1.00	4.81
W C Sand	1495 lbs	2.78	8.62
1/2" x #4 Gravel	1549 lbs	2.88	8.62
Entrapped Air (3%)			0.81
Admixtures:			
WRDA 64	29.0 ozs		
ADVA 195	29.0 ozs		

TESTING RESULTS (ASTM C 192)

Date Cast: August 8, 2017
Slump: 9.25 inches
% air: 3.4%
Temperature:
(Concrete/Air) 84^{o}/ 88^{o}

Plastic Unit Weight: 153.8 pcf

COMPRESSIVE STRENGTH RESULTS (ASTM C 39)

Number	7 Day	28 Day	56 Day	90 Days
1	5885 psi	8470 psi	8980 psi	9650 psi
2	5820 psi	7900 psi	8970 psi	9490 psi
3	5922 psi	8160 psi	8920 psi	9480 psi
Average	5880 psi	8180 psi	8950 psi	9570 psi

DRYING SHRINKAGE RESULTS (ASTM C 157 as modified by SEAOC)

Prism Size (ASTM C490): 4" x 4" x 11" (gage length = 10" ± 0.10")

Total Age (Days)	Air Dry Age (Days)	Shrinkage Percentage
7	0	0.000
14	7	0.021
21	14	0.026
28	21	0.034
35	28	0.037

CALPORTLAND®

Manufacturer's Certification

Report Date: 3/15/2019

We hereby certify that CalPortland Type I/II/V Low Alkali Cement meets the standard requirements of ASTM C150 and AASHTO M85 specification for Type I, Type II, and Type V cements. Additionally, CalPortland Type I/II/V Low Alkali Cement meets the optional requirement for low alkali (less than or equal to 0.60 total alkali). Reported are the average chemical and physical data for the month.

Month: February, 2019

Type I / II / V Low Alkali Cement

Source: Mojave, CA, USA

	ASTM C150 and AASHTO M85 Requirements			Analysis	Limestone
Chemical Properties	**Type I**	**Type II**	**Type V**	**Results**	**Analysis**
Silicon dioxide (SiO_2), %	---	---	---	**21.0**	**3.8**
Aluminum oxide (Al_2O_3), max, %	---	6.0	---	**3.9**	**1.1**
Ferric oxide (Fe_2O_3), max, %	---	6.0	---	**3.6**	**0.4**
Calcium oxide (CaO), %	---	---	---	**63.5**	**49.5**
Magnesium oxide (MgO), max, %	6.0	6.0	6.0	**2.1**	**1.2**
Sulfur trioxide (SO_3), max, %	3.0	3.0	2.3	**2.8**	**0.1**
Loss on ignition (LOI), max, %	3.5	3.5	3.5	**2.7**	
Insoluble residue (IR), max, %	1.5	1.5	1.5	**1.0**	**Base**
Alkalies ($Na_2O+0.658*K_2O$), max, %	0.60	0.60	0.60	**0.59**	**Cement**
Tricalcium silicate (C_3S), %	---	---	---	**53**	**55**
Dicalcium silicate (C_2S), %	---	---	---	**20**	**21**
Tricalcium aluminate (C_3A), max, %	---	8	5	**4**	**4**
Tetracalcium aluminoferrite (C_4AF), %	---	---	---	**11**	**11**
$C_4AF + 2(C_3A)$, max, %	---	---	25	**19**	
CO_2, %	---	---	---	**1.6**	
Limestone addition, max, %	5.0	5.0	5.0	**4.0**	
$CaCO_3$ in Limestone, min, %	70	70	70	**90**	
Physical Properties					
Air content of mortar, max, volume %	12	12	12	**7**	
Blaine Fineness, min, m^2/kg	260	260	260	**422**	
Autoclave expansion, max, %	0.80	0.80	0.80	**0.00**	
Compressive Strength, min					
3 Day, MPa	12.0	10.0	8.0	**28.2**	
3 Day, psi	1740	1450	1160	**4100**	
7 Day, MPa	19.0	17.0	15.0	**35.8**	
7 Day, psi	2760	2470	2180	**5200**	
28 Day (from previous month), MPa	---	---	21.0	**45.4**	
28 Day (from previous month), psi	---	---	3050	**6590**	
Vicat Setting Time, min-max, minutes	45 - 375	45 - 375	45 - 375	**155**	
C1038 expansion, max, %	0.020	0.020	0.020	**0.008**	

Apparatus and methods used in this laboratory have been checked by the Cement and Concrete Reference Laboratory of the National Institute of Standards and Technology. A copy of the report detailing their findings is available upon request. Major oxides are analyzed in accordance with ASTM C114.

Note: ASTM C150, Table 1, Note D, It is permissible to exceed the values in the table for SO_3 content, provided it has been demonstrated by Test Method C1038 that the cement with the increased SO_3 will not develop expansion exceeding 0.020% in 14 days.

Michael Stratford

Michael Stratford - Quality Control Superintendent

CalPortland Company 9350 Oak Creek Road Mojave, CA 93501-7738
www.calportland.com Customer Service 844-252-1527

BORAL RESOURCES

Materials Testing & Research Facility
2650 Old State Hwy 113
Taylorsville, GA 30178
770-684-0102

ASTM C618 / AASHTO M295 Testing of Pomona Terminal Fly Ash

Sample Date: 12/11 - 12/27/18
Sample Type: Composite
Sample ID: PO-026-18

Report Date: 2/27/2019
MTRF ID: 127PO

Chemical Analysis	Results		ASTM Limit Class F/C	AASHTO Limit Class F/C
Silicon Dioxide (SiO2)	58.13	%		
Aluminum Oxide (Al2O3)	19.94	%		
Iron Oxide (Fe2O3)	4.47	%		
Sum (SiO2+Al2O3+Fe2O3)	82.54	%	70.0/50.0 min	70.0/50.0 min
Sulfur Trioxide (SO3)	0.69	%	5.0 max	5.0 max
Calcium Oxide (CaO)	9.24	%		
Magnesium Oxide (MgO)	2.27	%		
Sodium Oxide (Na2O)	1.91	%		
Potassium Oxide (K2O)	1.17	%		
Moisture	0.05	%	3.0 max	3.0 max
Loss on Ignition	0.78	%	6.0 max	5.0 max

Physical Analysis				
Fineness, % retained on 45-µm sieve	17.89	%	34 max	34 max
Strength Activity Index - 7 or 28 day requirement				
7 day, % of control	87	%	75 min	75 min
28 day, % of control	95	%	75 min	75 min
Water Requirement, % control	94	%	105 max	105 max
Autoclave Soundness	0.01	%	0.8 max	0.8 max
Density	2.37			

The test data listed herein was generated by applicable ASTM methods. The reported results pertain only to the sample(s) or lot(s) tested. This report cannot be reproduced without permission from Boral Resources.

Doug Rhodes, CET
Facility Manager

AASHTO ACCREDITED

WRDA® 64

Water-reducing admixture

ASTM C494 Type A and D

Product Description

WRDA® 64 is a polymer based aqueous solution of complex organic compounds. WRDA 64 is a ready-to-use low viscosity liquid which is factory pre-mixed in exact proportions to minimize handling, eliminate mistakes and guesswork. WRDA 64 does not contain calcium chloride and weighs approximately 10.1 lbs/gal (1.21 kg/L).

Uses

WRDA 64 produces a concrete with lower water content (typically 8% to 10% reduction), greater plasticity and higher strength. It is used in ready-mix plants, block and concrete product plants, in lightweight and prestressed work wherever concrete is produced.

WRDA 64 also performs especially well in concrete containing fly ash and other pozzolans.

Finishability

The cement paste, or mortar, in WRDA 64 admixtured concrete has improved trowelability. The influence of WRDA 64 on the finishability of lean mixes has been particularly noticeable. Floating and troweling, by machine or hand, imparts a smooth, close tolerance surface.

Addition Rates

The addition rate of WRDA 64 is 3 to 6 fl oz/100 lbs (195 to 390 mL/100 kg) of cement. Pretesting is required to determine the appropriate addition rate for Type A and Type D performance. Optimum addition depends on the other concrete mixture components, job conditions, and desired performance characteristics.

Product Advantages

- Consistent water reduction and set times
- Improves performance concrete containing supplementary cementitious materials
- Produces concrete that is more workable, easy to place and finish
- High compressive and flexural strengths

Compatibility with Other Admixtures and Batch Sequencing

WRDA 64 is compatible with most GCP admixtures as long as they are added separately to the concrete mix, usually through the water holding tank discharge line. In general, it is recommended that WRDA 64 be added to the concrete mix near the end of the batch sequence for optimum performance. Different sequencing may be used if local testing shows better performance. Please see GCP Technical Bulletin TB-0110, *Admixture Dispenser Discharge Line Location and Sequencing for Concrete Batching Operations* for further recommendations.

Pretesting of the concrete mix should be performed before use, as conditions and materials change in order to assure compatibility, and to optimize dosage rates, addition times in the batch sequencing and concrete performance. For concrete that requires air entrainment, the use of an ASTM C260 air-entraining agent (such as Daravair® or Darex® product lines) is recommended to provide suitable air void parameters for freeze-thaw resistance. Please consult your GCP Applied Technologies representative for guidance.

Packaging & Handling

WRDA 64 is available in bulk, delivered by metered tank trucks, totes and drums.

WRDA 64 will freeze at about 28 °F (-2 °C), but will return to full strength after thawing and thorough agitation.

Dispensing Equipment

A complete line of accurate, automatic dispensing equipment is available. WRDA 64 may be introduced to the mix on the sand or in the water.

Specifications

Concrete shall be designed in accordance with *Standard Recommended Practice for Selecting Proportions for Concrete*, ACI 211.

The water-reducing (or water-reducing and retarding) admixture shall be WRDA 64, as manufactured by GCP Applied Technologies, or equal. The admixture shall not contain calcium chloride. It shall be used in strict accordance with the manufacturers' recommendations. The admixture shall comply with ASTM Designation C494, Type A water-reducing (or Type D water-reducing and retarding) admixtures. Certification of compliance shall be made available on request.

The admixture shall be considered part of the total water. The admixture shall be delivered as a ready-to-use liquid product and shall require no mixing at the batching plant or job site.

GCP Applied Technologies Inc., 62 Whittemore Avenue, Cambridge, MA 02140 USA.

In Canada, 294 Clements Road, West, Ajax, Ontario, Canada L1S 3C6.

GCP0083 CMD-366-1216

gcp applied technologies

gcp applied technologies

ADVA® 195

High-range water-reducing admixture

ASTM C494 Type A and F and ASTM C1017 Type I

Product Description

ADVA® 195 is a polycarboxlate-based high-range water-reducing admixture specifically formulated to meet the needs of the concrete industry. It is a low viscosity liquid, which has been formulated by the manufacturer for use as received. ADVA 195 is manufactured under closely controlled conditions to provide uniform, predictable performance and is formulated to comply with specifications for *Chemical Admixtures for Concrete*, ASTM Designation C494 as a Type A and F, and ASTM C1017 Type I admixture. ADVA 195 does not contain intentionally added calcium chloride. One gallon weighs approximately 8.8 lbs (1.1 kg/L).

Uses

ADVA® 195 superplasticizer produces concrete with extremely workable characteristics referred to as high slump. It also allows concrete to be produced with very low water/cement ratios for high strength.

While ADVA 195 is ideal for use in any concrete where it is desired to minimize the water/cementitious ratio yet maintain workability, ADVA 195 is primarily intended for use in ready-mix concrete, but may also be used in other applications such as precast concrete and self-consolidating concrete.

Addition Rates

ADVA 195 superplasticizer addition rates can vary with type of application, but will normally range from 3 to 15 fl oz/100 lbs (195 to 980 mL/100 kg) of cementitious. In most instances, the addition of 3 to 6 fl oz/ 100 lbs (195 to 375 mL/100 kg) of cementitious will be sufficient. At a given water/cementitious ratio, the slump required for placement can be controlled by varying the addition rate. Should conditions require using more than the recommended addition rates, please consult your GCP Applied Technologies representative.

ADVA 195 dosage requirements may also be affected by mix design, cementitious content and aggregate gradations. Please consult with your GCP Applied Technologies representative for more information and assistance.

Compatibility with Other Admixtures and Batch Sequencing

ADVA 195 is compatible with most GCP admixtures as long as they are added separately to the concrete mix. However, ADVA products are not recommended for use in concrete containing naphthalene-based admixtures including Daracem® 19 and Daracem 100, and melamine-based admixtures including Daracem 65. In general, it is recommended that ADVA 195 be

Product Advantages

- Highly efficient, producing high slump concrete at very low dosages
- Provides a combination of slump life with near neutral set time
- Consistent air entrainment
- Consistent performance across cement chemistries
- Concrete finishes easily without stickiness, spotty set or tearing

added to the concrete mix near the end of the batch sequence for optimum performance. Different sequencing may be used if local testing shows better performance. Please see GCP Technical Bulletin TB-0110, *Admixture Dispenser Discharge Line Location and Sequencing for Concrete Batching Operations* for further recommendations.

Pretesting of the concrete mix should be performed before use and as conditions and materials change in order to assure compatibility with other admixtures, and to optimize dosage rates, addition times in the batch sequencing and concrete performance. For concrete that requires air entrainment, the use of an ASTM C260 air-entraining agent (such as Daravair® or Darex® product lines) is recommended to provide suitable air void parameters for freeze-thaw resistance. Please consult your GCP Applied Technologies representative for guidance.

Packaging & Handling

ADVA 195 is available in bulk, delivered by metered tank trucks, in totes and drums.

It will begin to freeze at approximately 32°F (0°C), but will return to full strength after thawing and thorough agitation. In storage, and for proper dispensing, ADVA 195 should be maintained at temperatures above 32°F (0°C).

Dispensing Equipment

A complete line of accurate, automatic dispensing equipment is available.

ADVA 195 ASTM C494 Type F High-Range Water Reducer Test Data

	U.S. Units		Metric	
	Control	**ADVA 195**	**Control**	**ADVA 195**
Cement (pcy) (kg/m³)	517	517	307	307
Coarse aggregate (pcy) (kg/m³)	1944	1944	1153	1153
Fine aggregate (pcy) (kg/m³)	1144	1214	679	720
Water (pcy) (kg/m³)	235	204	396	344
w/cm	0.455	0.405	0.455	0.405
Slump (inches) (mm)	3.75	3.5	95	90
Plastic air (%)	5.5	5.4	5.5	5.4
Compressive strength				
1 day (psi) (MPa)	1860	2670	12.8	18.4
7 day (psi) (MPa)	4520	5530	31.2	38.1
28 day (psi) (MPa)	5440	6690	37.5	46.1
Initial set time (hr:min)	4:02	3:55	4:02	3:55
Length change 28 day (%)	-0.031	-0.028	-0.031	-0.028
Freeze-thaw resistance (RDME %)	92	98	92	98

GCP Applied Technologies Inc., 62 Whittemore Avenue, Cambridge, MA 02140 USA.

In Canada, 294 Clements Road, West, Ajax, Ontario, Canada L1S 3C6.

GCP0083 DC-64-1116

gcp applied technologies

APPENDEX C–Mill Certificate of W12x40 Section Used for CB6

Invoice No.	630268
Bill of Lading	152912
Customer No.	7950
Customer P.O	338-19

NUCOR-YAMATO STEEL CO.
P.O. BOX 1228: BLYTHEVILLE, AR 72316

CERTIFIED MILL TEST REPORT
100% Melted and Manufactured in U.S.A
All Shapes produced by Nucor-Yamato Steel are cast and rolled to a fully killed and fine grain practice

Date	2019-02-13

SOLD TO
HERRICK CORPORATION
BOX 8429
STOCKTON CA 95208
USA

SHIP TO
SAN BERNARDINO STEEL
C/O KEEP ON TRUCKING
RANCHO CUCAMONGA, CA FOR TRK DEL TO
SAN BERNARDINO CA 92235
USA

ASTM A992/A992M-11 A572/A572M GR50-15
ASTM A709/A709M-15 GR50 (345)
ASTM A709/A709M-15 GR50S (345S)
CSA G40.21-13 50WM (345WM)
ASTM A6/A6M-14

Item#	Item Description	QTY	Heat#	Mechanical Properties								
				Yield to Tensile Ratio	Yield Strength	Tensile Strength	ELONG	Charpy Impact: Temp	Charpy Impact: Impact Energy			Charpy Impact: Loc
					KSI	KSI	%	° F	ft• lbf			
					MPa	MPa	%	° C	J			
1	W12X040.0 62 ft 0 in W310X 60 (18.90 m)	2	420080	0.78 0.75	57 55 393 379	73 73 503 503	24.9 26.3	40 4	53 72	49 66	68 92	Fla

Item#	Chemical Properties: C	Mn	P	S	Si	Cu	Ni	Cr	Mo	V	Cb	CE	Sn	Pcm	CI
1	.08	1.00	.016	.025	.25	.28	.10	.12	.03	.00	.016	.30	.01	.16	

ELONGATION BASED ON 8.00 INCH GAUGE LENGTH
Pcm= C+Si/30+Mn/20+Cu/20+Ni/60+Cr/20+Mo/15+V/10+5B(B=Approx .0005)
Corrosion Index= 26.01(%Cu)+3.88(%Ni)+1.2(%Cr)+1.49(%Si)+17.28(%P)-7.29(%Cu)(%Ni)-9.10(%Ni)(%P)-33.39(%Cu)^2
ISO 9001:2015 certified (Registration # 0985-07).

CARBON EQUIVALENT CE= C+Mn/6+(Cr+Mo+V)/5+(Ni+Cu)/15
Mercury has not been used in the direct manufacturing of this material
This material was produced in accordance with the Nucor-Yamato Steel Quality Manual.

All mechanical testing is performed by the Quality Testing Lab, which is independent of the production departments.
The Charpy machine striker geometry used by Nucor-Yamato Steel is the 8 mm (0.315")striker (KV_8) per ASTM A370 Section 22.1.2 and ISO 148-1 Section 7.3.

I hereby certify that the contents of this report are accurate and correct. All test results and operations performed by this material manufacturer are in compliance with the requirements of the material specifications, and when designated by the purchaser, meet the applicable specifications.

Gary Lennell
Chief Metallurgist

State of Arkansas
County of Mississippi
Sworn to and subscribed before me

Deborah Ann Rhodes
on 2019-02-13
My commission expires on 07/17/2023

DEBORAH ANN RHODES
NOTARY
PUBLIC
STATE OF ARKANSAS-MISSISSIPPI COUNTY

APPENDEX D–Strain Gages

To measure strain in the longitudinal, diagonal, and transverse reinforcement and the steel section at locations of interest (as shown in **Figure**s **D-1** to **D-4**), prewired linear strain gages (KFH-6-120-C1-11L3M3R) manufactured by Omega Engineering, Inc. were used (**Table D-1**). The strain gage locations on the rebar and steel section were grinded and smoothed (**Figure**s **D-5** (***a***) and (***b***)). The prepared surfaces were then cleaned and degreased using suitable chemicals (M-Prep conditioner A and M-Prep Neutralizer 5A) and a procedure recommended by the manufacturer. The strain gages were installed carefully in the right locations using appropriate adhesive materials (**Figure**s **D-5** (***c***)) and a procedure recommended by the manufacturer. Then, the strain gages were waterproofed using silicon sealant and protected (**Figure**s **D-5** (***d***) and (***e***)) and secured using electrical tape to prevent the gage from damaging during cage and concrete placement (**Figure**s **D-5** (***f***)). It should be mentioned that the strain gages were tested twice before and after pouring the concrete to ensure they meet the requirements given by the manufacturer. Finally, the strain gages were labeled properly to prevent confusion when reading data.

Table D-1. Strain gage information

Strain gage number	KFH-6-120-C1-11L3M3R
Grid style	Linear
Grid length range	6 mm
Grid length	2 mm
Temperature range	-10 to 155°C (-14 to 320°F)
Connection type	Three 3 m leads
Resistance	120 Ω
STC number	ST
Maximum strain	50,000 µm
Features	Prewired

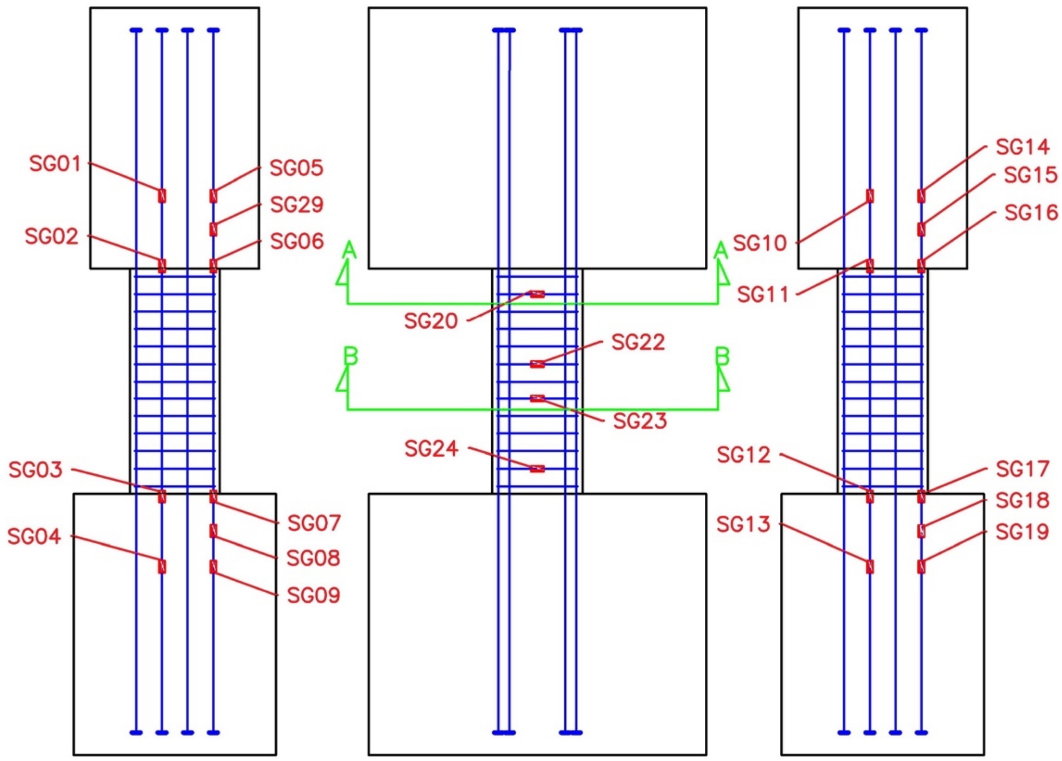

(*a*) Bottom (web) view (*b*) Side view (*c*) Top (slab) view

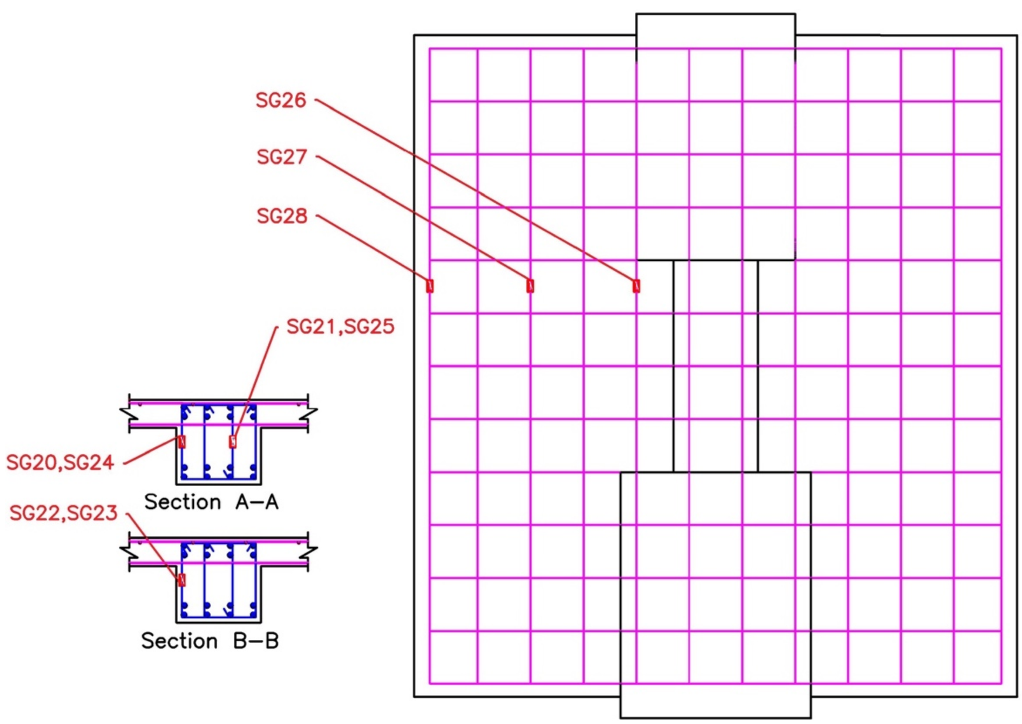

(*d*) Cross-section views (*e*) Top slab view

Figure D-1. Strain gage layout of CB1.

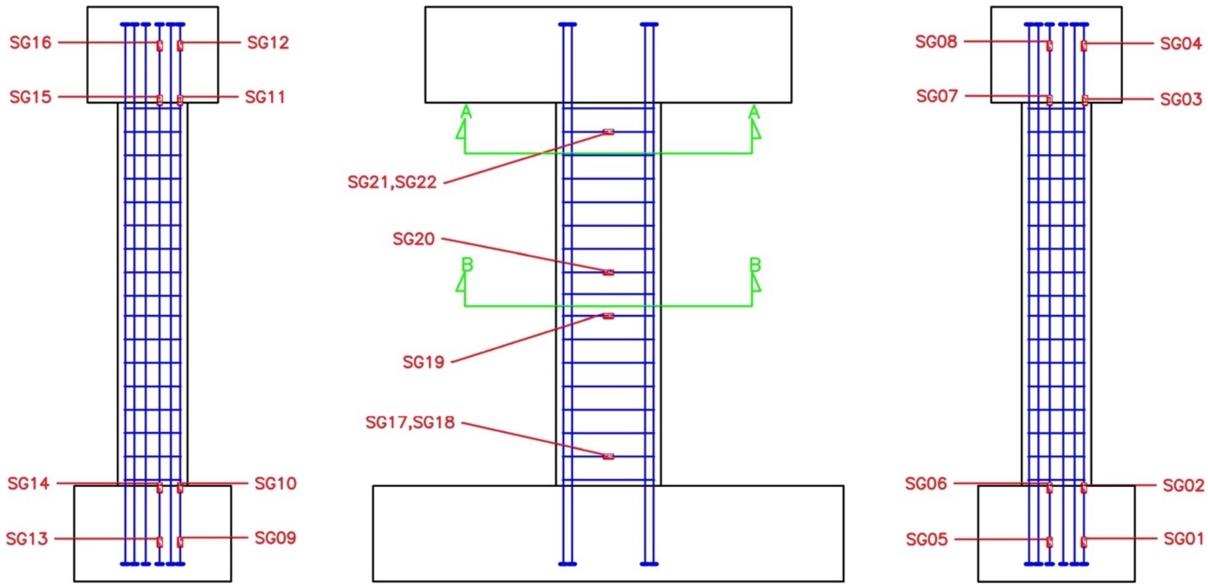

(*a*) Bottom (web) view (*b*) Side view (*c*) Top (slab) view

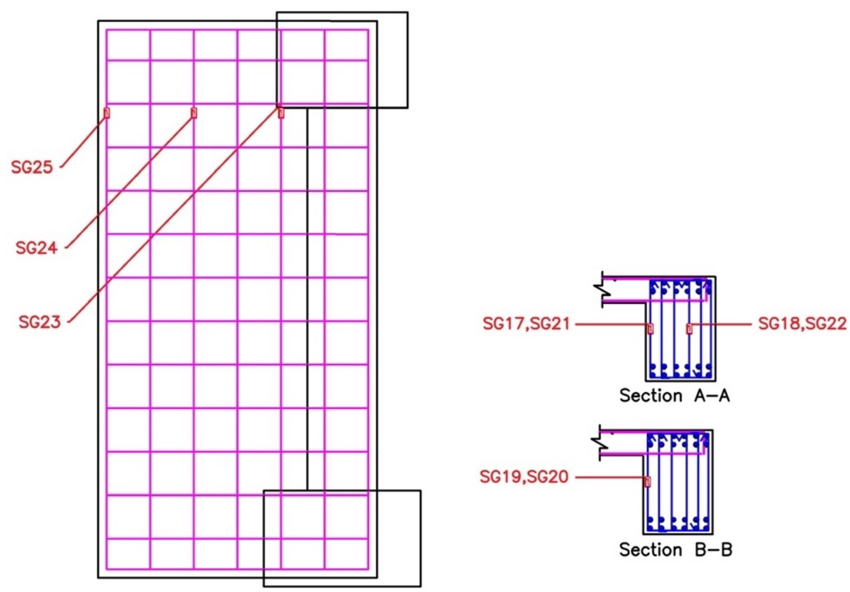

(*d*) Top slab view (*e*) Cross-section views

Figure D-2. Strain gage layout of CB2.

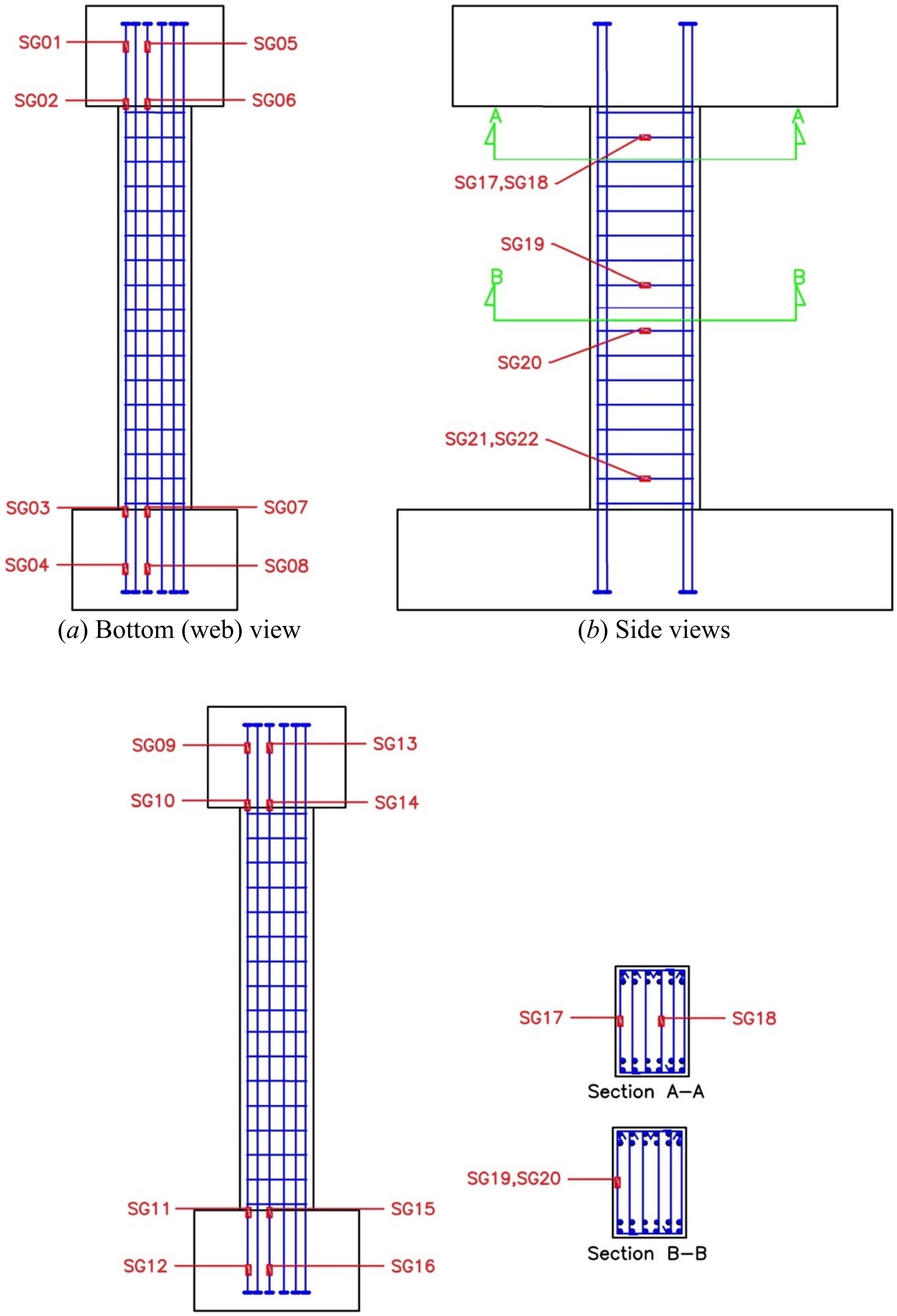

(*a*) Bottom (web) view (*b*) Side views (*d*) Top (slab) view (*e*) Cross-section views

Figure D-3. Strain gage layout of CB3.

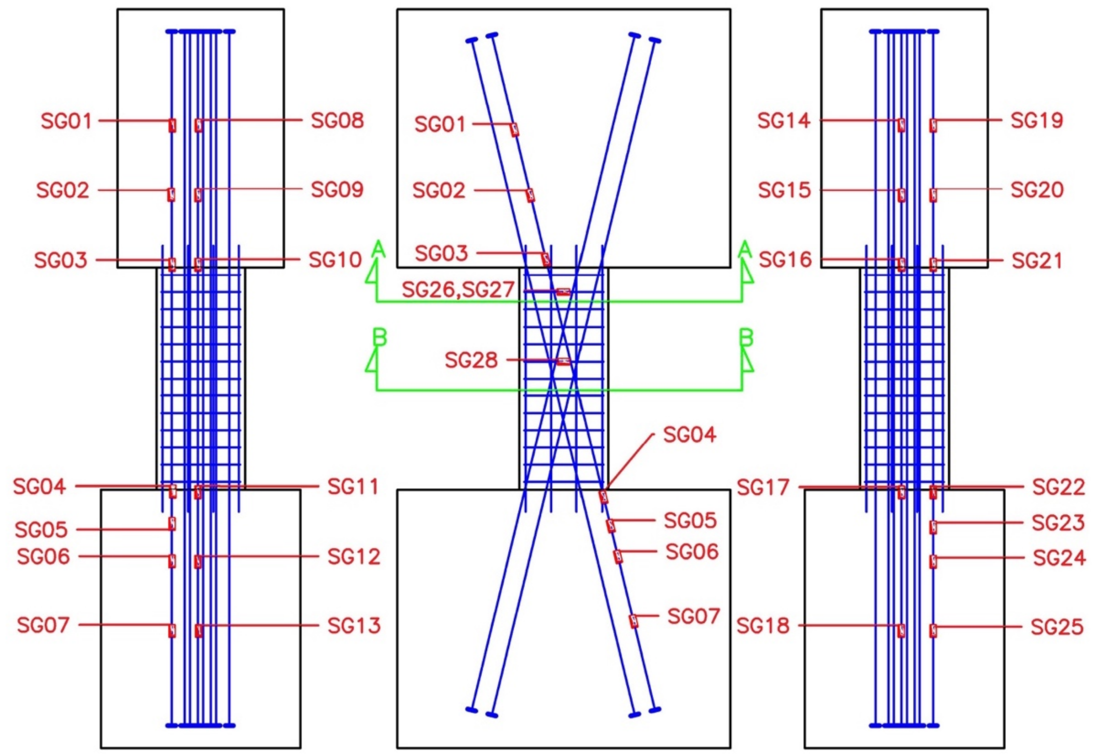

(*a*) Bottom (web) view (*b*) Side view (*c*) Top (slab) view

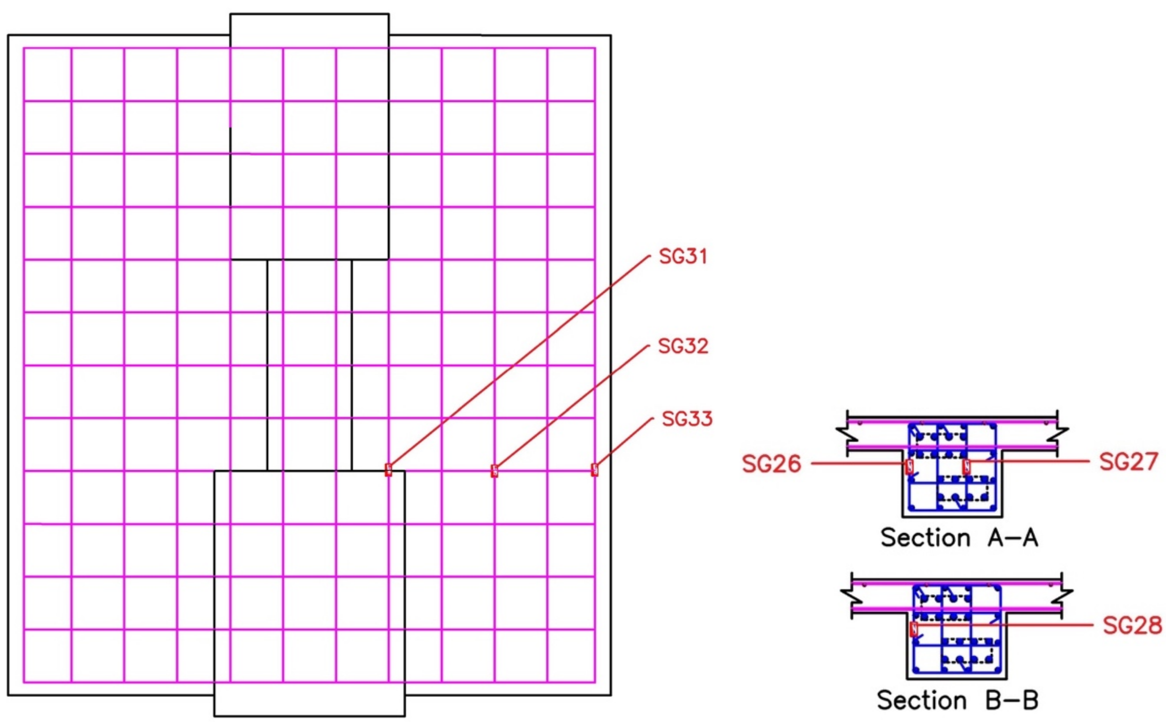

(*d*) Top slab view (*e*) Cross-section views

Figure D-4. Strain gage layout of CB4.

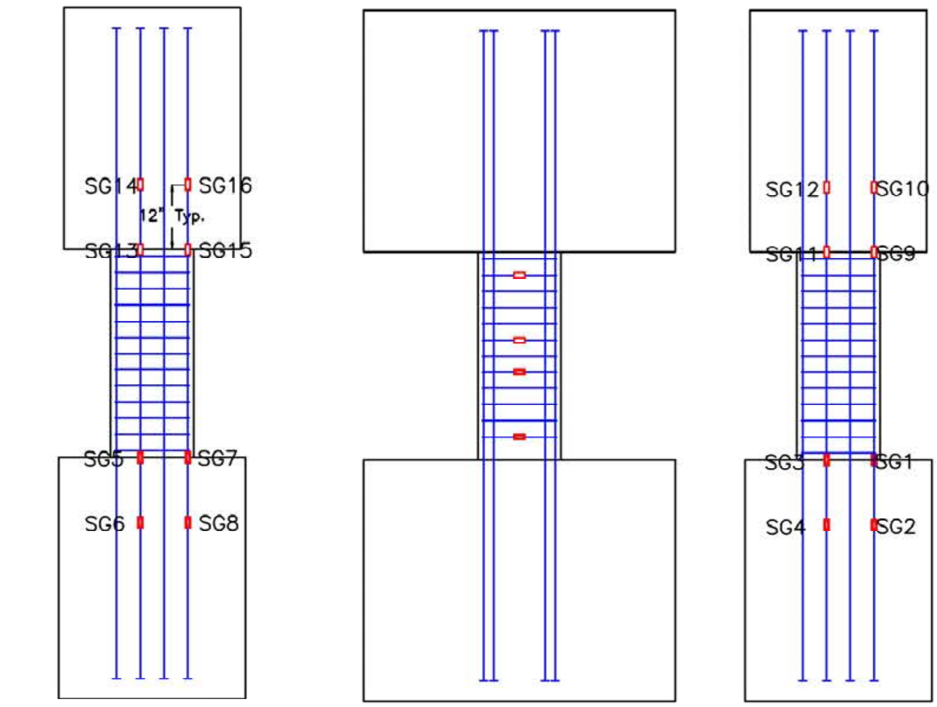

(*a*) Bottom (web) view (*b*) Side view (*c*) Top (slab) view

Figure D-5. Strain gage layout of CB5.

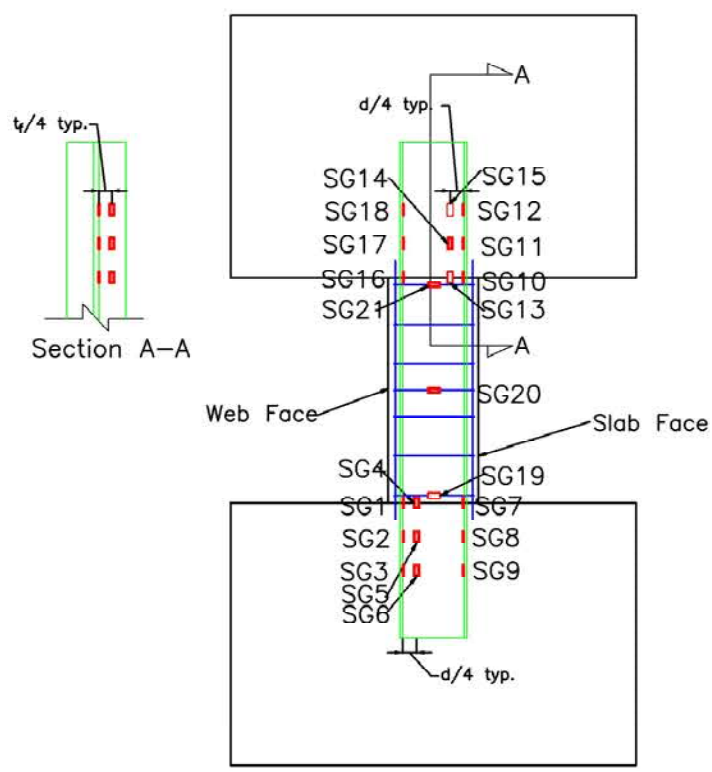

Figure D-6. Strain gage layout of CB6.

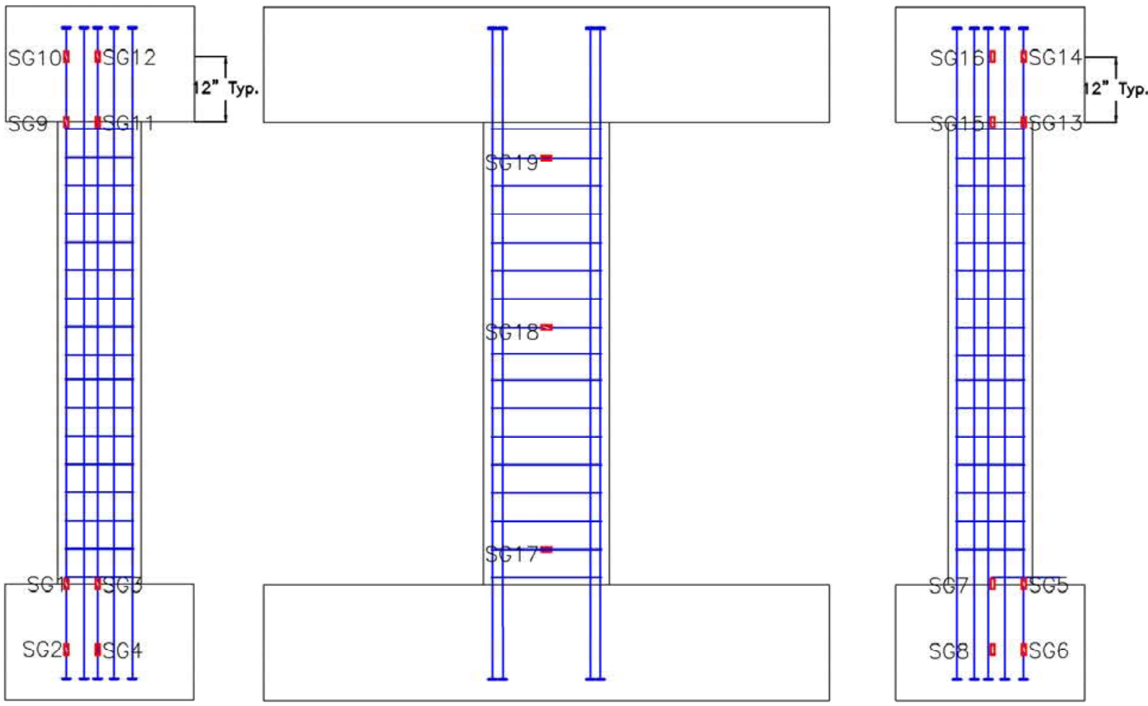

(*a*) Bottom (web) view (*b*) Side view (*c*) Top (slab) view

Figure D-7. Strain gage layout of CB7.

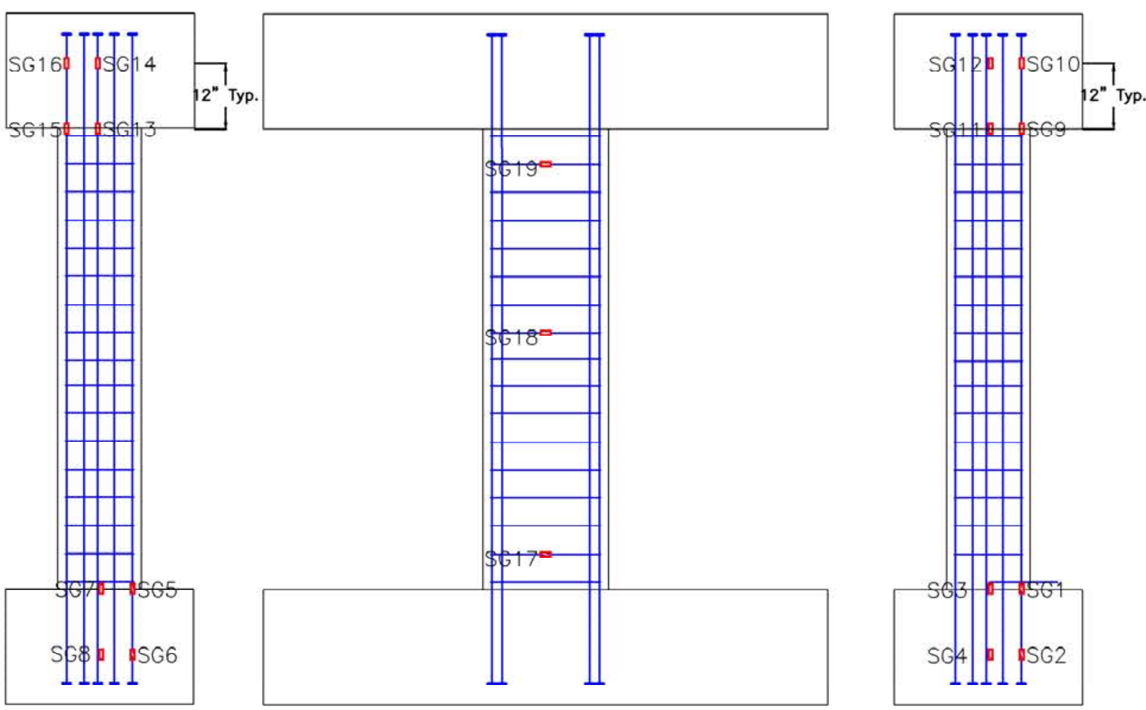

(*a*) Bottom (web) view (*b*) Side view (*c*) Top (slab) view

Figure D-8. Strain gage layout of CB8.

(*a*) Prepared rebar surfaces

(*b*) Close-up of prepared rebar surface

(*c*) Strain gage glued to rebar surface

(*d*) Waterproofing strain gages: steel section

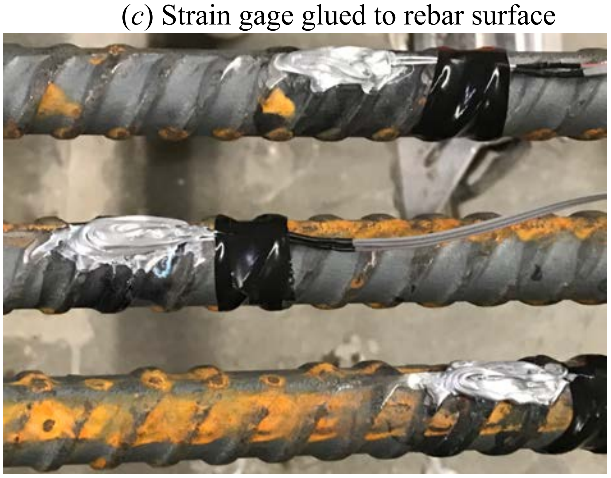

(*e*) Waterproofing strain gages: rebar

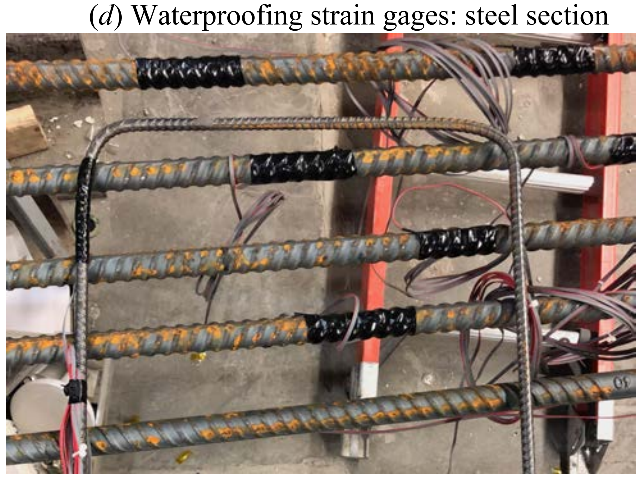

(*f*) Wrapping strain gages with electrical tape

Figure D-9. Wrapped strain gages on beam longitudinal and transverse bars.

APPENDEX E–Stiffness Calculations

The secant flexural stiffness values (commonly referred to as $E_c I_{se}$) of coupling beams with a fixed-fixed end condition (**Figure E-1** (***a***)) is given by **Equation E-1**:

$$E_c I_{se} = \frac{V l_n^2}{12\theta_{total}} \quad (\mathrm{E}-1)$$

Since the tested concrete compressive strength of the beams is greater than 6000 psi (41.4 MPa) as shown in **Table 2-4**, the concrete for all specimens can be considered high-strength concrete. Therefore, **Equation E-2** (ACI 363R-10) was used to calculate the concrete Young's modulus (E_c):

$$E_c(\mathrm{psi}) = 40000\sqrt{f'_{c,test}\ (\mathrm{psi})} + 10^6 \quad (\mathrm{E}-2a)$$

$$E_c(\mathrm{MPa}) = 3320\sqrt{f'_{c,test}\ (\mathrm{MPa})} + 6900 \quad (\mathrm{E}-2b)$$

Although the test setup was designed to provide zero rotation at the ends (**Figure E-1** (***a***)), a slight rotation of the top block was observed due to flexibility of the top structural steel beam and slight looseness in the connections between the vertical actuators and the structural steel beam (**Figure 2-12**), creating a fixed-partially fixed condition (**Figure E-1** (***b***)) that was found to slightly-to-moderately influence the stiffness calculations particularly at low, pre-yield, displacement demands. The top block rotation (θ_{top}) was measured and was accounted for in the stiffness calculations using **Equation E-3**:

$$E_c I_{se} = \frac{V l_n^2}{\left(12\theta_{total} - 6\theta_{top}\right)} = \frac{V l_n^2}{12\left(\theta_{total} - \frac{\theta_{top}}{2}\right)} \quad (\text{E}-3)$$

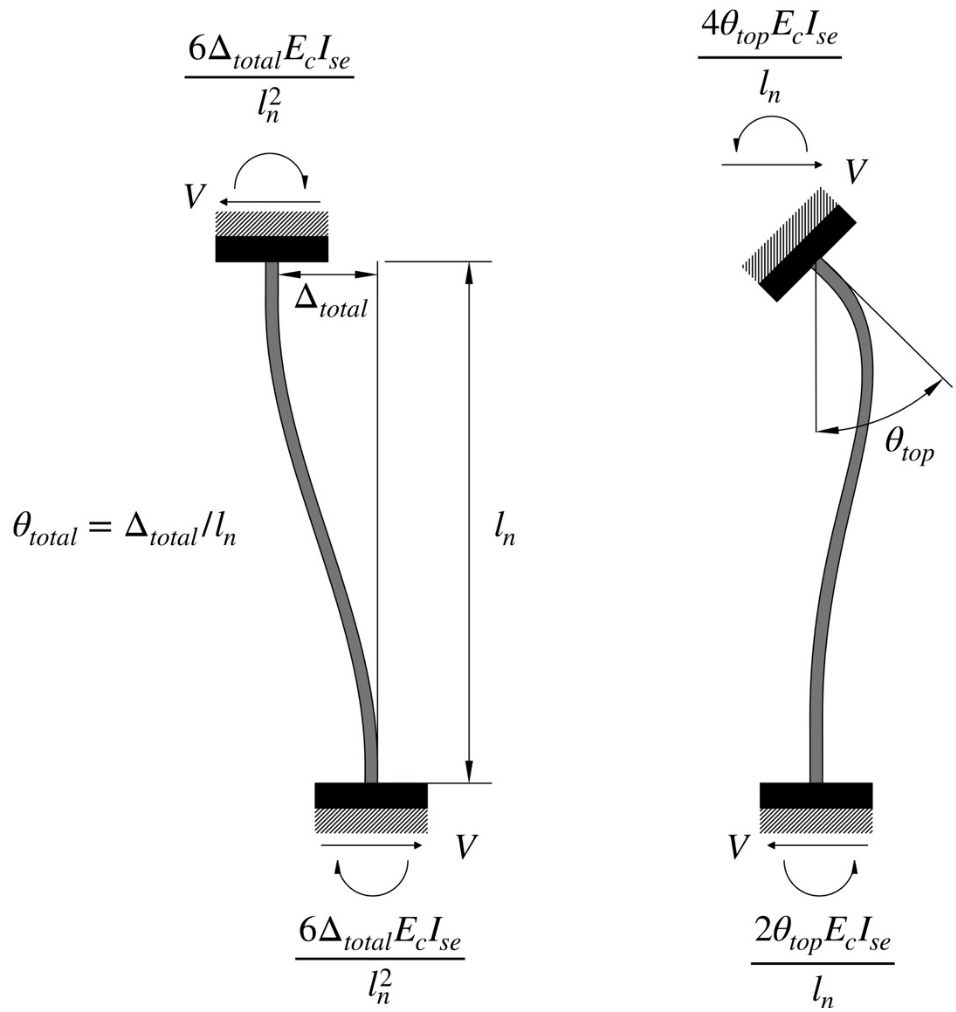

(*a*) Fixed-fixed beam (*b*) Fixed-partially fixed beam

Figure E-1. Test setup moment reactions.

APPENDEX F–Calculation of Components of Total Rotation

This appendix presents the approach used to compute the various sources of beam chord rotation from the sensor measurements. The sources consist of deformations due to slip/extension of bars or steel section from walls (end blocks), flexure (curvature), shear distortion, and sliding at the beam-wall interfaces, as shown in **Equation F-1** and **Figure F-1**. The flexure and shear deformations were determined using LVDTs attached to the coupling beams (vertical and X-shaped configurations), whereas the slip/extension deformations were determined from LVDTs spanning across the beam-wall interfaces, and the sliding displacements were determined from LVDTs installed at the beam-wall interfaces measuring the displacement of the beam ends relative to the walls in the direction of loading. Contribution of each deformation component to the total chord rotation during each load/displacement level was determined as shown in following sections:

$$\theta_{total} = \theta_{slip/ext} + \theta_{flexure} + \theta_{shear} + \theta_{sliding} \qquad (\mathrm{F}-1)$$

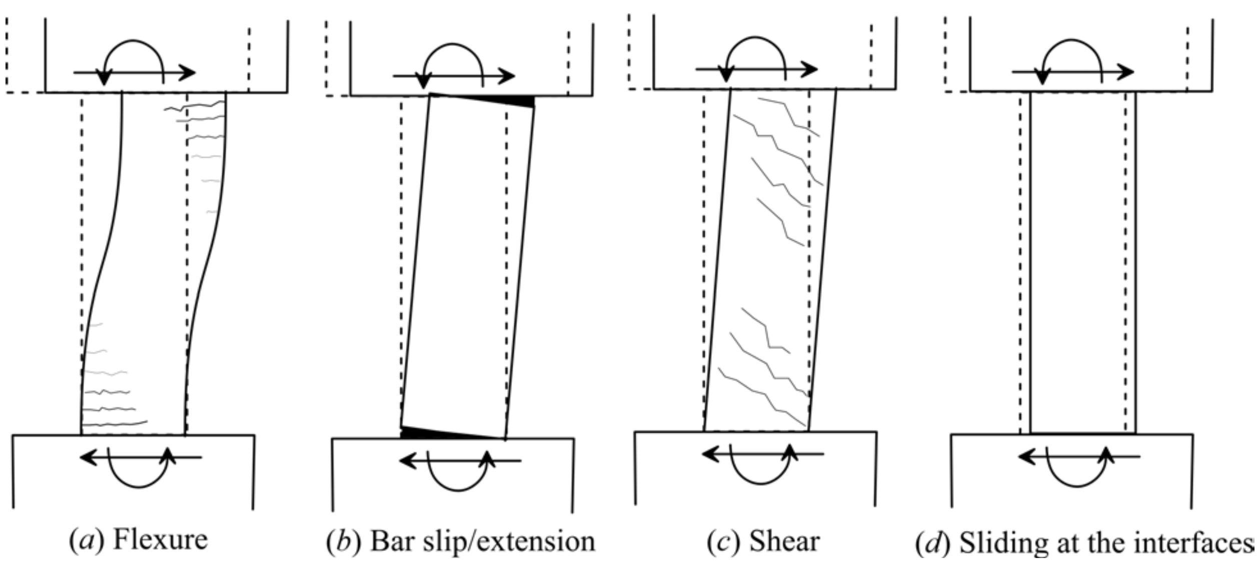

Figure F-1. Various sources of deformation in coupling beams.

1. Deformation due to Slip/Extension of Bars or Steel Section

As noted previously, the slip/extension of the longitudinal/diagonal bars or steel section from the walls was measured using the LVDTs spanning across the beam-wall interfaces, as shown in **Figure F-2**. In perfect double curvature test setup and identical embedment conditions (i.e., development lengths), the slip/extension rotation at one end of the beam would theoretically be equal to the slip/extension rotation at the other end and chord rotation (i.e., $\theta_{slip/ext,top} = \theta_{slip/ext,bottom} = \theta_{slip/ext}$), as illustrated in **Figure F-3**. However, as noted in the preceding appendix, a slight rotation of the top block was observed due to flexibility of the top structural steel beam and slight looseness in the connections between the vertical actuators and the structural steel beam, $\theta_{slip/ext,top}$ was not be equal to $\theta_{slip/ext,bottom}$. Furthermore, since rotation due to slip/extension is a rigid body rotation, only slip/extension at the bottom interface contributes to lateral displacement at the top end of the beam, **Equation F-2** was used to determine chord rotation contributed by slip/extension using measurements from the LVDT layout shown in **Figure F-2**.

$$\theta_{slip/ext} = \left(\frac{\delta_{LVDT1} + \delta_{LVDT2}}{l_1}\right) \qquad \text{(F} - 2)$$

Where δ_{LVDT1} and δ_{LVDT2} are displacements measured by LVDT1 and LVDT2, respectively, and l_1 is the horizontal distance between LVDT1 and LVDT2, as shown in **Figure F-2**.

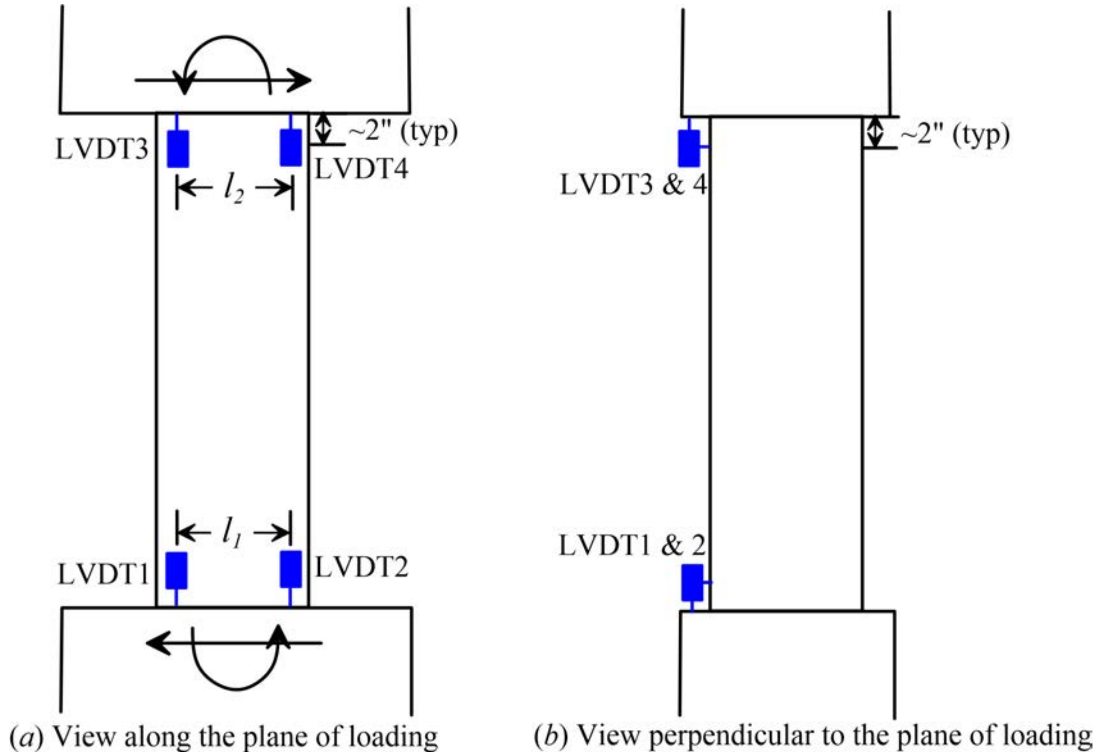

Figure F-2. A typical LVDTs layout to measure slip/extension deformations.

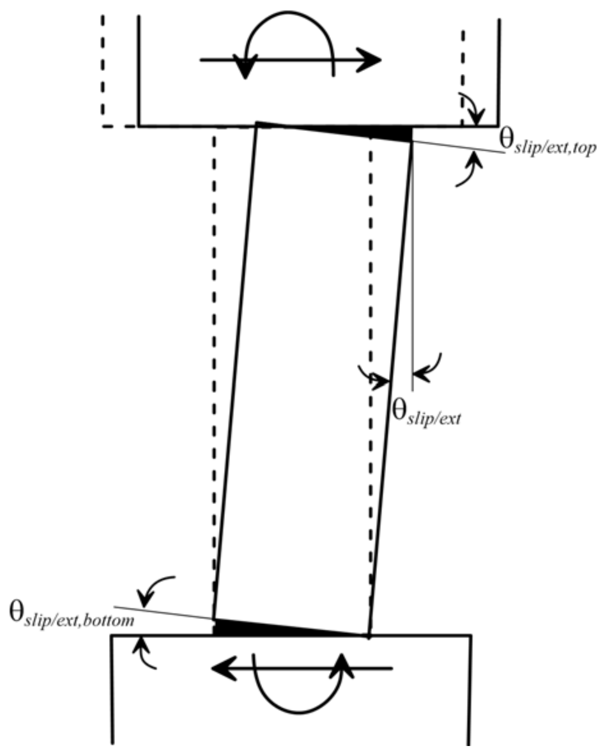

Figure F-3. Chord rotation due to slip/extension deformation.

2. Flexural Deformations

To calculate the flexural deformations (average curvature), five or six pairs (depending on the aspect ratio of the beam) of vertical LVDTs were placed along the beam web, as shown in **Figure F-4**, with the gage length (height of the element, h) of the first pair from each end being approximately equal to the plastic hinge length of the beam (taken as one-half the total beam depth). The flexural deformation (Δ_f) and rotation contribution (θ_f) of each element was calculated **Equation F-3** and **Equation F-4**, respectively

$$\Delta_f = \alpha_c \left(\frac{v_1 - v_2}{l}\right) h \qquad (\mathrm{F}-3)$$

$$\theta_f = \frac{\Delta_f}{h} \qquad (\mathrm{F}-4)$$

Where αh is the absolute distance from the top of the element to the centroid of the curvature diagram of that element (which varies from 0.67 to 0.5 times the gage length for triangular and rectangular curvature distributions, respectively), v_1 and v_2 are the measured displacements along the two side of the deformed region, l is the horizontal distance between the sensors, and h is the height of the element (gage length), as shown in **Figure F-4**.

The total chord rotation contributed by flexure ($\theta_{f,total}$) was calculated as the sum of chord rotations contributed by each element along the length of the beam as given by **Equation F-5**:

$$\boldsymbol{\theta_{f,total}} = \sum_{\mathbf{1}}^{\boldsymbol{n}} \boldsymbol{\theta_{fi}} \qquad (\mathrm{F}-5)$$

Where θ_{fi} is the flexural chord rotation contributed by i-th element as given by **Equation F-4**.

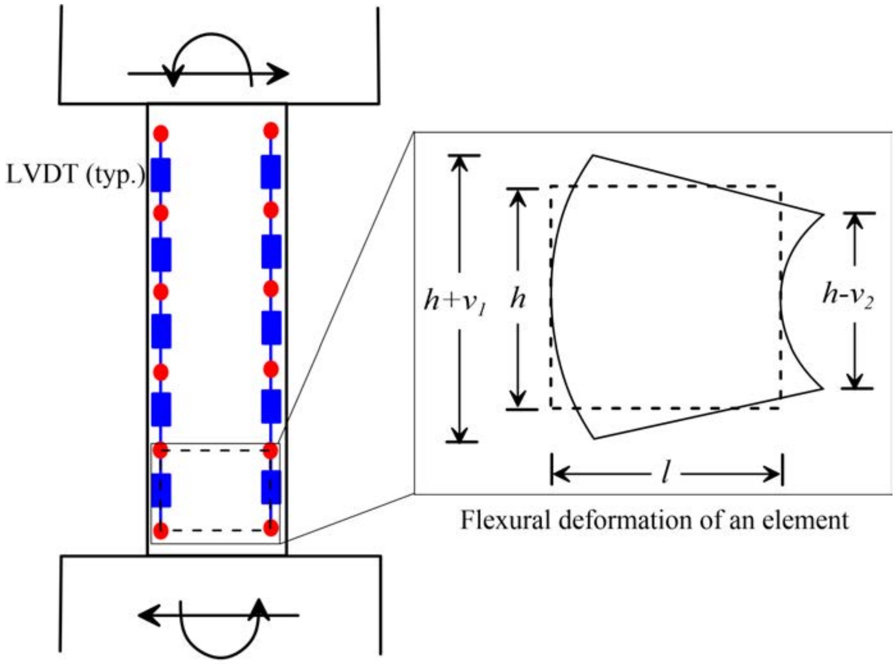

Figure F-4. Typical LVDT layout used to determine flexural deformations.

3. Shear Deformation

The shear deformation of each element was measured using an X-configuration of LVDTs along with the two vertical LVDTs used for flexural deformations, as shown in **Figure F-5**. Massone and Wallace (2004) reported that calculating shear deformations using only diagonal LVDTs in the yielding regions of structural walls, without accounting for the impact of the curvature distribution of the beam on the shear deformations (**Figure F-5**), tends to overestimate shear deformations by as much as 30%. Thus, they recommend calculating shear deformation of an element corrected for the impact of curvature distribution (U_S) using **Equation F-6**:

$$U_s = U_X + \left(\frac{1}{2} - \alpha_c\right) \times \theta_f \times h \qquad (\mathrm{F}-6)$$

Where U_X is the shear displacement of an element computed using **Equation F-7** and measurements from an X-configuration of LVDTs, α_c is the ratio of the distance from the top of the element to the centroid of the curvature diagram to length of the element (h) and was calculated for each element, and θ_f is the chord rotation of the element contributed by flexure and computed from **Equation F-4**.

$$U_X = \frac{\sqrt{\left(D_1^{measured}\right)^2 - h^2} - \sqrt{\left(D_2^{measured}\right)^2 - h^2}}{2} \qquad (\mathrm{F}-7)$$

Where $D_1^{measured}$ and $D_2^{measured}$ are the measurements from the two diagonal LVDTs, as shown in **Figure F-5**. Thus, the chord rotation contributed by shear displacement of each element (θ_s) was determined using **Equation F-8**. The total chord rotation ($\theta_{s,total}$) due shear deformation was calculated as the sum of chord rotations contributed by each element along the length of the beam as given by **Equation F-9**:

$$\theta_s = \frac{U_s}{h} \qquad (\mathrm{F}-8)$$

$$\theta_{s,total} = \sum_{i}^{n} \theta_{si} \qquad (\mathrm{F}-9)$$

Where θ_{si} is the shear chord rotation contributed by i-th element as given by **Equation F-8**.

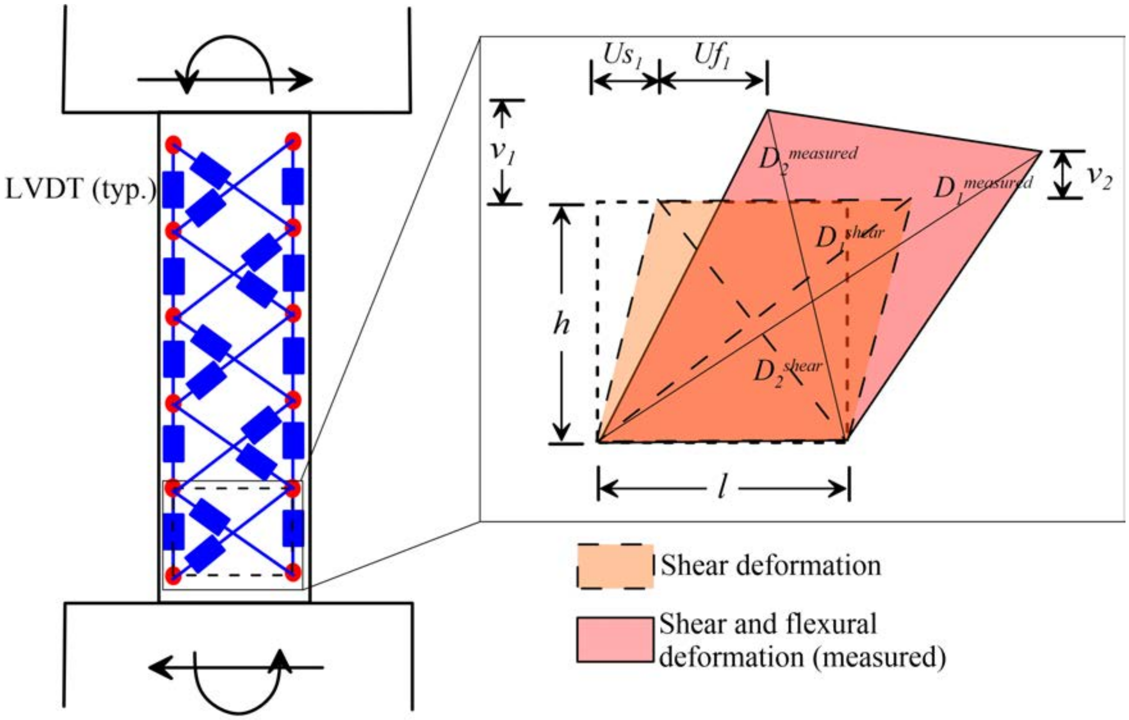

Figure F-5. Typical LVDT layout used to measure shear displacements and the model used to determine of shear deformation of an element (Massone and Wallace, 2004).

4. Sliding deformation at Beam-Wall Interfaces

Two LVDTs were used to measure sliding displacements (movement of the beam relative to the walls) taking place at each beam-wall interface in the direction of loading ($U_{slide\ top}$ and $U_{slide\ bottom}$), as shown in **Figure F-6**. The sliding displacements were taken as the average of the displacements measured by the two LVDTs as given by **Equation F-10** and **Equation F-11**.

$$U_{slide\ bottom} = \frac{\delta_{LVDT1} + \delta_{LVDT2}}{2} \qquad (\mathrm{F}-10)$$

$$U_{slide\ top} = \frac{\delta_{LVDT3} + \delta_{LVDT4}}{2} \qquad (F-11)$$

Where δ_{LVDT1} through δ_{LVDT4} are the displacement measured by LVDT1 through LVDT4, respectively, as shown in **Figure F-6**. The total chord rotation contributed by sliding at the interfaces (θ_{slide}) was calculated as the sum of sliding displacements of the interfaces divided by the beam clear length (l_n), as given by **Equation F-12**.

$$\theta_{slide} = \frac{U_{slide\ top} + U_{slide\ bottom}}{l_n} \qquad (F-12)$$

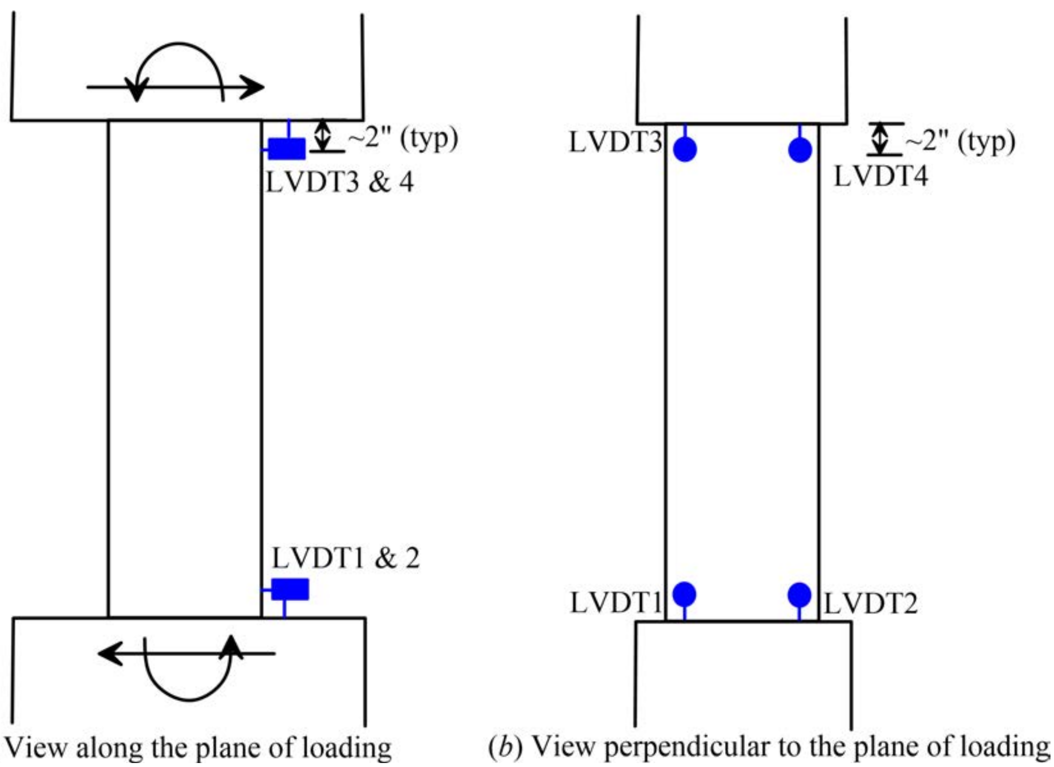

Figure F-6. Typical LVDT layout used to measure sliding displacement at the beam-wall interface.

APPENDEX G–Strain Gage Results

Strain gages were installed on longitudinal, diagonal, and transverse reinforcement and on steel section at various specified locations. Strain gage layouts of the specimens are shown in **Figure D-1** through **Figure D-4**. It is noted that few strain gages damaged during construction, and, thus, no data is available for these strain gages. The strain results are presented in **Figure G-1** through **Figure G-8** for CB1 through CB8, respectively. **Table G-1** presents what the labels of X-axis of **Figure G-1** through **Figure G-4** represent.

Table G-1. Labels of X-axis of Figure G-1 through Figure G-4 represent

Loading Stage	Loading Protocol	Loading Type	Loading Level
N1	Wind	Force-Controlled	0.15 M_{pr}
2	Wind	Force-Controlled	0.4 M_{pr}
3	Wind	Force-Controlled	0.75 M_{pr}
4	Wind	Displacement-Controlled	1.2 θ_y
5	Wind	Displacement-Controlled	1.5 θ_y
6	Wind	Displacement-Controlled	1.2 θ_y
7	Wind	Force-Controlled	0.75 M_{pr}
8	Wind	Force-Controlled	0.4 M_{pr}
9	Wind	Force-Controlled	0.4 M_{pr}
10	Seismic	Displacement-Controlled	1.5% θ
11	Seismic	Displacement-Controlled	2% θ
12	Seismic	Displacement-Controlled	3% θ
13	Seismic	Displacement-Controlled	4% θ
14	Seismic	Displacement-Controlled	6% θ
15	Seismic	Displacement-Controlled	8% θ
16	Seismic	Displacement-Controlled	10% θ
17	Seismic	Displacement-Controlled	12% θ

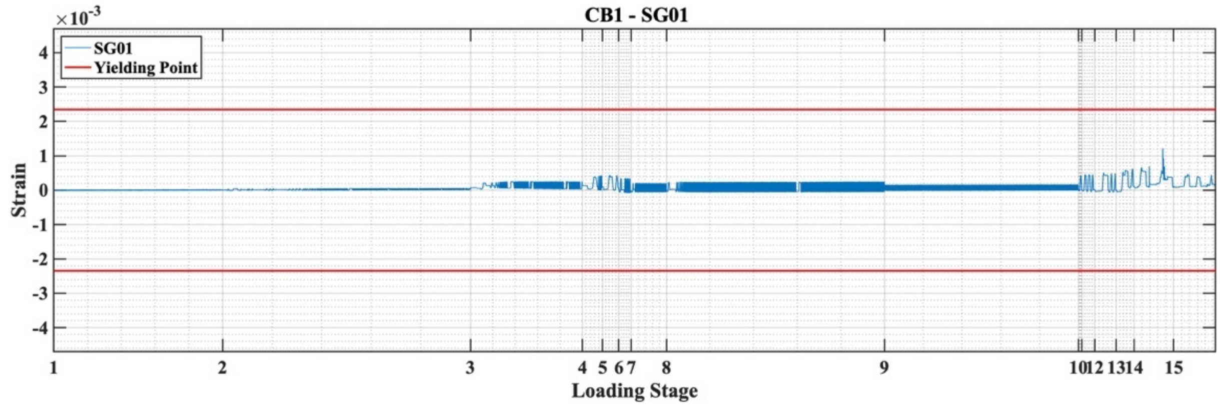
CB1 - SG01
×10^-3
SG01
Yielding Point
Strain
Loading Stage
1
2
3
4 5 6 7
8
9
1012 1314
15

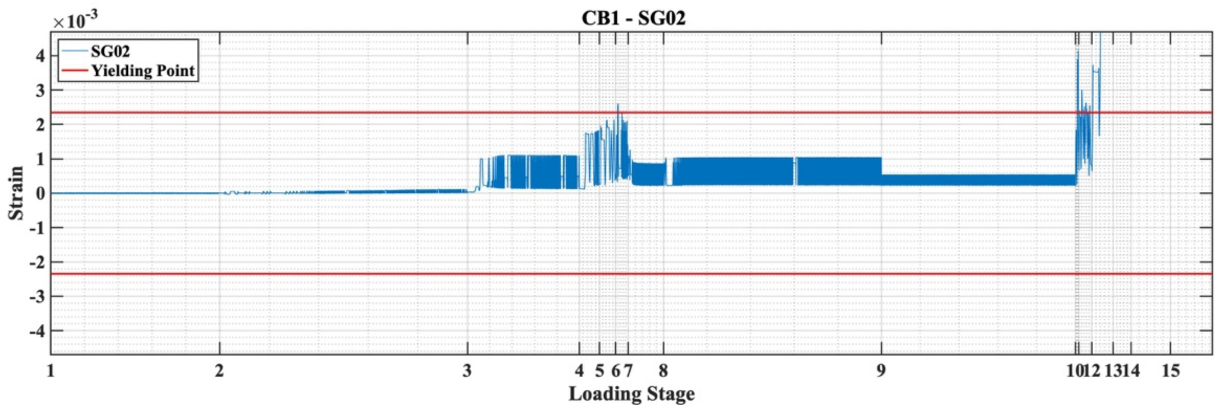
CB1 - SG02
×10^-3
SG02
Yielding Point
Strain
Loading Stage
1
2
3
4 5 6 7
8
9
1012 1314
15

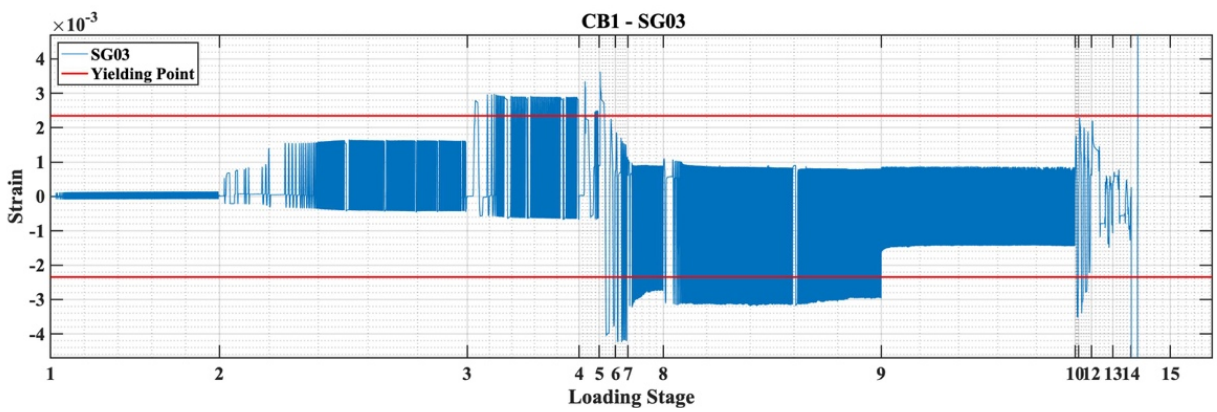
CB1 - SG03
×10^-3
SG03
Yielding Point
Strain
Loading Stage
1
2
3
4 5 6 7
8
9
1012 1314
15

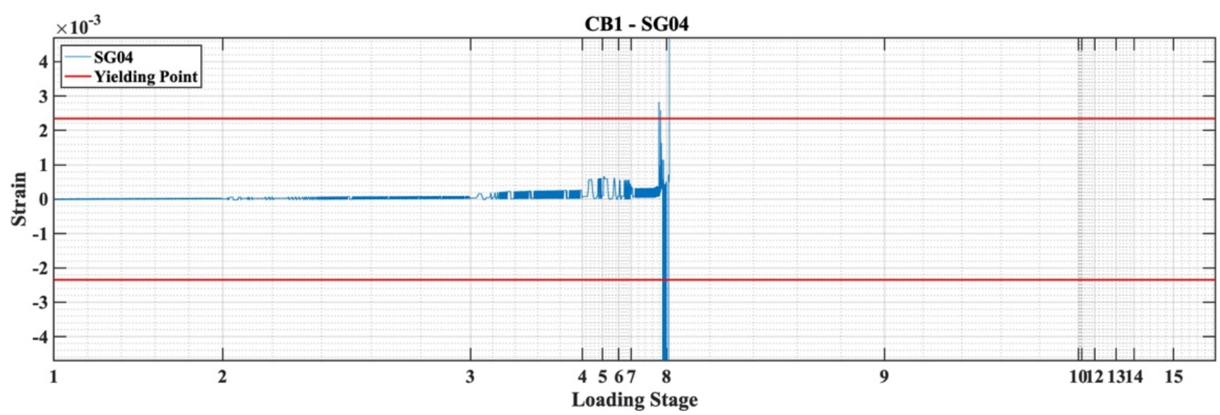
CB1 - SG04
×10^-3
SG04
Yielding Point
Strain
Loading Stage
1
2
3
4 5 6 7
8
9
1012 1314
15

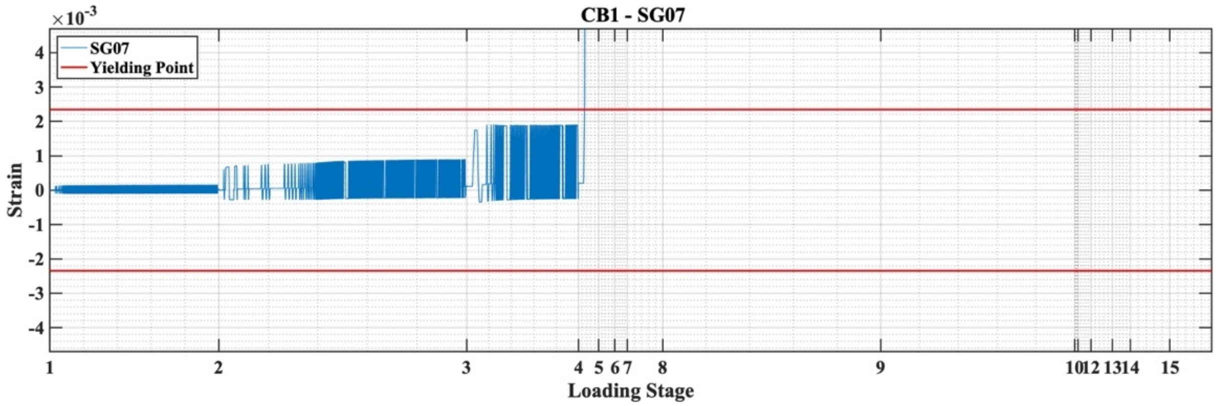
CB1 - SG07
×10^-3
SG07
Yielding Point
Strain
Loading Stage
4
3
2
1
0
-1
-2
-3
-4
1
2
3
4 5 6 7
8
9
10 12 13 14
15

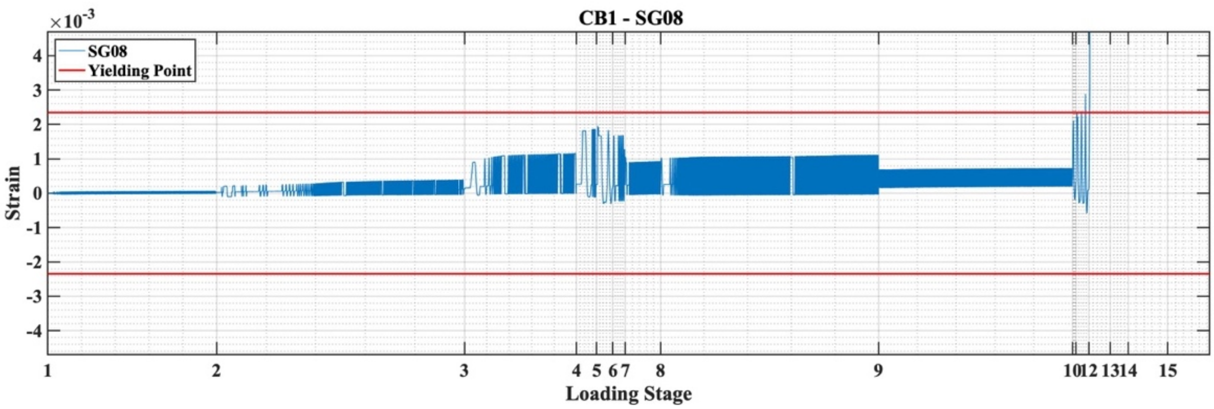
CB1 - SG08
×10^-3
SG08
Yielding Point
Strain
Loading Stage
4
3
2
1
0
-1
-2
-3
-4
1
2
3
4 5 6 7
8
9
10 12 13 14
15

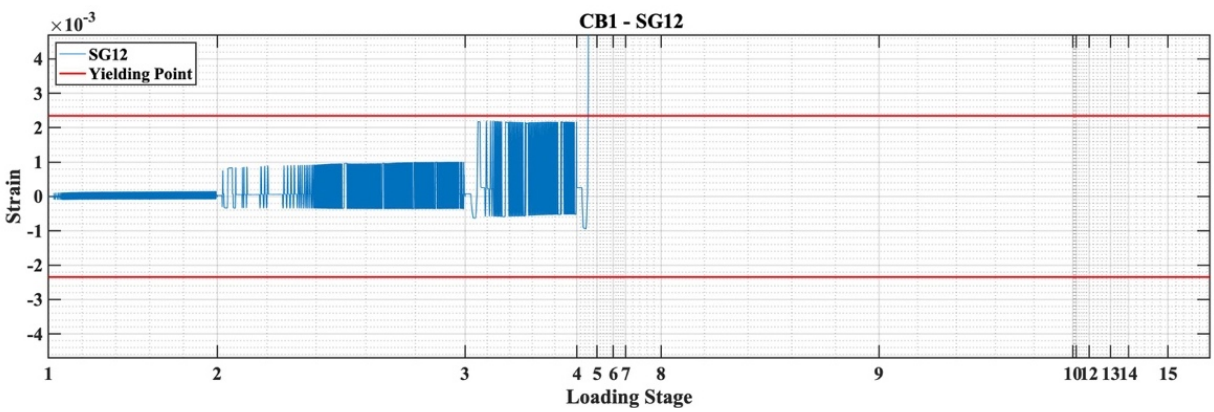
CB1 - SG12
×10^-3
SG12
Yielding Point
Strain
Loading Stage
4
3
2
1
0
-1
-2
-3
-4
1
2
3
4 5 6 7
8
9
10 12 13 14
15

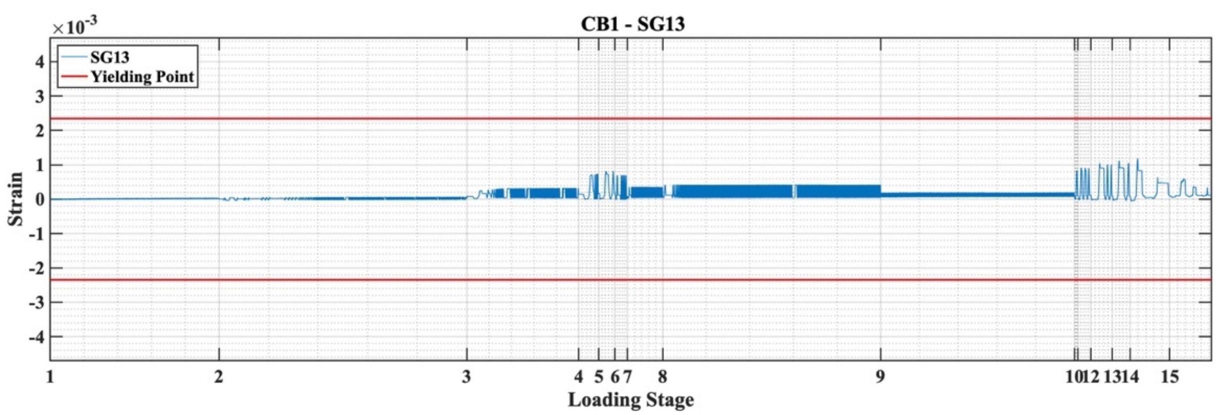
CB1 - SG13
×10^-3
SG13
Yielding Point
Strain
Loading Stage
4
3
2
1
0
-1
-2
-3
-4
1
2
3
4 5 6 7
8
9
10 12 13 14
15

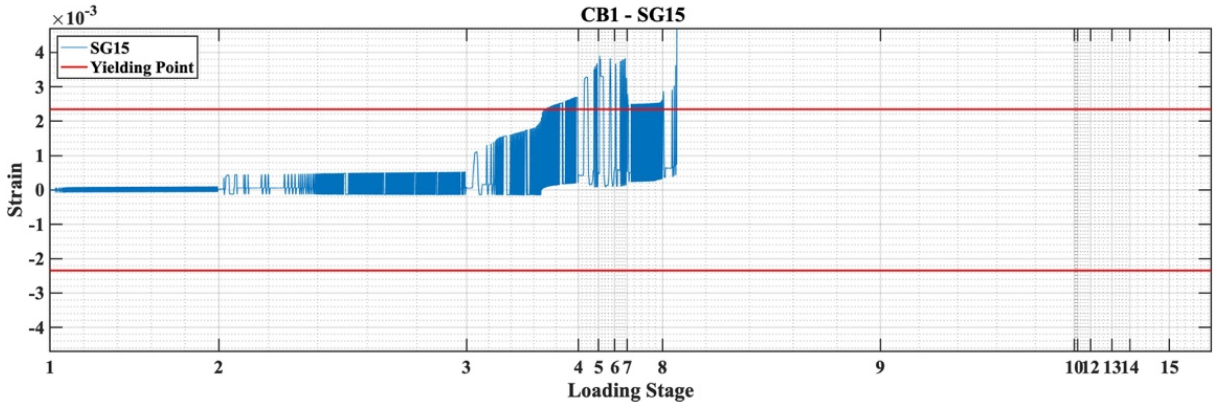

CB1 - SG15
SG15
Yielding Point
Strain
Loading Stage

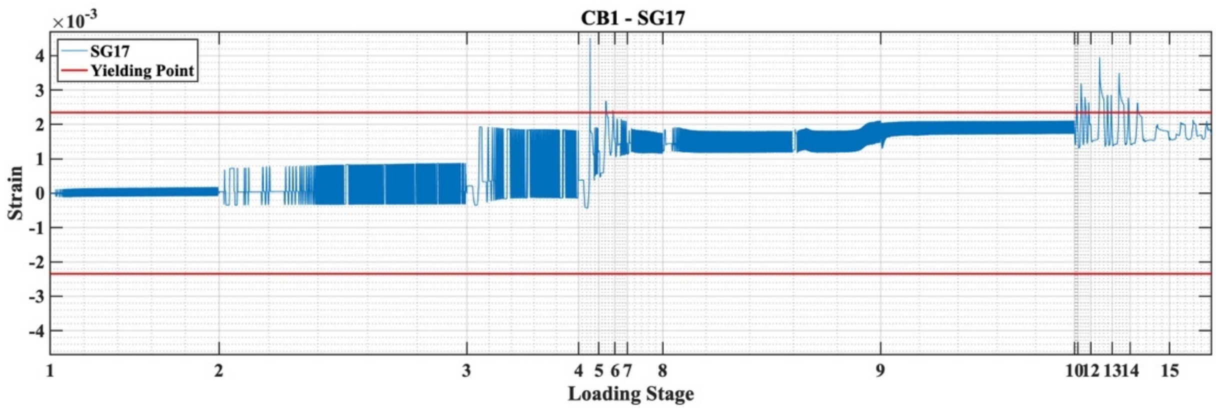

CB1 - SG17
SG17
Yielding Point
Strain
Loading Stage

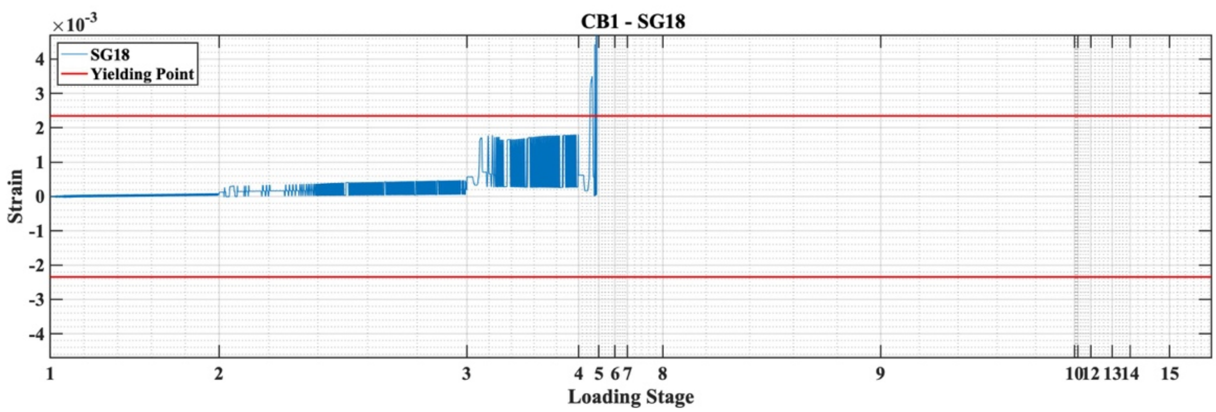

CB1 - SG18
SG18
Yielding Point
Strain
Loading Stage

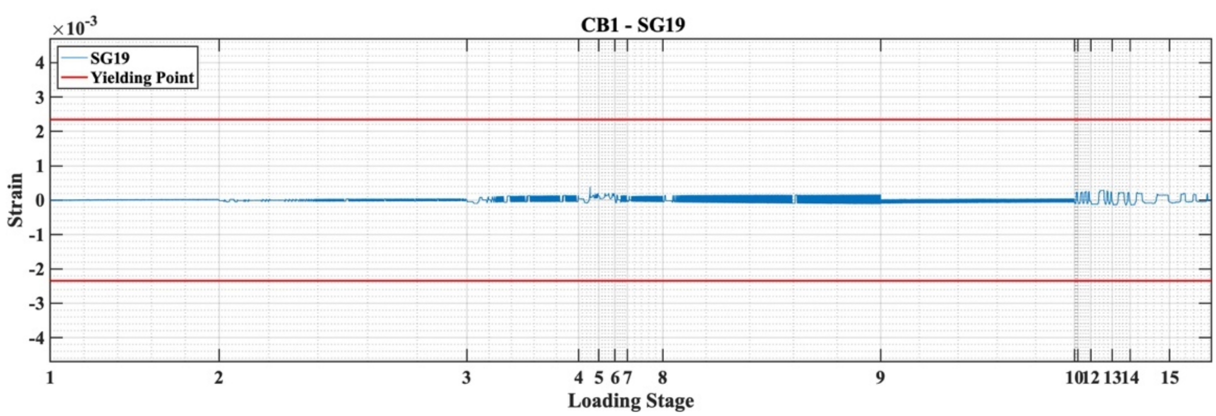

CB1 - SG19
SG19
Yielding Point
Strain
Loading Stage

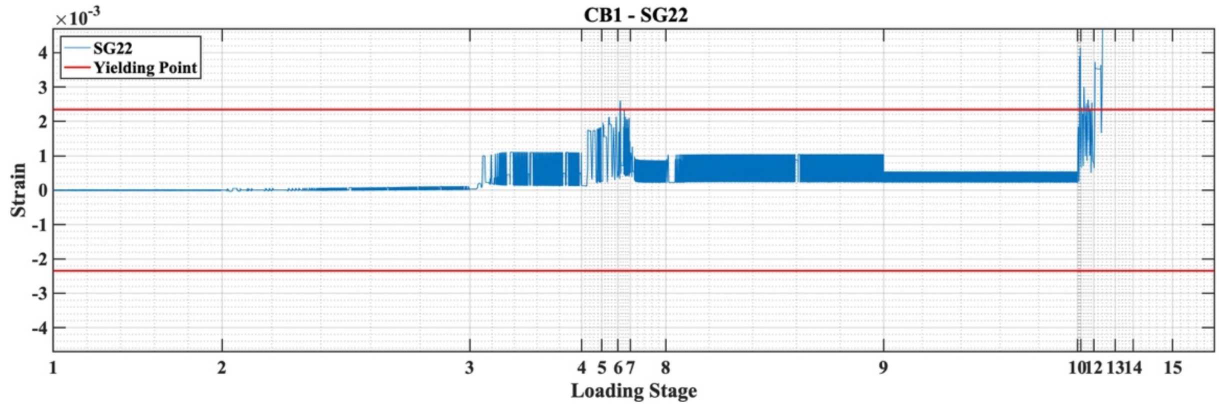
CB1 - SG22
×10-3
SG22
Yielding Point
Strain
Loading Stage
1
2
3
4 5 6 7
8
9
10 12 13 14
15

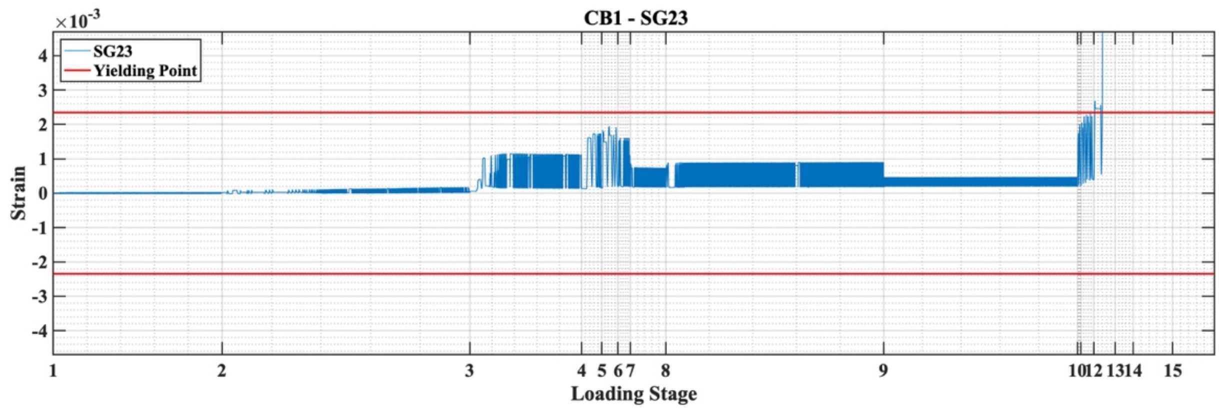
CB1 - SG23
×10-3
SG23
Yielding Point
Strain
Loading Stage
1
2
3
4 5 6 7
8
9
10 12 13 14
15

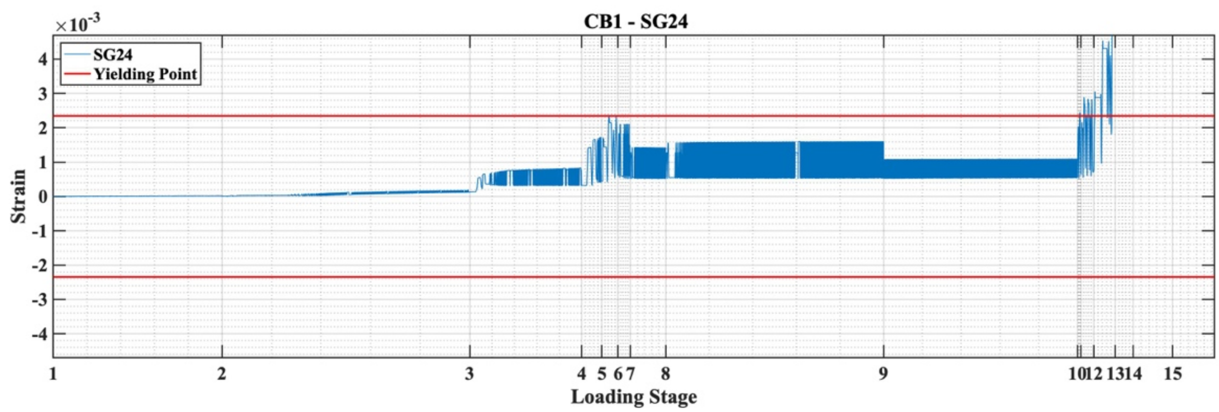
CB1 - SG24
×10-3
SG24
Yielding Point
Strain
Loading Stage
1
2
3
4 5 6 7
8
9
10 12 13 14
15

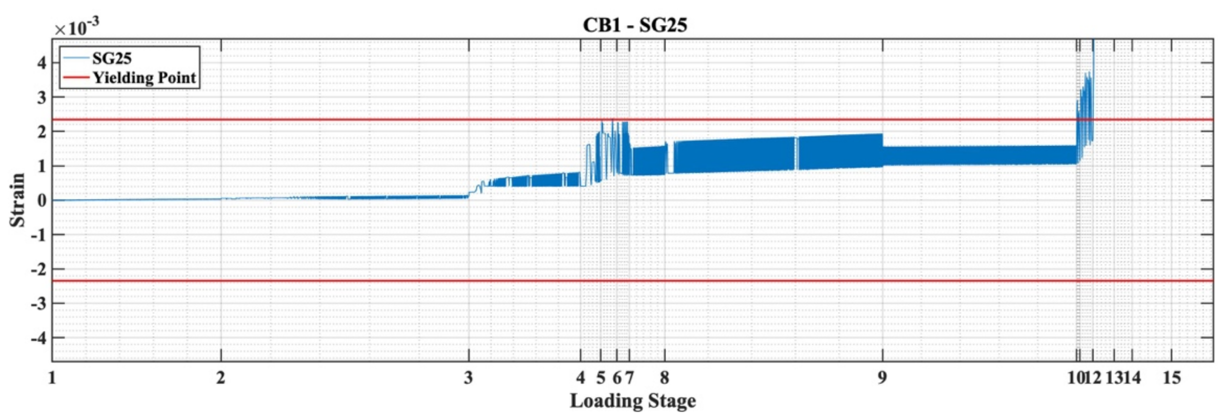
CB1 - SG25
×10-3
SG25
Yielding Point
Strain
Loading Stage
1
2
3
4 5 6 7
8
9
10 12 13 14
15

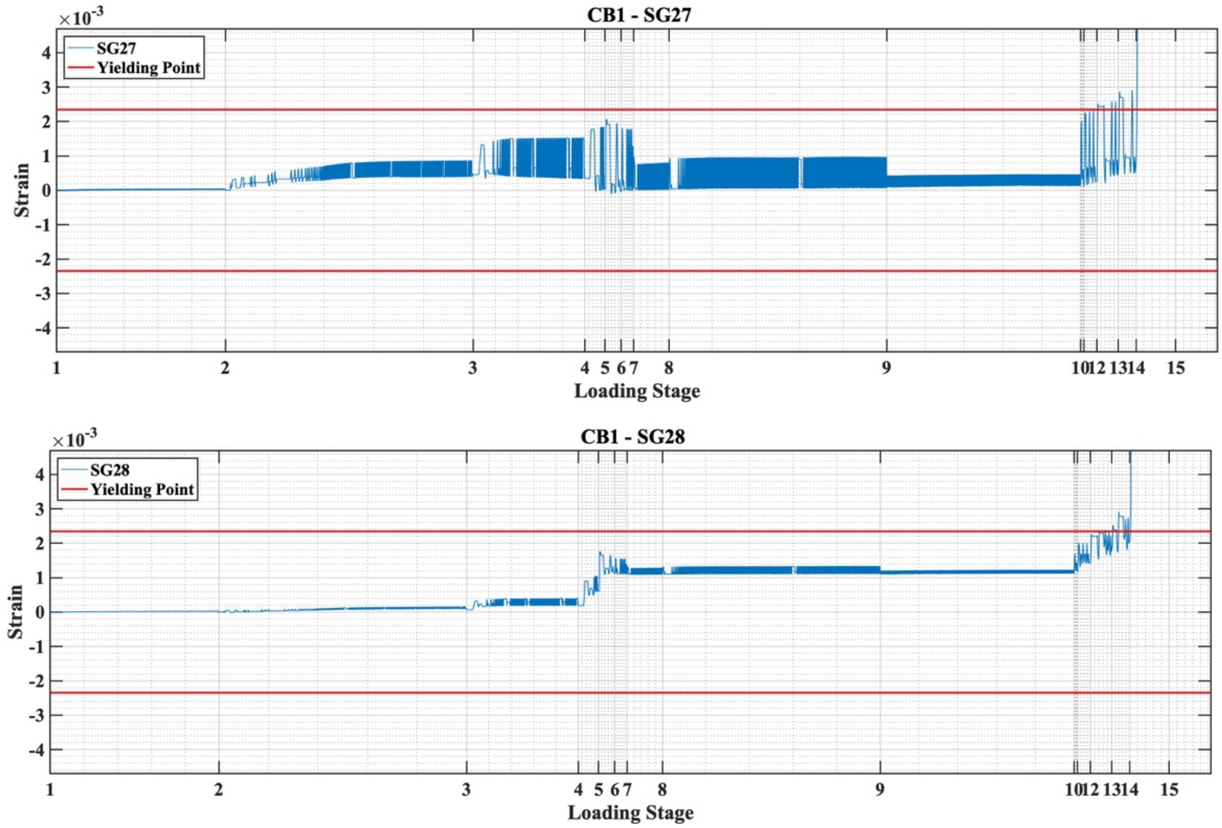

Figure G-1. Strain results from strain gages of CB1.

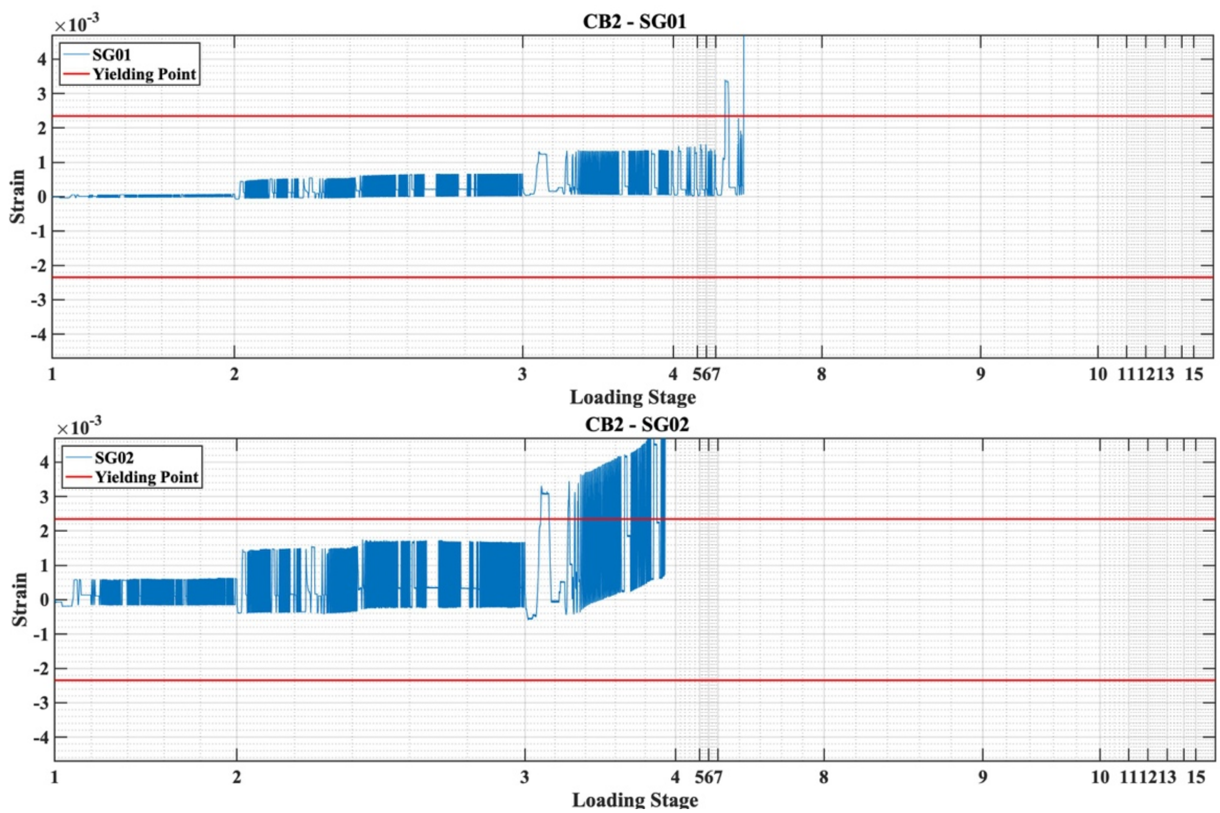

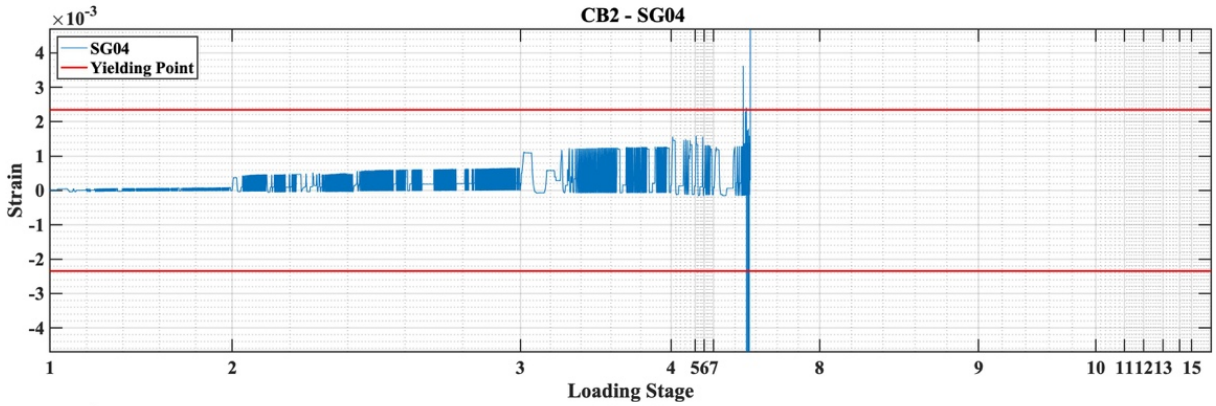

×10^-3
CB2 - SG04
SG04
Yielding Point
Strain
Loading Stage

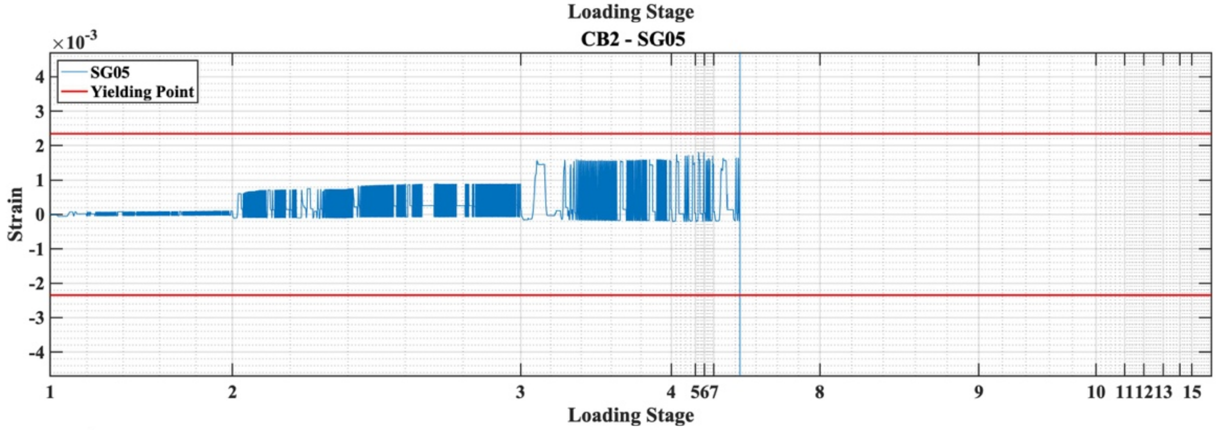

×10^-3
CB2 - SG05
SG05
Yielding Point
Strain
Loading Stage

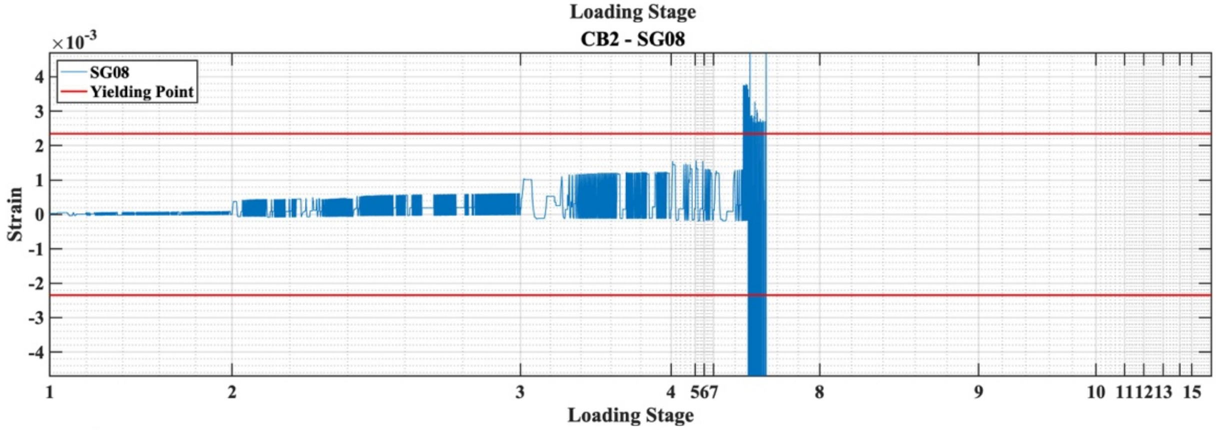

×10^-3
CB2 - SG08
SG08
Yielding Point
Strain
Loading Stage

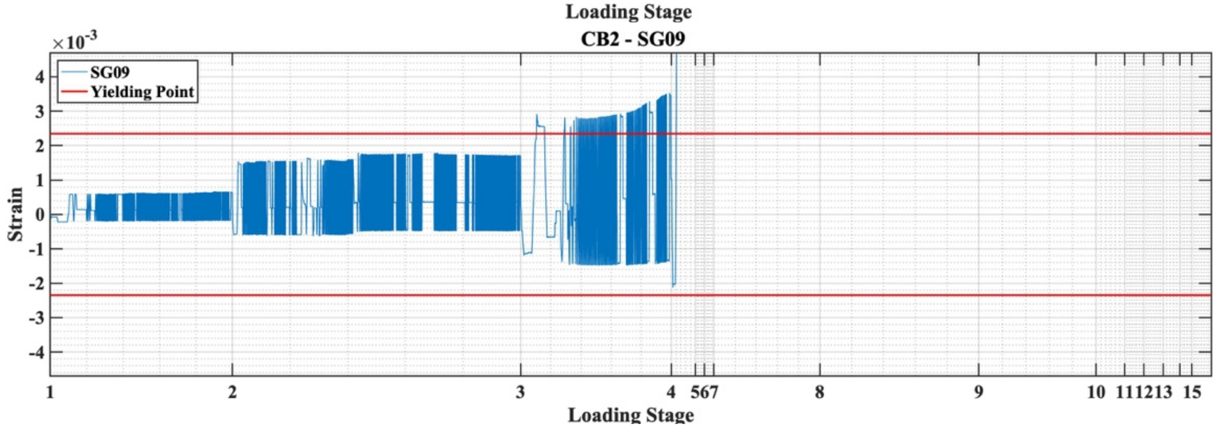

×10^-3
CB2 - SG09
SG09
Yielding Point
Strain
Loading Stage

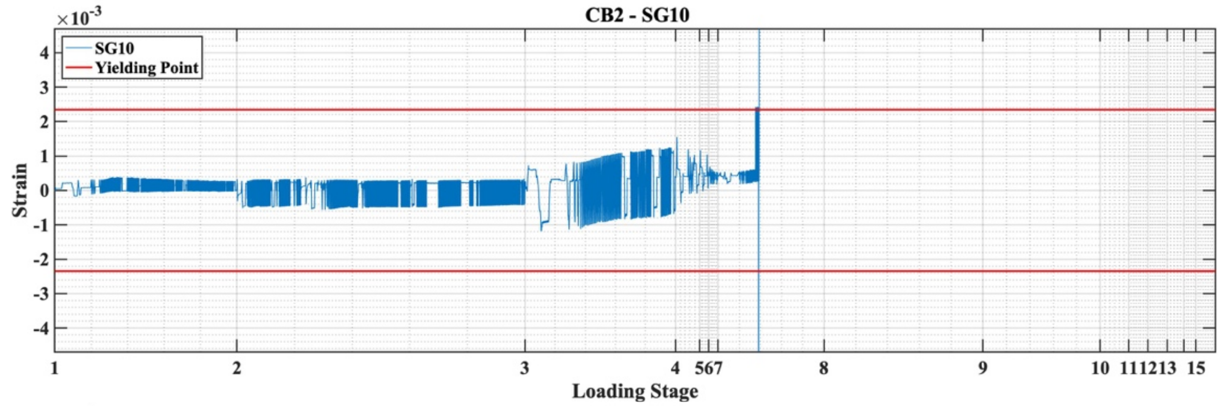
CB2 - SG10
×10^-3
SG10
Yielding Point
Strain
Loading Stage
1 2 3 4 5 6 7 8 9 10 11 12 13 15
4 3 2 1 0 -1 -2 -3 -4

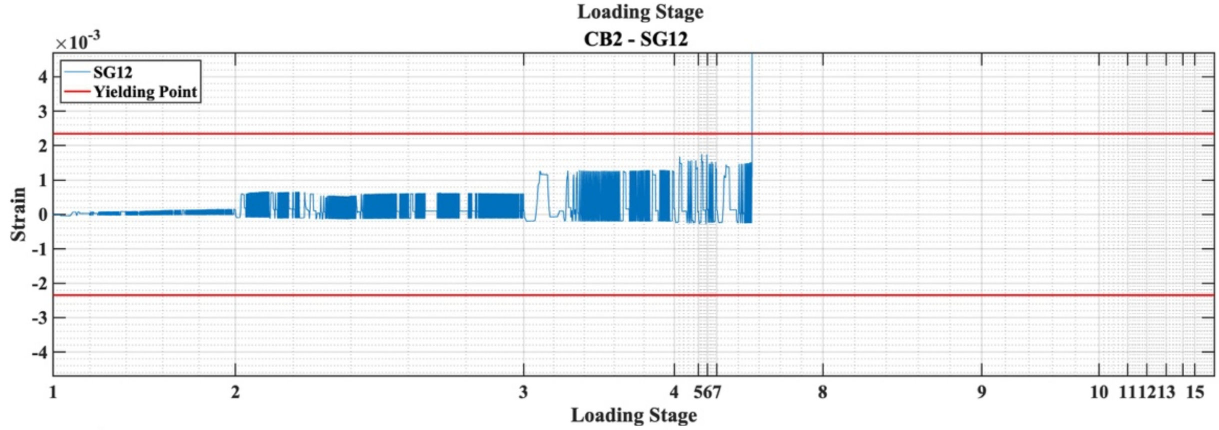
CB2 - SG12
×10^-3
SG12
Yielding Point
Strain
Loading Stage
1 2 3 4 5 6 7 8 9 10 11 12 13 15
4 3 2 1 0 -1 -2 -3 -4

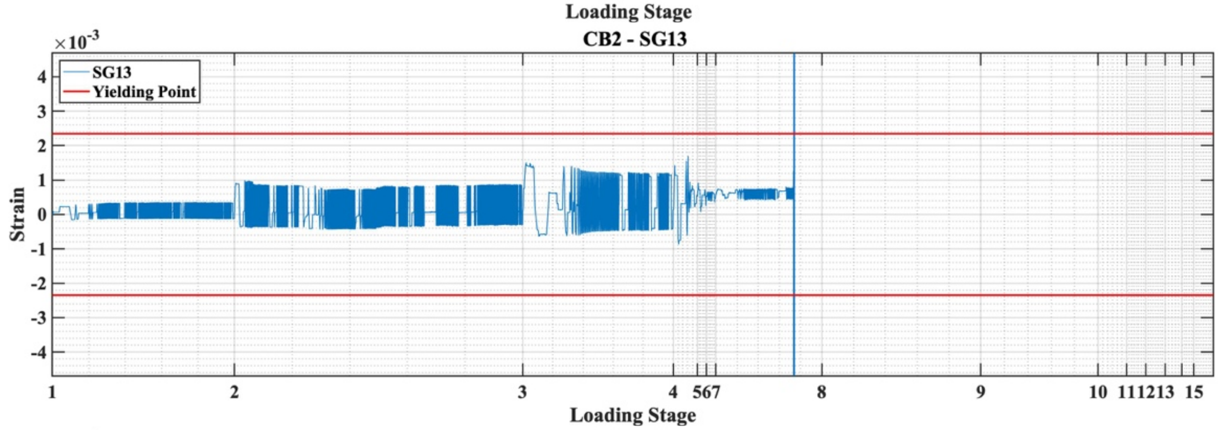
CB2 - SG13
×10^-3
SG13
Yielding Point
Strain
Loading Stage
1 2 3 4 5 6 7 8 9 10 11 12 13 15
4 3 2 1 0 -1 -2 -3 -4

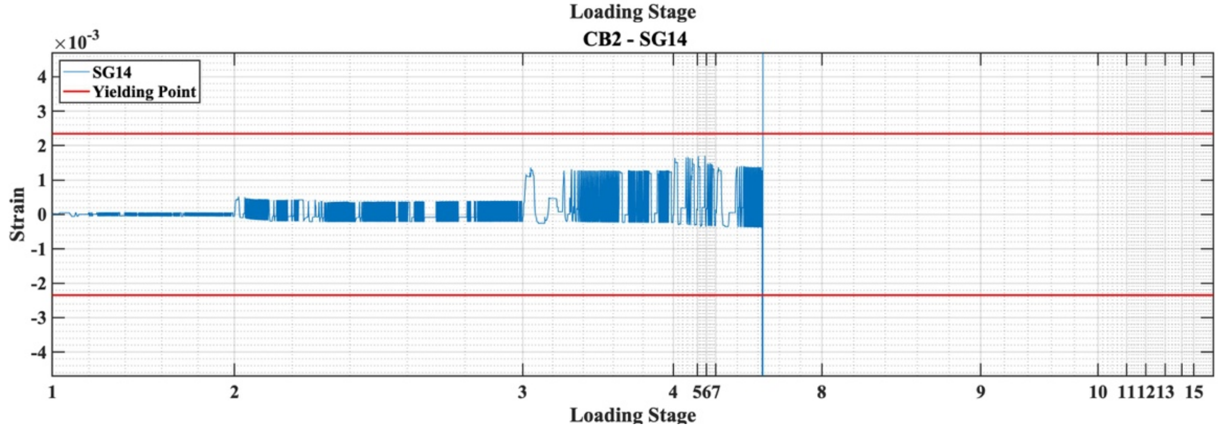
CB2 - SG14
×10^-3
SG14
Yielding Point
Strain
Loading Stage
1 2 3 4 5 6 7 8 9 10 11 12 13 15
4 3 2 1 0 -1 -2 -3 -4

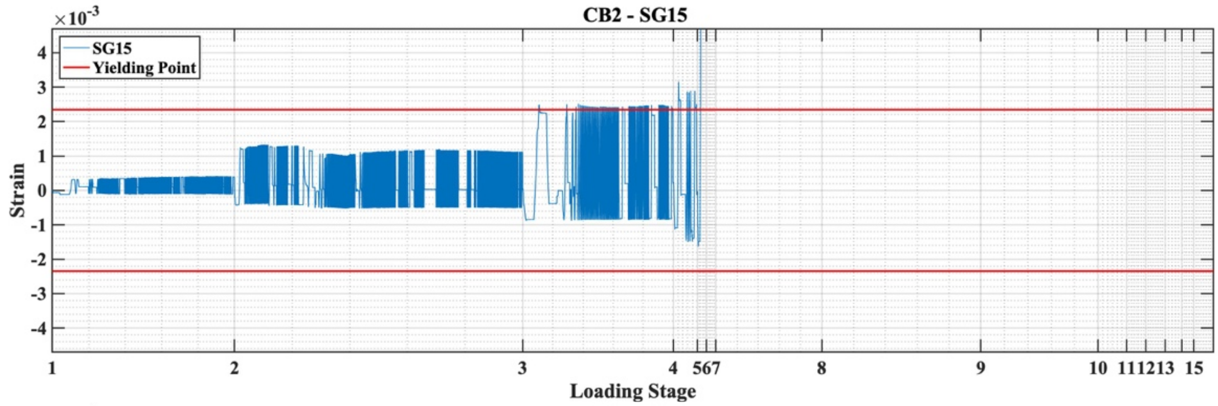
CB2 - SG15
×10^-3
SG15
Yielding Point
Strain
Loading Stage
1 2 3 4 567 8 9 10 111213 15

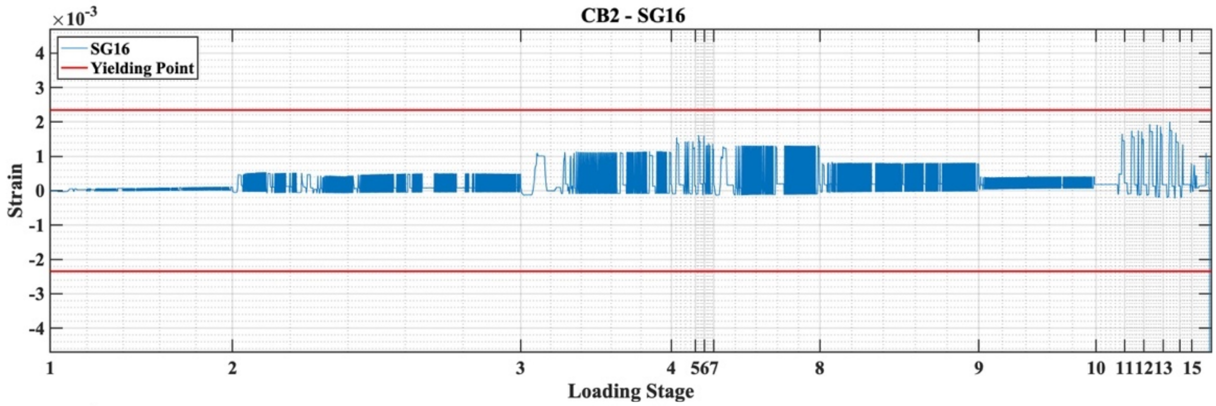
CB2 - SG16
×10^-3
SG16
Yielding Point
Strain
Loading Stage
1 2 3 4 567 8 9 10 111213 15

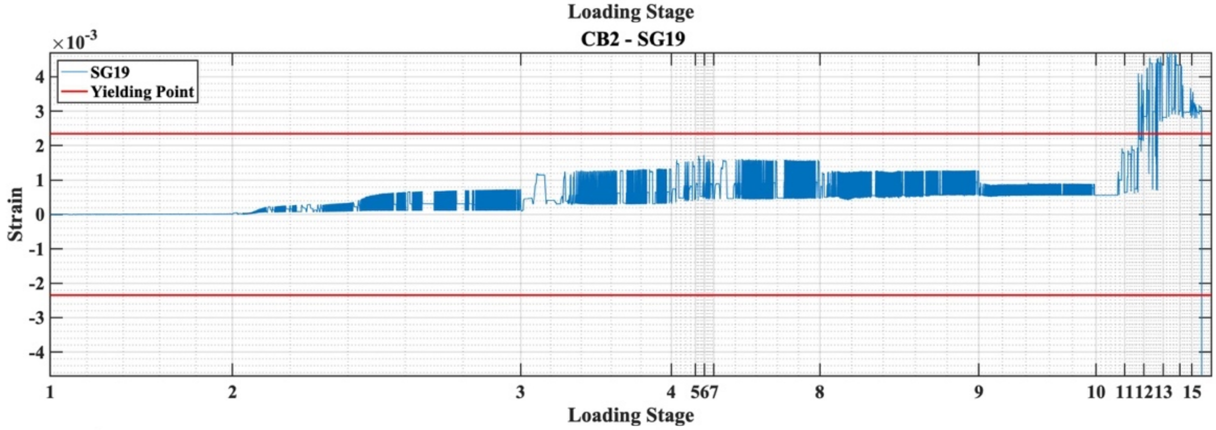
CB2 - SG19
×10^-3
SG19
Yielding Point
Strain
Loading Stage
1 2 3 4 567 8 9 10 111213 15

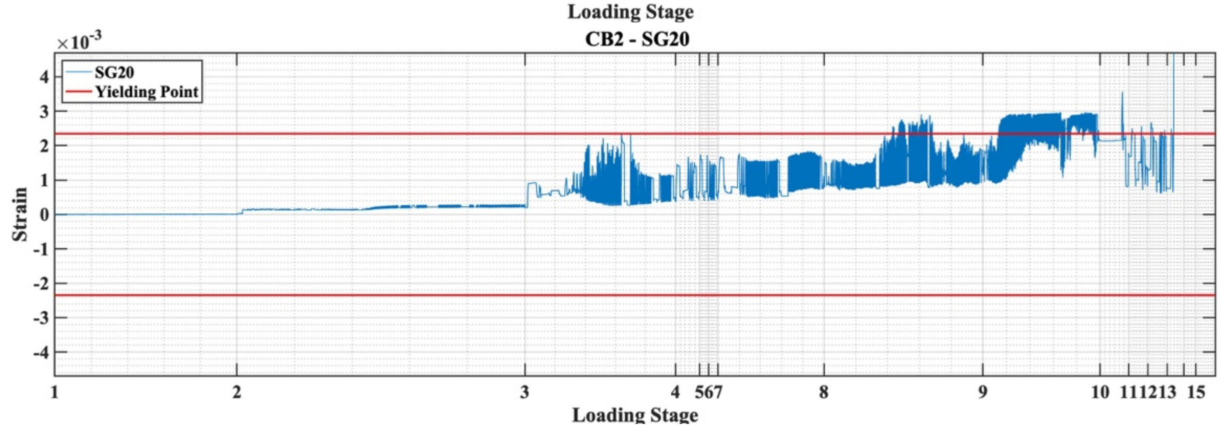
CB2 - SG20
×10^-3
SG20
Yielding Point
Strain
Loading Stage
1 2 3 4 567 8 9 10 111213 15

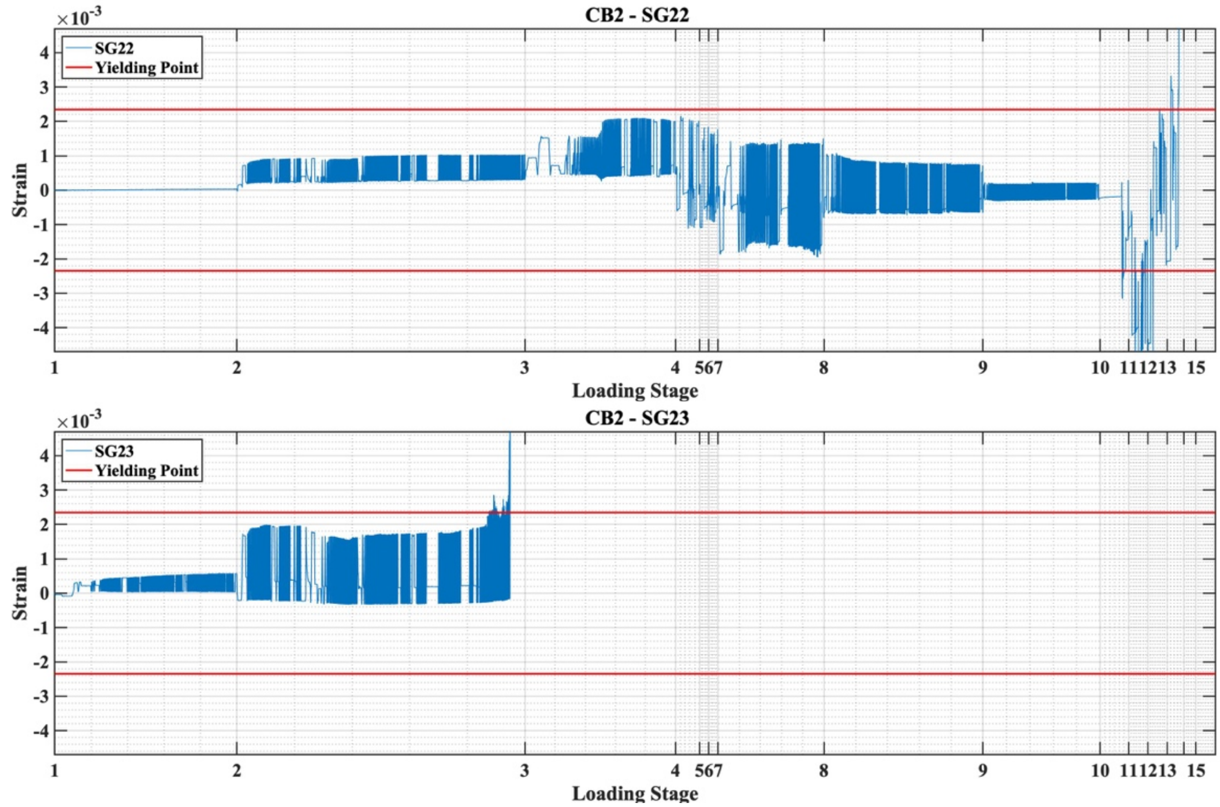

Figure G-2. Strain results from strain gages of CB2.

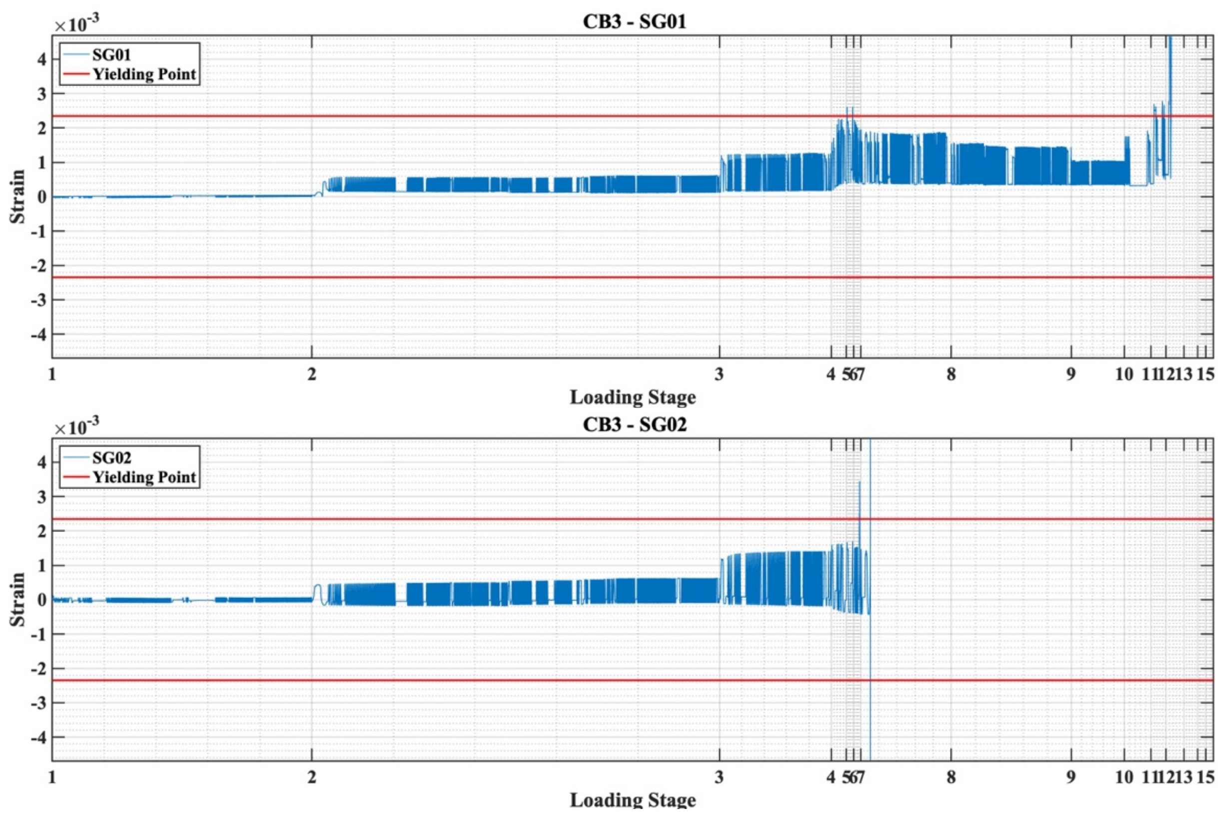

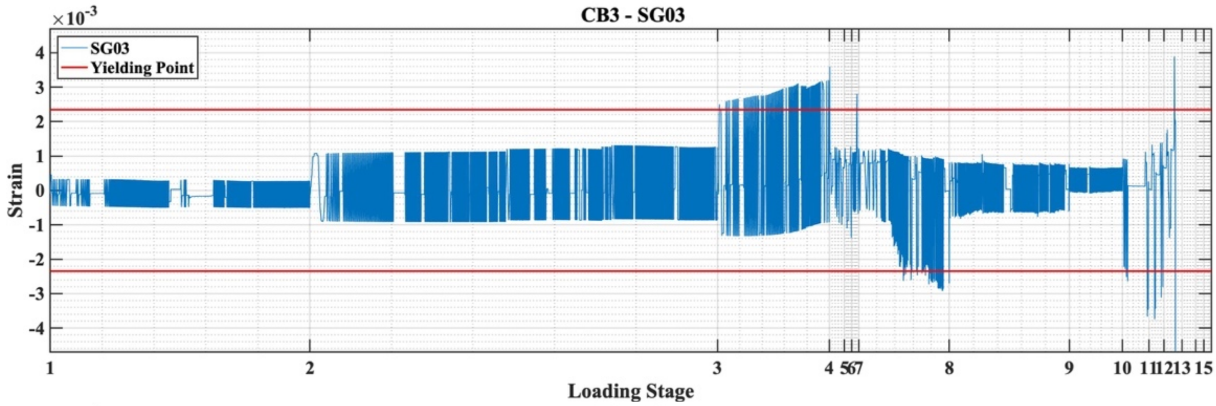
CB3 - SG03
$\times10^{-3}$
SG03
Yielding Point
Strain
Loading Stage
1 2 3 4 5 6 7 8 9 10 11 12 13 15

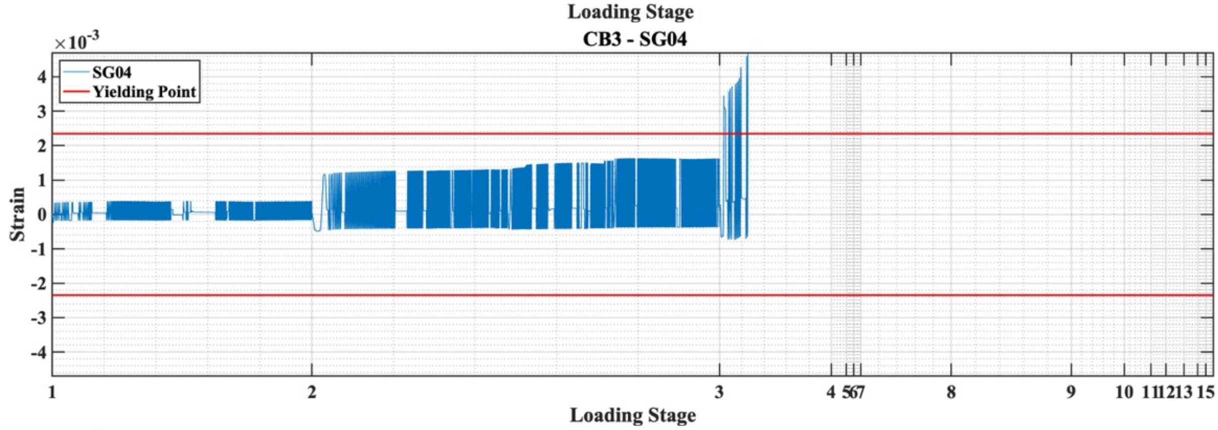
CB3 - SG04
$\times10^{-3}$
SG04
Yielding Point
Strain
Loading Stage
1 2 3 4 5 6 7 8 9 10 11 12 13 15

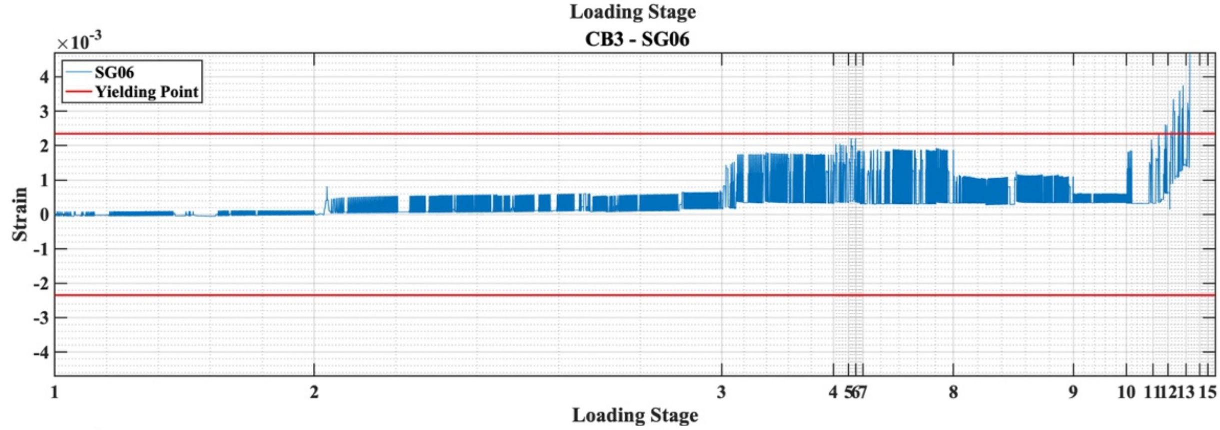
CB3 - SG06
$\times10^{-3}$
SG06
Yielding Point
Strain
Loading Stage
1 2 3 4 5 6 7 8 9 10 11 12 13 15

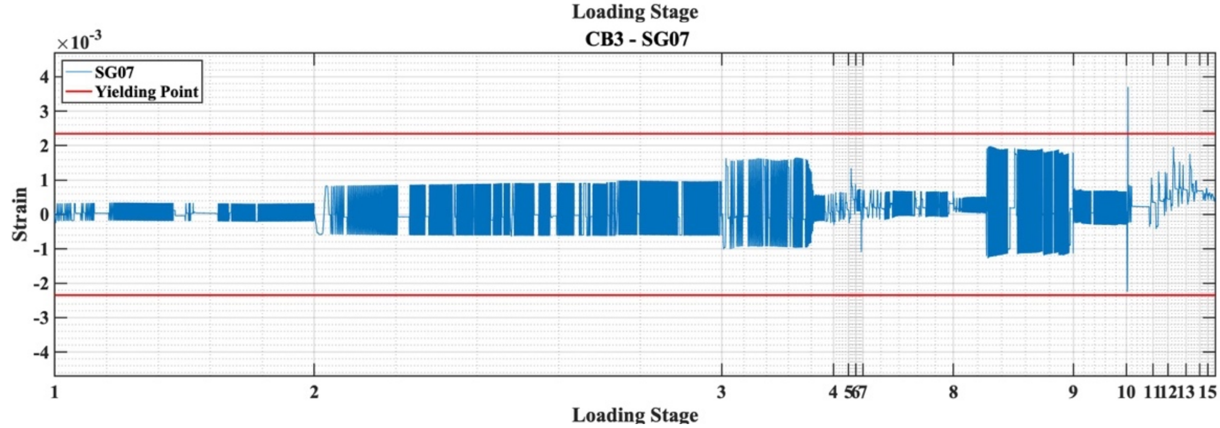
CB3 - SG07
$\times10^{-3}$
SG07
Yielding Point
Strain
Loading Stage
1 2 3 4 5 6 7 8 9 10 11 12 13 15

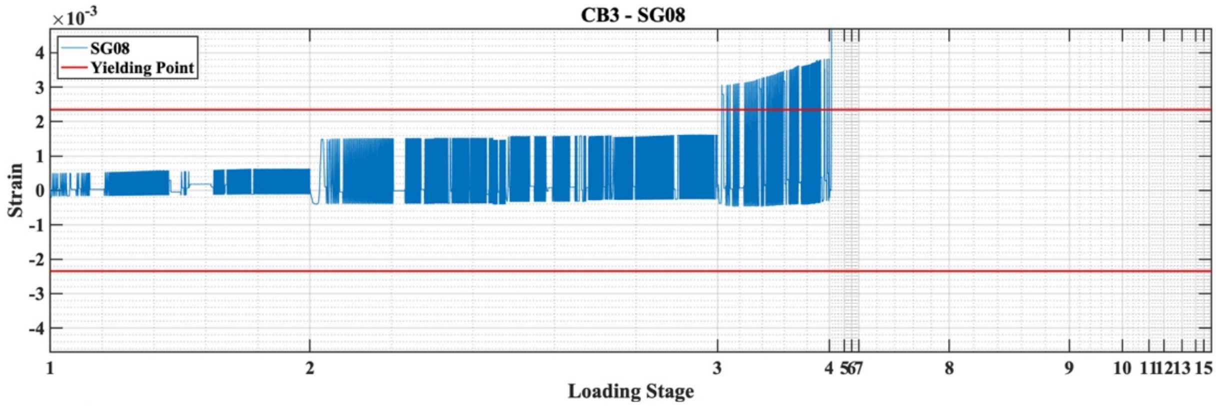

CB3 - SG08
×10^-3
SG08
Yielding Point
Strain
Loading Stage

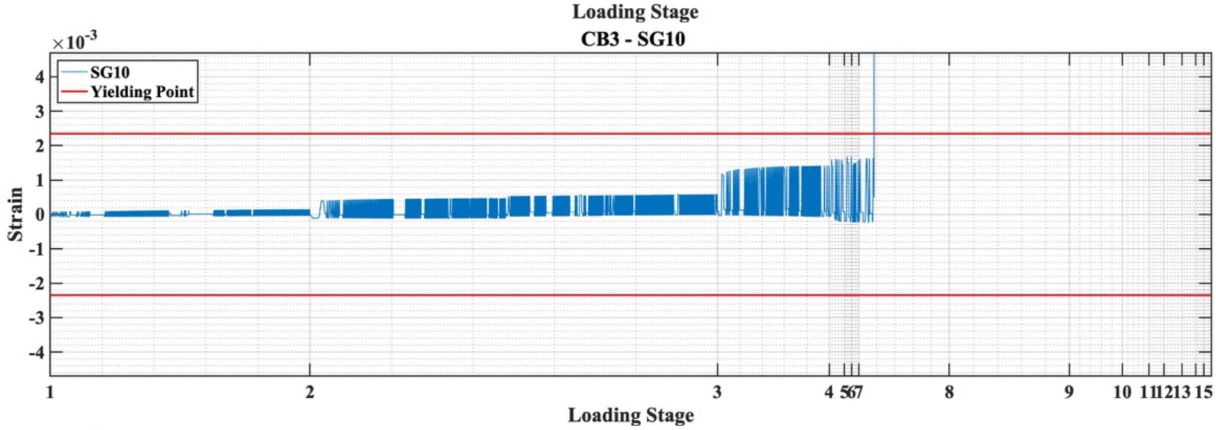

CB3 - SG10
×10^-3
SG10
Yielding Point
Strain
Loading Stage

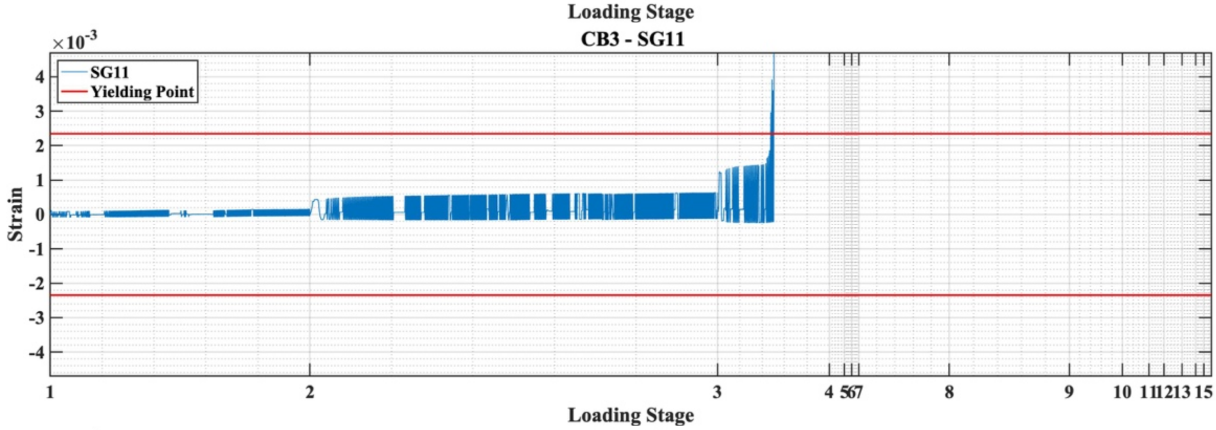

CB3 - SG11
×10^-3
SG11
Yielding Point
Strain
Loading Stage

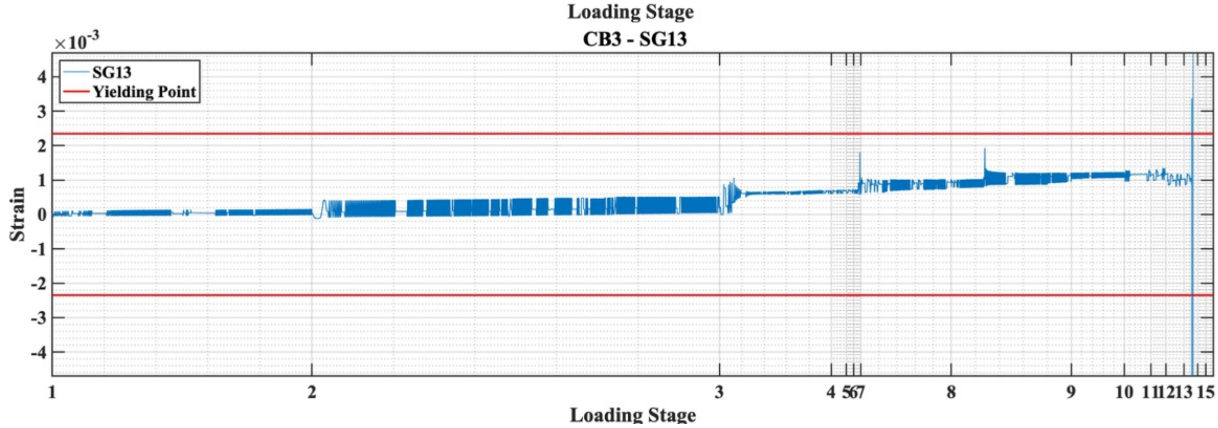

CB3 - SG13
×10^-3
SG13
Yielding Point
Strain
Loading Stage

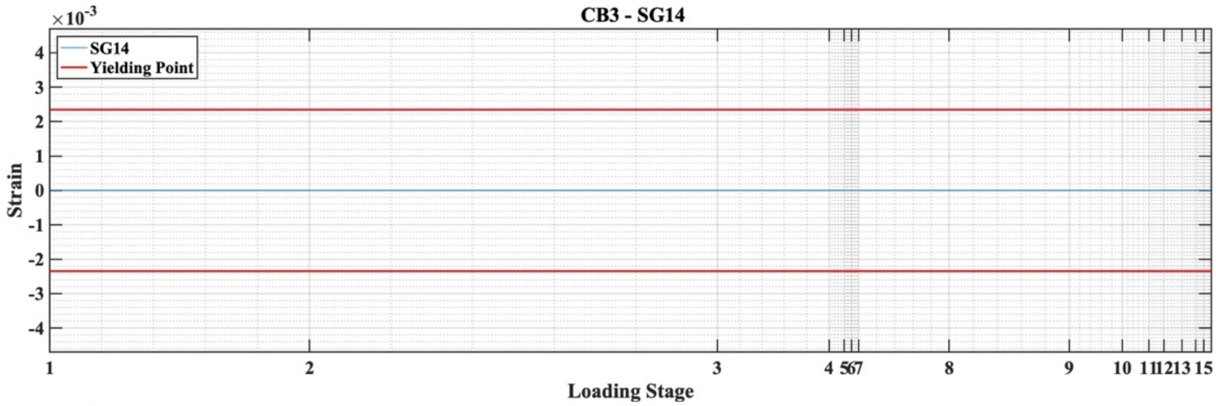

CB3 - SG14
×10^-3
SG14
Yielding Point
Strain
4
3
2
1
0
-1
-2
-3
-4
1
2
3
4 567
8
9
10 1112 13 15
Loading Stage

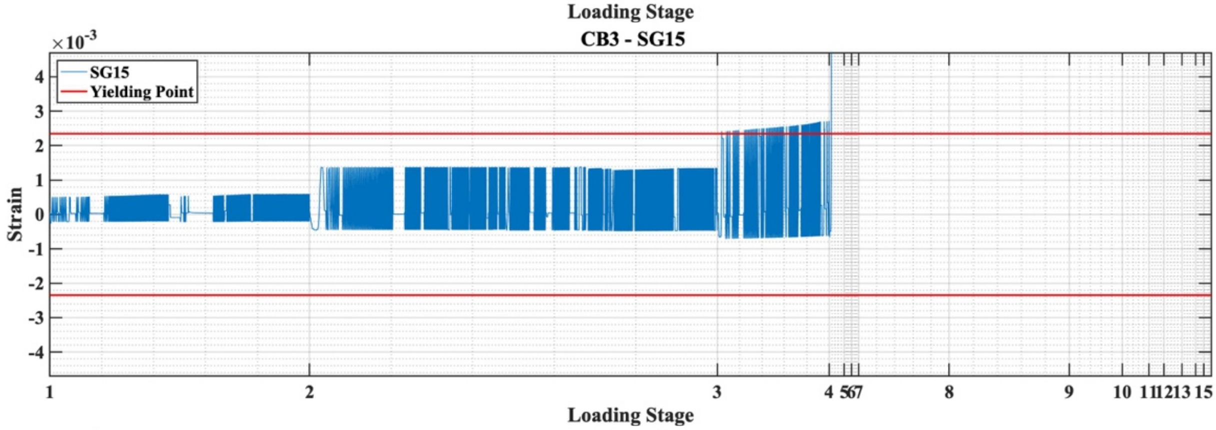

CB3 - SG15
×10^-3
SG15
Yielding Point
Strain
4
3
2
1
0
-1
-2
-3
-4
1
2
3
4 567
8
9
10 1112 13 15
Loading Stage

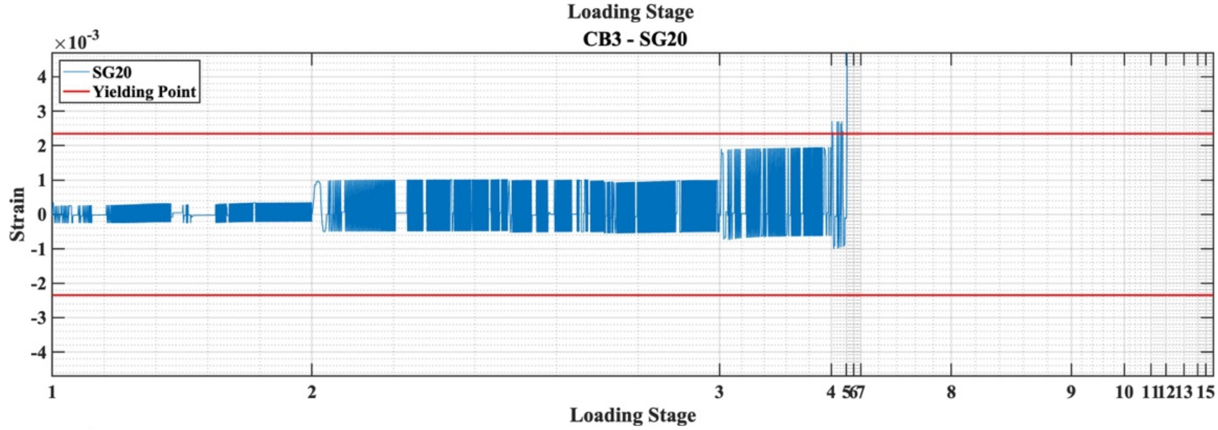

CB3 - SG20
×10^-3
SG20
Yielding Point
Strain
4
3
2
1
0
-1
-2
-3
-4
1
2
3
4 567
8
9
10 1112 13 15
Loading Stage

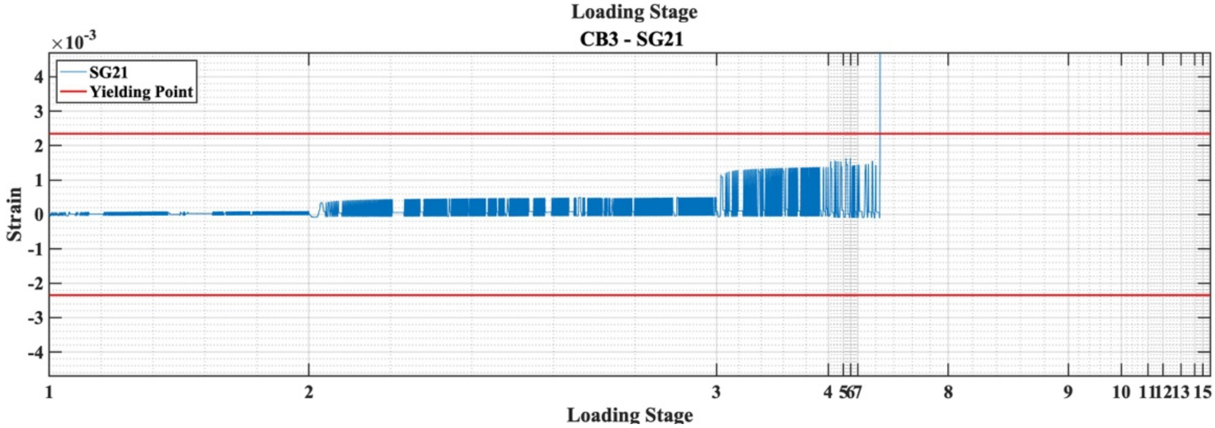

CB3 - SG21
×10^-3
SG21
Yielding Point
Strain
4
3
2
1
0
-1
-2
-3
-4
1
2
3
4 567
8
9
10 1112 13 15
Loading Stage

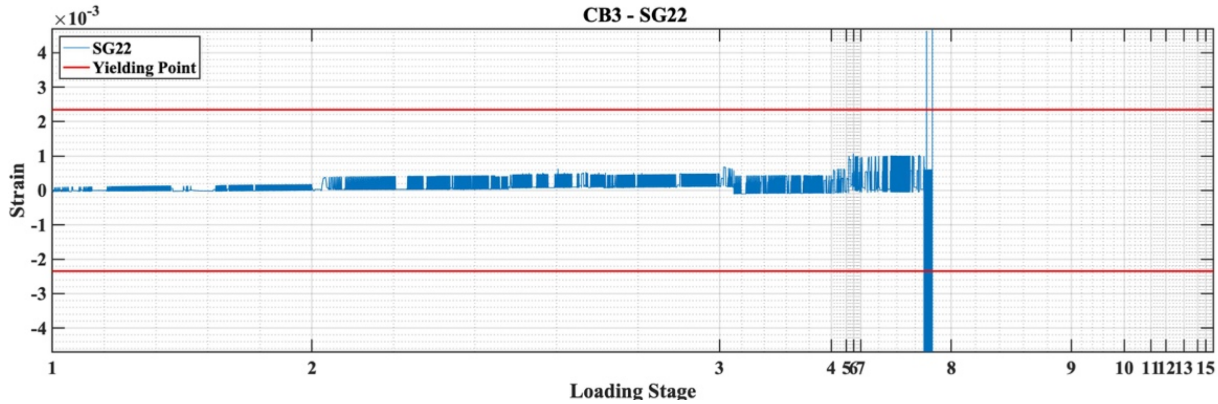

Figure G-3. Strain results from strain gages of CB3.

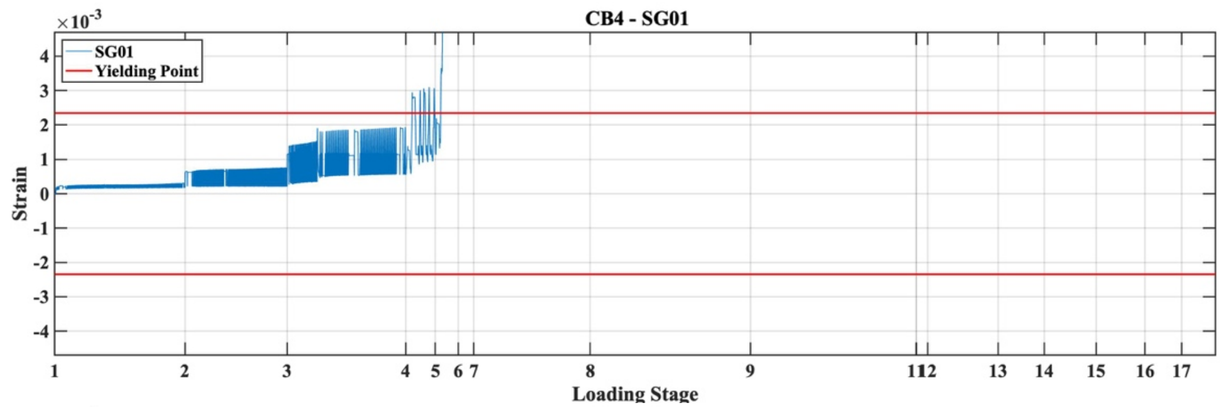

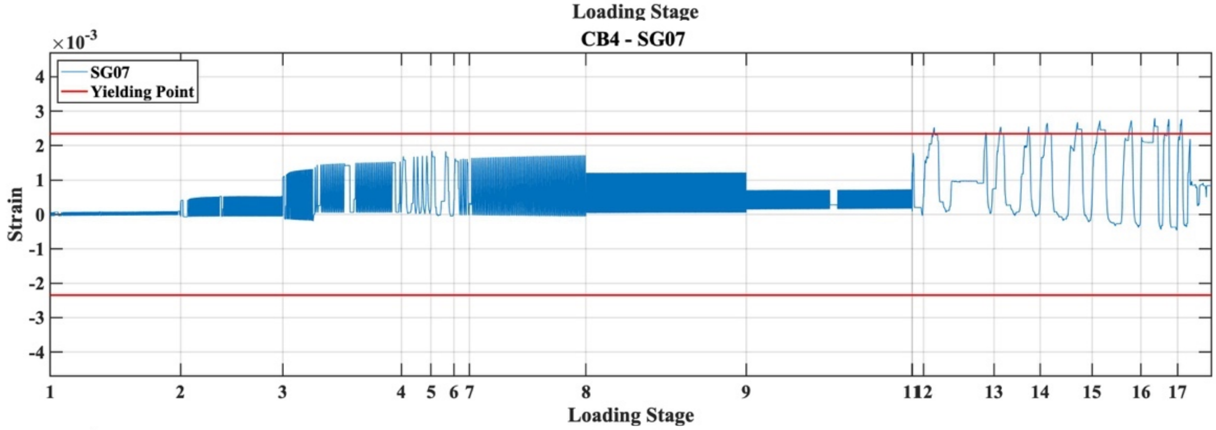

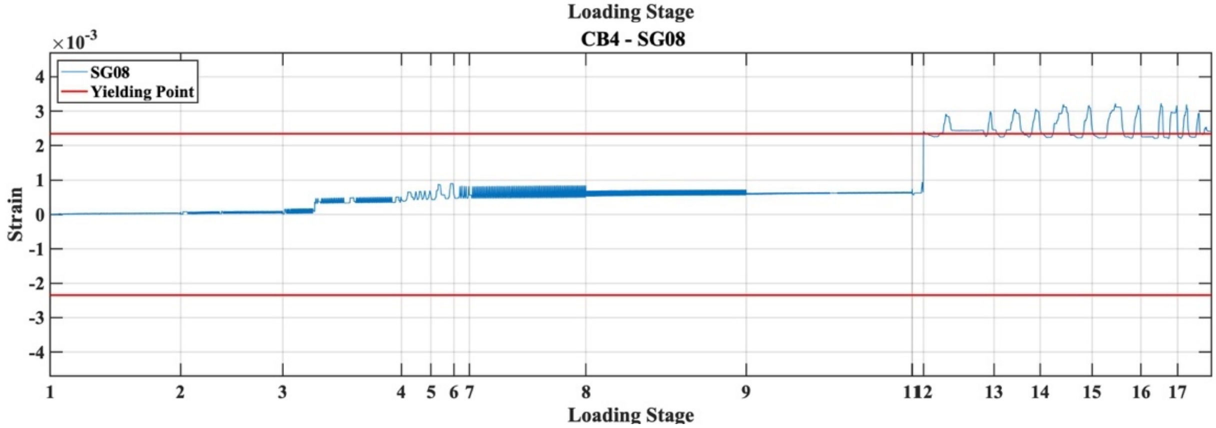

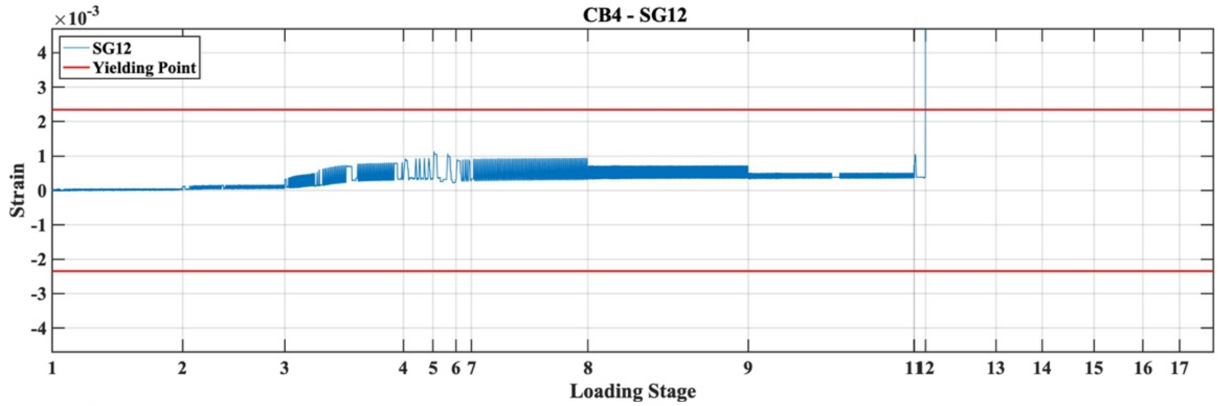
CB4 - SG12
×10^-3
SG12
Yielding Point
Strain
Loading Stage
1 2 3 4 5 6 7 8 9 1112 13 14 15 16 17

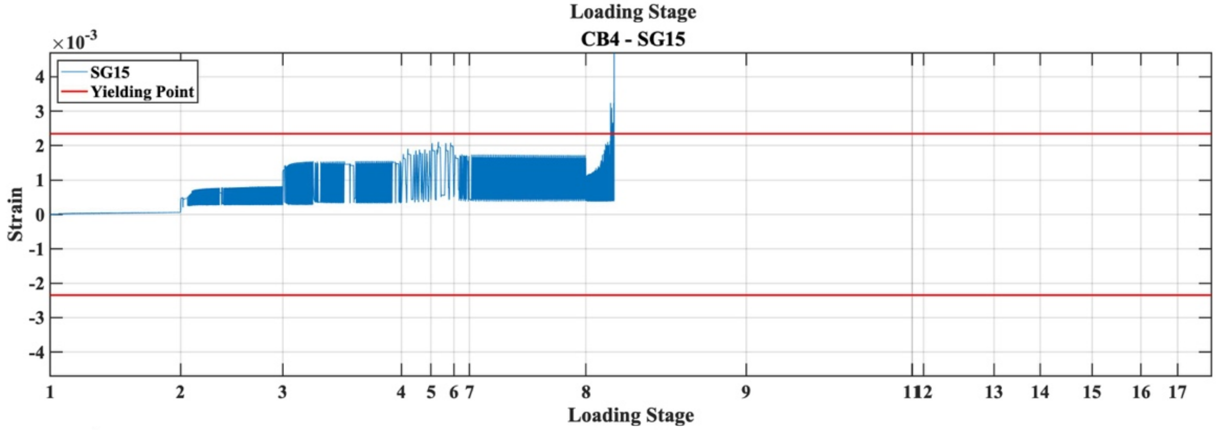
CB4 - SG15
×10^-3
SG15
Yielding Point
Strain
Loading Stage
1 2 3 4 5 6 7 8 9 1112 13 14 15 16 17

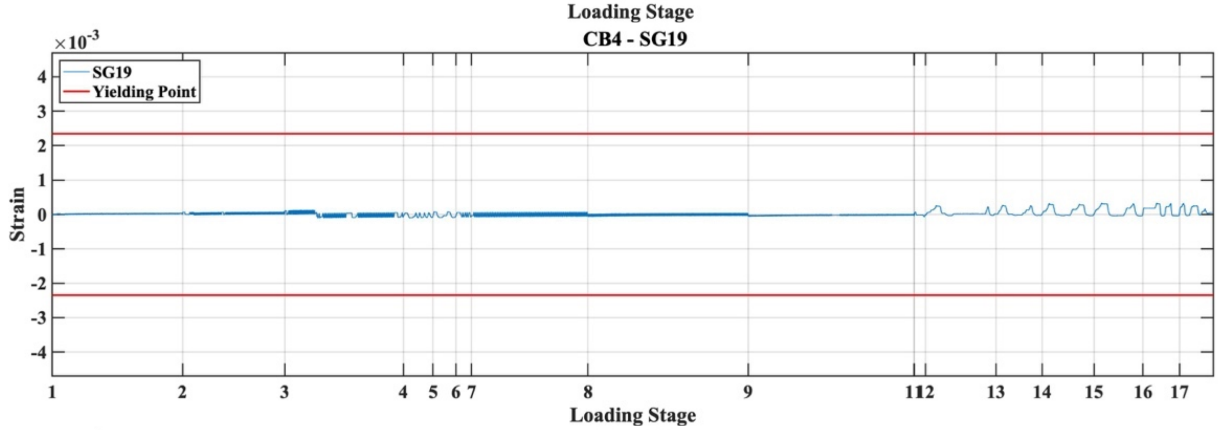
CB4 - SG19
×10^-3
SG19
Yielding Point
Strain
Loading Stage
1 2 3 4 5 6 7 8 9 1112 13 14 15 16 17

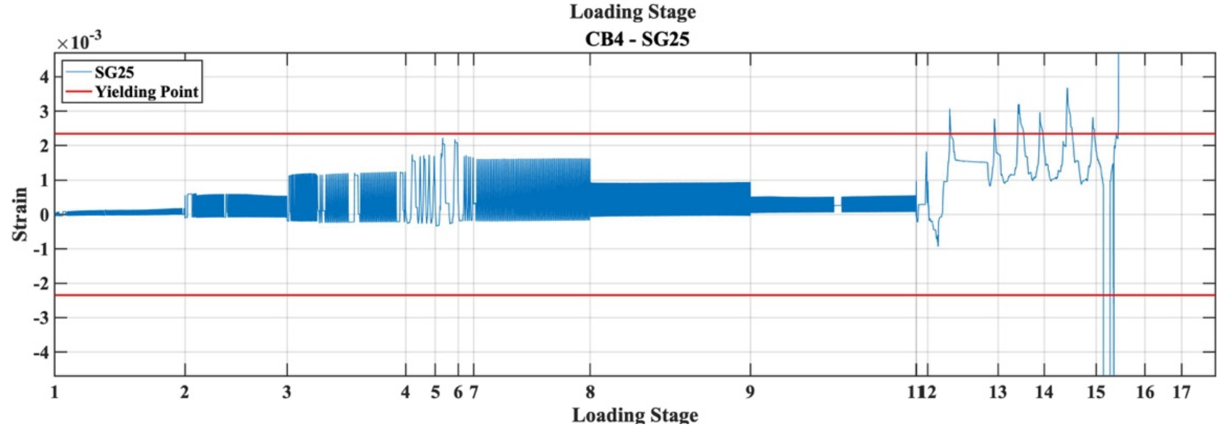
CB4 - SG25
×10^-3
SG25
Yielding Point
Strain
Loading Stage
1 2 3 4 5 6 7 8 9 1112 13 14 15 16 17

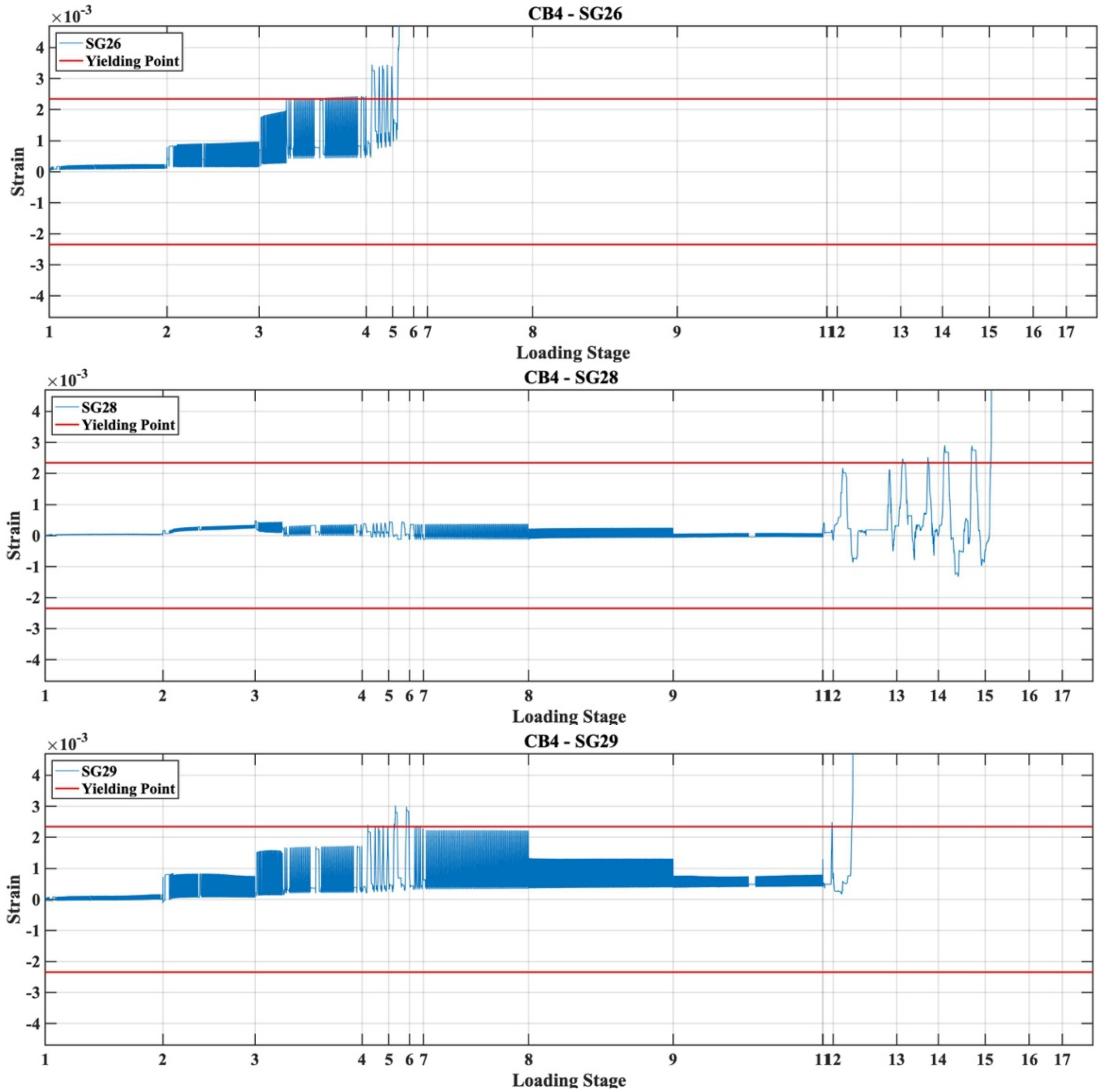

Figure G-4. Strain results from strain gages of CB4.

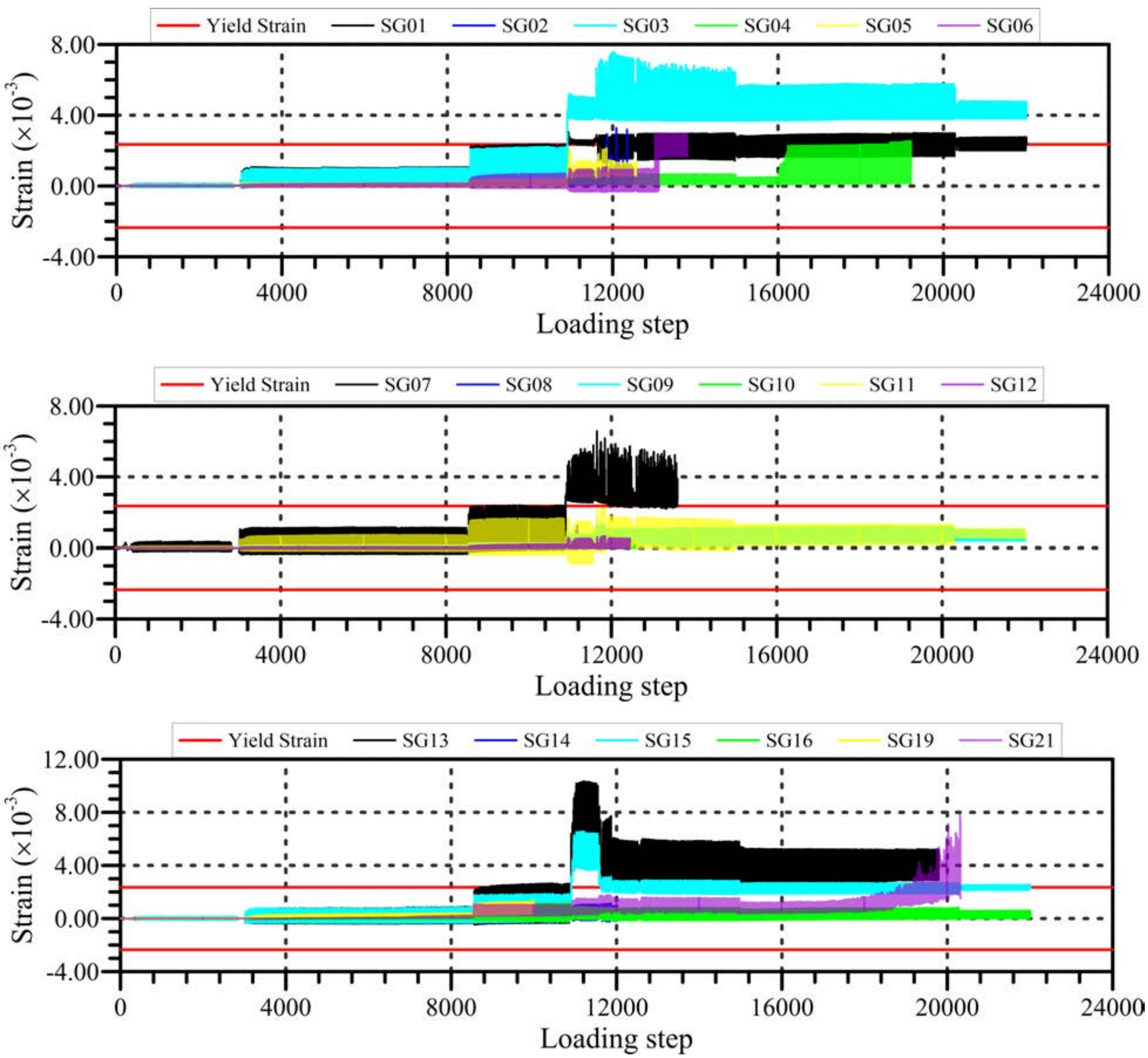

Figure G-5. Strain results from strain gages of CB5.

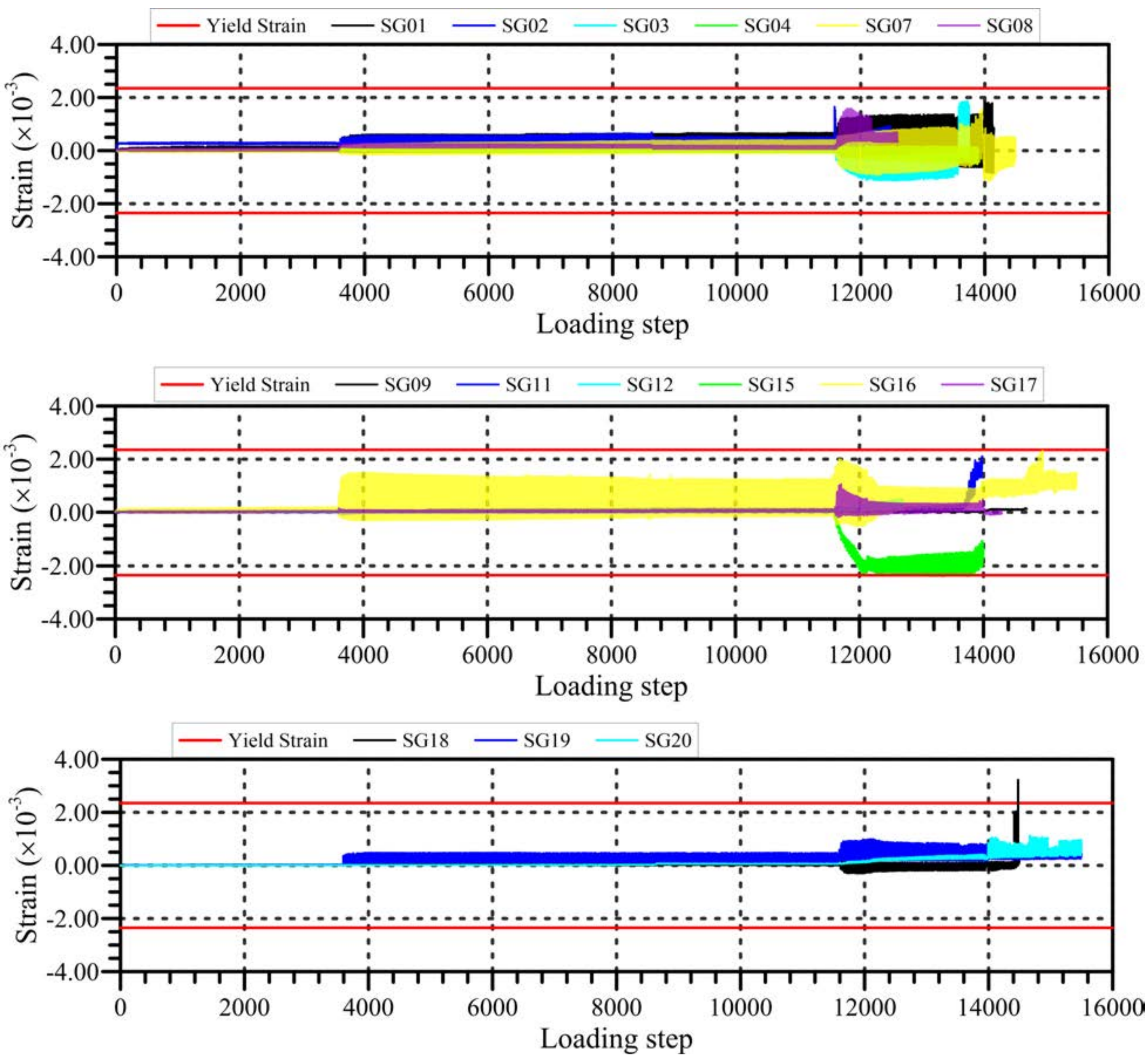

Figure G-6. Strain results from strain gages of CB6.

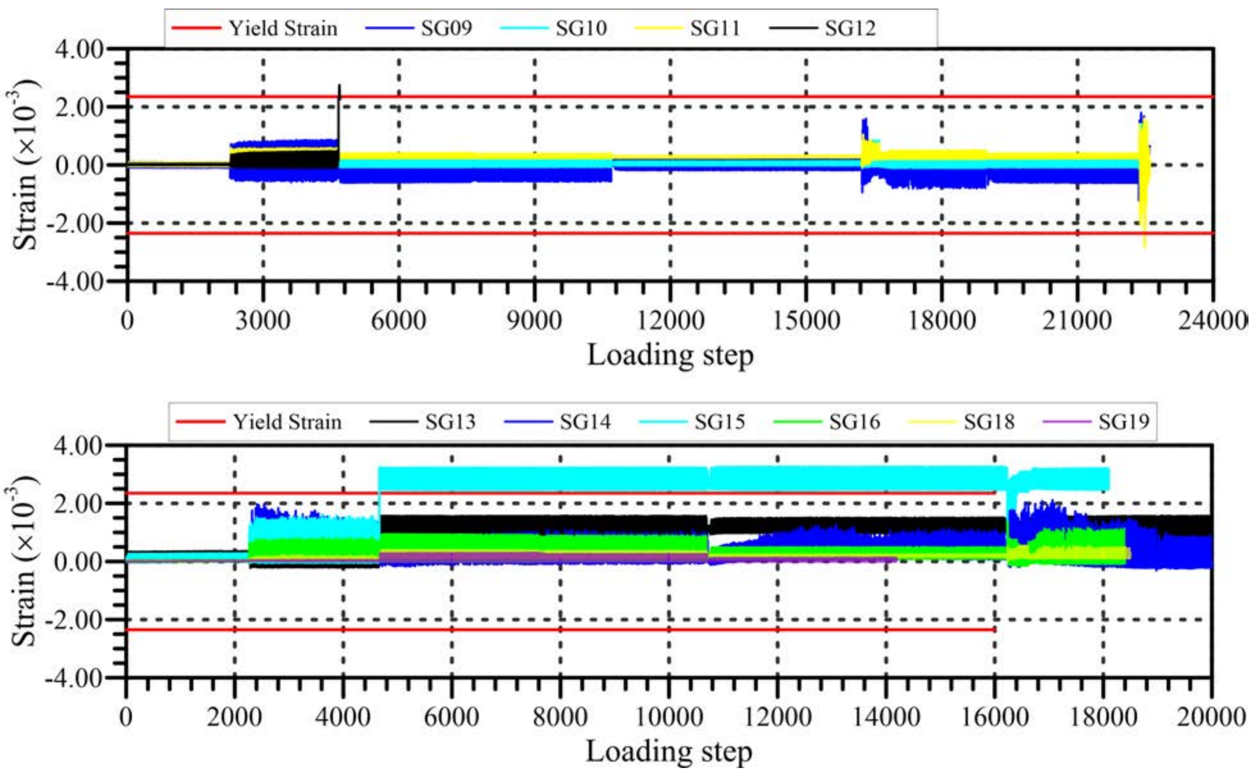

Figure G-7. Strain results from strain gages of CB7.

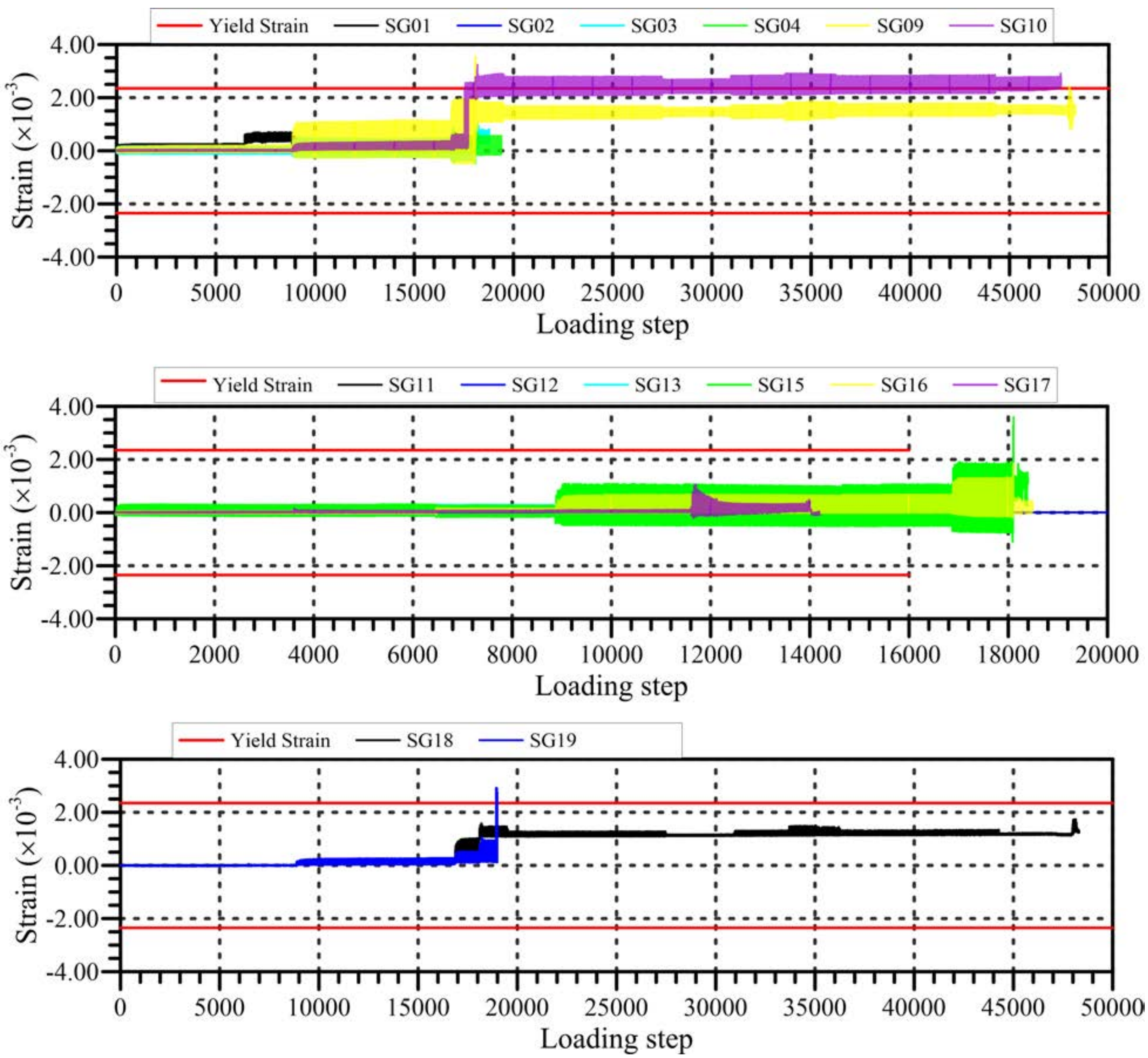

Figure G-8. Strain results from strain gages of CB8.

APPENDEX H–Digital Image Correlation Results

This appendix includes results of surface strains, crack widths, and crack patterns obtained using an optical non-contact measurement system, referred to as Digital Image Correlation (DIC), during the wind loading protocols. The results include surface strains and crack pattern and widths (mostly diagonal shear cracks) during the last cycle at peak ductility demand of 1.5 in both directions of loading (e.g., see **Figure H-1** for results for CB1), crack width history during last cycle at peak ductility demand of 1.5 (e.g., see **Figure H-2** for results for CB1), and residual surface strains and residual crack widths at the end of the wind loading protocol at zero rotation demand (e.g., see **Figure H-3** for results for CB1).

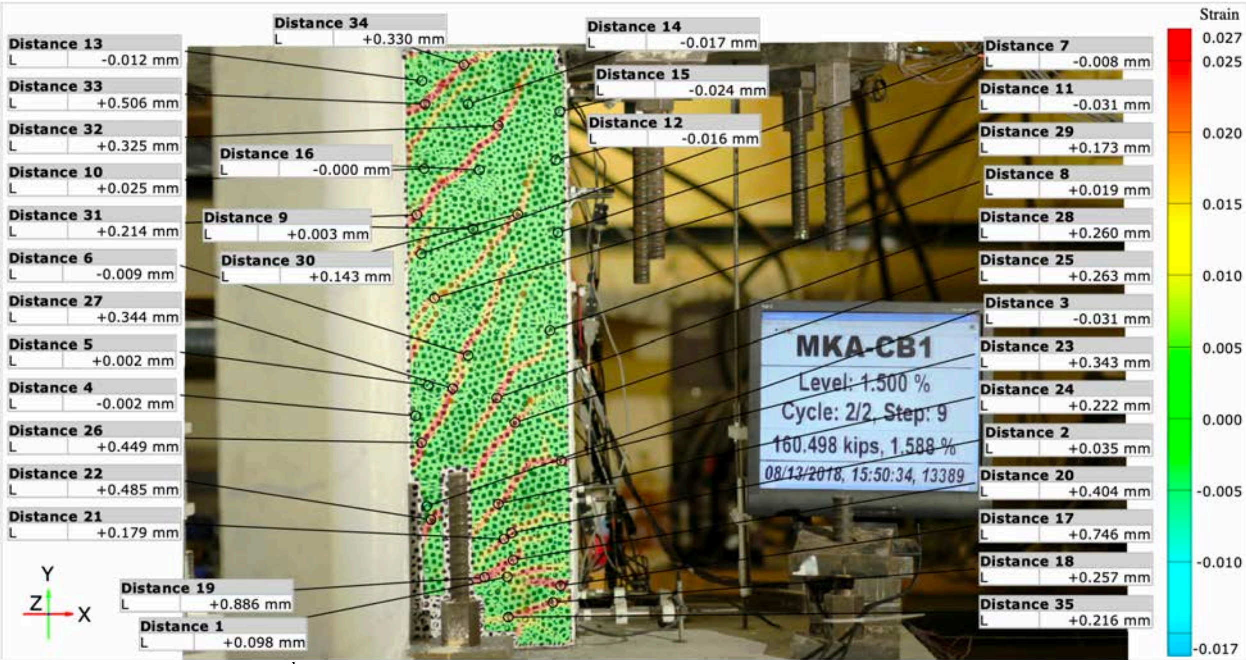

(*a*) 2nd cycle at peak ductility demand of 1.5 in the positive direction

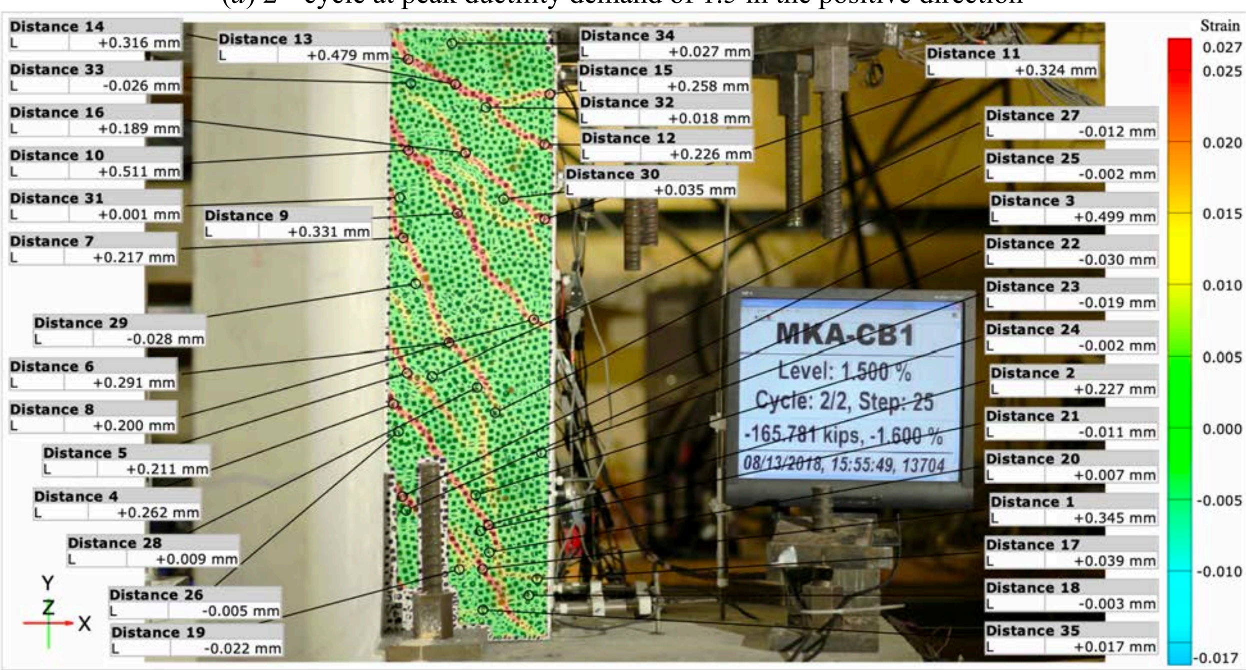

(*b*) 2nd cycle at peak ductility demand of 1.5 in the negative direction

Figure H-1. Crack pattern and widths obtained from DIC for CB1. (Note: 1 mm = 0.0394 in.)

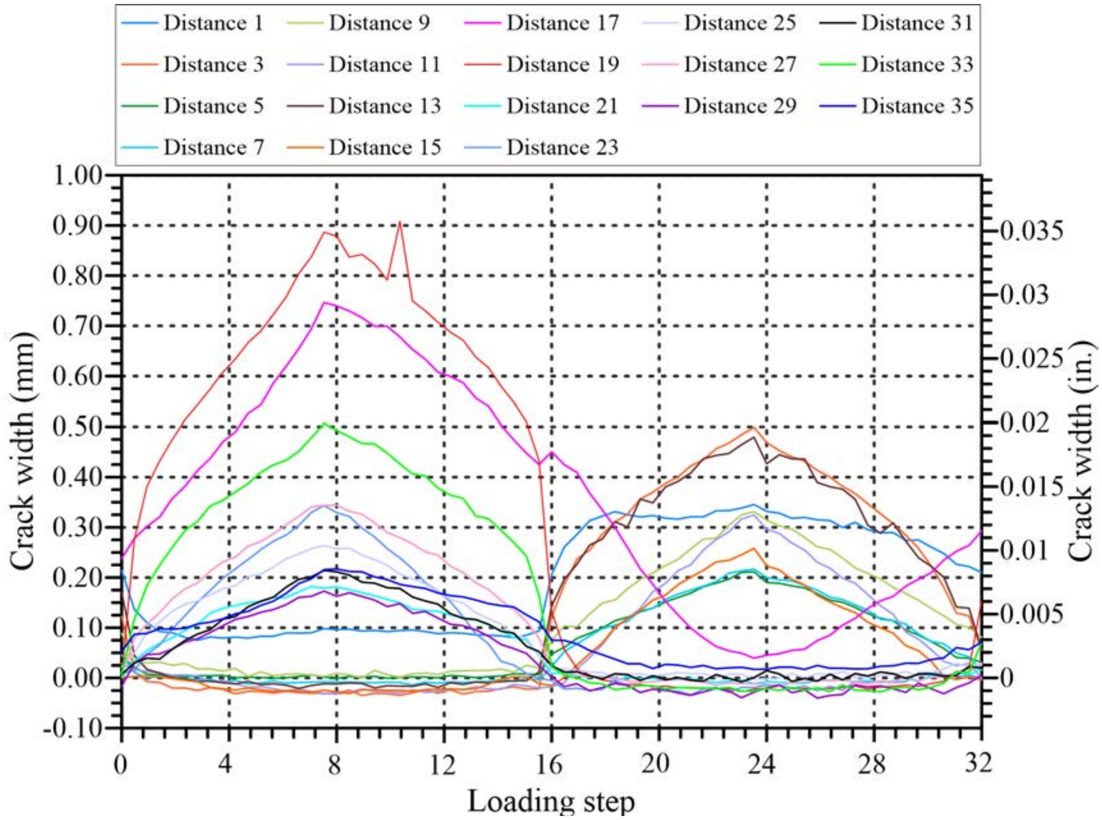

Figure H-2. Crack width history during 2nd cycle at ductility demand of 1.5 for CB1.

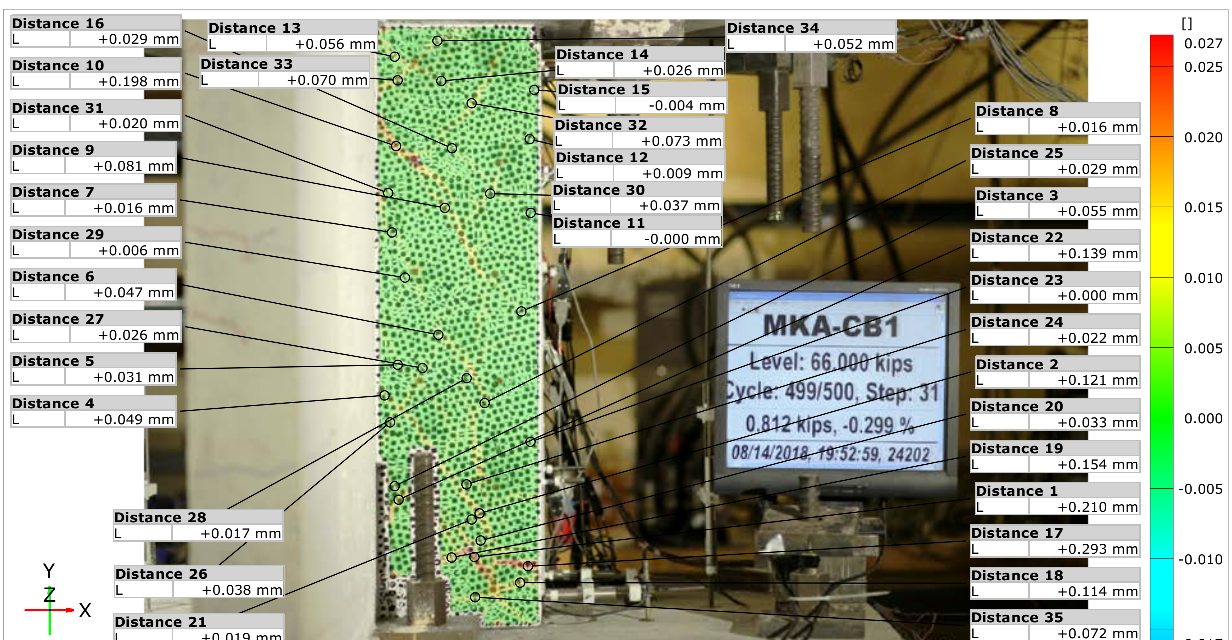

Figure H-3. Crack pattern and widths obtained from DIC for CB1 at zero rotation at end of wind loading protocol. (Note: 1 mm = 0.0394 in.)

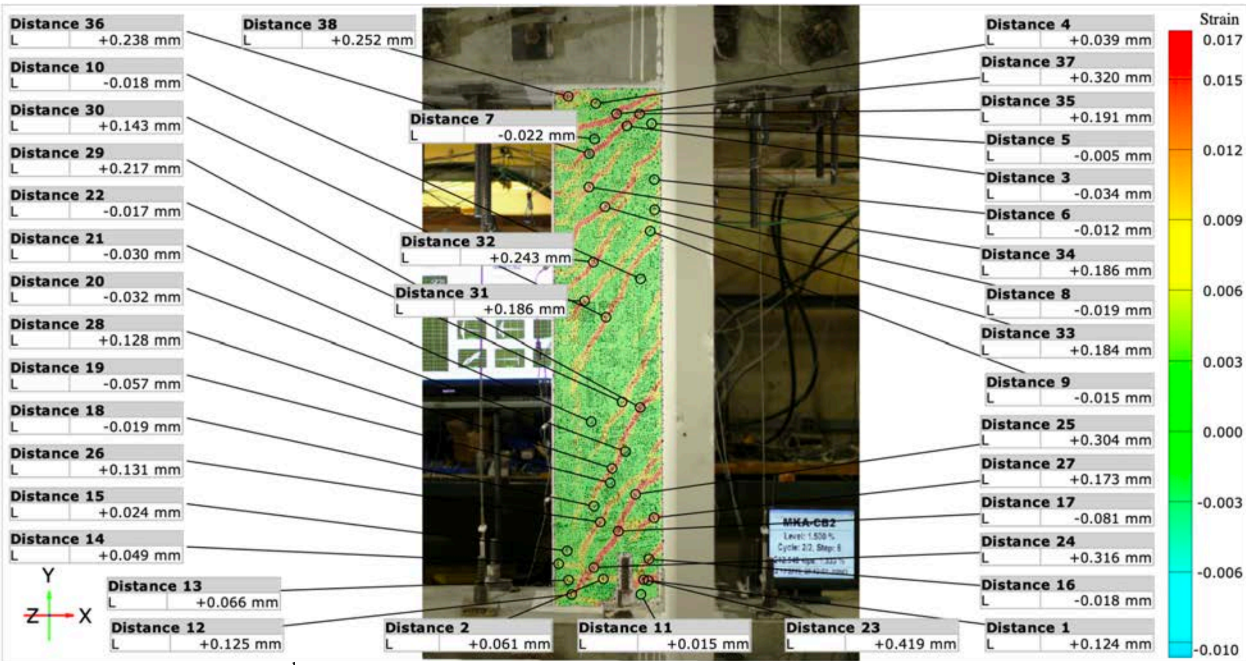

(*a*) 2nd cycle at peak ductility demand of 1.5 in the positive direction

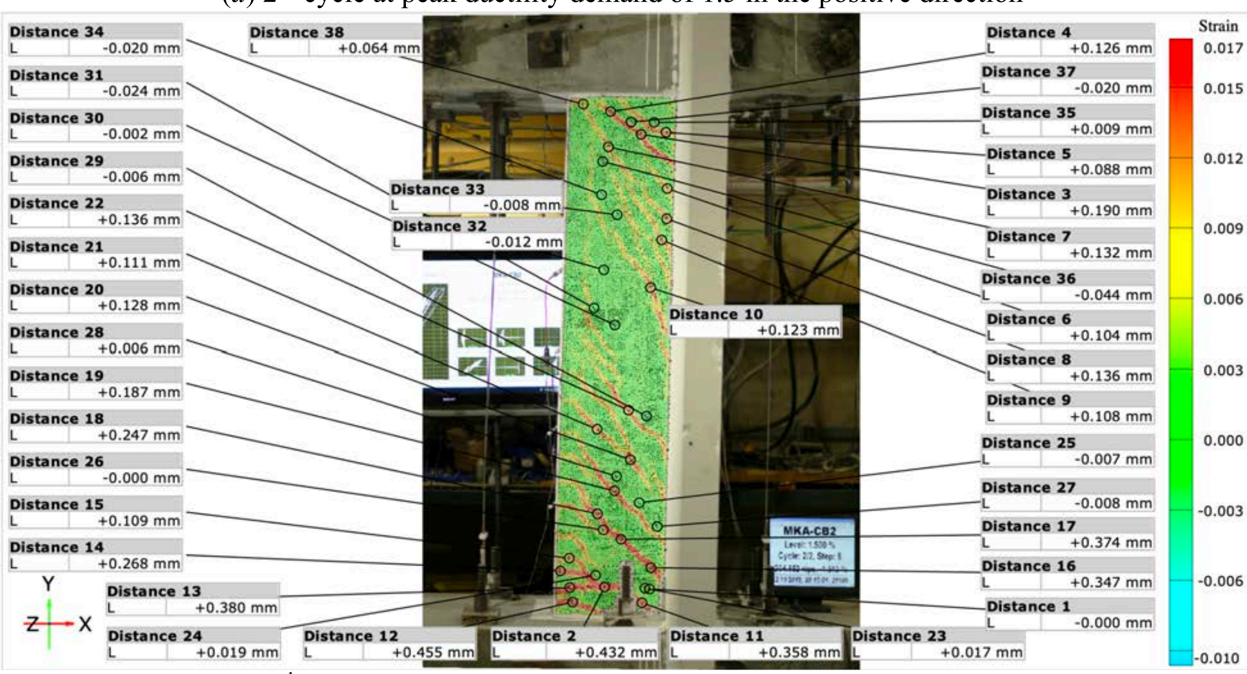

(*b*) 2nd cycle at peak ductility demand of 1.5 in the negative direction

Figure H-4. Crack pattern and widths obtained from DIC for CB2. (Note: 1 mm = 0.0394 in.)

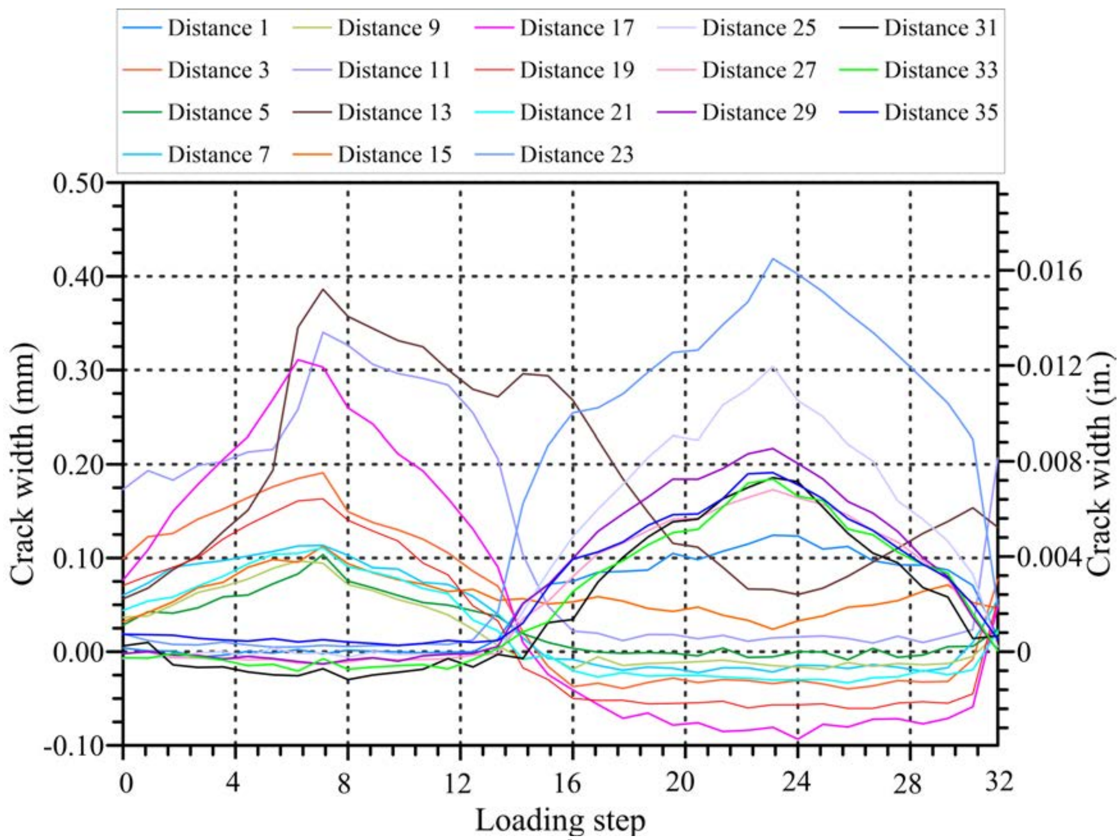

Figure H-5. Crack width history during 2nd cycle at ductility demand of 1.5 for CB2.

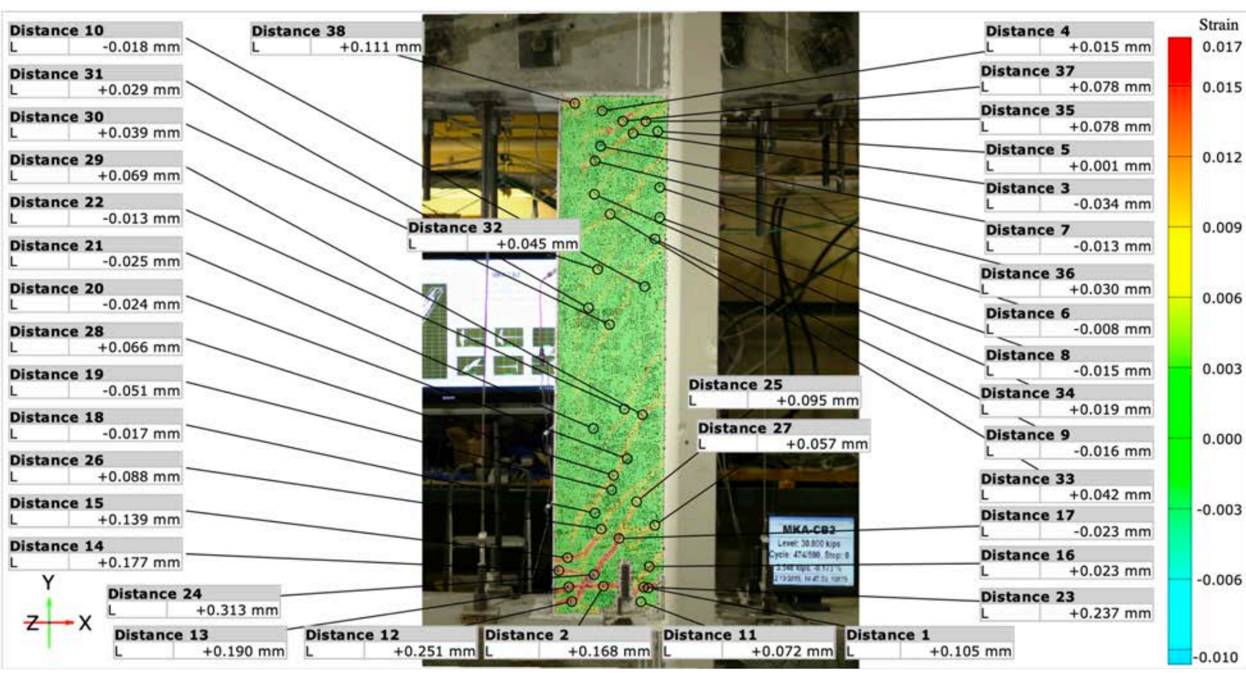

Figure H-6. Crack pattern and widths obtained from DIC for CB2 at zero rotation at end of wind loading protocol. (Note: 1 mm = 0.0394 in.)

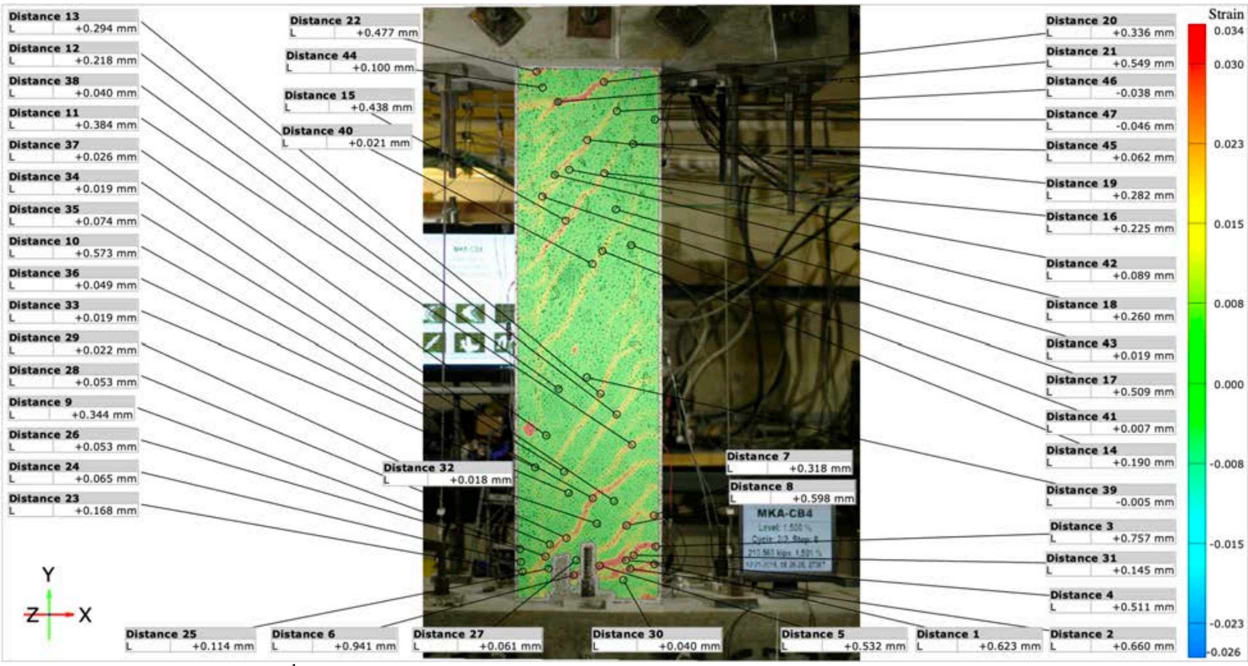

(*a*) 2nd cycle at peak ductility demand of 1.5 in the positive direction

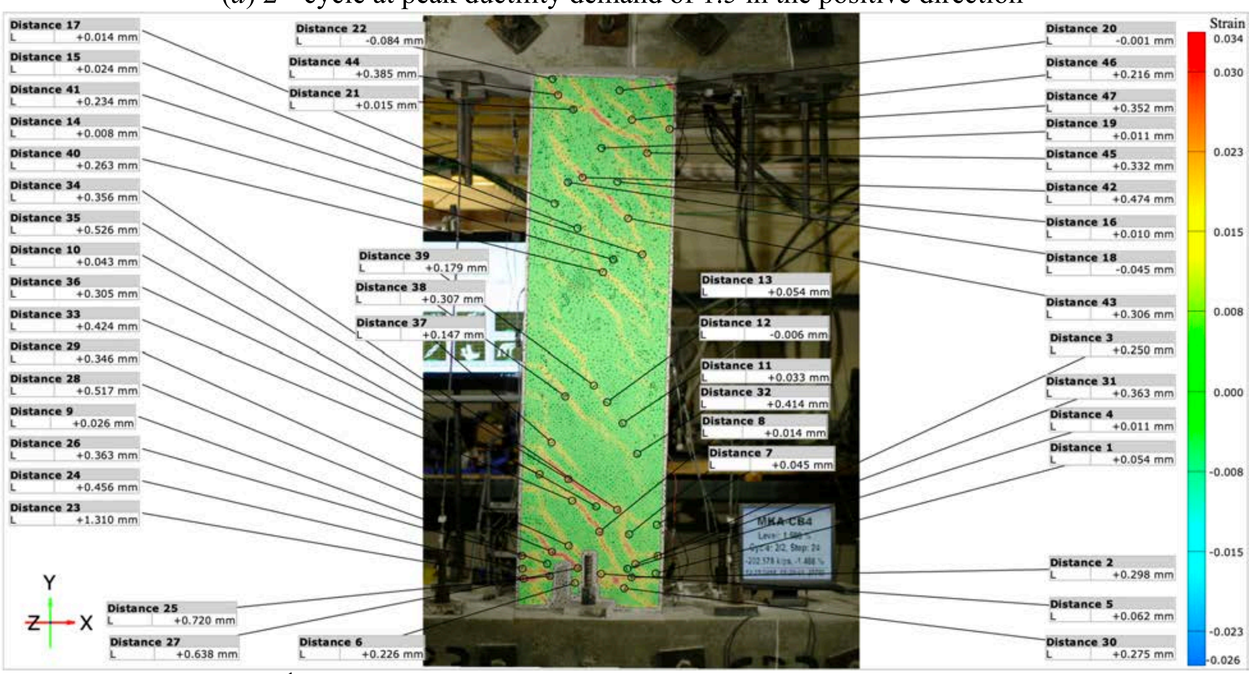

(*b*) 2nd cycle at peak ductility demand of 1.5 in the negative direction

Figure H-7. Crack pattern and widths obtained from DIC for CB3. (Note: 1 mm = 0.0394 in.)

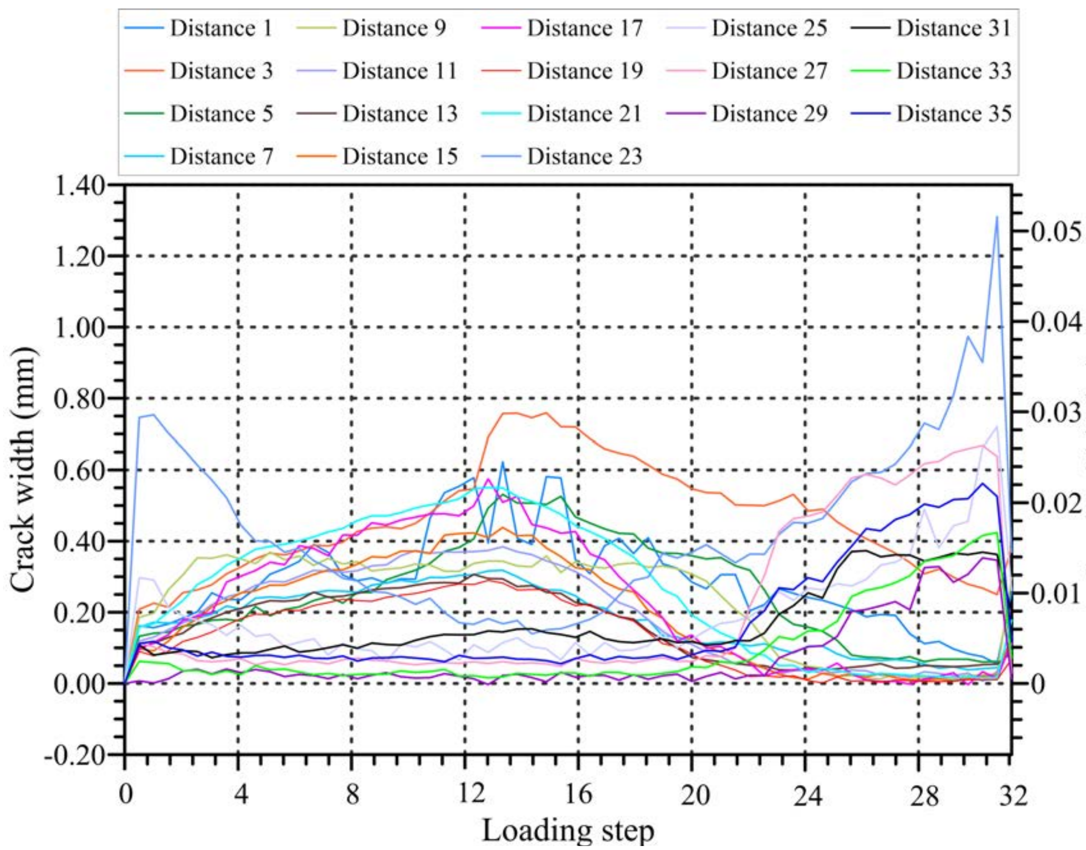

Figure H-8. Crack width history during 2nd cycle at ductility demand of 1.5 for CB3.

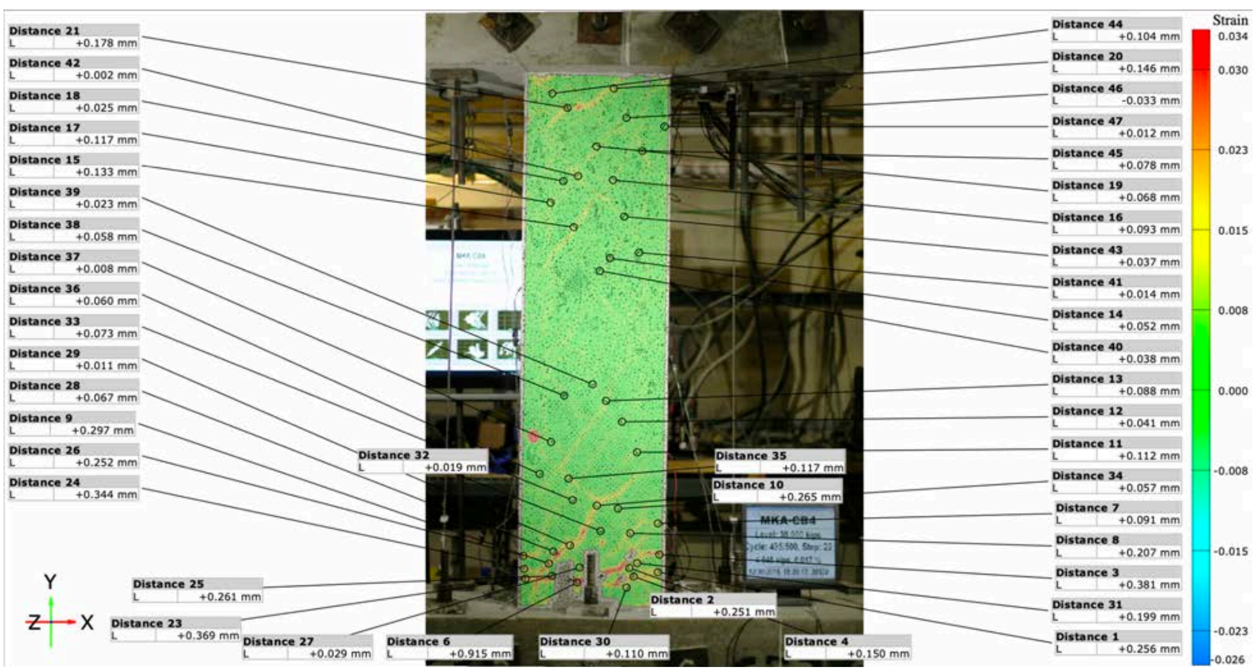

Figure H-9. Crack pattern and widths obtained from DIC for CB3 at zero rotation at end of wind loading protocol. (Note: 1 mm = 0.0394 in.)

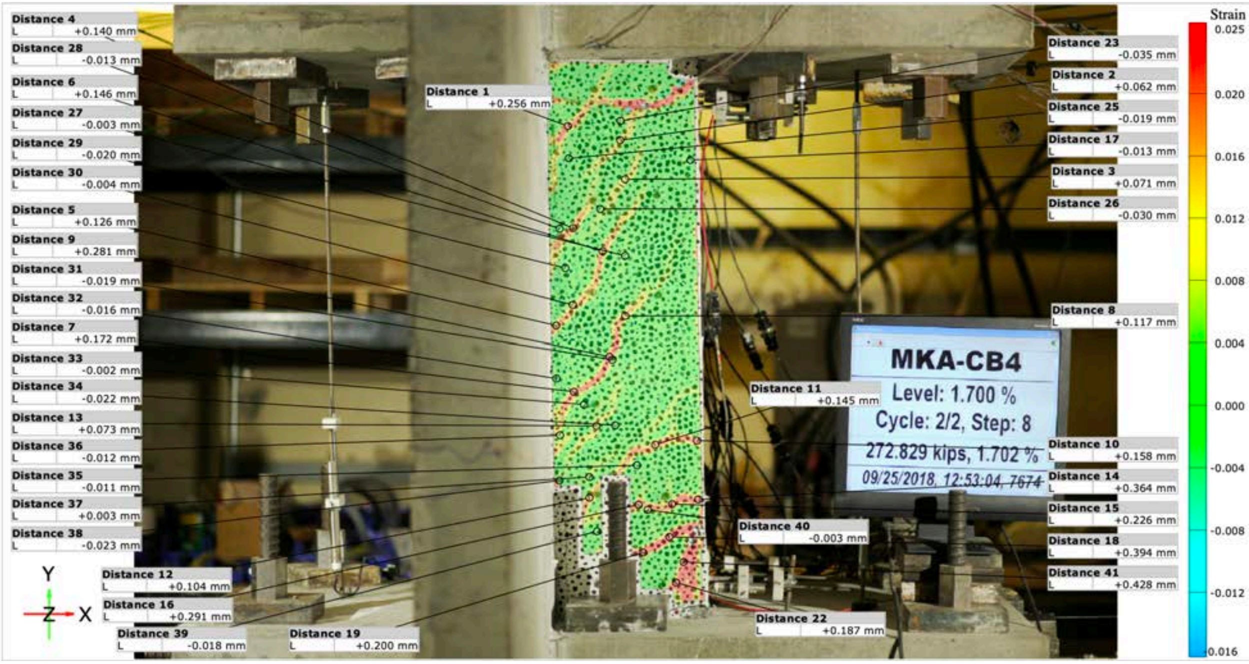

(H) 2nd cycle at peak ductility demand of 1.5 in the positive direction

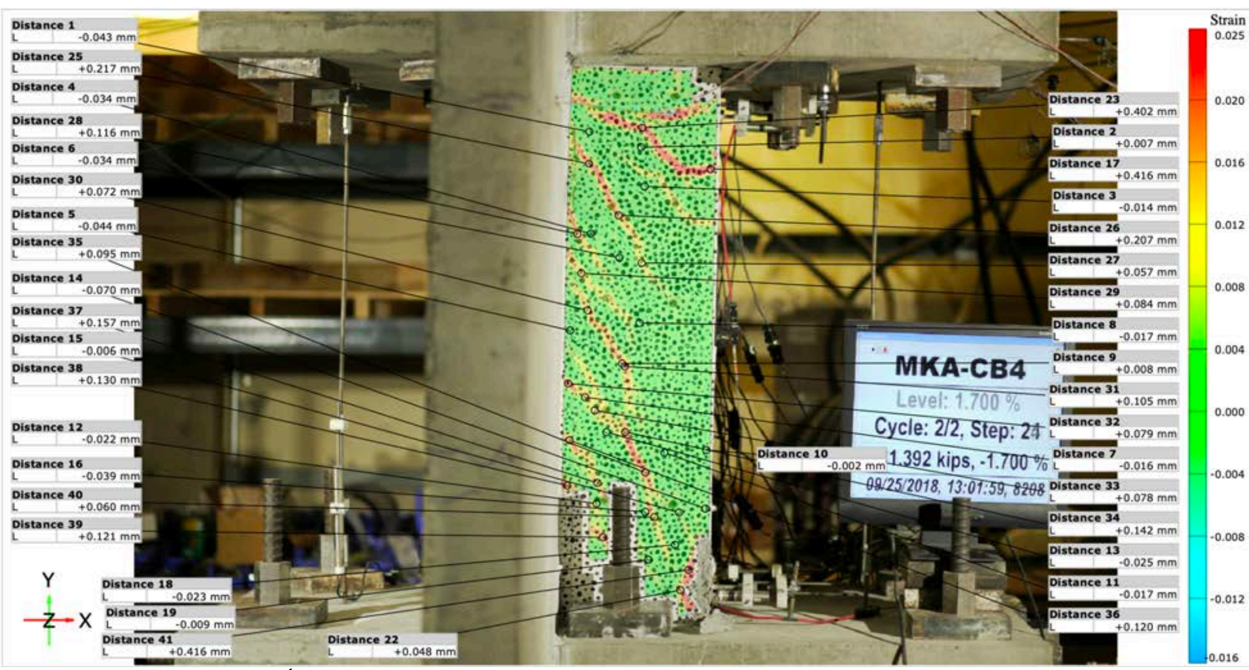

(*b*) 2nd cycle at peak ductility demand of 1.5 in the negative direction

Figure H-10. Crack pattern and widths obtained from DIC for CB4. (Note: 1 mm = 0.0394 in.)

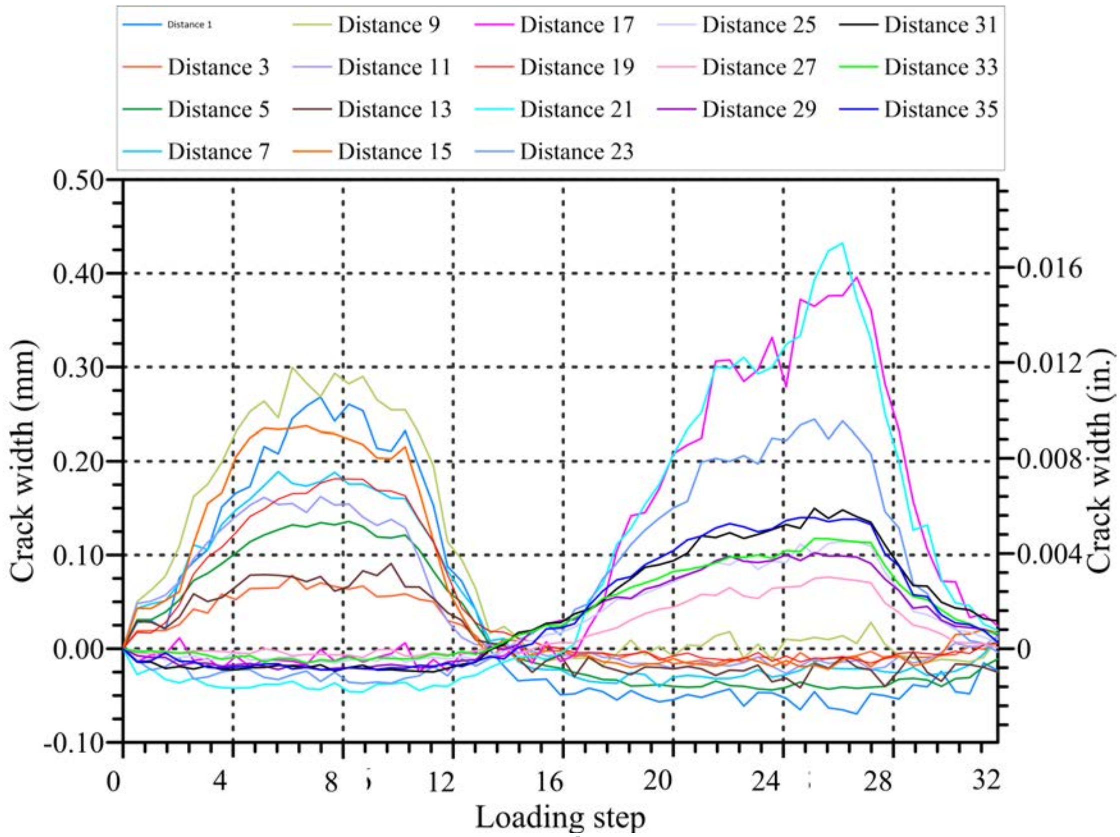

Figure H-11. Crack width history during 2nd cycle at ductility demand of 1.5 for CB4.

Figure H-12. Crack pattern and widths obtained from DIC for CB4 at zero rotation at near the end of wind loading protocol. (Note: 1 mm = 0.0394 in.)

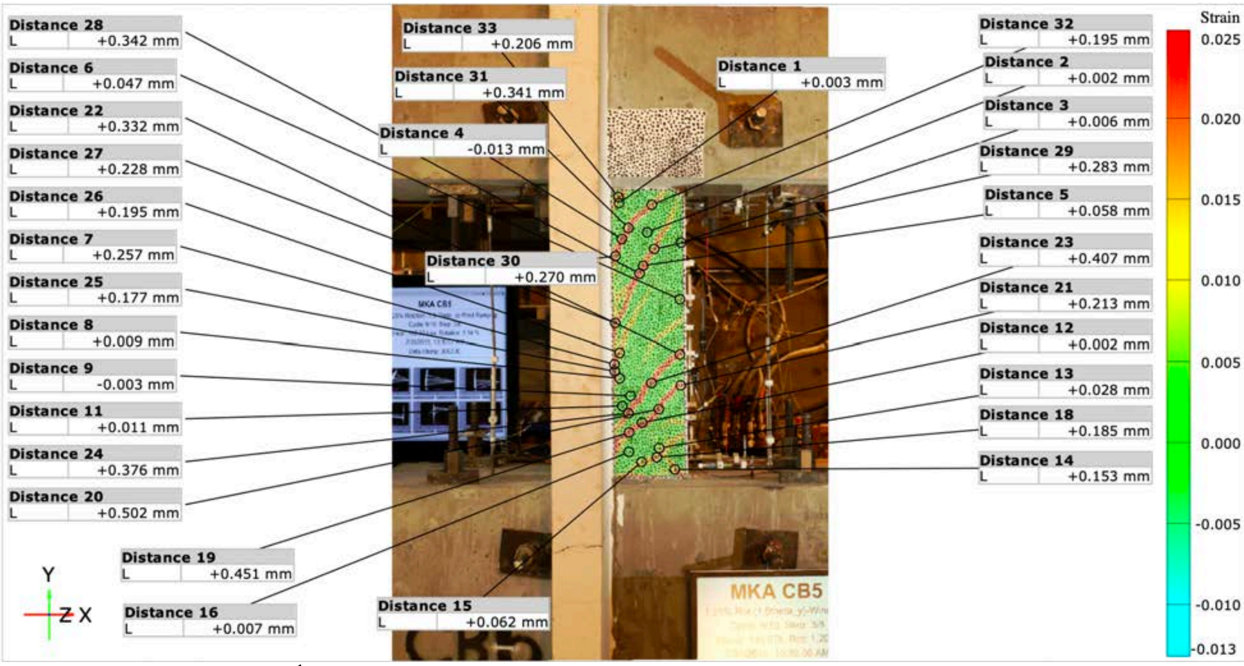

(*a*) 10nd cycle at peak ductility demand of 1.5 in the positive direction

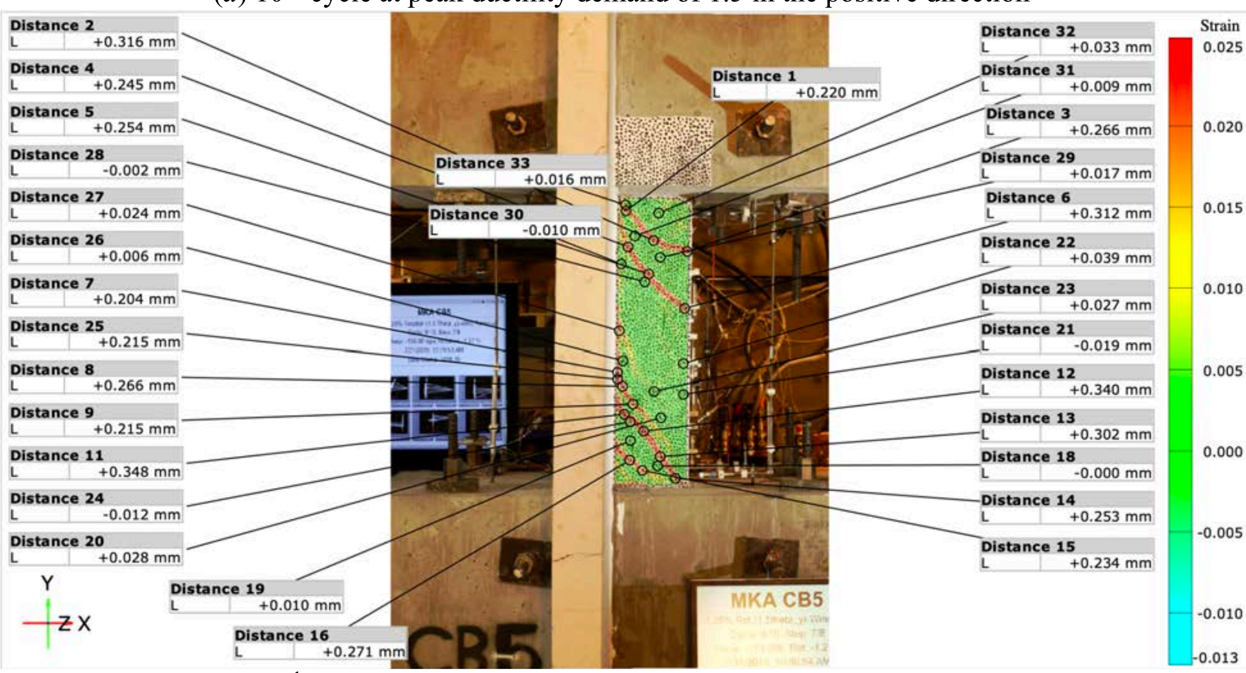

(*b*) 10nd cycle at peak ductility demand of 1.5 in the negative direction

Figure H-13. Crack pattern and widths obtained from DIC for CB5. (Note: 1 mm = 0.0394 in.)

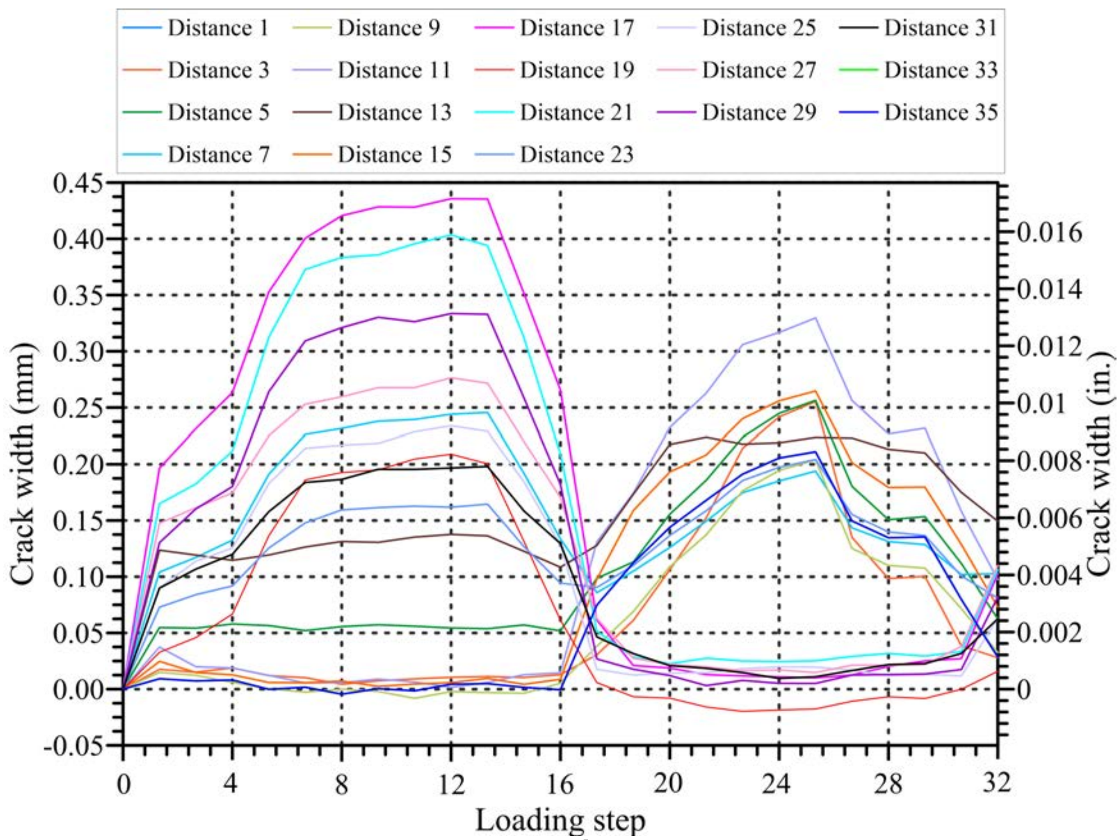

Figure H-14. Crack width history during 10nd cycle at ductility demand of 1.5 for CB5.

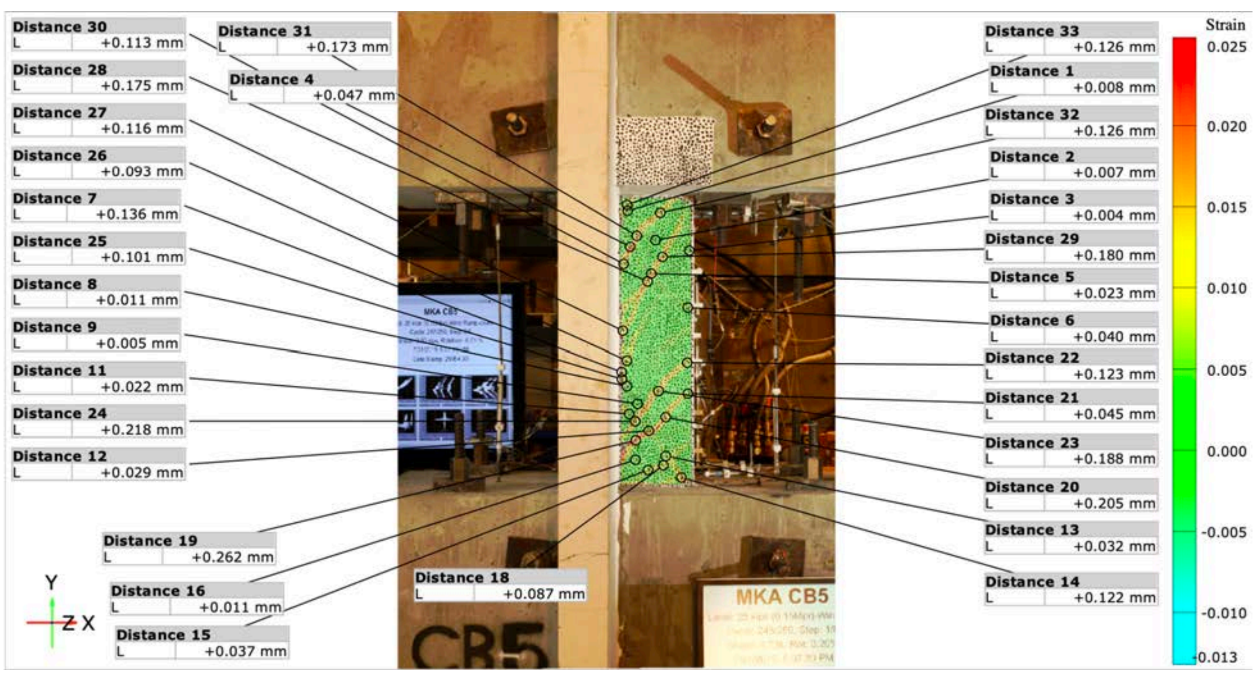

Figure H-15. Crack pattern and widths obtained from DIC for CB5 at zero rotation at end of wind loading protocol. (Note: 1 mm = 0.0394 in.)

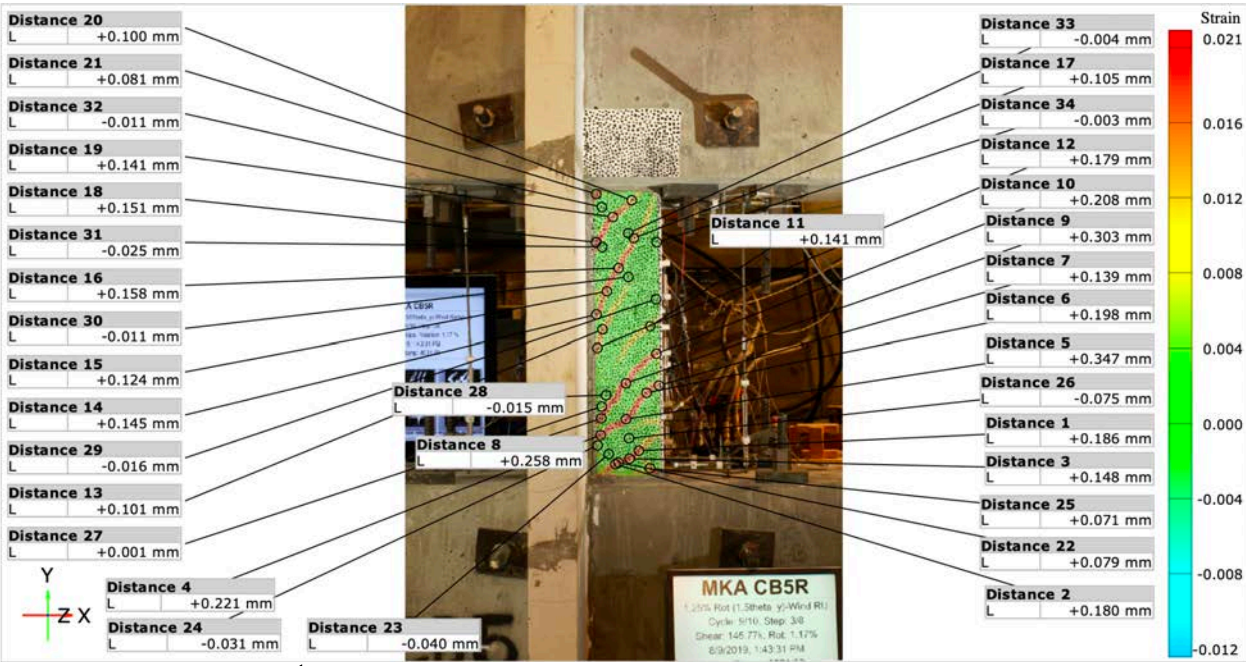

(*a*) 10nd cycle at peak ductility demand of 1.5 in the positive direction

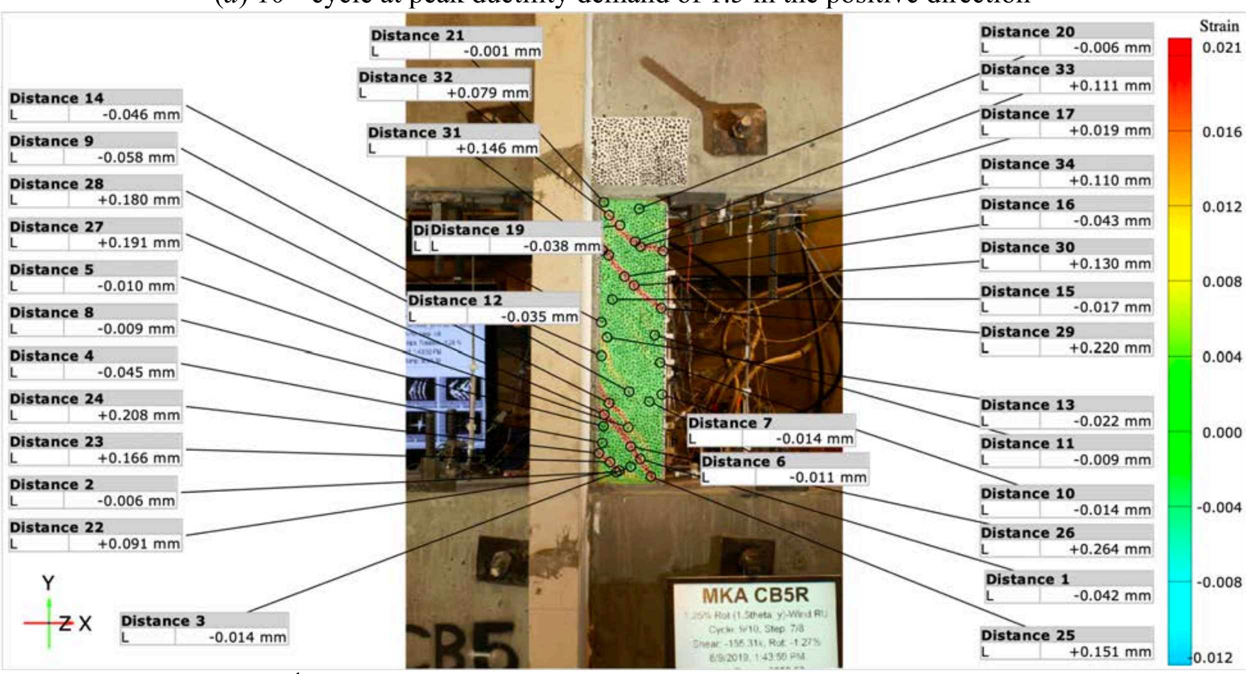

(*b*) 10nd cycle at peak ductility demand of 1.5 in the negative direction

Figure H-16. Crack pattern and widths obtained from DIC for CB5R. (Note: 1 mm = 0.0394 in.)

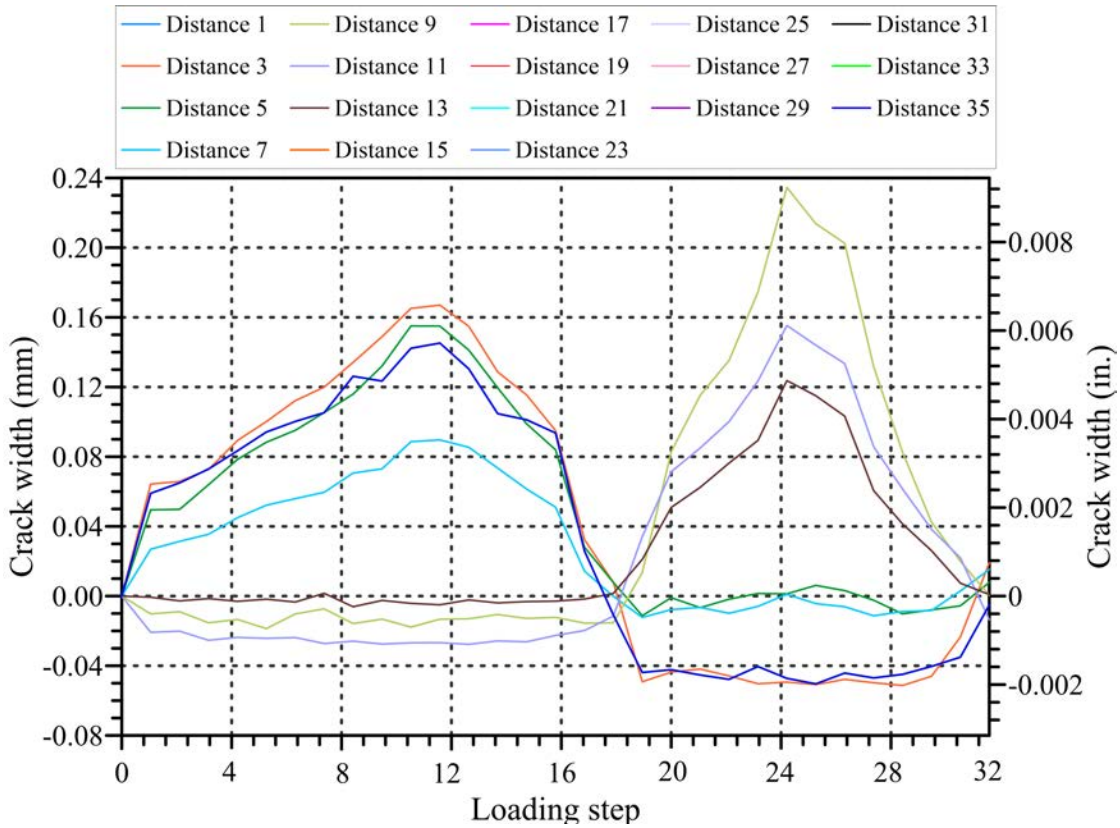

Figure H-17. Crack width history during 10nd cycle at ductility demand of 1.5 for CB5R.

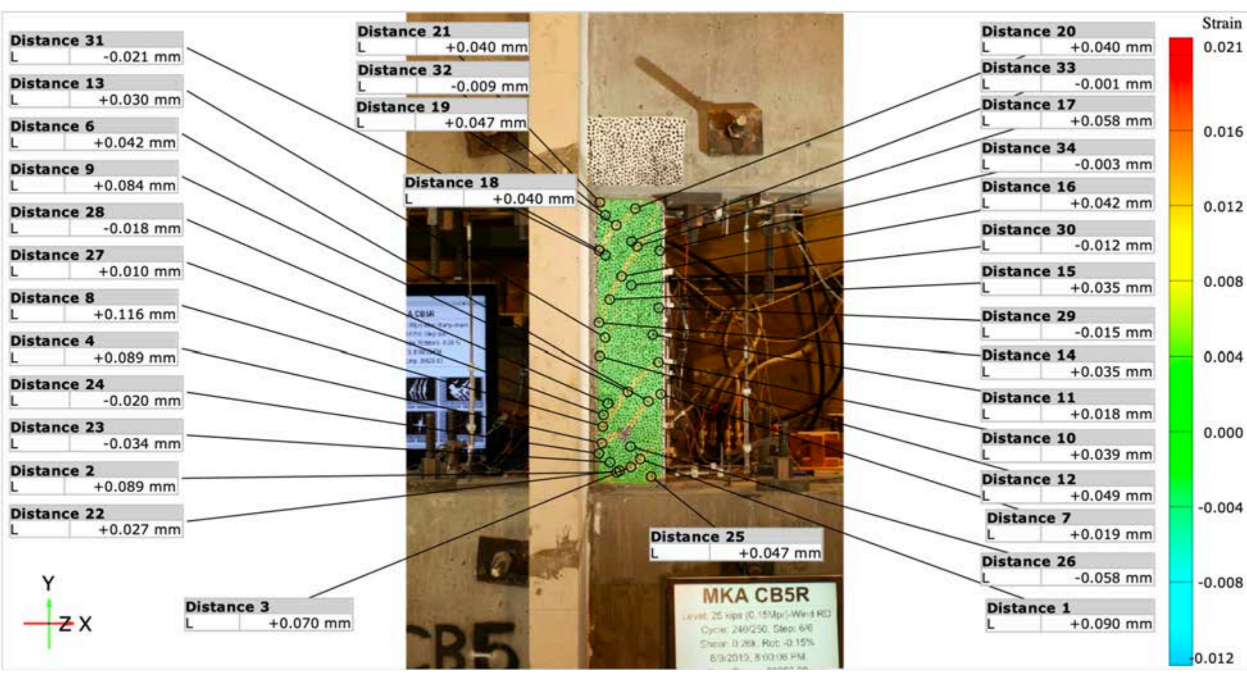

Figure H-18. Crack pattern and widths obtained from DIC for CB5R at zero rotation at end of wind loading protocol. (Note: 1 mm = 0.0394 in.)

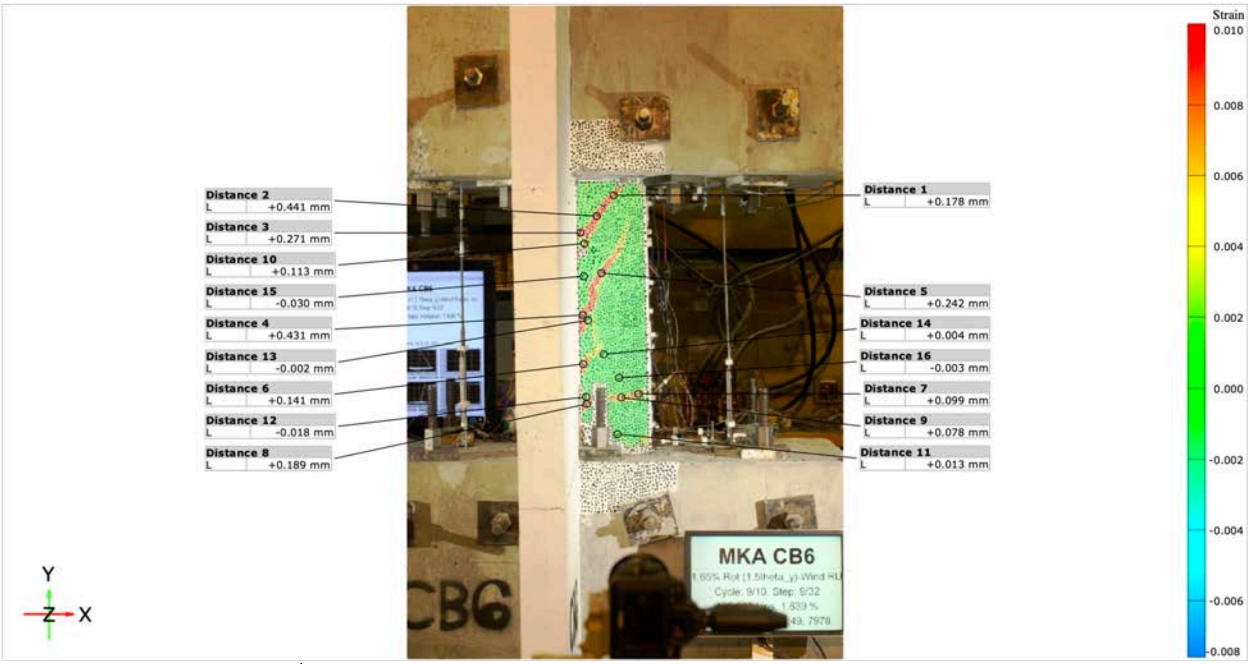

(*a*) 10nd cycle at peak ductility demand of 1.5 in the positive direction

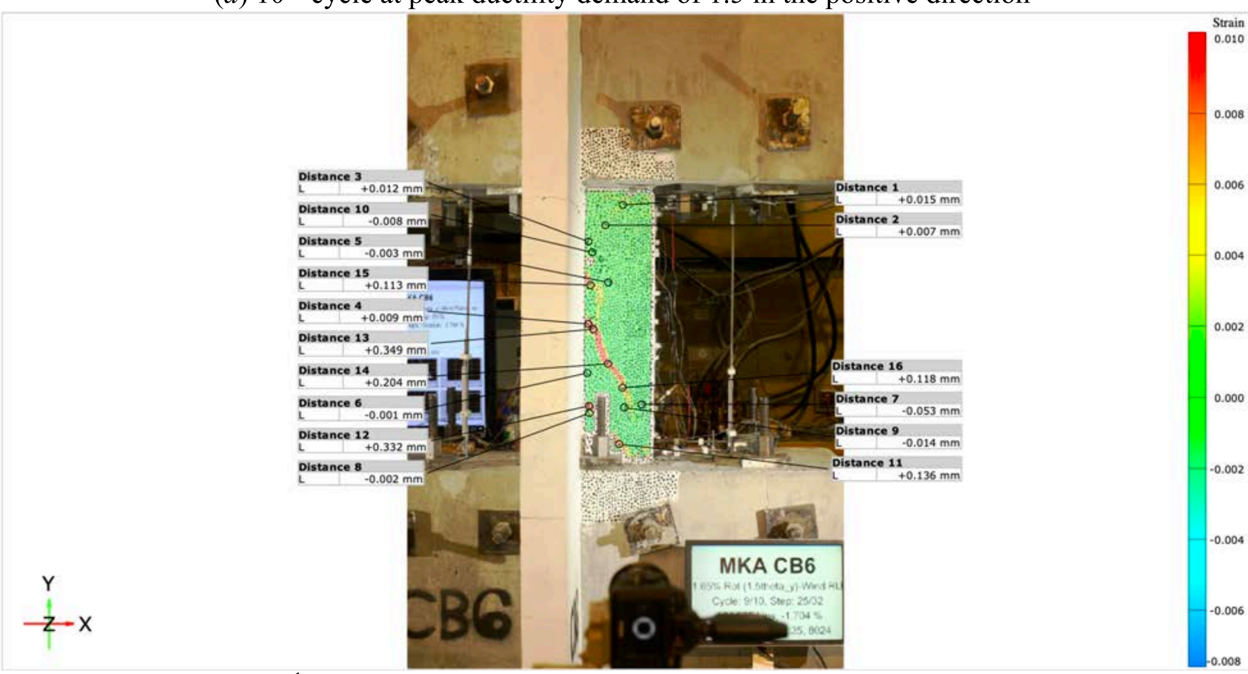

(*b*) 10nd cycle at peak ductility demand of 1.5 in the negative direction

Figure H-19. Crack pattern and widths obtained from DIC for CB6. (Note: 1 mm = 0.0394 in.)

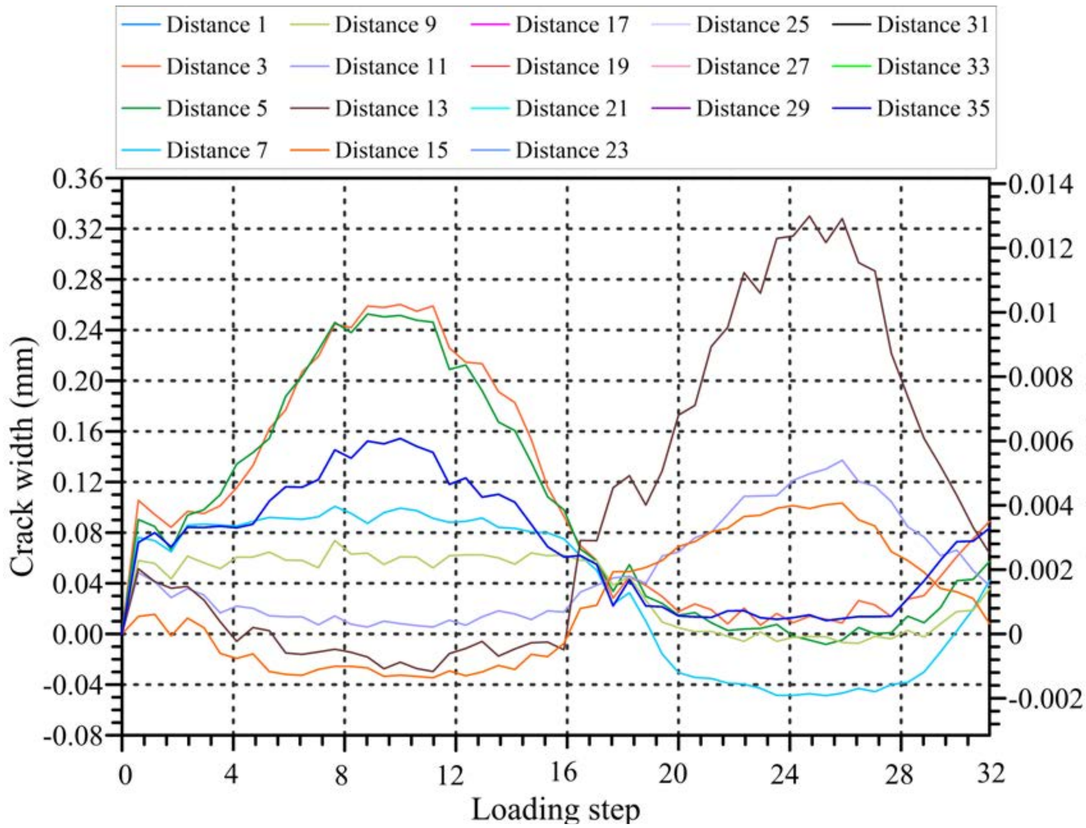

Figure H-20. Crack width history during 10nd cycle at ductility demand of 1.5 for CB6.

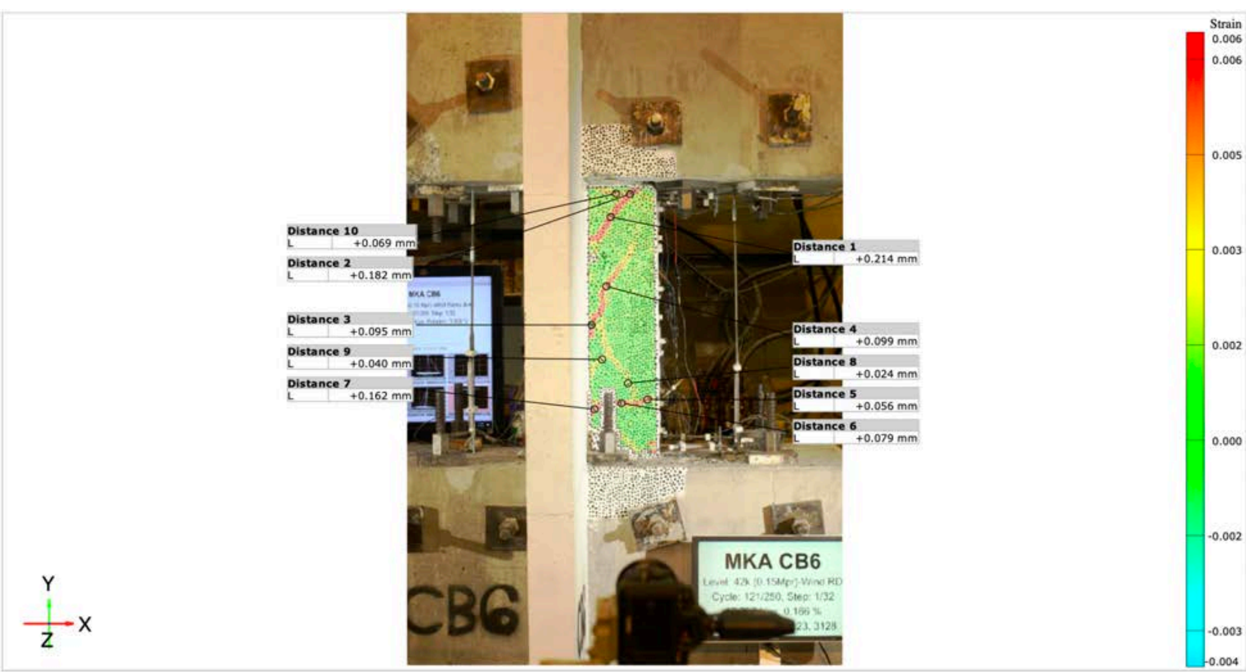

Figure H-21. Crack pattern and widths obtained from DIC for CB6 at zero rotation at end of wind loading protocol. (Note: 1 mm = 0.0394 in.)

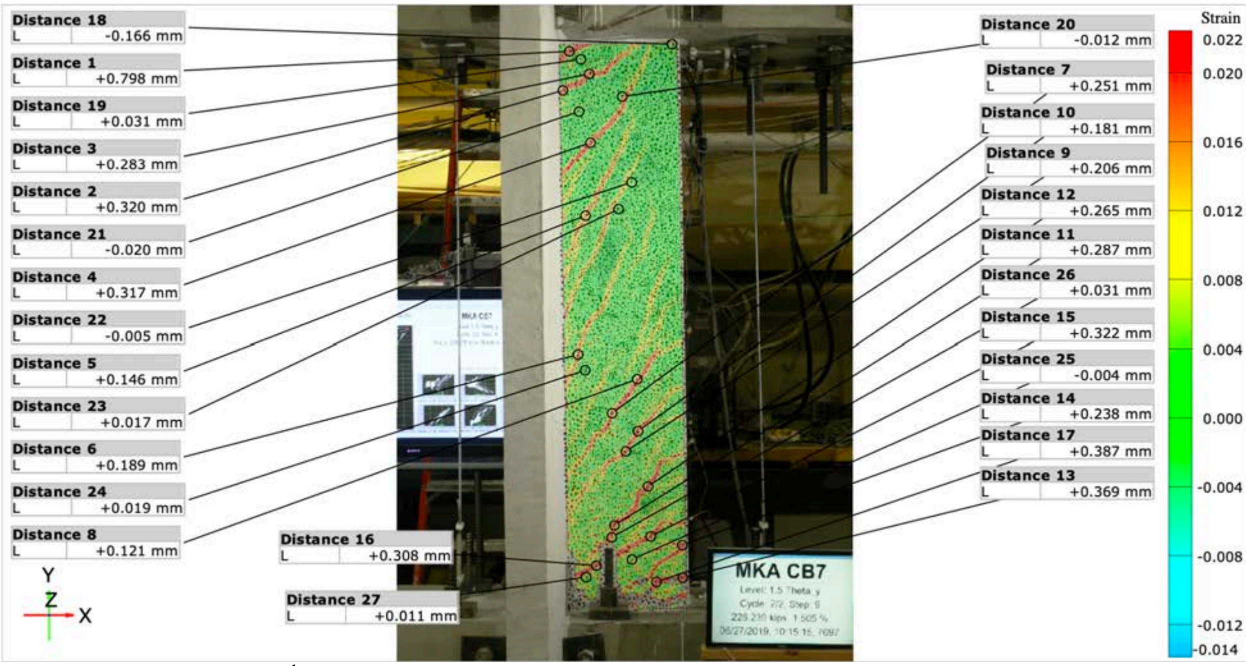

(*a*) 2nd cycle at peak ductility demand of 1.5 in the positive direction

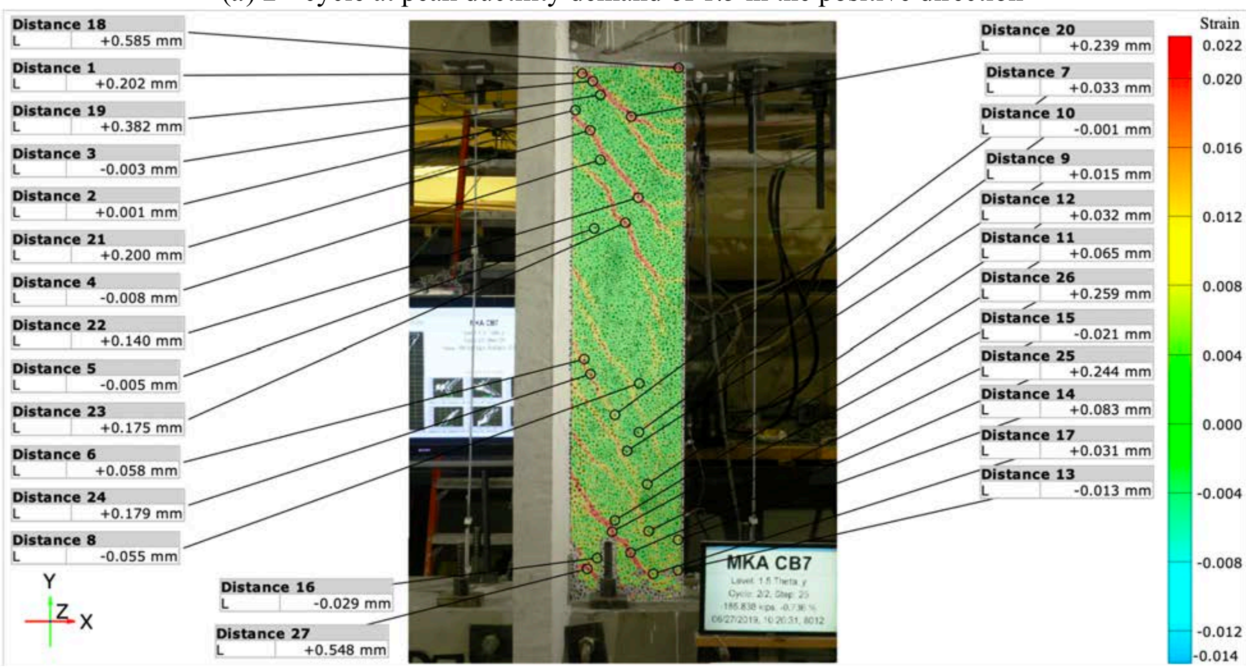

(*b*) 2nd cycle at peak ductility demand of ~ 0.75 in the negative direction

Figure H-22. Crack pattern and widths obtained from DIC for CB7. (Note: 1 mm = 0.0394 in.)

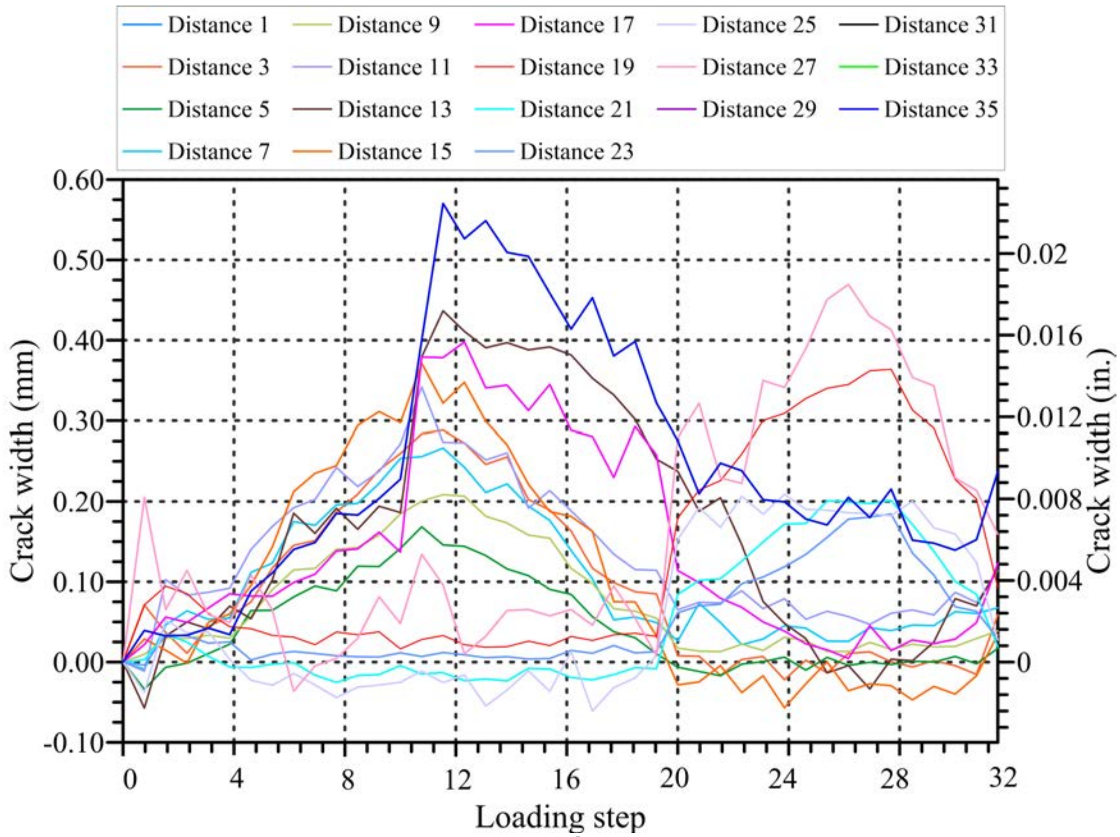

Figure H-23. Crack width history during 2nd cycle at ductility demand of 1.5 for CB7.

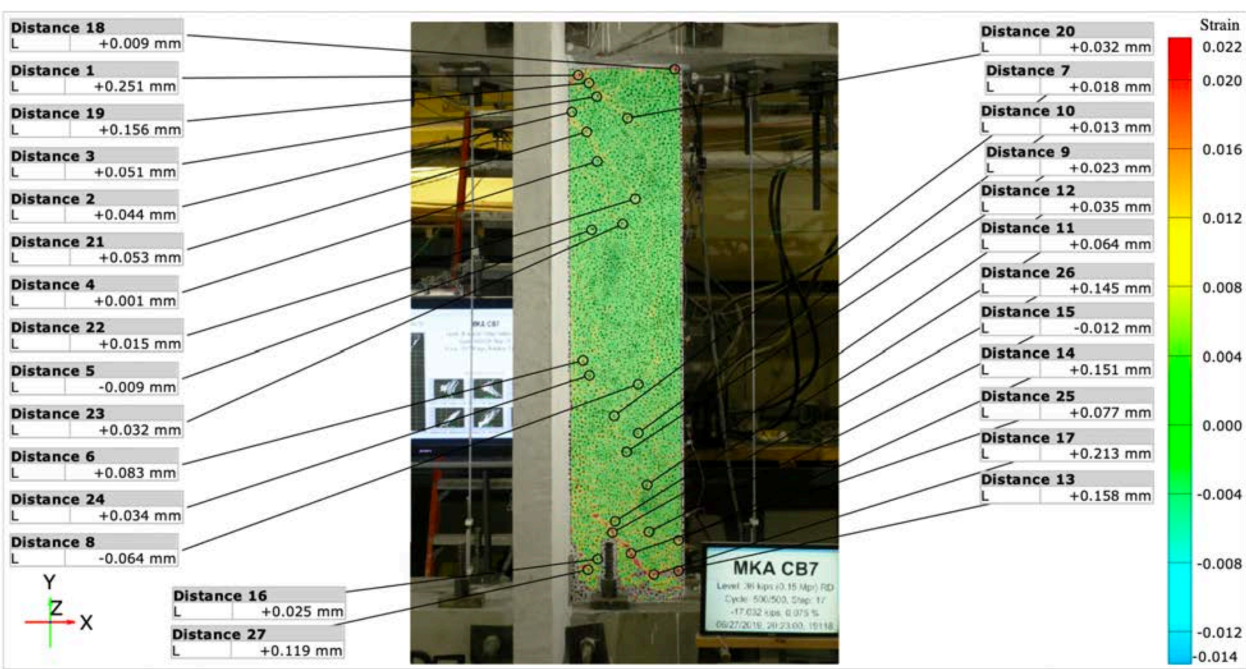

Figure H-24. Crack pattern and widths obtained from DIC for CB7 at zero rotation at end of wind loading protocol. (Note: 1 mm = 0.0394 in.)

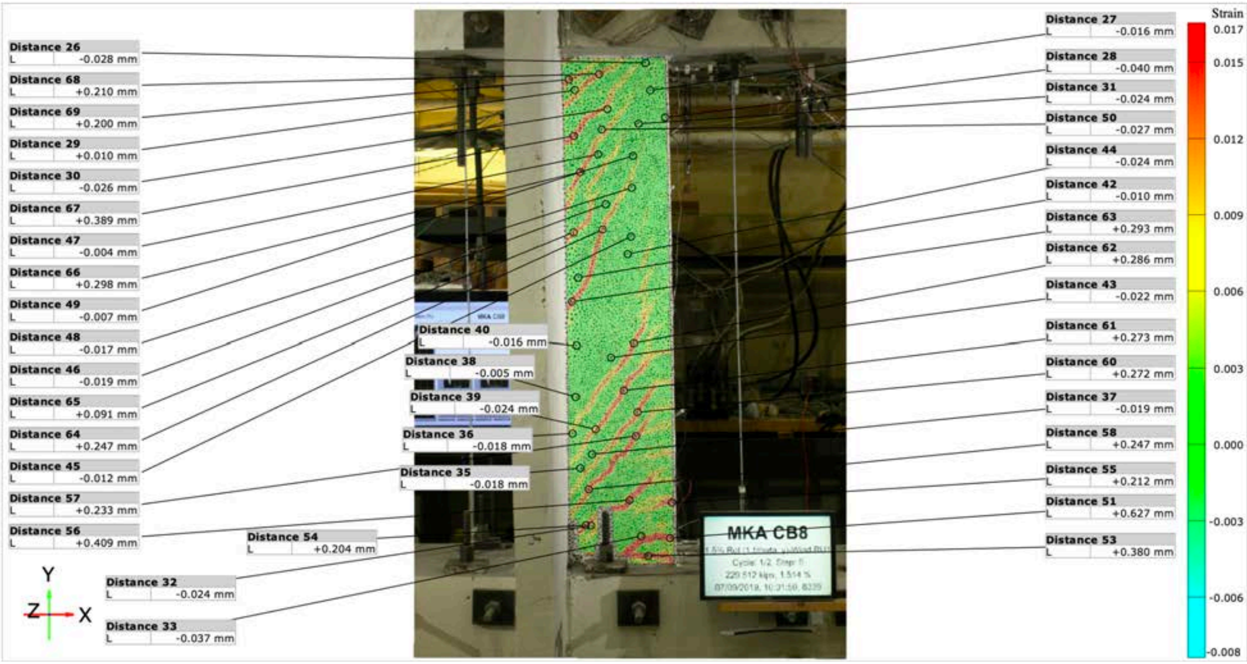

(*a*) 1st cycle at peak ductility demand of 1.5 in the positive direction during first ramp-up

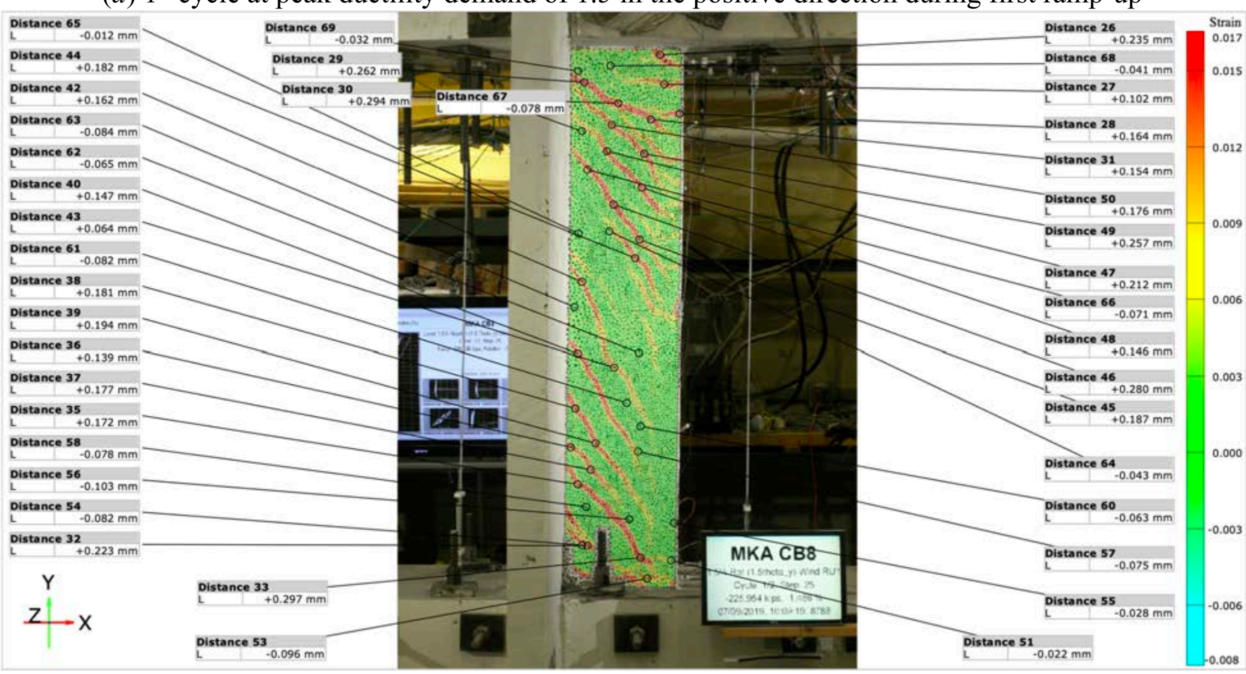

(*b*) 1st cycle at peak ductility demand of 1.5 in the negative direction during first ramp-up

Figure H-25. Crack pattern and widths obtained from DIC for CB8. (Note: 1 mm = 0.0394 in.)

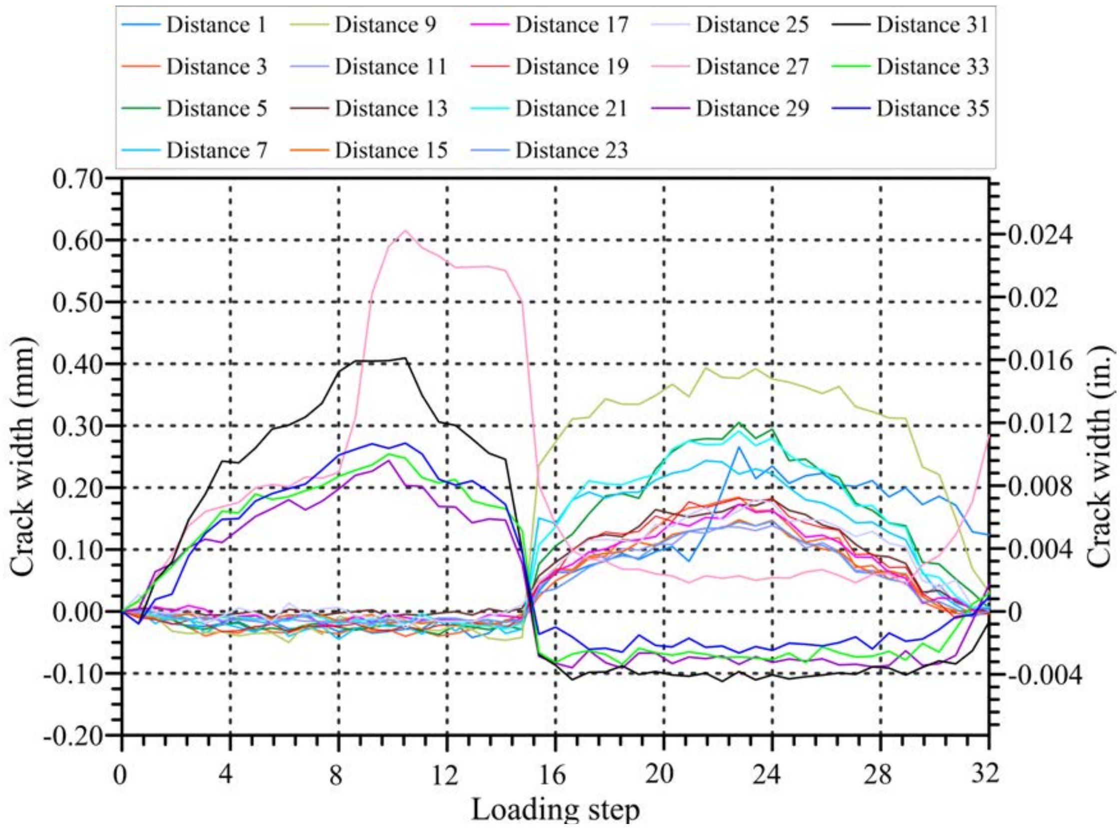

Figure H-26. Crack width history during 2nd cycle at ductility demand of 1.5 for CB8.

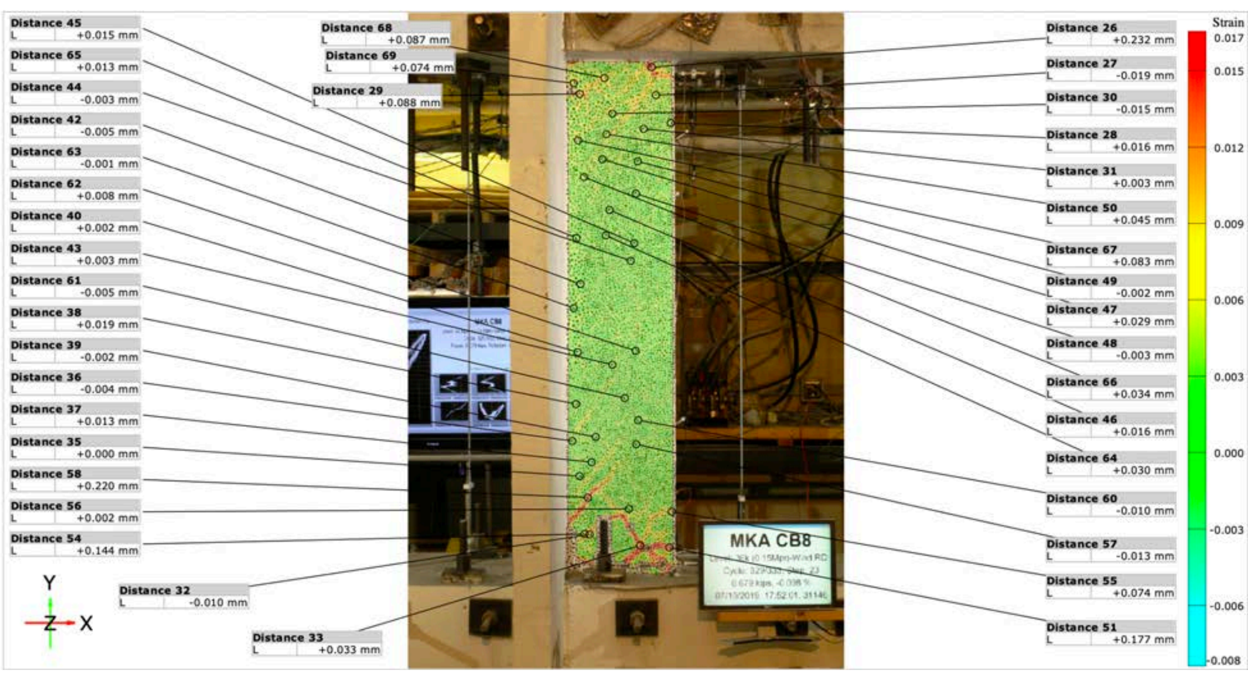

Figure H-27. Crack pattern and widths obtained from DIC for CB9 at zero rotation at end of wind loading protocol. (Note: 1 mm = 0.0394 in.)